Title

The Application of Luminescence to Tectonics: Improvements to Luminescent Dating and its Utilization in High-Energy Depositional Environments

Author

Lawson, Michael

Publication Date

2017

UNIVERSITY OF CALIFORNIA

Los Angeles

The Application of Luminescence to Tectonics:

Improvements to Luminescent Dating and its Utilization in High-Energy Depositional Environments

A dissertation submitted in partial satisfaction of the
requirements for the degree Doctor of Philosophy
in Geology

by

Michael Joseph Lawson

2017

ABSTRACT OF THE DISSERTATION

The Application of Luminescence to Tectonics:
Improvements to Luminescent Dating and its Utilization in High-Energy Depositional Environments

by

Michael Joseph Lawson
Doctor of Philosophy in Geology
University of California, Los Angeles, 2017
Professor Edward J. Rhodes, Co-Chair
Professor An Yin, Co-Chair

The dissertation presents improvements made to luminescent dating in tectonic areas, with examples of the application of luminescence to tectonic questions north of Death Valley, CA. The study of tectonics is incomplete without an understanding of fault processes through time. This can be difficult in areas with limited Quaternary age control. The technique of luminescence dating can provide absolute ages, but tectonic areas tend to exhume fresh material that can have poor luminescent properties. The "quartziness test" is outlined which numerically accesses the contamination of feldspar grains within quartz samples for small aliquots and single grain measurements. A new illumination protocol called Sinusodially Modulated Optically Stimulated Luminescence (SM-OSL) is presented which can also address contamination through trap component analysis and provides more rapid measurement then tranditional Linearly

Modulated Optically Stimulated Luminescence (LM-OSL)

Post- infrared infrared-stimulated luminescence (pIRIR) has been shown to be effective dating protocol that does not fade to the same degree as traditional IRSL measurements. Post-IRIR is applied to several studies pairing luminescence dating with geomorphic analysis. In Deep Springs Valley, a series of shorelines have been rotated vertically due to local extension. Two shorelines are dated as having ages of 7.51 ± 0.67 ka and 10.94 ± 0.95 ka, suggesting ~0.3 mm/yr vertical slip on the Deep Springs fault. These are comparable to long-term rates of 0.2 mm/yr (vertical and horizontal). In Eureka Valley, a tectonically controlled basin east of Deep Springs, slip recurrence is analyzed by pairing pIRIR with geomorphic modeling to produce a new mass diffusivity constant (κ) of 1.79 m^2ka^{-1}. In this area, a 6.1 moment magnitude earthquake occurred on May 17, 1993. Geomorphic modeling of the northern strand of this oblique-normal fault suggests a vertical slip rate of 0.6 mm/yr. Field mapping in the area uncovered a right lateral fault that may be the cause of an observed decrease of slip on the Fish Lake Valley Fault Zone (FLVFZ).

The dissertation of Michael Joseph Lawson is approved.

Raymond V. Ingersoll

Seulgi Gi Moon

Gilles F. Peltzer

Edward J. Rhodes, Committee Co-Chair

An Yin, Committee Co-Chair

University of California, Los Angeles

2017

DEDICATIONS

Dedicated to my wife Nicky for believing I could finish,

and to my Dad who passed away before it was done.

TABLE OF CONTENTS

ABSTRACT OF THE DISSERTATION II

DEDICATIONS V

TABLE OF CONTENTS VI

LIST OF FIGURES IX

LIST OF ACRONYMS XI

ACKNOWLEDGEMENTS XII

VITA XIV

PUBLICATIONS XV

I: INTRODUCTION TO THE DISSERTATION 1

1.1 Introduction 1

1.2 Dissertation Organization 1

1.3 A Note on Terminology 2

1.4 Chapter Bibliography 4

II. INTRODUCTION TO LUMINESCENCE DATING APPLICATION IN TECTONICS 5

2.1 Introduction 5

2.2 Sensitivity Change 11

2.3 Sample collection and preparation 12

2.4 Analysis 13

2.5 Environmental dose rate 14

2.6 Applications: Usefulness for the dating of geological materials 14

2.7 Limitations of OSL and IRSL, and means to overcome them 16

2.8 Conclusion 17
2.9 Images 18
2.10 Chapter Bibliography 22
III. OSL AND IRSL CHARACTERISTICS OF QUARTZ AND FELDSPAR FROM SOUTHERN CALIFORNIA, USA 30
IV. ASSESSING OPTICALLY STIMULATED LUMINESCENCE (OSL) SIGNAL CONTAMINATION WITHIN SMALL ALIQUOTS AND SINGLE GRAIN MEASUREMENTS UTILIZING THE COMPOSITION TEST 37
V. SINUSOIDALLY MODULATED OPTICALLY STIMULATED LUMINESCENCE (SM-OSL) 46
5.1 Chapter Abstract: 46
5.2 Introduction 47
5.3 Theoretical Illumination 50
5.4 First-order kinetics 53
5.9 Conclusions 59
5.10 Images 60
VI. GEOMORPHOLOGIC SCARP ANALYSIS WITH FAST STATIC GPS AND LUMINESCENCE DATING IN EUREKA VALLEY, DEATH VALLEY NATIONAL PARK 64
6.1 Chapter Abstract 64
6.2 Introduction 65
6.3 Regional structures 67
6.4 Geomorphic modeling 71

6.5 Methods..72

6.6 Results..79

6.7 Discussion..87

6.8 Conclusions..88

6.9 Plate descriptions 90

6.10 Images...91

6.10 Chapter Bibliography...111

APPENDIX A- GPS MEASUREMENTS.. 116

APPENDIX B - DETAILS OF THE SAGITTA CORRECTION.. 149

APPENDIX C - GEOLOGIC OBSERVATIONS... 153

LIST OF FIGURES

Figure 2.1 Summary of the Quartz model 18

Figure 2.2 Diagram illustrating the band gap model comparing metals, semiconductors and insulators.. 19

Figure 2.3 Schematic model of the feldspar model (from Jain and Ankjaergaard 2011). 20

Figure 2.4 a) Raw luminescence in pIRIR 225 vs. IR 50 21

Figure 5.1 Comparison of OSL Stimulation Profiles.. 60

Figure 5.2 Example of the natural signal in Quartz 61

Figure 6.1 Major tectonic structures south of the study area. 91

Figure 6.2 EV Paleolake field area. 92

Figure 6.3 Geological map of the Dedeckera field area. 93

Figure 6.4 Error in Trimble data by site location... 94

Figure 6.5 Results from a measurement time test at Eureka Valley Paleolake Site. 95

Figure 6.6 Details of how scarp profiles were calculated. 96

Figure 6.7 Graphic detailing surveys 97

Figure 6.8 Details of how scarp model parameters were determined. 98

Figure 6.9 Post IRIR samples taken within 500 feet of the Loreta Mine road. 99

Figure 6.10 Details of streams in the Hanging Rock Canyon Field area, north of the road. 100

Figure 6.11 Details from the southern portion of Casteel thesis map (1984). 101

Figure 6.12 Scarp Profiles within Hanging Rock Canyon Field Area. 102

Figure 6.13 A-J Dedeckera scarp profiles... 105

Figure 6.14 Deep springs rotational data. 106

Figure 6.15 Eureka Valley Paleolake Rotation... 107

Figure 6.16 A & B Active stream traces, suggesting offset in the active streams...................... 108

Figure 6.17 Complex of faults accomodating shear. 109

LIST OF ACRONYMS

CW- Continuous Wave

ECSZ - Eastern California Shear Zone

FLVFZ - Fish Lake Valley Fault Zone

GPS – Global Positioning System

ICP- MS - Ion Coupled Plasma Mass Spectrometry

IRSL - Infrared Stimulated Luminescence

LIDAR – Light Detection and Ranging

LCT - Last Chance Thrust fault

LST - Light-Sensitive Traps

LM-OSL – Linearly Modulated - OSL

OSL - Optically Stimulated Luminescence

pIRIR225 – Post- IRIR measurement at 225º C

SM-OSL – Sinusoidally Modulated OSL

TL – Thermal Luminescence

VIR – Visible Radiation (~400 - 800 nm)

WLSZ – Walker Lane Shear Zone

ACKNOWLEDGEMENTS

I first must thank my dad, who inspired my earliest interests in geology. Second, I thank my committee for helping me work through this dissertation, with good advice and direction. Ed, thank you so much for all of your late night work editing. Thank you to Gilles for helping me with the math in Chapter 5. I thank Steve Okubo for his contributions to the mapping of the Eureka Valley normal fault complex (see plate 2). Also, thank you to Jeff Knott for paving the way in Eureka Valley.

Chapters Three and Four are reprinted from the scientific journals “Radiation Measurements” and “Quaternary International,” respectively. I appreciate the reviewers and editors for their helpful comments.

I also thank Southern California Earthquake Center (SCEC) for funding portions of this research. Thank you also to Harold and Mayla Sullwold, as well as Clem Nelson for their generous scholarship support.

Thanks to my fellow graduate students, especially Tig, Chris and Nate for checking my runs, and helping me balance children and graduate school. Thanks to friends and colleagues in the field. Thanks to Kevin, whose conversation always brought a smile to my face. Thanks to Debbie for helping me with the analysis of microseismicity in Death Valley. Thanks to the great people at the Space Physics Center at UCLA for helping me along the path. Thank you to the students, staff and faculty on the UCLA Elfin CubeSat project for giving me healthy distractions from academic work. Thank you to Liz and Nicky for helping me out with the formatting.

I couldn’t have completed my thesis without some amazing caregivers for my children while I was in the field. Thank you to Miss Sharon, Lena, and especially Gail. To Marvin and

Danny, thank you for forcing me to take a day off in the Eureka Valley Sand Dunes. To my family, thanks for suffering through long absences, missed gatherings, and forgotten phone calls. Thanks to my Mom and Dad for supporting me through it all.

Finally, I give special thanks to my sons Graham and Bryce for making every day special and fun with little things. To my wife Nicky, thank you for being with me on this long and complicated journey. What big project should we start next?

VITA

2008	Clem Nelson Scholarship Award University of California, Los Angeles
2008	B.A. in Geology, Departmental Valedictorian University of California, Los Angeles
2008- 2017	Flight Certified Electronics Technician, Space Physics Center Institute of Geophysics and Planetary Physics University of California, Los Angeles
2008- 2011	Field Work: Magnetometer Installation Various Locations University of California, Los Angeles
2009	Certificate of Recognition for Heroism State of California Senate
2012	Harold and Mayla Sullwold Scholarship University of California, Los Angeles
2013	Christmas Canyon Garlock fault Dating Project, Ridgecrest, CA
2013	Walker Lane Paleoshoreline Dating Project, Hawthorne, NV
2013- 2017	Teaching Assistant Earth, Planetary, and Space Sciences University of California, Los Angeles
2014	Planetary Science Summer School Jet Propulsion Laboratory, CA
2015	Field Work: Denali fault Trenching Project, Cantwell, AK
2015- 2016	Field Work: Eureka, Deep Springs, and Fish Lake Valleys, CA and NV

PUBLICATIONS

Lawson, M.J., Daniels, J.T.M., Rhodes, E.J., 2015, Assessing Optically Stimulated Luminescence (OSL) Signal Contamination within Small Aliquots and Single Grain Measurements Utilizing the Composition Test, Quaternary International, v. 362, p. 34-41.

Lawson, M.J., Roder, B., Stang, D., Rhodes, E. J., 2012, OSL and IRSL characteristics of quartz and feldspar from southern California, USA, Radiation Measurements, v. 47i (9), p. 830-836.

Roder, B., **Lawson, M.J.,** Rhodes, E., Dolan, J., McAuliffe, L, McGill, S., 2012, Assessing the potential of luminescence dating for fault slip rate studies on the Garlock fault, Mojave Desert, California, USA, Quaternary Geochronology, v. 10, p. 285 – 290.

SELECTED PRESENTATIONS

Lawson, M.J., & Rhodes, E.J., 2016, Sinusoidally Modulated - Optically Stimulated Luminescence (SM-OSL): a more rapid Linearly Modulated- OSL (LMOSL) and the quest for the medium component, 11th New World Luminescence Dating Workshop, University of Nebraska- Lincoln

Amador, E., Parcheta, C., Zareh, S., Sheehan, J.P., Albuja, A., & **Lawson, M.J.**, 2014, Enceladus Environmental Explorer (EVE), Planetary Science Summer School, Jet Propulsion Laboratory, California

Lawson, M.J., Yin, A., & Rhodes, E. 2015, The Role of source material in basin sedimentation, as illustrated within Eureka Valley, Death Valley National Park, CA, AGU

Watkins, J., Scully, J., **Lawson, M.J.**, Rhodes, E., & Yin, A., 2015, Emplacement Mechanisms and Evolution of the Long-runout Quaternary Eureka Valley Landslide in Eastern California, AGU

Lawson, M.J., Yin, A., & Rhodes, E., 2015, Preliminary investigations into the Fish Lake Valley Fault Zone (FLVFZ) and its interactions with normal faulting within Eureka and Deep Springs Valleys, SCEC

I: INTRODUCTION TO THE DISSERTATION

1.1 Introduction

The dissertation examines the application of luminescence to tectonic investigations. Luminescence dating has been used extensively (Wintle, 2008) and has great potential to solve a number of geological questions, but its application has been difficult in tectonically active areas (explained in greater detail in chapter 2). The goal of this research is, therefore, to improve the technique in its applications toward solving problems within the field of tectonics.

To address these issues, a “quartziness test” is developed utilizing differences in thermal responses to determine whether OSL samples had been contaminated by errant feldspar grains. This is typical in tectonically active areas where quartz is dim due to a lack of sensitization, but where feldspar samples tend to have inherently strong signals (see chapter 3). This is true of bedrock samples, and suggests that areas of rapid exhumation are poor for quartz-based luminescence techniques. For this reason, feldspar IRSL based techniques are becoming the preferred technique utilized by the luminescence dating community despite the challenges of anomalous fading (for TL: Wintle, 1973; for optical: Spooner, 1992).

Therefore, newer feldspar IRSL techniques, specifically post- IR IR at 225ºC (abbreviated to pIRIR225), are then applied to determine geomorphic slip rates of oblique-normal faulting in Eureka Valley. Preliminary results in Death Valley utilize luminescence ages and scarp denudation modeling to refine the mass diffusivity constant, which is subsequently applied to other scarps within Eureka Valley.

1.2 Dissertation Organization

The dissertation offers improvements in optical and infrared luminescence and their application to tectonics. It is divided into three sections: introduction to the problem, improvements to optical and infrared luminescence, and applications of luminescence to the study of tectonics.

The first section is composed of two chapters. Chapter One summarizes the major themes that the thesis covers, providing a road map of the dissertation structure and expanding upon the chapter abstracts. Chapter Two presents details on the optical and infrared luminescence techniques used in the dissertation, and reviews the literature on tectonic applications of optical and infrared luminescence.

Section two presents the author's contributions toward improving the application of optical and infrared luminescence in areas undergoing recent tectonic formation. Chapter Three is a reprint of the author's 2012 article, "OSL and IRSL Characteristics of Quartz and Feldspar from Southern California, USA" (Lawson et al., 2012). Chapter Four is a reprint of the author's 2015 article, "Assessing Optically Stimulated Luminescence (OSL) Signal Contamination within Small Aliquots and Single Grain Measurements Utilizing the Composition Test" (Lawson et al., 2015). Chapter Five introduces a new measurement technique called sinusoidally modulated optically stimulated luminescence (SM-OSL) that can decrease measurement time for traditional linearly modulated optically stimulated luminescence (LM-OSL).

Finally, section three covers the applications of optical and infrared luminescence in tectonically active settings. Chapter Six explores infrared luminescence with geomorphological techniques in Eureka Valley in the northwest of Death Valley National Park.

1.3 A Note on Terminology

In this dissertation, "Optical and Infrared Luminescence" is used to refer to the field of study that utilizes visible or infrared light to stimulate the emission of luminescence from a natural mineral. The field of study is generally known as Optically Stimulated Luminescence

(OSL), but this is imprecise as OSL is also the name of a specific quartz-based technique where stimulation is accomplished with blue green light (~470 nm stimulation, Bøtter-Jensen et al., 2003). This can be doubly confusing since feldspar luminesces in both optical (typically seen as a contaminant in quartz OSL measurement; Lawson et al., 2015) and infrared (IRSL, ~870 nm stimulation; Bøtter-Jensen et al., 2003) wavelengths.

The specific techniques of OSL and IRSL are too intertwined in the literature, and too physically similar not to be grouped together in some way. Their principal difference is that one technique is stimulated by a wavelength that is invisible to the human eye. Conversely, the term "Luminescence" is too broad, as it can also refer to other fields of inquiry (Cathodoluminescence, Thermo-Luminescence, or Radioluminescence), or to various physical processes (triboluminescence, piezoluminescence, etc.). "Photoluminescence" is a term used in the material sciences and nanotechnology fields, denoting the spontaneous emission of light following photon stimulation but not necessarily with visible radiation (VIS; ~400 - 800 nm). This area of study involves very similar processes as seen in OSL and IRSL, but typically involves man-made materials that can have very different characteristics than those utilized in geology.

To avoid confusion, each measurement technique is given a qualifier to denote the specific mineral targeted for measurement. Thus, quartz OSL is termed qOSL to indicate that it reflects OSL measurements of a sample that has been treated through density separation and chemical treatments such that the majority of the grains are quartz. Secondly, quartz is not the only material that can luminesce in the optical range (plagioclase, halite, zircon & olivine to name a few). Measurements involving alkali feldspars are termed kIRSL if using standard density separation (Wintle, 1997), or skIRSL to denote "super-K" separation (separated to be <

2.565gcm^3; Brown et al., 2015).

1.4 Chapter Bibliography

Bøtter-Jensen, L., Andersen, C. E., Duller, G. A. T., and Murray, A. S., 2003, Developments in radiation, stimulation and observation facilities in luminescence measurements: Radiation Measurements, v. 37, p. 535–541.

Brown, N.D., Rhodes, E.J., Antinao, J.L., and McDonald, E.V., 2015, Single-grain post-IR IRSL signals of K-feldspars from alluvial fan deposits in Baja California Sur, Mexico: Quaternary International, v. 362, p. 132- 138.

Lawson, M.J., Daniels, J.T.M., and Rhodes, E.J., 2015, Assessing Optically Stimulated Luminescence (OSL) signal contamination within small aliquots and single grain measurements utilizing the composition test: Quaternary International, v. 362, p. 34-41.

Lawson, M.J., Roder, B.J., Stang, D.M., and Rhodes, E.J., 2012, OSL and IRSL characteristics of quartz and feldspar from southern California, USA: Radiation Measurements, v. 47, p. 830–836.

Spooner, N.A., 1992, Optical dating: preliminary results on the anomalous fading of luminescence from feldspars: Quaternary Science Review, v. 11, p. 139-145.

Wintle, A.G., 2008, Luminescence dating: where it has been and where it is going: Boreas, v. 37, p. 471-482.

Wintle, A.G., 1997, Luminescence Dating: Laboratory Procedures and Protocols: Radiation Measurements, v. 27, p. 769-817.

Wintle, A.G., 1973, Anomalous fading of thermoluminescence in mineral samples: Nature, v. 245, p 143-144.

II. INTRODUCTION TO LUMINESCENCE DATING APPLICATION IN TECTONICS

2.1 Introduction

Optically Stimulated Luminescence (OSL) is the physical process by which ionizing environmental radiation is absorbed within a mineral, and later released as light upon exposure to an optical wavelength of photon stimulation (Murray and Wintle, 2000), first introduced by Huntley et al. (1985) who refer to it as Optical Dating. The process has since been applied to two different light-exposure dating techniques: Optically Stimulated Luminescence (OSL; Huntley et al., 1985) and Infrared Stimulated Luminescence (IRSL; Hütt et al., 1988). These can both be described in simple terms as having several steps: a gradual trapping of electrons, exposure to light leading to detrapping, travel to recombination centers through one of several pathways, and emission of light with some energy loss in the form of heat as recombination occurs (Huntley et al., 1985). These processes are explained in greater detail below where relevant to the application of dating within tectonics.

First, some action adds energy from ionizing radiation to a crystal lattice in the form of a trapped charge (as either an electron or a hole). In the case of OSL and IRSL, natural environmental radiation is absorbed by the mineral, and if the material is buried (i.e. not being stimulated by optical or infrared photons) trapped charge builds up with time. In a simple system, we may consider electrons that become trapped between the valence and conduction bands within mineral grains.

Quartz is the simplest system (see Figure 1) and is commonly used for dating sediments, consisting of several discrete trap types responsible for the fast, medium, and slow OSL components (Smith and Rhodes, 1994). Work on the different quartz OSL components (Bailey et al., 1998; Singarayer and Bailey, 2003) has led to the construction of a numerical model for quartz luminescence (Bailey et al., 1997). This numerical model is a “wire diagram” for the internal wiring of the quartz luminescence system.

Feldspar probably consists of a single dominant trap type (Hütt et al., 1988, Baril and Huntley, 2003) unlike quartz, which has over 4 or 5 traps (known as ultrafast, fast, medium, slow1, slow2, etc.). Thus while feldspar has probably only a single trap depth, quartz has several (at differing depths denoting the difficulty in stimulating the electron to detrap to the conduction band). In quartz, this difference in trap depth is observable in Linearly Modulated OSL (see Chapter 5) where stimulation intensity is increased linearly through the observation (Bulur 1996).

In feldspar, this signal is obscured, as several pathways exist for detrapping. Conduction band tails have been observed in low temperature measurements (Poolton et al., 2002), and would make the transition into the conduction band “fuzzier,” allowing for a continuum of pathways for detrapped electrons below the boundary of the conduction band. As well, several quantum tunneling pathways exist: ground state tunneling (known as anomalous fading), tunneling from any number of excited states, or tunneling from the continuum of band tail states below the conduction band (Jain and Ankjaergaard, 2011). These two effects make feldspar IRSL emission appears as a continuum of any number of trap depths (Poolton et al., 2002). Jain and Ankjaergaard (2011) provide a model for feldspar IRSL production. This process is not entirely understood in OSL or IRSL, but these two conceptual models exist for the physical aspects of traps.

For quartz OSL, trapping probably occurs either at point defects within the crystal structure and/or is associated with interstitial ions within the material. Defects within the crystal structure are for example where Si is replaced by Ti in the quartz lattice (Rhodes, 2011). Charge is balanced by interstitial ions; examples include an electron trap constituted as $[TiO_4/ Li^+]^0$ or a hole center comprising $[AlO_4]^0$ (Weil, 1984, Rhodes, 2011). Upon exposure to light of appropriate energy, trapped electrons are detrapped, move within the crystal structure, and upon interaction with luminescence centers, emit light whose intensity is related to the original trapped charge population (and therefore their absorbed dose).

Trapped electrons have been shown to be stable in quartz OSL. Aitken (1985) calculates a trap lifetime of 100 million years at 15ºC for the 325ºC TL trap associated with OSL (Smith et al., 1986). Other researchers utilize isothermal decay of quartz OSL signal to show that the mean trap lifetime is indeed in the order of 10^8 years (Smith et al., 1990; Murray and Wintle, 1999). Alkali feldspars are shown to have a trap due to a single defect (Hütt et al., 1988). This trap is less stable, however, and can fade anomalously (Spooner, 1992). This process known as anomalous fading will be described in greater detail below.

Traps are exceedingly rare things in these systems in terms of the number of physical traps per the volume of a crystal. As an example, Malibu beach sand (J0048) has a very bright quartz signal. Curve fitting through LM-OSL measurements (described in detail below in chapter 5) shows the total number of electron recombination events measured to be ~ 10^4- 10^5 for each of the component within the crystal (fast, medium and three slow components) with an aliquot of c. 100 grains. Typically in quartz, that signal is from a small number of bright grains mixed among less responsive grains. Hypothetically, imagine that the signal is spread equally to those 100 grains, each would then be responsible for ~ 10^2- 10^3 traps. Also imagine a sand grain of quartz that is 125 μm in diameter; quartz (SiO_2) has a density of 2.65 g/cm^3. Using Avogadro's number this represents ~10^{13} atoms per sand grain. Thus, rough calculation suggests that there is one trap for every 10^{11} atoms in a quartz crystal. It should be noted that industrially, even high purity quartz is seen as anything with less than 50 ppm impurities (Harben, 2002).

The method of stimulation that detraps electrons varies depending upon the method of luminescence. Energy can be applied in the form of heat (as in Thermoluminescence, or TL (Aitken, 1985)), or combined with light in the case of Optically Stimulated Luminescence (OSL) or Infrared Stimulated Luminescence (IRSL). OSL can be measured utilizing either quartz (Smith et al., 1986) or feldspar (Godfrey-Smith et al., 1988), while IRSL is produced by feldspar but not quartz (Hütt et al., 1988). The energy of the emitted photon is lower in wavelength (and thus higher in energy) than the energy used to excite the photon, and differs from florescence where a mineral releases a photon of lesser energy than the excited photon.

Several forms of luminescence exist, including Triboluminescence, Radioluminescence (RL)/ Radiofluorescence, Piezoluminescence, Thermoluminescence (TL), Optically Stimulated Luminescence (OSL) and Infrared Stimulated Luminescence (IRSL), though only the final three are of direct interest when dating tectonically disturbed sediments.

Quartz OSL is stimulated in the visible spectrum with blue-green photons, utilizing LEDs typically at 470 nm in systems built by Risø (Bøtter-Jensen et al., 2000), 458 ± 5 nm or at 525 ± 20 nm in an alternative Lexsygsmart system, or with laser stimulation (532 nm 10 mW laser for the Risø single grain reader, 445 ± 3 nm Lexsygsmart). Additional traps may be accessible through violet (405 nm) stimulation (Jain, 2009), and “red” stimulation (Martini et al., 2009). Feldspar can be stimulated at several wavelengths, including blue-green, red (Stokes and Fattahi, 2003) and within the infrared (Duller, 1997). Most feldspar measurements for the dating of materials utilize infrared stimulation, at 870 nm IR LEDS (for Risø), 850 ± 20 nm (Lexsygsmart) or IR diode modulated laser (830 nm Risø, or 850 ± 3 nm for Lexsygsmart). All measurements for this dissertation have utilized a Risø TL-DA-20 TL/OSL reader. Both OSL and IRSL are usually measured above room temperature. There is no standard measurement temperature, but Quartz OSL typically is measured at 125ºC, while feldspar IRSL is often measured at 50ºC as well as higher temperatures.

After stimulation from traps, liberated electrons travel within the crystal structure (see Figure 2.2). With quartz, electrons are interpreted to travel in the conduction band and then recombine with other centers (notably luminescence centers, but also different forms of recombination centers as described below (Bailey, 2001)). In feldspar, a multitude of pathways exist, including direct recombination through quantum tunneling (Jain and Ankjaergaard, 2011), through conduction band tail states (Poolton et al, 2002) and different combinations of those processes. Quantum tunneling from the trapped electron's ground state is believed to be the cause of anomalous fading (Jain and Ankjaergaard, 2011), which has hindered earlier development of the feldspar IRSL technique. Newer approaches, such as post-IR IRSL, described below, have the potential to overcome fading.

Finally, those electrons recombine at hole centers emitting energy equivalent to the change in energy states. These can be either radiative or non-radiative centers. Chithambo et al. (2008) suggested that quartz has three radiative centers (L_h, L_l, and L_s). In quartz, these have been linked to the "Al centers" (Halliburton et al., 1981) or specifically to $[AlO_4]^0$ recombination centers (Martini et al., 2009). For Thermoluminescence, Martini et al. (1987) suggested 395 nm emission (3.1 eV) occurred at "dry" O^2- peroxy hole centers and 380 nm (3.2 eV) emission at a $(H_3O_4)^0$ hole center (Yang and Mckeever, 1990). For Cathodoluminescence, the 340 nm (3.6 eV) hole center is related to coupled Al^{3+} - Li^+ substitutes of Si^{4+} (Demars et al., 1996) while the 290 nm emission (4.3 eV) is linked to single oxygen vacancy centers (Feigl et al., 1974; Jones and Embree, 1976). Also there exist Non-Radiative centers (Aitken and Smith, 1988) also known as Killer, or “K” centers). These centers have been linked to oxygen vacancies in the crystal structure (Poolton et al., 2000). Annealing can decrease these vacancies, and thus increase sample sensitivity during exposure to high temperatures (500-600ºC) which retraps holes that form killer centers at new locations where they act as luminescence centers, leading to sensitivity change (Bøtter-Jensen et al., 1995). In quartz, some energy is emitted in the form of phonons, which are vibrations within the crystal structure that eventually become heat. It is believed that this is the cause of thermal quenching in quartz, where measurement at higher temperatures results in progressively weaker luminescence due to losses as phonons (Spooner 1994). Poolton et al., (2002a) suggest that the electronic gap within feldspar allows direct transitions, and thus no phonons are necessary for electronic transitions within or across the gap.

Thermal effects also exist within these systems. Thermal transfer of charge during the preheat in glacigenic quartz was shown to induce a signal equivalent to 10 Gy (Rhodes and Bailey, 1997). Quartz OSL also exhibits thermal quenching, which reduces the size of the emitted luminescence signal when measured at raised temperatures, as mentioned previously (Spooner 1994). Conversely, feldspar IRSL (and quartz OSL) also exhibit thermal assistance, an observation where measurement at higher temperatures results in greater intensity (Wiggenhorn, 1994). These are explained in greater details in chapter 3 and 4.

Some of the processes discussed above also play a significant role in dating protocols, or may cause unwanted effects when samples are contaminated with small volumes of other minerals, such as feldspar inclusions within quartz grains. For example, the traps responsible for quartz OSL emission are closely related to the 325º C TL peak (Smith et al., 1986; Wintle and

Murray, 1998) and form the basis for the preheat used in quartz OSL dating based on a multiple aliquot additive dose (MAAD) protocol (e.g. Rhodes, 1988). A preheat is used to remove charge from unstable traps following laboratory irradiation before OSL measurements (Rhodes 1988, Wintle and Murray, 1998). Progressively higher temperature preheats cause an increase in OSL signal between 140ºC and 210ºC, perceived to be from the transfer of charge from thermally unstable traps to those that are optically bleachable and more thermally stable (Rhodes 1988). As the donating traps are less stable, in natural samples these are partially empty due to natural thermal fading, with transfer already having occurred (Rhodes 1988). The requirement to have natural and irradiated OSL signals that are directly comparable to allow the construction of a meaningful growth curve means that a preheat is employed before both natural and irradiated OSL measurements.

2.2 Sensitivity Change

As mentioned above, quartz luminescence measured in the blue to UV region can change sensitivity as the availability of suitable luminescence centers in the crystal lattice change as a function of different treatments such as heating, irradiation, and UV light exposure (Zimmerman, 1971). So-called “killer centers” may convert to luminescence centers when quartz grains are heated if they have been subject to a large radiation dose previously, raising the sensitivity.

Feldspar tends to have greater luminescence sensitivity in natural samples, but minerology is an important consideration. Significant feldspar IRSL and OSL signals are observed from bedrock samples or grains recently eroded from bedrock. This makes feldspar both a potentially important mineral for dating in contexts where quartz sensitivity is low (Lawson et al., 2012), but also renders it a potentially problematic contaminant for quartz OSL studies in these circumstances (Lawson et al., 2015).

Different feldspar minerals have different sensitivities and other properties, with potassium feldspar often having higher IRSL sensitivities than other compositions (Rhodes, 2015; Daniels, 2016). Density separations using lithium metatungstate (LMT) or sodium polytungstate are used to separate different quartz and feldspar mineralogies.

2.3 Sample collection and preparation

Samples are collected from the field in ways to prevent their exposure to light before measurement in the laboratory, typically from shallow pits or trenches to access stratigraphically relevant materials. Samples are preferentially collected in material of optimum grain size (fine to medium sand) where significant layering is noted and visible lamination suggests that the sample has had little reworking by bioturbation. After cleaning the face, steel or aluminum tubes (approximately 15 cm long and 7.5 cm in diameter, providing approximately 1500 grams of material per sample) are hammered into the sediment using an aluminum cap that prevents light exposure and damage to the end of the tube. After collection, samples are capped with an opaque plastic cap that prevents sediment from escaping and prevents light exposure. The sample hole in the sediment is deepened and a gamma spectrometer inserted into each hole to determine the in-situ gamma ray dose rate from the surrounding sediment (as outlined in Rhodes (2015).

In the laboratory, samples are treated as outlined by Rhodes (2015) for feldspar. Under laboratory lighting conditions, samples are removed from the sampling tubes with care taken to separate the outer two to three centimeters (known as ends) which may have been exposed to light; this material is used to determine the in-situ water content of the sample and the concentration of U, Th and K using ICP-MS or ICP-OES. Water acts as shielding to irradiation, and estimating attenuation is necessary for environmental dose rate calculations. These portions of the sample are later used for inductively coupled plasma mass spectrometry (ICP-MS) analysis to determine the sample's bulk uranium and thorium concentrations, and ICP-OES (optical emission spectrometry) for bulk potassium values. The remaining portion of the sample within the tube is separated by grain size using wet sieving to isolate the 177 to 200µm fraction, followed by hydrochloric acid treatment of this fraction to remove carbonates. After drying, heavy liquid separation with lithium meta-tungstate (LMT) with a density of 2.565 g.cm^{-3} is used to isolate potassium feldspar (known in the lab as "Super- k"), which targets the most potassic grains, which typically have higher sensitivity (Brown et al., 2015; Rhodes, 2015). Quartz is separated using standard techniques (Rhodes et al., 2010; Wintle, 1997). For some samples, an etch in 10% HF (hydrofluoric acid) for 10 minutes is used to etch the surfaces of the grains, improving light transmission into and out of the grains. However, where sample yields were low, no HF treatment is used, as this tends to reduce the volume of sample significantly. Etched samples undergo a second sieve treatment at 177 µm to remove grain fragments and heavily etch grains.

Samples are measured on a Risø TL-DA-20 reader equipped with a calibrated strontium 90 beta source. Quartz samples are measured on aluminum disks upon which a small dab of silicone oil adheres grains in aliquots comprising 50 – 200 grains (Wintle and Murray, 2006). For single grain measurements, samples are measured in Risø single grain disks, which have 100 holes of 300 µm diameter, suitable for grains in the range 125-250 µm (Duller, et al. 2000). . Samples are measured either with an IR laser (in the case of feldspar), or with a blue-green laser for quartz samples.

2.4 Analysis

Given the possibility of partial bleaching of OSL samples, different statistical age models are utilized: either the minimum age model (which expresses the minimum possible age of the deposit), the central age model (Galbraith et al., 1999), or the finite mixture model developed by Rhodes (2015) and Brown et al. (2015) based on selection of discrete single grain values.

2.5 Environmental dose rate

The environmental dose rate is measured in-situ with a calibrated EG&G ORTEC MicroNOMAD portable NaI gamma spectrometer. Portions of each sample are also measured for the environmental concentration of radioactive elements, the principal ones being uranium, thorium and potassium. Inductively coupled plasma mass spectrometry (ICP-MS) analysis is used to determine the samples bulk uranium and thorium concentrations. ICP-OES (optical emission spectrometry) is utilized for bulk potassium values.

The dose rate is assumed to be constant, but there is the potential for beta dose rate heterogeneity in laboratory irradiation (Rhodes, 2011). There is also the possibility of Uranium series disequilibrium (Rhodes, 2011). This is primarily due to the loss of Radon gas (^{222}Rn; a daughter of Uranium (^{238}U) decay chain). The other elements in this chain are solids, but Radium is a gas and the possibility exists that it can leave the environment. Comparison between the in-situ NaI gamma spectrometer determination of U concentration, based on ^{214}Bi near the based of the ^{238}U decay series and the U concentration estimated from the ICP-MS analysis which measures ^{238}U directly provides an approximate assessment of U-disequilibrium (Rhodes et al., 2006).

2.6 Applications: Usefulness for the dating of geological materials

Luminescence has been applied as an archaeological and geological dating technique, notably TL, OSL or IRSL for more than 20 years (Rhodes, 2011). Murray and Olley (2002) compare OSL and independent ages, and conclude that quartz OSL works well from the last century to at least 350 ka. As previously stated, the minerals absorb ambient radiation and when stimulated by light or heat, emit blue or UV photons whose intensity is related to the dose absorbed. Through the comparison of the amount of radiation a grain has absorbed and the annual in situ radiation exposure it experiences, a burial date for a material can be determined (Huntley et al., 1985).

Numerous protocols exist, but the most successful has been Single Aliquot Regenerative-dose (SAR) protocol for quartz OSL (Murray & Wintle, 2000); Murray and Wintle 2003. This method provides correction for sensitivity change, and involves applying multiple doses followed by measurement to experimentally determine how a material reacts to laboratory irradiation. In broad terms, this SAR approach can be applied to single grain measurements in both quartz (Murray & Roberts, 1997) and feldspar (Brown et al., 2015).

Given that luminescence dating utilizes minerals that are ubiquitous in the sedimentary record (quartz OSL and feldspar IRSL), this tool works well in desert environments where a lack of suitable material often hinders carbon 14 dating. Further OSL and IRSL allow for the dating of the material much older than carbon 14, allowing for sediments to be dated to up to 200,000 years or more for both approaches. The dating of Quaternary environments has been dominated by radiocarbon dating, but this can be difficult in fluvial and tectonic environments where there is often a shortage of suitable material. With OSL or IRSL, deposited materials are dated directly, while radiocarbon relies upon finding pieces of charcoal embedded within deposited beds. This allows for more systematic sampling strategies, for example sampling every 1.5 cm (Stang et al., 2012). Luminescence dating techniques are not without limitations, however, the greatest being incomplete bleaching of the signal at the time of deposition and anomalous fading of feldspar signals, discussed further below.

2.7 Limitations of OSL and IRSL, and means to overcome them

Luminescence dating has issues with partial bleaching, fading in ISRL, and bioturbation. Partial bleaching occurs when a sample isn't completely reset upon deposition. This is more common when deposition is rapid, for instance in a rockslide. As well, it is possible that grains are not exposed to light, such as in a rigid block landslide where material can move as a nearly coherent block. This is a greater issue in small aliquots, where an averaging occurs between the grains. Single grain measurements can be a way around this, as it allows for grains to be measured individually. Partial bleaching is especially an issue in arid areas for OSL. Lack of water in the desert makes fluvial systems rare and ephemeral. As previously mentioned, fluvial cycling has been shown to improve sensitivity in quartz (Pietsch et al., 2008). This can be very problematic in the case of quartz samples, where quartz signals are weak due to a lack of sensitivity.

Reliable ages can be determined however in some instances of partial bleaching. If a resetting event has occurred in a heterogeneous way, single grain measurements can rigorously evaluate the Equivalent dose of many grains at a time. A single grain disk has 100 holes for grains, typically containing one to several grains within in them. By measuring multiple disks, it is possible to understand the statistical spread of the resetting signal. The most recent resetting event is not necessarily the youngest grain in your sample, as bioturbation could have errantly mixed in grains that were not representative of the event we were trying to assess.

For this reason, OSL researchers sample in well preserved stratigraphic units. Fluvial units are preferred for sampling as well, since they reflect a depositional environment that is more favorable to complete resetting. In dry areas, wind can brings an influx of finer grained materials from above. For this reason we target larger grain sizes (125 -250 μm), assuming they are less mobile in the stratigraphy (Owen et al., 2011).

Sometimes dose heterogeneity is also a problem. OSL researchers assess this with in situ gamma spectroscopy that reflects the current gamma dose at the site where samples were taken. My lab utilizes a gamma spectrometer that is placed physically inside the hole left by the removal of the sample. This technique is favorable, since it gives a more complete picture of dose rate changes in stratigraphy. A complex stratigraphic sequence can contain layers that have different dose rates, for instance clay deposits can be slightly enriched while a very pure quartzofeldspathic sandstone would have a lower dose (Rhodes et al., 2006).

2.8 Conclusion

Luminescence dating as a technique has come a long way in the past 20 years. Additional work is necessary to gain a complete understanding of how these systems work. Sensitivity change in both quartz and feldspar suggest that these systems can be dynamic.

2.9 Images

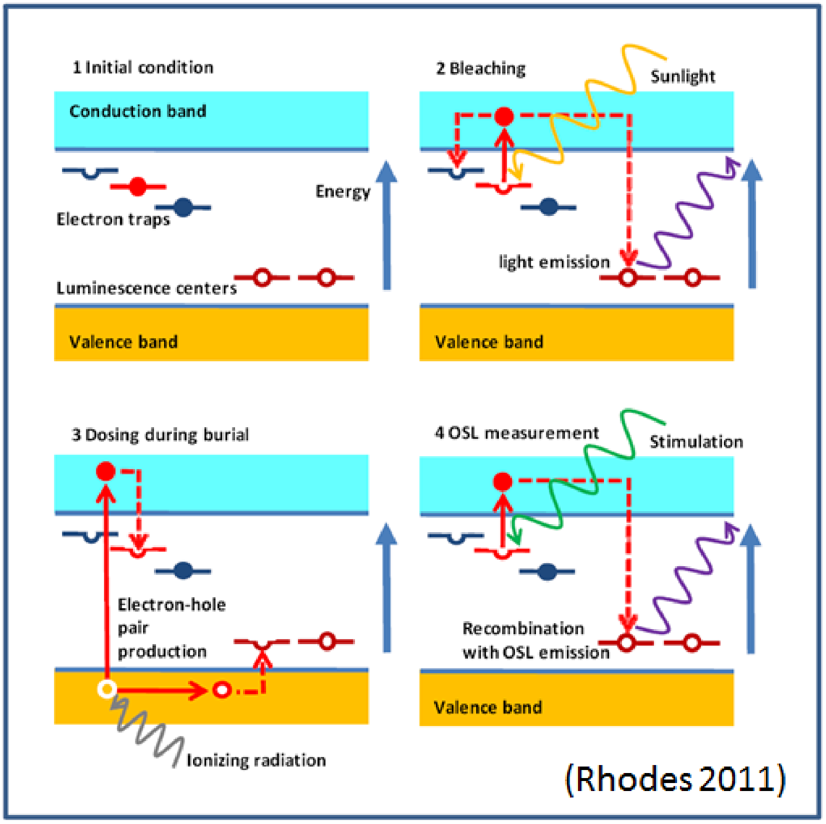

Figure 2.1 Summary of the Quartz model

(Modified from Rhodes, 2011). Several electron traps exist in quartz (fast, medium, and slow components). Sunlight stimulation adds energy to trapped electrons that move through the conduction band to luminescence or recombination centers. Ionizing radiation creates a donor-hole pair that increases with time. Stimulation in the lab detraps these electrons whose luminescence is observed.

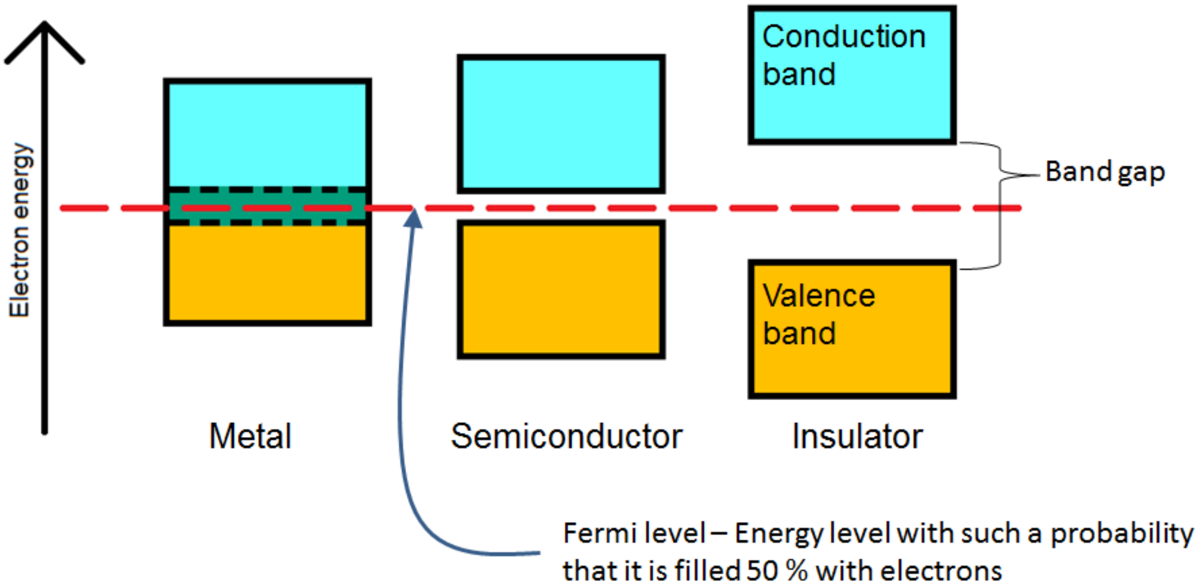

Figure 2.2 Diagram illustrating the band gap model comparing metals, semiconductors and insulators.

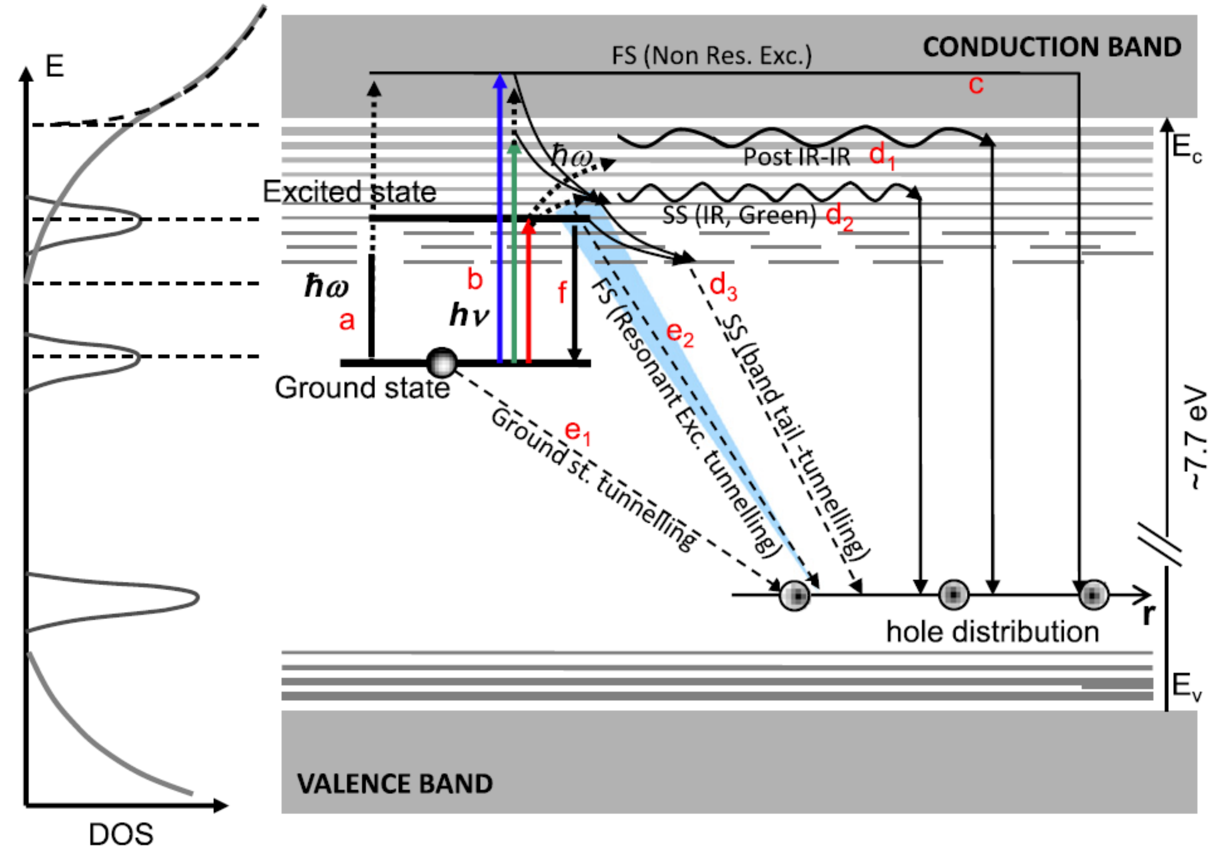

Figure 2.3 Schematic model of the feldspar model (from Jain and Ankjaergaard 2011).
Each of the arrows denotes the various pathways a detrapped electron can take to recombine with a hole and emit a photon: a) thermal excitations, b) optical excitations, c) recombination through the conduction band. d1) & d2) are end member paths through the band tail states, which make the transition into the conduction band "fuzzy." d1) high energy, high mobility states, d2) low energy, low mobility state, d3) deepest disconnected states. Several pathways exist for quantum tunneling: e2) tunneling from the exited state (related to TL e1) ground state tunneling, also known as anomalous fading. FS denotes "fast signal" while SS denotes "slower signal."

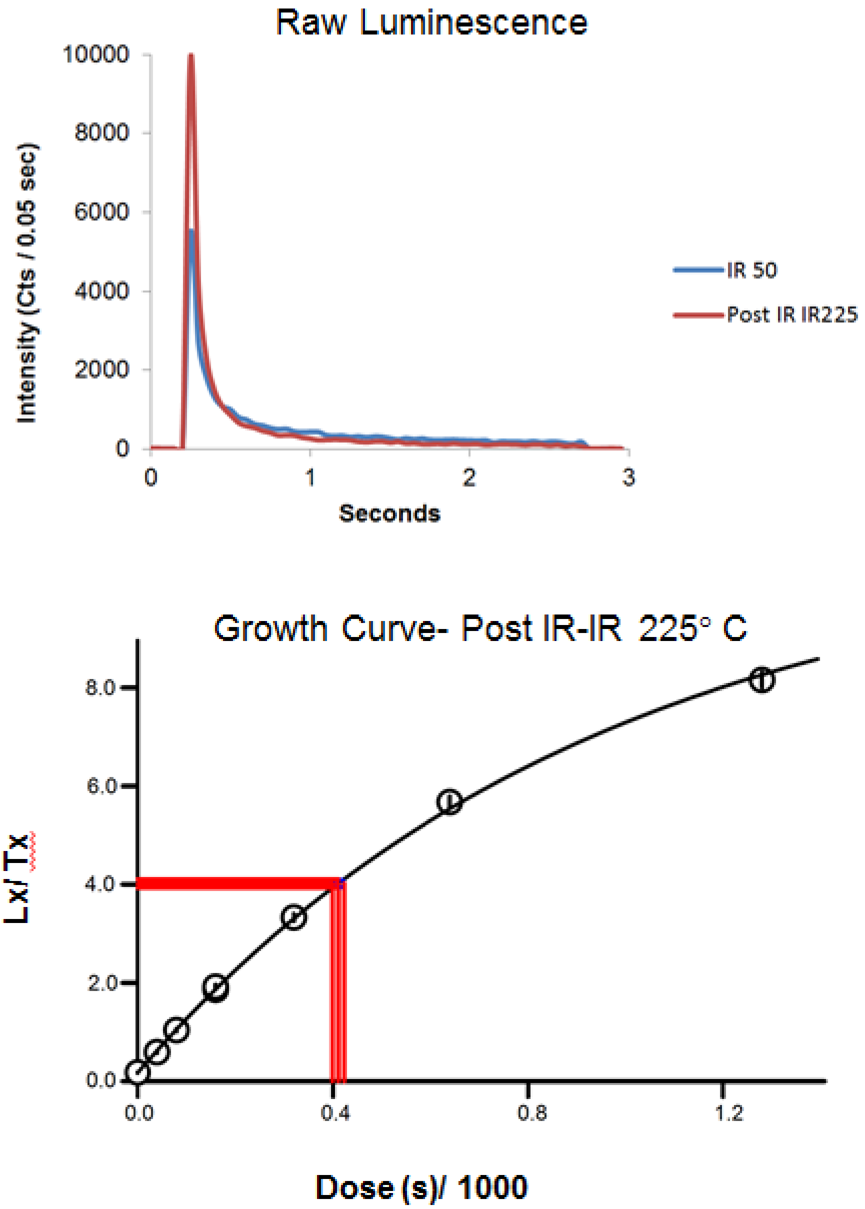

Figure 2.4 a) Raw luminescence in pIRIR 225 vs. IR 50

A), pIRIR225 (in red) compared to the IR 50 luminescence (in blue). B) Example of a growth curve following post IRIR 225 protocol.

2.10 Chapter Bibliography

Aitken, M.J., 1985, Thermoluminescence dating: past progress and future trends: Nuclear Tracks, v. 10, p. 3-6.

Aitken, M.J. and Smith, B.W., 1988, Optical Dating: Recuperation after bleaching: Quaternary Science Review, v. 7, p. 387-393.

Auclair, M., Lamothe, M., and Huot, S., 2003, Measurement of anomalous fading for IRSL using SAR: Radiation Measurements, v. 37, p. 487-492.

Bailey, R.M., 2001, Towards a general Kinetic model for optically and thermally stimulated luminescence for quartz: Radiation Measurements, v. 33, p. 17-45.

Baril, M.R., and Huntley, D.J., 2003, Optical excitation spectra of trapped electrons in irradiated feldspars: Journal of Physics: Condensed Matter, v. 15, p. 8011-8027.

Bøtter-Jensen, L., Bulur, E., Duller, G.A.T., and Murray, A.S., 2000, Advances in luminescence instrument systems: Radiation Measurements, v. 32, p. 523-528.

Bøtter-Jensen, L., Andersen, C. E., Duller, G.A.T., and Murray, A.S., 2003, Developments in radiation, stimulation and observation facilities in luminescence measurements: Radiation Measurements, v. 37, p. 535–541.

Bøtter-Jensen, L., Larsen, N.A., Mejdahl, V., Poolton, N.R.J., Morris, M.F., and McKeever, S.W.S., 1995, Luminescence sensitivity changes in quartz as a result of annealing: Radiation Measurements, v. 24, p. 535-541.

Brown, N.D., Rhodes, E.J., Antinao, J.L. and McDonald, E.V., 2015, Single-grain post-IR IRSL signals of K-feldspars from alluvial fan deposits in Baja California Sur, Mexico: Quaternary International, v. 362, p. 132-138.

Buylaert., J.P., Murray, A.S., Thomsen, K.J., and Jain, M., 2009, Testing the potential of an elevated temperature IRSL signal from K- feldspar: Radiation Measurements, v. 44, p. 560- 565.

Chithambo, M.L., Ogundare, F.O., Feathers, J. and Hong, D.G., 2008, On the dose-dependence of luminescence lifetimes in natural quartz: Radiation Effects and Defects in Solids, v. 163 (12), p. 945-953.

Demars, C., Pagel, M., Deloule, E. and Blanc, P., 1996, Cathodoluminescence of quartz from sandstones: Interpretation of the UV range by determination of trace element distributions and fluid-inclusion P-T-X properties in authigenic quartz: American Mineralogist, v. 81, p. 891-901.

Duller, G.A.T., 1997, Behavioural studies of stimulated luminescence from feldspars: Radiation Measurements, v. 27, p. 663-694.

Duller, G.A.T., Bøtter-Jensen, L., and Murray, A.S., 2000, Optical dating of single sand-sized grains of quartz: sources of variability: Radiation Measurements, v. 32, p. 453-457.

Fattahi, M. and Stokes, S., 2003, Dating volcanic and related sediments by luminescence methods: a review: Earth-Science Reviews, v. 62, p. 229-264.

Fattahi, M., Walker, R.T., Khatib, M.M., Dolati, A. and Bahroudi, A., 2007, Slip-rate estimate and past earthquakes on the Doruneh fault, eastern Iran: Geophysical Journal International, v. 168, p. 691–709.

Feigl, F.J., Fowler, W.B., and Yip, K.L., 1974, Oxygen vacancy model for the E 1′ center in SiO_2: Solid State Communications, v. 14 (3), p. 225-229.

Galbraith, R.F., Roberts, R.G., Laslett, G.M., Yoshida, H., and Olley, J.M., 1999, Optical dating of single and multiple grains of quartz from Jinmium rock shelter, northern Australia:

Part I, experimental design and statistical models: Archaeometry, v. 41 (2), p. 339-364.

Godfrey-Smith, D.I, Huntley, D.J., and Chen, W.H., 1988, Optical dating studies of quartz and feldspar sediment extracts: Quaternary Science Reviews, v. 7, p. 373-380.

Halliburton, L.E., Koumvakalis, N., Markes, M.E., and Martin, J.J., 1981, Radiation effects in crystalline $Si0_2$: The role of aluminum: Journal of Applied Physics, v. 52 (5), p. 3565-3574:

Harben P.W., 2002, The Industrial Mineral Handybook – A Guide to Markets, Specifications, and Prices, Industrial Mineral Information: Worcester Park, United Kingdom, Metal Bulletin PLC, 4th edition, 412 p.

Huntley, D. J., and Baril, M. R., 1997, The K content of the K-feldspars being measured in optical dating or in thermoluminescence dating: Ancient TL, v. 15 (1), p. 11-13.

Huntley, D.J., Godfrey-Smith, D.I, Thewalt, M.L.W., 1985, Optical dating of sediments: Nature, v. 313, p. 105-107.

Huntley, D.J., and Lamothe, M., 2001, Ubiquity of anomalous fading in K-feldspars and the measurement and correction for it in optical dating: Canadian Journal of Earth Science, v. 38, p. 1093-1106.

Hütt, G., Jaek, I., and Tchonka, J., 1988, Optical Dating: K-feldspars optical response stimulation spectra: Quaternary Science Reviews, v. 7, p. 381-385.

Jain, M., 2009, Extending the dose range: Probing deep traps in quartz with 3.06 eV photons: Radiation Measurements, v. 44, p. 445-452.

Jain, M., and Ankjaergaard, C., 2011, Towards a non-fading signal in feldspar: Insight into charge transport and tunnelling from time-resolved optically stimulated luminescence: Radiation Measurements, v. 46 (3), p. 292-309.

Jain, M., Murray, A.S. and Bøtter-Jensen, L., 2003, Characterization of blue-light stimulated luminescence components in different quartz samples: implication for dose measurement: Nuclear Measurements, v. 37, p. 441-449.

Jones, C.E., and Embree, D., 1976, Correlations of the 4.77–4.28-eV luminescence band in silicon dioxide with the oxygen vacancy: Journal of Applied Physics, v. 47(12), p. 5365-5371.

Lawson, M.J., Daniels, J.T.M., and Rhodes, E.J., 2015, Assessing Optically Stimulated Luminescence (OSL) signal contamination within small aliquots and single grain measurements utilizing the composition test: Quaternary International, v. 362, p. 34-41.

Lawson, M.J., Roder, B.J., Stang, D.M., and E.J. Rhodes, 2012, OSL and IRSL characteristics of quartz and feldspar from southern California, USA: Radiation Measurements, v. 47 (9), p. 830–836.

Martini, M., Fasoli, M., and Galli, A., 2009, Quartz OSL emission spectra and the role of [AlO_4] recombination centres: Radiation Measurements, v. 44, p. 458–461.

Martini M., Spinola, G., and Vedda, A., 1987, Thermally stimulated luminescence of thermally grown SiO_2 films: Radiation Effects, v. 105, p. 107 -116.

Müller, A., Lennox, P., and Trzebski, R., 2002, Cathodoluminescence and micro-structural evidence for crystallization and deformation processes of granites in the Eastern Lachlan Fold Belt (SE Australia): Contributions to Mineralogy and Petrology, v. 143(4), p. 510-524.

Murray, A.S. and Olley, J.M., 2002, Precision and accuracy in the optically stimulated luminescence dating of sedimentary quartz: A status review: Geochronometria, v. 21, p. 1-16.

Murray, A.S. and Roberts, R.G., 1997, Determining the burial time of single grains of quartz using optically stimulated luminescence: Earth and Planetary Science Letters, v. 152(1), p. 163-180.

Murray, A, and Wintle, A., 1999, Isothermal decay of optically stimulated luminescence in quartz: Radiation Measurements, v. 30(1), p. 119-125.

Murray, A.S. and Wintle, A.G., 2000, Luminescence dating of quartz using an improved single-aliquot regenerative- dose protocol: Radiation Measurements, v. 32, p. 57-73.

Murray, A.S., Roberts, R.G., and Wintle, A., 1997, Equivalent dose measurement using a single aliquot of quartz: Radiation Measurements, v. 27(2), p. 171-184.

Owen, G., and Moretti, M., 2011, Identifying triggers for liquefaction-induced soft-sediment deformation in sands: Sedimentary Geology, v. 235 (3-4) p. 141-147.

Owen, G., Moretti, M., and Alfaro, P., 2011, Recognizing triggers for soft-sediment deformation: Current understanding and future directions: Sedimentary Geology, v. 235(3-4), p. 133-140.

Pietsch, T., Olleya, J., and Nanson, G., 2008, Fluvial transport as a natural luminescence sensitiser of quartz: Quaternary Geochronology, v. 3(4), p. 365-376.

Poolton, N.R.J., et al, 2002a, Electrons in feldspar I: on the wave function of electrons trapped at simple lattice defects: Physics and Chemistry of Minerals, v. 29(3), p. 210-216.

Poolton, N.R.J., et al., 2002b, Electrons in feldspar II: a consideration of the influence of conduction band-tail states on luminescence processes: Physics and Chemistry of Minerals, v. 29, p. 217-225.

Poolton, N.R.J., et al., 2000, Luminescence sensitivity changes in natural quartz induced by high temperature annealing: a high frequency EPR and OSL study: Journal of Physics D:

Applied Physics, v. 33(8), p. 1007.

Porat, M., Levi, T. and Weinberger, R., 2007, Possible resetting of quartz OSL signals during earthquakes-Evidence from late Pleistocene injection dikes, Dead Sea basin, Israel: Quaternary Geochronology, v. 2., p. 272- 277.

Porat, N., Duller, G.A.T, Roberts, H.M. and Wintle, A.G., 2009, A simplified SAR protocol for TT-OSL: Radiation Measurements, v. 44, p. 538-542.

Preusser, F., Ramseyer, K., and Schlüchter, C., 2006, Characterisation of low OSL intensity quartz from the New Zealand Alps: Radiation Measurements, v. 41(7), p. 871-877.

Rhodes, EJ., 1988, Methodological considerations in the optical dating of quartz: Quaternary Science Reviews, v. 7(3-4), p. 395-400.

Rhodes, E.J., 2011, Optically stimulated luminescence dating of sediments over the past 200,000 years: Annual Review of Earth and Planetary Science, v. 39, p. 461-488.

Rhodes, E.J., 2015, Dating sediments using potassium feldspar single-grain IRSL: Initial methodological considerations: Quaternary International, v. 362, p. 14-22.

Rhodes, E.J. and Bailey, R.M., 1997, The effect of thermal transfer on the zeroing of the luminescence of quartz from recent glaciofluvial sediments: Quaternary Science Reviews, v. 16, p. 291- 298.

Rhodes, E.J. and Pownall, L., 1994, Zeroing of the OSL signal in Quartz from young glaciofluvial sediments: Radiation Measurements, v. 23, p. 581-585.

Rittenour, R.M, 2008, Luminescence dating of fluvial deposits: applications to geomorphic, paleoseismic and archaeological research: Boreas, v. 37, p. 613-635.

Smith BW, Aitken MJ, Rhodes EJ, Robinson PD, and Geldard DM., 1986, Optical dating: methodological aspects: Radiation Protection Dosimetry, v. 17, p. 229-233.

Smith, B.W., Rhodes, E.J., Stokes, S., Spooner, N.A., 1990, The optical dating of sediments using quartz: Radiation Protection Dosimetry, v. 34, p.75-78.

Smith, B. W. and Rhodes, E.J., 1994, Charge movements in quartz and their relevance to optical dating: Radiation Measurements, v. 23, p. 329-333.

Spooner, N.A., 1992, Optical dating: preliminary results on the anomalous fading of luminescence from feldspars: Quaternary Science Reviews, v. 11, p. 139-145.

Spooner, N.A., 1994, The anomalous fading of infrared-stimulated luminescence from feldspars: Radiation Measurements, v. 23, p. 625- 632.

Stang, D.M., Rhodes, E.J. & Heimsath, A.M., 2012, Rapid assessment of soil mixing processes and rates using a portable OSL-IRSL reader: Quaternary Geochronology 10, 314-319, doi: 10.1016/j.quageo.2012.04.02.

Steffen, D., Preusser, F., and Schlunegger, F., 2009, OSL quartz age underestimation due to unstable signal components: Quaternary Geochronology, v. 4, p. 353–362.

Stokes, S. and Fattahi, M., 2003, Red emission luminescence from quartz and feldspar for dating application: an overview: Radiation Measurements, v. 37, p. 383-395.

Thomsen, K.J., Murray, A.S., Jain, M. and Bøtter-Jensen, L., 2008, Laboratory fading rates of various luminescence signals from feldspar- rich sediment extracts: Radiation Measurements, v. 43, p. 1474-1486.

Wallinga, J., 2002, Optically stimulated luminescence dating of fluvial deposits: a review: Boreas, v. 31(4), p. 303-322.

Wiggenhorn, H., 1994, IRSL dating of k-feldspar at elevated-temperatures and infrared bleaching of TL: Radiation Measurements, v. 23(2-3), p. 387-391.

Wintle, A., 1973, Anomalous fading of thermoluminescence in mineral samples: Nature, v.

245(5421), p. 143-144.

Wintle, A,G., 1997, Luminescence Dating: Laboratory Procedures and Protocols: Radiation Measurements, v. 27 (5/6), p. 769-817.

Wintle, A. and Murray, A., 1998, Towards the development of a preheat procedure for OSL dating of quartz: Radiation Measurements, v. 29(1), p. 81-94.

Wintle, A.G. and Murray, A.S., 2006, A review of quartz optically stimulated luminescence characteristics and their relevance in single-aliquot regeneration dating protocols: Radiation Measurements, v. 41, p. 369-391.

Yang, X. H. and McKeever, S.W.S., 1990, The pre-dose effect in crystalline quartz: Journal of Physics D: Applied Physics, v. 23(2), p. 237.

III. OSL AND IRSL CHARACTERISTICS OF QUARTZ AND FELDSPAR FROM SOUTHERN CALIFORNIA, USA

Contents lists available at SciVerse ScienceDirect

Radiation Measurements

journal homepage: www.elsevier.com/locate/radmeas

OSL and IRSL characteristics of quartz and feldspar from southern California, USA

Michael J. Lawson*, Belinda J. Roder, Dallon M. Stang, Edward J. Rhodes

Department of Earth and Space Sciences, University of California, Los Angeles, 595 Charles Young Drive East, Los Angeles, CA 90095 1567, USA

A R T I C L E I N F O

Article history:
Received 19 October 2011
Received in revised form
2 February 2012
Accepted 26 March 2012

Keywords:
Southern California
Luminescence
Signal contamination
Scanning electron Microscope (SEM)
Thermal quenching
Neotectonics

A B S T R A C T

Southern California comprises of a wide range of diverse landscapes and environments, from high mountains with glacial and periglacial sediments to deserts with large sand dunes, extensive alluvial fans and ephemeral playas. Highly active tectonic processes has exposed ancient (c. 2 Ga) plutonic and metamorphic basement from deep within the crust, while similar Palaeozoic, Mesozoic and Cenozoic rocks are also common. A rich array of volcanic lithologies extending into the late Quaternary complement many thick sedimentary sequences that formed in equally diverse ancient environments typical of an accreting active continental margin. In some locations, notably in the Coachella Valley close to Palm Springs and the Salton Sea, low OSL sensitivity and poor characteristics restrict the application of the quartz SAR protocol to date late Pleistocene and Holocene fluvial sediments. In other locations such as the Malibu coastline, high sensitivity of the quartz OSL signal is observed, despite local source rocks being dominated by volcanic lithologies. Problems of poor quartz characteristics, along with uncertainty in predicting quartz OSL behavior for future dating campaigns poses a significant problem for projects, in particular for neotectonic contexts. While K-feldspar has been used extensively to date eolian and fluvial sediments in southern California, little information regarding signal stability is available. We explore the characteristics of both quartz and feldspar sub-samples from eolian, fluvial, lacustrine environments, in order to help develop mineral selection criteria for optical dating applications and clarify these issues. The importance of radiation quenching in quartz grains recently eroded from bedrock and the role of fires in enhancing OSL sensitivity are considered. The relative bleachability of quartz and feldspar fractions, along with thermal stability considerations is discussed. A simple test for quartz OSL signal contamination based on thermal quenching and assistance, and the susceptibility of the OSL signal to IR bleaching is introduced.

1. Introduction

Southern California is one of the most tectonically active regions in the continental United States, with a major plate boundary and an associated fault system within highly populated regions. Fault motion and earthquake hazard studies depend upon good chronometry to assess rupture reoccurrence intervals typically dated with radiocarbon, terrestrial cosmogenic nuclides (TCN), and uranium series. Optically stimulated luminescence (OSL) and Infrared Stimulated Luminescence (IRSL) dating of local materials typically have low sensitivity, high thermal transfer and low bleachability, reducing the suitability of the technique. Southern California has a wide range of environmental conditions that create tremendous variability in OSL characteristics (Rhodes, 2011). This is further complicated by depositional contexts characterized by high energy, active tectonics, and mountainous terrain.

Regionally, the use of OSL dating in Southern California has been hindered by difficulties in dating quartz: problems with underestimation of known age samples, incomplete zeroing and bioturbation. IRSL dating has encountered issues with anomalous fading. Delong and Arnold (2007) examined alluvial deposits from the Western Transverse Ranges with OSL, and found scatter that they felt resulted from a combination of poor exposure and methodological problems that they could not discern. Mahan et al. (2007), studying alluvial fans, found partial bleaching, signal saturation and anomalously young IRSL ages possibly from fading in the northeastern Mojave. Sohn et al. (2007) minimized contributions from partially bleached materials by sampling well-sorted eolian interbeds while dating alluvial fans in Southern Death Valley.

The poor suitability of local materials has been blamed for suboptimal luminescence signals, but so far no general assessment has been made about the range of these problems. Most papers on OSL/IRSL applied to this region report ages with error estimates, but comment little about the signal characteristics that may have hindered the application and accuracy of the method. In this study, we attempt to give an overview of OSL and IRSL signals observed in several locations across Southern California, highlight some of the issues encountered with samples, and present a numerical test for assessing feldspar- or quartz-like behaviors, based in part on methods presented by previous authors.

2. Locations

Samples were selected from a variety of locations in Southern California (Fig. 1, Table 1); samples from Point Dume and the Mojave Desert represent the extremes in terms of sample characteristics. Sample J0048 is from a Holocene cliff-top dune close to Point Dume in Malibu, California (Supplementary S1). Christmas Canyon West samples (J0118, J0119) are Holocene, sandy alluvial fan deposits proximal to the central Garlock fault from the Mojave Desert, California (Supplementary S2, and Roder et al., in press).

In the context of a signal contamination test presented below, a number of samples will also be discussed. Lake Elsinore core LEDC10-1 samples J0052 are sand deposit potentially from an eolian sand from when the lake was dry. Sample J0054 are hill slope colluvium taken near the crest of the San Gabriel mountain range. Sample J0084 is a dune sand collected from Rice Valley Dune in the eastern Mojave Desert, near the Colorado River. El Paso Peaks sample (J0145) was collected from a playa deposit, composed of distinct layers of sand and silt, interpreted to represent the individual flood events that were disturbed by the Garlock fault (Dawson et al., 2003).

3. Preparation

Samples were collected from vertical faces exposed in trenches, which had their surfaces cleaned and any significant layering noted. Sample J0052 was collected from a core sample taken from Lake Elsinore. For the remaining samples, steel tubes were hammered in and a gamma spectrometer was inserted into each hole to determine gamma dose rate for uranium, thorium and potassium concentrations. Additional sediment samples were taken to determine the water content.

In the laboratory, samples were treated as outlined by Wintle (1997). Samples were removed from the tubes with care taken to remove the ends that had been exposed to light, portions of which are isolated for inductively coupled plasma mass spectrometry (ICP-MS) analysis of uranium and thorium concentrations and ICP-OES (optical emission spectrometry) for potassium. The remaining portion of the tube was separated by grain size using wet sieving, followed by hydrochloric acid treatment to remove carbonates. Heavy liquid separation with lithium meta-tungstate (LMT) with a density of 2.58 g cm^{-3} was used to isolate potassium feldspar. The fraction denser than 2.58 g cm^{-3} was treated with 40% hydrofluoric acid for a minimum of 100 min to remove plagioclase and etch the alpha irradiated exterior of quartz grains. A further gravity separation of 2.70 g cm^{-3} was used to remove denser minerals from quartz samples, and was followed by a second sieve treatment.

Samples were measured on aluminum disks upon which a small dab of silicone oil adheres grains in aliquots comprising 50–200 grains for measurement on a Risø TL-DA-20 reader equipped with a strontium 90 beta source and U340 filter.

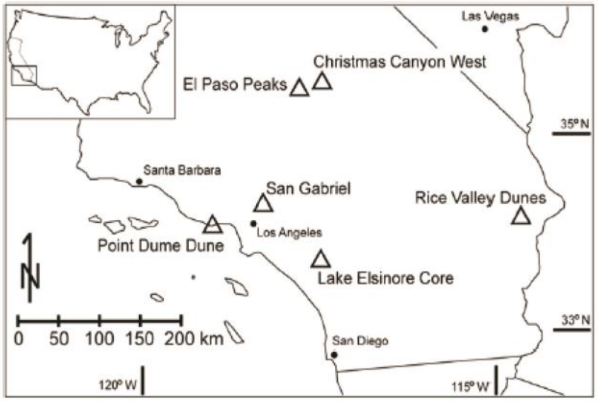

Fig. 1. Sample locations in southern California (see Table 1).

Table 1
Sample locations.

Project	Location	Sample
P4	Point Dume Cliff Dune, CA, USA	J0048
P6	Lake Elsinore Core, CA, USA	J0052
P7	San Gabriel Soil, CA, USA	J0054
P9	Rice Valley Dunes, CA, USA	J0084
P11	Christmas Canyon West, CA, USA	J0118, J0119
P14	El Paso Peaks Paleoseismic, CA, USA	J0145

4. Results – OSL/IRSL data

4.1. General

Quartz OSL and feldspar IRSL characteristics from Southern California vary significantly, making a summary of all characteristics difficult given the breadth of sample locations. The study will focus on the characteristics of two samples that represent the extremes of characteristics.

4.2. Decay, growth and sensitivity

Samples ranged greatly in OSL sensitivity, with Malibu and the Mojave quartz samples representing the maximum and minimum end members respectively. The Malibu cliff-top dune sample (J0048) had a bright natural OSL signal (20,000 counts.s^{-1}.mg^{-1}.Gy^{-1}) with a rapid decay typical of the quartz fast component, while the Mojave quartz (J0119) in contrast was around two orders of magnitude less sensitive (140 counts.s^{-1}.mg^{-1}.Gy^{-1}; Fig. 2a, c). This latter sample has a slower decay possibly from a feldspar component, though the low intensity makes this hard to determine based on OSL decay shape alone. Growth of the sensitivity-corrected quartz OSL as a function of dose was somewhat similar for both samples (Fig. 3a, b), with most aliquots displaying linear plus exponential growth. Typical D_0 values for the exponential fraction ranged widely, but were in the range of 10–200 Gy.

The K-feldspar fraction of sample J0048 has a bright IRSL signal (15,000 counts.s^{-1}.mg^{-1}.Gy^{-1}), while J0119 varied very widely in intensity, with IRSL sensitivities ranging from 110 to 11,000 counts.s^{-1}.mg^{-1}.Gy^{-1} (Fig. 2b, d). Growth for both samples were only slightly sub-linear over the low dose range studied (to c. 24 Gy; Fig. 3c), implying larger D_0 values for the IRSL signals than for quartz OSL.

4.3. Bleaching

A direct comparison of the relative bleaching rates of quartz OSL and feldspar IRSL was made for sample J0048 from Malibu. Irradiated discs were exposed for different periods of time to daylight through a relatively small window with restricted line-of-sight to daylight. This leads to a reduced bleaching rate in comparison to direct daylight exposure, providing a clearer picture of the initial bleaching behavior. Measurements were made using short shines;

5% power for 1.0 s for both OSL and IRSL measured at room temperature provided a signal with significant counts but causing negligible additional bleaching. It can clearly be seen (Fig. 4) that the quartz OSL signal is reduced more rapidly, achieving a lower fractional value at all measurement times. It should be noted that the reduced intensity lighting conditions mean that the exposure times are not representative of the bleaching rates under full sunlight exposure which would be much lower. Similar measurements were also made for the quartz and K fspr fractions of the Mojave Desert sample (J0119) using OSL and IRSL respectively. The quartz intensity was too low to measure using this short shine technique, whilst the IRSL signals follow those of sample J0048, but were more scattered owing to lower signal intensity.

4.4. *Thermal transfer behavior*

A "zeroing plateau" (modified from Rhodes, 2000), in which residual doses are determined at different preheat treatments following a 1 h direct sunlight bleach of the natural signal was conducted for quartz from sample J0048 and both quartz and K-feldspar for sample J0119. Initial bleaching of the natural signals was conducted inside a window for 30 min, with no direct sunlight exposure, but relatively bright daylight conditions for J0119 subsamples, and for 1 h in direct sunlight for J0048 quartz. J0048 quartz showed little thermal transfer (<0.05 Gy) and little temperature dependence (Fig. 5a). Sample J0119 however showed very large equivalent dose values after its half hour bleach of between 2 and 10 Gy, potentially due to either high thermal transfer or large residual doses from difficult to bleach components (Fig. 5b). The feldspar component (J0119K), after a half hour bleach, also had large equivalent doses between 2 and 12 Gy (Fig. 5c) due to either high thermal transfer or difficult to bleach components.

4.5. *Dose recovery*

In order to compare the dating performance of bright and dim quartz samples, and also K-feldspar IRSL signals, dose recovery experiments were performed on aliquots of both J0048 (quartz only) and J0119 (both quartz and feldspar), using a SAR protocol to recover a dose of 2.7 Gy (Murray and Wintle, 2000). Identical bleaching conditions were used for these samples as for the previous zeroing plateau experiment. The Malibu quartz sample (J0048) (Fig. 6a) has a greater precision reflecting its brighter signal (uncertainties are contained within symbols). In contrast, both portions of the Mojave sample J0119, (Fig. 6b, c) provide a striking overestimate with their large uncertainties on results from individual quartz aliquots, associated with its poor signal to noise ratio. The significant overestimate for sample J0119 is probably caused primarily by incomplete bleaching and/or thermal transfer.

Observations of sample J0048 during the dose recovery test show a recycling ratio of 1.00 ± 0.09 suggesting good repeatability of sensitivity-corrected luminescence signals (Duller, 2008), and a thermal transfer zero dose cycle estimate of 4.6 ± 1.3% of the

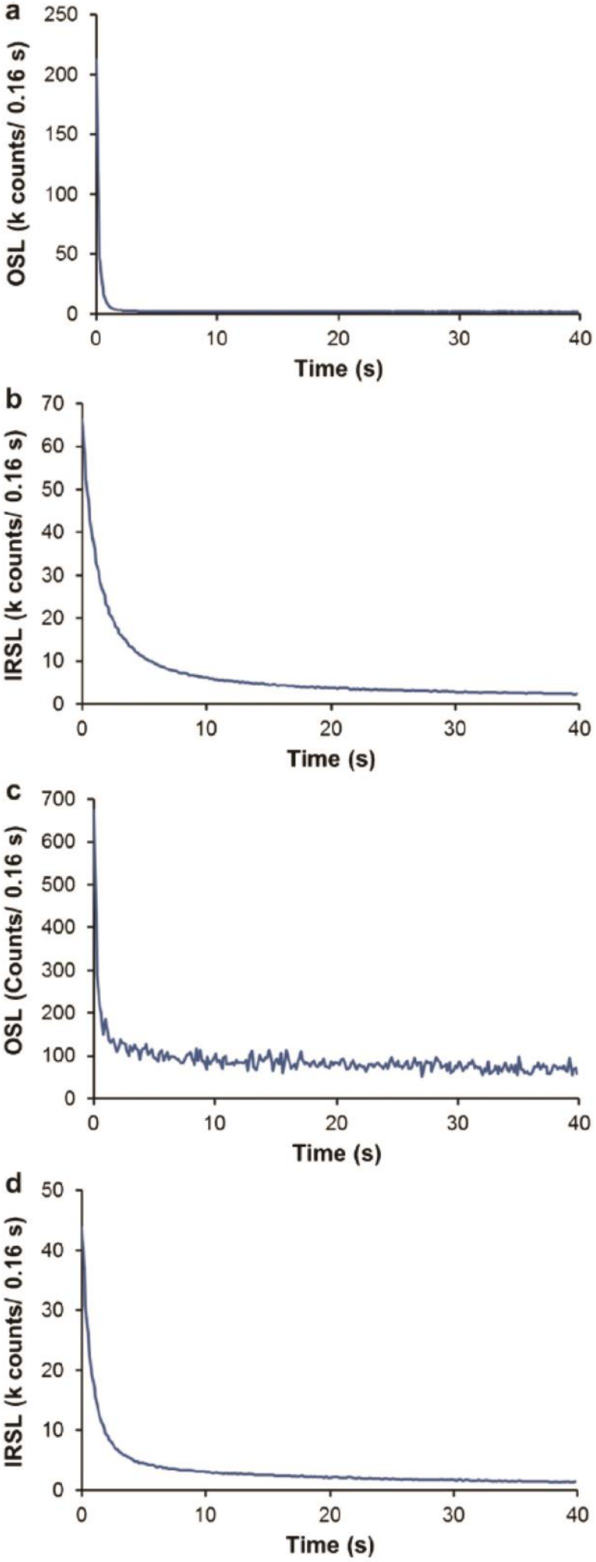

Fig. 2. Natural OSL and IRSL decays for quartz and feldspar fractions from Point Dume dune, Malibu (J0048) and Christmas Canyon west, Mojave desert (J0119), California. (a) Natural OSL decay from quartz fraction of J0048 from Malibu showing a bright, rapidly decaying signal typical of the fast component. (b) Natural IRSL decay from K-feldspar fraction of J0048 showing a bright signal with decay slower than quartz OSL, typical of feldspar samples. (c) Natural OSL decay from the quartz fraction of J0119 from the Mojave desert showing poor signal to noise ratio and a slower decay at later exposure times. Signal contamination is a concern with dim quartz grains, whose OSL signals can potentially be dominated by a small number of feldspar grains. (d) Natural IRSL decay from the feldspar fraction of J0119 showing a large signal comparable to that of K-feldspar sample J0048 from Malibu (plot b).

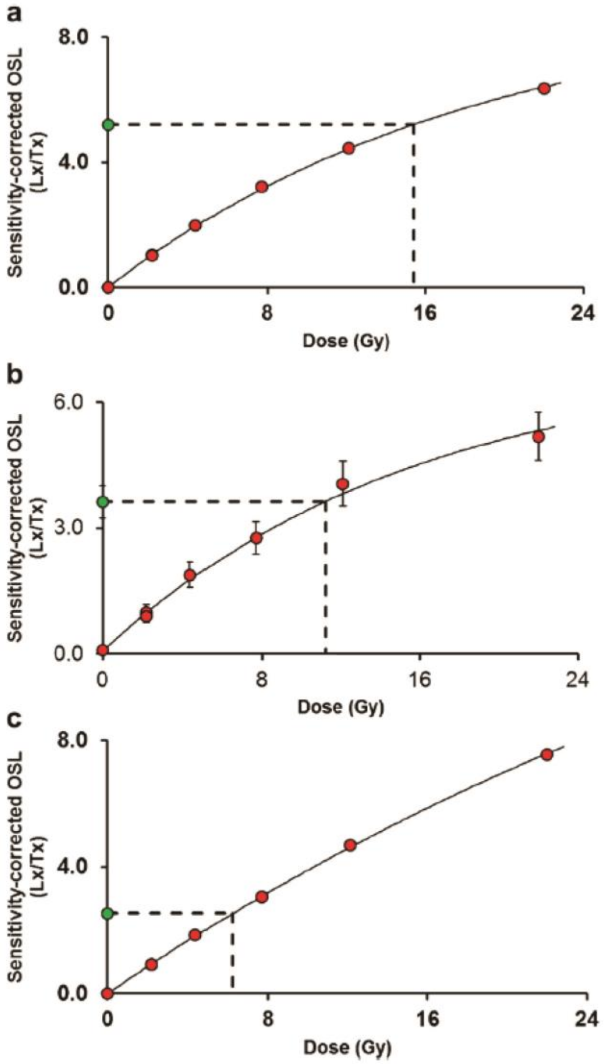

Fig. 3. OSL and IRSL SAR growth response curves (red symbols), showing natural signals (green symbols) and equivalent dose determination (dashed lines). (a) OSL from J0048 quartz (Malibu). (b) OSL from quartz fraction of J0119 (Mojave desert), illustrating larger errors owing to lower signal to noise ratios. (c) IRSL from K-feldspar fraction of J0119 (Mojave). (For interpretation of the references to colour in this figure legend, the reader is referred to the web version of this article.)

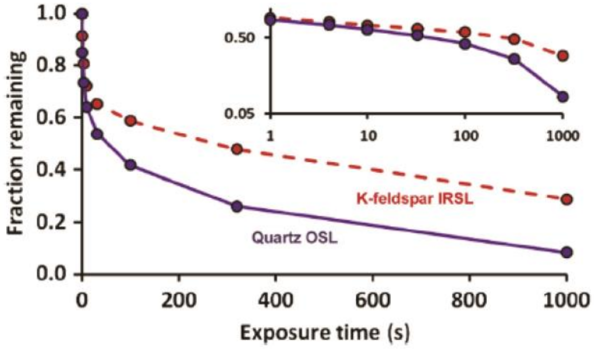

Fig. 4. Bleaching of quartz OSL and K-feldspar IRSL fractions of sample J0048 by reduced intensity daylight through clear glass, normalized to initial intensity. Both fractions contain significant residual signals after long bleaching times (over 15 min) at this reduced intensity. Inset graph shows the same data using logarithmic axes. Neither decay displays exponential behavior. Note that the reduced daylight intensity used in this experiment means that the exposure times do not equate to natural bleaching times.

recovered dose value (i.e. the "natural" signal; Fig. 6a). J0119 quartz OSL had a recycling ratio of 1.06 ± 0.34 for and a thermal transfer zero dose cycle estimate of 42 ± 14%. Feldspar IRSL for J0119 had a recycling ratio of 1.00 ± 0.03, and a thermal transfer value of 0.6 ± 0.2%.

5. Discussion

5.1. Sample characteristics

Great variability exists with OSL/IRSL signal characteristics in the Southern California region. California has a very complex tectonic history as outlined in Ingersoll (2008), which has created a variety of source materials for sediments, ranging from the Cretaceous Sierra Nevada batholith (a massive body responsible for delivering a huge volume of quartz and feldspar grains into the Mojave desert during the Quaternary period), Cretaceous magmatic arc subduction complexes, quartz-rich mid-Tertiary ignimbrite volcanics associated with slab roll-back, and more recent

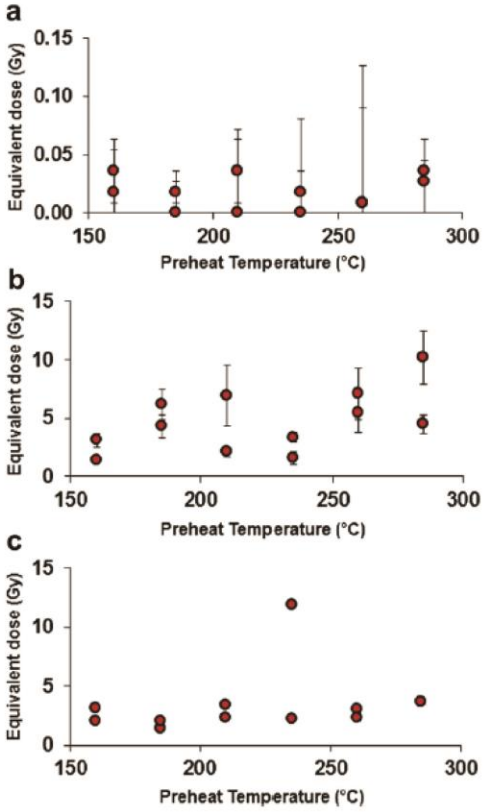

Fig. 5. Zeroing plateau (modified from Rhodes, 2000) For (a) OSL of quartz from J0048 and (b) J0119 and (c) IRSL of K-feldspar fraction of J0119; see text for details. The quartz OSL for J0048 has low thermal transfer (apparent dose <0.05 Gy) and little temperature dependence. The quartz OSL for J0119 has large residual doses (2–10 Gy); the K-feldspar IRSL for J0119 also displays large residual dose values (2–12 Gy).

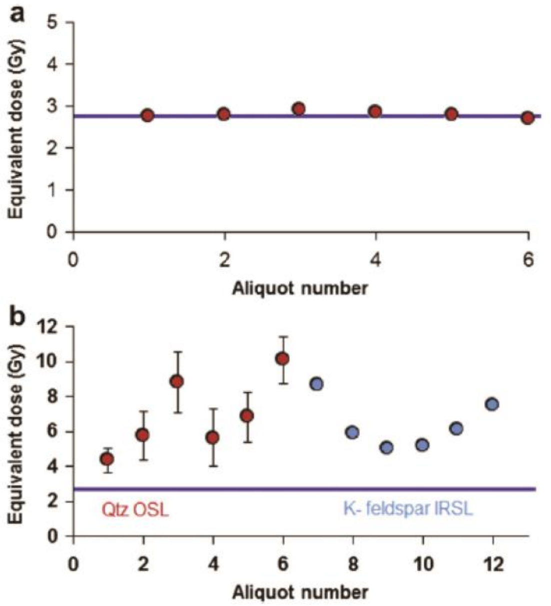

Fig. 6. Dose recovery experiments for J0048 (quartz OSL only, plot a) and J0119 (plot b; quartz OSL results to left, K-feldspar IRSL on right). The horizontal solid line represents the given dose of 2.7 Gy in both plots. Both quartz OSL and K-feldspar IRSL for sample J0119 (b) show significant over estimates of the given dose.

Oligocene-Miocene basin sediments associated with a change in plate dynamics circa 30 Ma ago.

Furthermore, the region remains tectonically active, continuously exposing new bedrock through thrust faulting, such as in the Santa Monica and San Gabriel Mountains in the west, and normal faulting associated with Basin and Range extension to the east. This more recent tectonic activity provides fresh material to the surface, which is eroded, and rapidly fills subsiding basins before significant grain reworking is possible. Pietsch et al. (2008), while working with Australian quartz that had long sedimentary histories, involving multiple cycles of reworking and burial, noted increases in sensitivity of quartz grains through repeated irradiation and bleaching. This observation is consistent with the behavior of our Mojave Desert samples, which dominantly have relatively, short sedimentary histories, typically being eroded from bedrock and being deposited nearby. The Malibu sample (J0048) has good quartz OSL characteristics possibly caused by heating in anthropogenic fires, besides cycles of reworking. Point Dume is part of the Western Transverse Ranges (WTR), which has been exposed for 20–18 Ma (Ingersoll, 2008). Eroded material from the block could then be reworked by wave action and coastal storms, allowing for multiple burials and bleaching cycles. The Mojave sample (J0119) in contrast, is an alluvial fan deposit composed in part from local bedrock but also with an input from further traveled material during the last glacial maximum and late interglacial, in an alluvial system that drained into Searles Lake. This lake shoreline material is dominated by recently eroded grains from major massifs to the east and west of this lake basin. Vegetation may also be a control, as Malibu is more temperate than the Mojave Desert, with greater precipitation that can support more plant life. The resulting vegetation may have subsequently burned more often and more intensely in the regular Southern California wildfires. Heating during burning has been shown to sensitize grains in other contexts and is often the basis of thermoluminescence sensitivity increase (Mazess and Zimmerman, 1966). We note that additional TL measurements and geochemical studies could help to resolve some of these issues. Tectonically active regions, such as Southern California, may be non-ideal for quartz-based OSL because of the high rate of input of new grains and the effective locking away in deep sediment piles of transported grains.

Feldspar IRSL can provide strong signals, but also can be problematic due to anomalous fading that can apparently give rise to underestimates for known age samples (i.e. Mahan et al., 2007). Feldspar signals are also less bleachable than quartz OSL (Godfrey-Smith et al., 1988, Fig. 4), so their usefulness for dating sediments from high energy environments may be limited by this consideration. As signal resetting takes longer, partial bleaching may lead to age over estimates. We note that the apparent thermal transfer effects (which may include a component of recuperation) observed in the dose recovery experiments for Mojave sample J0119 (Fig. 6b) are different for quartz and K-feldspar sub-samples. The quartz effect persists through the SAR measurement cycle so that the zero dose cycle has a significant thermal transfer signal (42 ± 14% of the "natural" signal); in contrast, the K-feldspar IRSL exhibits a negligible thermal transfer signal in the zero dose cycle (0.6 ± 0.2%), though the high dose recovery values indicate that thermal transfer was present in the first cycle. These observations suggest to us that different processes of charge migration are taking place in these two experiments.

5.2. Signal contamination

Signal contamination has the potential to be problematic in a region with low OSL and IRSL sensitivities. This is evident in Mojave sample J0119 (Fig. 2c), in which the quartz fraction has a very low signal while the signal from feldspar is two orders of magnitude brighter (Fig. 2d). IRSL from feldspar suffers anomalous fading (Wintle, 1973), differential bleaching characteristics, and an additional potassium radiogenic component in comparison to OSL quartz. The two components are routinely separated as outlined by Wintle (1997) through gravity and chemical treatments (see preparation section). Shen et al. (2007), however, found feldspar contamination remaining after 20 min 20% HF treatment for fine grained polymineral samples. One dune sand from the Rice Valley (see Table 1) sample also proved problematic; sample J0084 was sieved, treated with HCl acid to remove carbonates, separated by density, and the fraction >2.58 g cm^{-3} was then treated with two 100 min treatments of 40% HF acid, and yet retained a significant IRSL component typical of feldspar (Supplementary Fig. S3) that was similar in form to that from the sample's K-feldspar fraction (Supplementary Fig. S4). Despite being HF treated twice this sample still retained an intense IRSL component typical of feldspar.

A Scanning Electron Microscope (SEM) was utilized to confirm feldspar contamination in sample J0084 "quartz" using LEO 1430 VP system and electron-dispersive X-ray (EDX) spectroscopy to determine the chemical composition of the targeted grains (Fig. 7, Supplementary Table B). One grain, sample location 2, is identified as a quartz grain with an oligoclase inclusion, and two tabular voids from dissolved inclusions. As well, a clearly twinned andesine crystal was identified, suggesting that the density separation was inadequate to separate a suite of relatively unweathered minerals, which are more prevalent in neotectonic environments where less stable mineral components have yet to be chemically and physically eroded into smaller grain sizes. Further, the SEM analysis confirmed the absence of tungstate on the exteriors of grains.

Several tests have been suggested to ascertain whether a quartz sample is pure (Supplementary Table A). The presence of an IRSL component in a quartz sample is considered by some authors to be a clear sign of feldspar signal contamination (Stokes, 1992), as does IRSL bleaching of the OSL component (Duller, 2003). Furthermore,

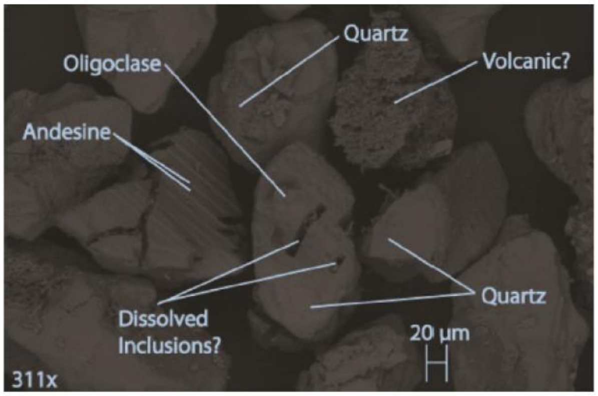

Fig. 7. Scanning electron Microscope (SEM) image of sample J0084 magnified 311 times and chemically analyzed by electron-dispersive X-ray (EDX) spectroscopy to determine mineralogy (Table S2). In the center is a grain of quartz, containing hollowed out tabular inclusions interpreted to be a less chemically stable mineral removed by preceding HF treatments. This grain also has an oligoclase inclusion. The grain to the left displays clear twinning with dark and light bands interpreted by EDX analysis to be andesine. Grains above and to the right are quartz. A grain to the upper right is fine grained and porous, and is interpreted to be a volcanic tuff; this grain did not provide sufficient EDX count rate for chemical analysis.

the shape of the decay can be diagnostic: quartz OSL is typically a rapid decay dominated by the fast component, while feldspar OSL is more gradual (Rhodes, 2011). Linearly modulated (LM-OSL) offers greater analytical power, as the quartz signal is the sum of several exponential decays (Smith and Rhodes, 1994; Bulur et al., 1999), while feldspar IRSL generally follows a power law decay (Huntley, 2006). This is evident in our samples: the LM-OSL for the "quartz" fraction of the Lake Elsinore core (J0052, supplementary Fig. S7) proved diagnostic of signal contamination. LM-OSL was measured for 3600 s, from 0 to 95% LED power, but the decay is more typical of our feldspar samples (J0084) with a rapidly decaying component followed by a linear residual signal. In contrast, LM-OSL from our Malibu dune quartz sample (J0048) had discernable fast, medium, and slow components.

We have created a quantitative test to determine signal contamination by comparison with quartz and feldspar standards. This test combines multiple discrimination techniques, as proposed by Mauz and Lang (2004).

Table 2
Detailed description of the combined signal contamination test procedures, properties assessed and relevant references.

Step				Assesses	
1	OSL Bleach	125 °C	120 s		
2	Beta dose		100 s		
3	Preheat	220 °C			
4	IRSL	50 °C	40 s	IRSL presence	(Stokes, 1992)
5	OSL	125 °C	40 s		
Repeat 2–4					
6	Elevated T OSL	200 °C	40 s	Thermal quenching (Step 6/5)	(Smith and Rhodes, 1994)
Repeat 2 and 3					
7	IRSL	50 °C	40 s		
8	OSL	125 °C	40 s	Sensitivity Change	
Repeat 2 and 3					
9	OSL without pre IRSL	125 °C	40 s	Post-IR OSL/OSL ratio (Step 9/7)	(Duller, 2003)
Repeat 2 and 3					
10	LM-IRSL	125 °C	180 s	Component analysis	(Bulur et al., 1999)
11	LM-OSL	125 °C	180 s	Component analysis	(Bulur, 1996)
Repeat 2 and 3					
12	Elevated T IRSL	150 °C	40 s	Thermal assistance (Step 12/4)	(Wiggenhorn, 1994)
13	OSL	125 °C	40 s	Sensitivity change	

Table 3
Results from quartz and K-feldspar standards used to calibrate the combined signal contamination test. Determination of sensitivity changes proved to be useless in distinguishing quartz and K-feldspar and were not used further, but the thermal quenching/assistance test and infrared bleaching of the OSL signal were good discriminators; see text for details of the tests.

	Sensitivity	Thermal quenching/Assistance	IR bleach of OSL
Q std ave	0.98	0.3	1.02
K Fspr ave	0.99	2	18
Diff		1.7	16.98

Thermal quenching (Smith and Rhodes, 1994) is a systematic decrease in signal intensity at increasing measurement temperature exhibited by quartz samples (supplementary S8). Feldspar exhibits thermal assistance (Wiggenhorn, 1994) with larger IRSL intensities at increasing measurement temperatures. Duller et al. (1995) used these two dissimilar effects in samples with varying feldspar and quartz concentrations. Shen et al. (2007) proposed using a thermal quenching/assistance test to determine feldspar components.

Our combined signal contamination test assesses thermal quenching and IRSL bleaching to determine feldspar- or quartz-like behavior (see Table 2). Thermal quenching is assessed through elevated OSL/IRSL measurements: OSL measurements at 125 °C and 200 °C; IRSL measurements at 50 °C and 150 °C. The bleachability of the OSL signal by IR is assessed through a post-IR OSL/OSL ratio (Duller, 2003). Initial intensity has background subtracted and two ratios are calculated: post-IR OSL/OSL ratio and a thermal quenching value. Results are then scaled against known quartz and feldspar samples that show the greatest change from the post-IR OSL/OSL ratio and thermal quenching tests (see Table 3) so that

Table 4
Results of the combined signal contamination test showing test scores for different quartz (Q) and K-feldspar (K) Samples. "TQ/A test scaled to standard" and "IR bleach test scaled to standard" denote values that are scaled to those values in Table 3, resulting in a scale that varies between zero to around one. The right-hand column is the average of the two scaled test scores, where 1.0 is "quartz-like" and 0 is the most "K-feldspar-like". Note that J0048 Q scores are slightly above 1.0 as it performed better than the quartz standard, and that there is a wide variation in K-feldspar values, possibly reflecting subtle differences in chemical composition.

Sample		Thermal quenching/ assistance	IR bleach of OSL	TQ/A test scaled to standard	IR bleach test scaled to standard	Ave of 2 tests
J0048	Q	0.27	1.02	1.02	1.00	1.01
J0048	Q	0.25	1.03	1.03	1.00	1.02
J0048	K	1.37	5.46	0.37	0.74	0.55
J0048	K	1.34	5.20	0.39	0.75	0.57
J0054	Q	0.32	1.12	0.99	0.99	0.99
J0054	Q	0.39	1.09	0.95	1.00	0.97
J0054	K	1.91	17.14	0.05	0.05	0.05
J0054	K	1.74	15.28	0.16	0.16	0.16
J0084	"Q"	1.56	7.43	0.26	0.62	0.44
J0084	"Q"	1.55	8.75	0.26	0.54	0.40
J0084	K	1.75	10.19	0.15	0.46	0.30
J0084	K	1.71	11.10	0.17	0.41	0.29
J0118	Q	0.61	1.11	0.82	0.99	0.91
J0118	Q	0.73	1.02	0.75	1.00	0.87
J0118	K	1.64	8.36	0.21	0.57	0.39
J0118	K	1.62	8.23	0.22	0.58	0.40
J0119	Q	0.46	1.13	0.91	0.99	0.95
J0119	Q	0.50	1.03	0.88	1.00	0.94
J0119	K	1.58	8.94	0.25	0.53	0.39
J0119	K	1.48	7.28	0.31	0.63	0.47
J0145	Q	0.42	1.16	0.93	0.99	0.96
J0145	Q	0.44	1.28	0.92	0.98	0.95
K fspr	K	1.78	8.34	0.13	0.57	0.35
K fspr	K	1.75	8.74	0.15	0.55	0.35

the values are zero to one, with quartz-like samples typically at 0.95 or greater, while lower values denote progressively more feldspar-like behavior. The two scaled ratios are then averaged to give an overall assessment. The quartz fraction of sample J0084 "Q" is of note, as its average resulted in values of 0.44 and 0.40, a score lower than several of the feldspar samples (ie J0048 K). This test is a useful tool to assess quartz- or feldspar-like behavior in materials isolated following to Wintle (1997), and allows for comparison of multiple sample populations (see Table 4). Future work will assess this test's potential at distinguishing between other minerals, such as zircon inclusions.

The test proposed also has the potential for assessing more parameters for more in-depth analysis of sample characteristics (see Table 2). The presence of IRSL is tested, as is sensitivity change which can provide valuable information about characteristics of the sample. We also included LM-OSL measurements within our test to allow for more in-depth curve fitting analysis of samples as an operator check upon validity of the test. While Duller (2003) felt that decay shape was a poor marker of contamination, LM-OSL offers more numerical analysis of feldspar and quartz components decay curves than in CW-OSL, with multiple exponentials discernable through curve fitting for feldspars (Bulur, 1996) and for quartz (Bulur et al., 1999). Sample characteristics can be determined through the combined signal contamination test, and then confirmed through LM-OSL signal analysis before more time intensive, large number aliquot SAR cycles are performed on inadequate samples.

6. Conclusions

Quartz signals measured in samples from across Southern California are variable in intensity and the degree to which they suffer from unwanted characteristics (high thermal transfer, slow bleaching rate, signal contamination from other minerals). Feldspar signals suffer from reduced daylight bleaching rates, high thermal transfer and a poor dose recovery after a short daylight bleach.

The combined signal contamination test is quite capable of discerning "quartz-like" and "feldspar-like" behaviors in samples from Southern California, and assesses the behavior of a wide range of samples with varying luminescence characteristics. The test applied here combined post-IR OSL/OSL ratio (Duller, 2003), and thermal quenching (Smith and Rhodes, 1994) observations to assess signal characteristics, and offers the potential to be developed into a more sophisticated investigation based on a number of other parameters (see Table 2). We note that the EDX spectroscopy conducted within the SEM provides definitive identification of the mineralogy of individual grains, but EDX determinations are highly time consuming, cannot be conducted on every grain, and cannot be used to identify the composition of inclusions contained entirely within grains. EDX is extremely useful in establishing which minerals are present for a given sample, but unlikely to become a routine method for assessing sample composition. We consider that our combined signal contamination test is more efficient and robust, and represents a useful addition to existing approaches.

Acknowledgments

We would like to thank Southern California Earthquake Center (SCEC) for their funding of portions of this research (SCEC number #11198). Thank you to Sunshine Abbott (UCLA) for her expertise on SEM analysis, and to all collaborators on all the projects from which samples were selected for this study. We would also like to thank our anonymous reviewer for their insightful comments.

Appendix A. Supplementary material

Supplementary data associated with this article can be found, in the online version, at doi:10.1016/j.radmeas.2012.03.025.

References

Bulur, E., 1996. An alternative technique for optically stimulated luminescence (OSL) experiment. Radiation Measurements 26, 701–709.

Bulur, E., Bøtter-Jensen, L., Murray, A.S., 1999. Optically stimulated luminescence from quartz measured using the linear modulation technique. Radiation Measurements 32, 407–411.

Dawson, T.E., McGill, S.F., Rockwell, T.K., 2003. Irregular recurrence of paleoearthquakes along the central Garlock fault near El Paso Peaks, California. Journal of Geophysical Research 108, 1–29.

Delong, S.B., Arnold, L.J., 2007. Dating Alluvial deposits with optically stimulated luminescence, AMS C14 and Cosmogenic techniques, western Transverse Ranges, California, USA. Quaternary Geochronology 2, 129–136.

Duller, G., Bøtter-Jensen, L., Poolton, N., 1995. Stimulation of mineral-specific luminescence from multimineral samples. Radiation Measurements 24, 87–93.

Duller, G.A.T., 2008. Luminescence Dating: Guidelines on Using Luminescence Dating in Archaeology. English Heritage, Swindon.

Duller, G., 2003. Distinguishing quartz and feldspar in single grain luminescence measurements. Radiation Measurements 37 (2), 161–165.

Godfrey-Smith, D.I., Huntley, D.J., Chen, W.H., 1988. Optical dating studies of quartz and feldspar sediment extracts. Quaternary Science Reviews 7, 373–380.

Huntley, D.J., 2006. An explanation of the power-law decay of luminescence. Journal of Physics: Condensed Matter 18, 1359–1365.

Ingersoll, R.V., 2008. Reconstruction southern California. Arizona Geological Society Digest 22, 409–417.

Mahan, S.A., Miller, D.M., Menges, C.M., Yount, J.C., 2007. Late Quaternary stratigraphy and luminescence geochronology of the northeastern Mojave Desert. Quaternary International 166, 61–78.

Mauz, B., Lang, A., 2004. Removal of feldspar-derived luminescence component from polymineral fine silt samples for optical dating applications: evaluation of chemical treatment protocols and quality control procedures. Ancient TL 22, 1–8.

Mazess, R.B., Zimmerman, D.W., 1966. Pottery dating from thermoluminescence. Science 152, 347.

Murray, A.S., Wintle, A.G., 2000. Luminescence dating of quartz using an improved single-aliquot regenerative-dose protocol. Radiation Measurements 32, 57–73.

Pietsch, T., Olleya, J., Nanson, G., 2008. Fluvial transport as a natural luminescence sensitizer of quartz. Quaternary Geochronology 3, 365–376.

Rhodes, E.J., 2000. Observations of thermal transfer OSL signals in glacigenic quartz. Radiation Measurements 32, 595–602.

Rhodes, E.J., 2011. Optically stimulated luminescence dating of sediments over the past 200,000 years. Annual Review of Earth and Planetary Science 39, 461–488.

Roder, B.J., Rhodes, E.J., Lawson, M.J., Dolan, J.F., McAuliffe, L., McGill, S.F. Assessing the potential of luminescence dating for fault slip rate studies on the Garlock fault, Mojave Desert, California, USA. Quaternary Geochronology, in press.

Shen, Z., Muaz, B., Lang, A., Bloemendal, J., Dearing, J., 2007. Optical dating of Holocene lake sediments: elimination of the feldspar component in fine silt quartz samples. Quaternary Geochronology 2, 150–154.

Smith, B.W., Rhodes, E.J., 1994. Charge movements in quartz and their relevance to optical dating. Radiation Measurements 23, 329–333.

Sohn, M., Mahan, S., Knott, J., Bowman, D., 2007. Luminescence ages for alluvial-fan deposits in Southern Death Valley: implications for climate-driven sedimentation along a tectonically active mountain front. Quaternary International 166, 49–60.

Stokes, S., 1992. Optical dating of young (modern) sediments using quartz-results from a selection of depositional-environments. Quaternary Science Reviews 11, 153–159.

Wiggenhorn, H., 1994. IRSL dating of K-feldspar at elevated-temperatures and infrared bleaching of TL. Radiation Measurements 23, 387–391.

Wintle, A., 1973. Anomalous fading of thermoluminescence in mineral samples. Nature 245, 143–144.

Wintle, A.G., 1997. Luminescence dating: laboratory procedures and protocols. Radiation Measurements 27, 769–817.

IV. ASSESSING OPTICALLY STIMULATED LUMINESCENCE (OSL) SIGNAL CONTAMINATION WITHIN SMALL ALIQUOTS AND SINGLE GRAIN MEASUREMENTS UTILIZING THE COMPOSITION TEST

Contents lists available at ScienceDirect

Quaternary International

journal homepage: www.elsevier.com/locate/quaint

Assessing Optically Stimulated Luminescence (OSL) signal contamination within small aliquots and single grain measurements utilizing the composition test

Michael J. Lawson*, Jillian T.M. Daniels, Edward J. Rhodes

Earth and Space Sciences, UCLA, Los Angeles, CA 90095, USA

ARTICLE INFO

Article history:
Available online 5 June 2014

Keywords:
Optically Stimulated Luminescence (OSL)
Contamination
Feldspar
Single grain
Thermal quenching
Scanning Electron Microscope (SEM)

ABSTRACT

Quartz in tectonically active regions can suffer from signal contamination when utilized for Optically Stimulated Luminescence (OSL) dating. Typically, these environments bring quartz-bearing bedrock to the surface, which erodes and enters geomorphic systems with little fluvial reworking, resulting in dim OSL signal response. Conversely, feldspars often have an inherently brighter signal, even among bedrock or freshly eroded samples. Environments with dim quartz can be difficult to date as the signal contribution from errant feldspars may dominate the measured signal. Further, immature sediments may retain mineral inclusions within quartz grains that would have been physically or chemically eroded in more mature sediments. Previously, we presented a signal composition test which utilizes thermal quenching and IR bleaching susceptibility to assess the purity of a quartz sample. Additional measurements have been made, looking at the systematics of how small volumes of feldspar can affect the results of aliquots analyzed with this composition test. Further, different feldspar samples have been assessed for their response to the composition test and chemical compositions were determined using energy-dispersive X-ray (EDX) spectroscopy with a scanning electron microscope (SEM). Finally, we present a single grain protocol for the composition test.

1. Introduction

California has very diverse geological environments, and is characterized by active tectonics along its western margin, where a plate boundary exists between the North American and Pacific plates. Regionally in Southern California, researchers have found that quartz OSL can have poor characteristics, such as low bleachability, low sensitivity, and high thermal transfer which have hindered its application towards geological research problems (Lawson et al., 2012; Roder et al., 2012). Further, there is wide variation in the depositional environments, which complicates OSL dating (Rhodes, 2011). This is compounded in rapidly deposited sediments related to tectonics, as well as the subsequent erosion of fault related offsets. While some of the difficulties associated with these settings, such as incomplete zeroing and the effect of bioturbation can be mitigated using single grain measurement (Porat et al., 2009), the effects of signal contamination are still a concern.

Regionally, quartz has been shown to vary widely in genesis and this affects quartz's amenability to OSL dating (Sawakuchi et al., 2011). Fluvial recycling has been shown to increase quartz OSL sensitivity (Pietsch et al., 2008), and it stands to reason that freshly eroded material, which has seen few if any fluvial cycles, would therefore lack sensitivity. Freshly eroded material can also contain mineral inclusions, which due to the fresh exposure of the minerals, have not yet been chemically or mechanically removed from crystal edges, or can be completely encased within a shell of more resistant quartz.

Feldspar typically has bright signals, so contamination can be a problem (i.e. feldspar in quartz samples) such that even small inclusions of feldspar within quartz grains can dominate signals in samples that have been chemically and physically separated using standard procedures (Lawson et al., 2012). Given the differences in luminescence properties, feldspar and quartz need to be measured separately. The TL and IRSL signals from feldspar have been shown to fade due to anomalous and poorly understood properties (Wintle, 1973; Spooner, 1992, 1994). Furthermore, alkali feldspars (including K-spar) have an internal potassium content which needs to be taken into account to correct for the amount of radiation grains receive for the determination of ages. For this reason, feldspars and quartz typically are isolated from each other, and in some applications, have been used in parallel to produce robust dates, but frequently serve as a fallback if one or other minerals have poor characteristics (Jaiswal et al., 2009).

For this study, we expanded upon previous research that assesses the amount of contamination within a sample using the luminescence signal, rather than relying upon chemical and physical treatments (Lawson et al., 2012). Many tests have been proposed to detect feldspar contamination within quartz aliquots: (i) the routine presence of an IRSL signal even though only quartz is prepared (Stokes, 1992), (ii) the susceptibility of the OSL signal to IRSL bleaching known as the OSL IR depletion ratio (Duller, 2003), and (iii) the shape of IRSL and OSL decay curves as quartz has a rapid decay related to the fast component, while feldspar has a more gradual decay (Rhodes, 2011). Feldspar follows a power law decay in continuous wave IRSL (Huntley, 2006) while quartz is the sum of several exponentials consisting of the fast, medium and slow components (Smith and Rhodes, 1994; Bulur et al., 2000). LM-OSL offers the ability to analyze these fundamental differences in signal shape through curve fitting (Bulur, 1996; Bulur et al., 2000).

Our previous work (Lawson et al., 2012) utilized thermal quenching (Smith and Rhodes, 1994) and a modified OSL IR depletion ratio (Duller, 2003) as a test to determine the presence of feldspar within quartz samples. Thermal quenching has been demonstrated in quartz and is a progressive decrease in OSL signal intensity at higher measurement temperatures (Smith and Rhodes, 1994). Conversely, feldspars have been shown to exhibit thermal assistance, where IRSL intensity increases at greater measurement temperatures (Wiggenhorn, 1994) which has been subsequently demonstrated in OSL signals (Duller, 1997). This composition test, however, was not assessed for the limits of contamination detection within quartz aliquots. For further examination into the contamination issue of feldspar, we created an experiment with artificially mixed samples as detailed below, in which we purposely contaminated quartz samples with potassium feldspar (K-spar) and plagioclase grains of known origin and luminescence characteristics. This experiment was primarily carried out using single grains and the protocol has been developed with single grain dating in mind.

2. Material and methods

2.1. Mixture experiment

The mixture experiment was created as an assessment of the composition test, as outlined in our previous work (Lawson et al., 2012). For the mixture experiment, we blended a bright quartz sample with relatively dim potassium feldspar (K-spar) and plagioclase samples in 1%, 3%, 10%, and 30% proportions by mass (Table 1). In this experiment, we used natural Brazilian dune quartz (sample J0239; Fig. 1A). The sample was quite sensitive to a test dose, and gave bright signals with an initial intensity greater than 9000 counts per second (Fig. 2A). This sample was prepared using standard procedures as outlined by Wintle (1997). The sample was collected in the field in steel tubes 6 cm in diameter and 10 cm in length, holding approximately 280 cm^3, or 800 g of material. These were hammered into the deposit utilizing an aluminum cap which prevented its exposure to light. Once in the lab, the sample was removed from the tube, and wet sieved to isolate the modal grain

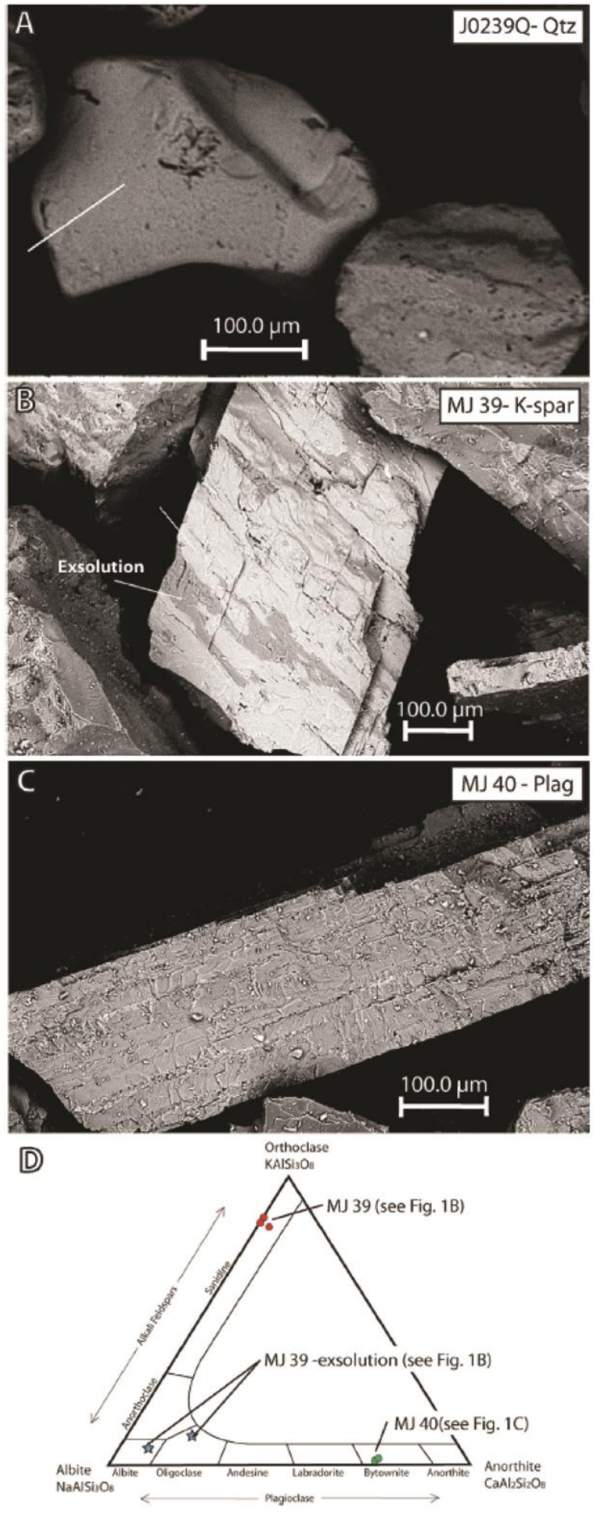

Fig. 1. Scanning Electron Microscope (SEM) images of the samples used in the mixture experiment. Scale bars are consistently 100.0 μm. (A) Brazilian dune sand (sample J0239Q). (B) Image of MJ39 K-spar, showing albitic exsolution lamellae. (C) Image of MJ40 plagioclase, with tabular fracture. (D) Ternary diagram of the chemical composition of MJ39 and MJ40 derived by EDX spectroscopy. Plotting software by Graham and Midgley (2000).

size. Utilizing a binocular microscope illuminated with subdued safelights, we found little cementation between grains. The sample was then treated with hydrochloric acid to remove any carbonate coatings that would negatively affect the lithium meta-tungstate (LMT) used subsequently during heavy liquid separation. The LMT density was accessed utilizing a hydrometer, and mixed to 2.58 g/cm^3 to isolate the quartz portion of the samples. The fraction greater than this density was then treated with 40% hydrofluoric acid for a minimum of 100 min, more than twice the standard treatment of 40 min (Fleming, 1970; Wintle, 1997) to remove surface inclusions and alpha dose effects. The sample was also examined by a LEO 1430 Scanning Electron Microscope (SEM), which allowed for morphologic verification as well as chemical analysis through energy-dispersive X-ray (EDX) spectroscopy (Fig 1A; Table 2).

Table 1
Experimental set up and actual values.

				Actual values[a]			
Sample	Quartz (Q0239)	Plag (MJ40)	K-spar (MJ39)	Sample	Quartz (Q0239)	Plag (MJ40)	K-spar (MJ39)
	Percent	Percent	Percent		Percent	Percent	Percent
QP00	100%	0%		QP00	100%	n/a	
QP01	99%	1%		QP01	99.0% ± 0.3%	1.0% ± 0.3%	
QP03	97%	3%		QP03	97.0% ± 0.3%	3.0% ± 0.3%	
QP10	90%	10%		QP10	90.0% ± 0.3%	10.0% ± 0.3%	
QP30	70%	30%		QP30	70.1% ± 0.3%	29.9% ± 0.3%	
QK01	99%		1%	QK01	98.9% ± 0.3%		1.1% ± 0.3%
QK03	97%		3%	QK03	97.0% ± 0.3%		3.0% ± 0.3%
QK10	90%		10%	QK10	90.0% ± 0.3%		10.0% ± 0.3%
QK30	70%		30%	QK30	70.0% ± 0.3%		30.0% ± 0.3%

[a] Instrument drift ~ 0.0002 g.

Table 2
Energy-dispersive X-ray (EDX) spectroscopy results.

Sample	Na_2O	Al_2O_3	SiO_2	K_2O	CaO	Total	Ca/(Na + Ca)	K/(K + Na)	Na	K	Ca	Total
	Percent	Percent	Percent	Percent	Percent	Percent	Percent	Percent	Percent	Percent	Percent	Percent
MJ39	1.70	14.32	73.37	10.38	0.23	100	21.30	85.93	6.67	0.11	93.22	100
MJ39	1.76	15.55	71.80	10.89	0.00	100	0.00	86.09	7.21	0.00	92.79	100
MJ39	1.88	13.31	74.89	9.92	0.00	100	0.00	84.07	6.24	0.00	93.76	100
MJ39 (exsolution)	9.51	16.20	71.66	1.39	1.24	100	20.68	12.75	7.45	0.57	91.98	100
MJ39 (exsolution)	12.28	13.63	72.55	0.92	0.62	100	9.17	6.97	6.36	0.29	93.35	100
MJ40	6.89	18.36	64.37	0.51	9.87	100	74.13	6.89	8.04	4.32	87.63	100
MJ40	6.95	19.13	62.87	0.62	10.43	100	75.01	8.19	8.33	4.54	87.12	100

Two types of feldspar were used as contaminates for the mixture experiment: potassium-feldspar (K-spar) and plagioclase. These samples were museum collection samples without previous origin recorded, and previously prepared by W.E. Reed, UCLA. Both samples were isolated in the petrology lab at UCLA, sieved to ~125 μm size, imaged and chemically analyzed using the SEM (Fig. 1B and C; Table 2). Several grains were adhered to a standard SEM peg using carbon tape, mounted into an 8-pin carousel, and pumped down to high vacuum (~15 Pa or ~10^{-4} atm). The backscatter detector was used to record the images. Lighter shades generally indicate higher atomic numbers. We employed EDX spectroscopy, which utilizes X-ray stimulation to determine the chemical composition (in oxide percent) of sections of the mineral grains. The spot size in these measurements is approximately 1 μm, much smaller than the features being investigated. The potassic feldspar (sample MJ39; Fig 1B) was found to have an approximate composition of $Ab_{15}Ks_{85}$. Further, the K-spar sample had darker streaks within it, which were consistent chemically with perthitic exsolution lamellae. The effects of such lamellae on the IRSL signal are not well known, but are being investigated. The plagioclase sample (MJ40; Fig. 1C) was found to be a bytownite ($An_{80}Ab_{20}$) using the same procedures. Both samples had very dim responses to test doses (Fig. 2B, C), and were considered ideal for the experiment given their dimness (by a factor of 10) relative to the Brazilian dune sand previously described (Fig 2A).

Bright Brazilian quartz (J0239) was mixed with plagioclase/K-spar, targeted to 0, 1, 3, 10, and 30% by weight using a Mettler AE 240 four-figure accuracy scale. Instrument drift was determined using a set mass, which was tracked through the experiment for the calculation of error introduced by instrumental drift and found to be ~0.2 mg (Table 1). While both feldspar samples were well bleached, the Brazilian quartz still had a natural signal, so samples were weighed in darkroom conditions, using reduced intensity safe lights. Once appropriate weights were assessed, samples were placed in small black pots, which were then briefly shaken to mix the two populations. Samples were then measured on aluminum disks, upon which grains were secured using small dots of silicone oil that captured between 50 and 100 grains. Samples were measured on a Risø TL-DA-20 reader, using a strontium-90 beta source and detected with a photomultiplier tube equipped with U-340 filters (Bøtter-Jensen et al., 2000). Aliquots were stimulated with blue LEDs and IR diodes, while single grain measurements were stimulated with a green (532 nm) solid-state diode-pumped laser (Bøtter-Jensen et al., 2000).

2.2. Normalized quenching factor

The composition test is determined by the protocol set down in our previous work (Lawson et al., 2012; Table 3), which we have since modified to decrease measurement time. We have removed the LM-OSL and LM-IRSL measurements which are time-intensive. We have also removed the elevated temperature IRSL measurement (150 °C for 40 s) at the end of the test, since it was no more effective at determining contamination than the quenching assessment detailed below. For the quenching factor, samples are given an initial bleach at 125 °C for 120 s, followed subsequently by a 100-s beta dose (~11 Gy) and then a preheat to 220 °C at 5 °C per second. After background is subtracted, three 40-s OSL measurements at 125 °C ($OSL_{125°C}$; Table 3: steps 5, 8 and 11) and one 40-s measurement at 200 °C ($OSL_{200°C}$; Table 3: step 6) determine the quenching factor (Q_f):

$$\text{Where:}\quad Q_f = \frac{OSL_{200°C}}{\left(\frac{\sum OSL_{125°C}}{3}\right)}$$

Table 3
Small aliquot composition test procedures, properties assessed, and relevant references.

Step				Assesses	
1	OSL bleach	125 °C	120 s		
2	Beta dose (~11 Gy)		100 s		
3	Preheat	220 °C			
4	IRSL	50 °C	40 s		
5	OSL	125 °C	40 s		
	Repeat 2–4				
6	Elevated temperature OSL	200 °C	40 s	Thermal quenching (steps 5, 6, 8 & 11)	(Smith and Rhodes, 1994)
	Repeat 2 and 3				
7	IRSL	50 °C	40 s		
8	OSL	125 °C	40 s	Sensitivity change	
	Repeat 2 and 3				
9	OSL without pre IRSL	125 °C	40 s	OSL IR depletion ratio (steps 5, 8, 9, 11)	(Duller, 2003)
	Repeat 2 and 3				
10	IRSL	50 °C	40 s		
11	OSL	125 °C	40 s	Sensitivity change	

The quenching factor is a dimensionless ratio. To aid in analysis, we modify this value in such a way that pure quartz samples would plot ~1, as detailed below. From Lawson et al. (2012), the greatest quenching factor of a pure quartz sample was found to be 0.3, which we set as a quartz standard ($Q_{f\ Q\ std}$). The purity of this sample was confirmed through SEM analysis (Lawson et al., 2012) The greatest quenching factor of a feldspar sample was found to be 2.0, which was set as a feldspar standard ($Q_{f\ K\ std}$) From this, the normalized thermal quenching factor is assessed:

$$\text{Normalized Thermal Quenching Factor} = 1 - \left(\frac{Q_f - Q_{f\ Q\ std}}{Q_{f\ K\ std} - Q_{f\ Q\ std}}\right)$$

The normalized thermal quenching factor should then give a value between 1 and 0, where quartz like behavior is 1, and thermally assisted feldspars should be ~0.

2.3. Normalized post-IR ratio

The OSL IR depletion ratio was originally outlined by Duller (2003), but is modified here in such a way that quartz-like behavior is ~1. This is done to simplify comparison between different samples. As detailed above, samples are given an initial bleach at 125 °C for 120 s, then a 100-s beta dose (~11 Gy) and a preheat to 220 °C. The OSL IR depletion ratio is measured with three 40-s OSL measurements that are preceded by IRSL bleaching ($OSL_{w\ IRSL}$; Table 3: steps 5, 8, and 11), and one 40-s measurement with no IRSL bleach ($OSL_{w\ o\ IRSL}$; Table 3: step 9). After background is subtracted, the OSL IR depletion ratio is determined as:

$$\text{OSL IR depletion ratio} = \frac{\text{average}(OSL_{w\ IRSL})}{OSL_{w\ o\ IRSL}}$$

Given that this is a dimensionless ratio, we modified it in a similar way such that the quartz-like behavior ~1. From Lawson et al. (2012), the least affected quartz sample as measured by this test was 1.02, and was set as a quartz standard ($Q_{PIR\ Q\ std}$), while the most affected feldspar sample measured 18.00, and was similarly set as the feldspar standard ($Q_{PIR\ K\ std}$). From this we calculated the normalized post-IR ratio:

$$\text{Normalized Post-IR Ratio} = 1 - \left(\frac{PIR - PIR_{Q\ std}}{PIR_{K\ std} - PIR_{Q\ std}}\right)$$

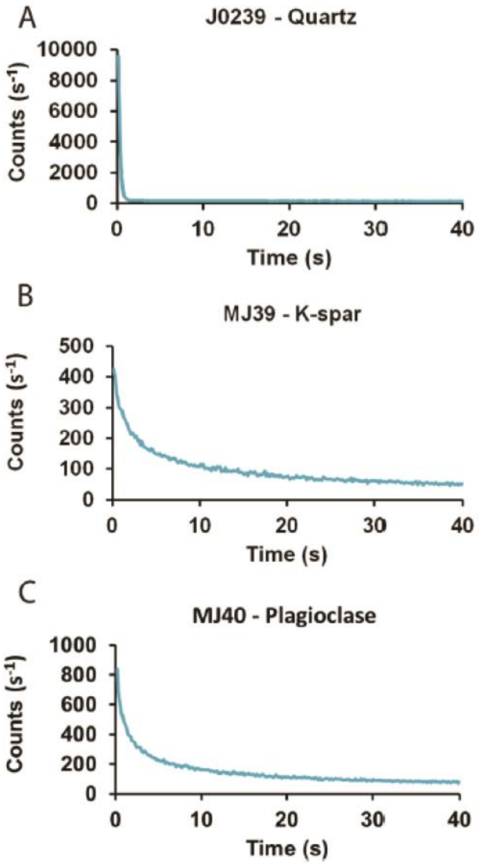

Fig. 2. Decay curves of small aliquots of pure samples used in the mixture experiment, after an 11.1 Gy beta dose (100 s). (A) Quartz portion of Brazilian dune sample J0239, showing a bright signal. (B) Sample MJ39 K-spar, showing a dim feldspar-like decay. (C) MJ40 plagioclase showing a dim response to the test dose.

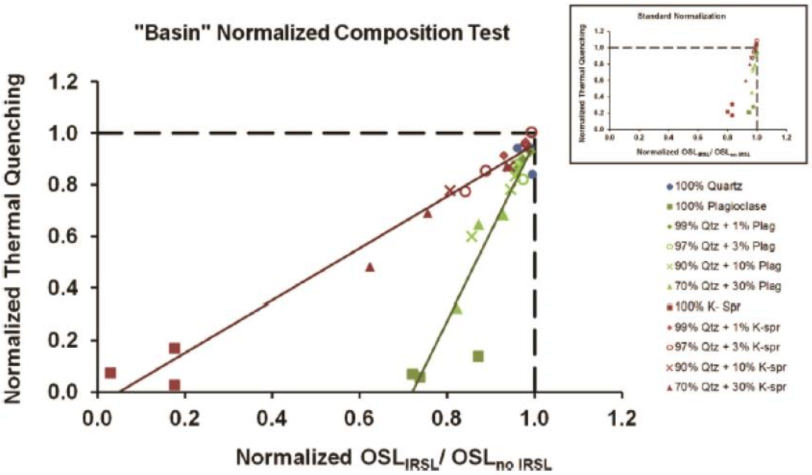

Fig. 3. Results from the small aliquot mixture experiment. In the "basin" normalized plot, the normalization values are modified to reflect the response by the most contaminated of the samples in the specific catchment. If local contamination is known, this would allow researchers to focus in greater detail on the spread of the results. The upper right plot is the results with standard normalization, per Lawson et al. (2012).

2.4. *Composition test*

The composition test is based upon the normalized post-IR ratio and the normalized thermal quenching factor. These are plotted such that quartz like behavior should be at the (1,1) point and progressively more feldspar-like behavior plots away from this position towards the origin.

2.5. *Single grain measurement*

In addition to developing the normalized quenching factor and the normalized post-IR ratio, we developed a single grain protocol using single grain measurements. Sample J0048 was dune beach sand, sampled from a Holocene cliff-top dune near Point Dume in Malibu California. Sample J0048 was used previously in the development of the composition test because of its bright response (Lawson et al., 2012). Sample J0442, which was a well-sorted shallow lake deposit from northern Egypt, was also used in the single grain protocol because it did not have a bright signal and generally performed suboptimally when compared to the Malibu beach sand. Both samples were prepared as detailed above: wet sieved, the quartz fraction isolated using gravity separation, and then treated with hydrofluoric acid. Two single grain disks of each sample were used, comprising ~200 grains in total.

3. Results and interpretation

3.1. *Mixture experiment*

The mixture experiment produced results that were consistent with expectations; that is, the samples with the greatest K-feldspar and plagioclase contamination plotted the furthest away from the (1,1) point, which represents the most quartz-like behavior (Fig. 3).

The main plot in Fig. 3 is "basin" normalized, which allows researchers to specify actual mineralogical contaminations, if they are known. Given that we had "pure" values for these samples, we modified the typical normalization with quartz and feldspar standards to reflect the material being investigated. For instance, if research shows the quartz comes from a discrete location within a basin or other geomorphic feature sourced from plutonic source rock with distinctive feldspars, researchers can compare the "basin" samples against the "pure" or standard samples and use this comparative information to clarify the amount and type of potential feldspar contamination within a larger basin.

For "basin" normalized analysis, researchers would assess their samples using the standard procedure as outlined above (Lawson et al., 2012), measuring crushed feldspar samples that represent potential contamination within their sample basin. Once their quenching factor and post-IR ratios are determined, the crushed feldspar is used as the feldspar standard for the post IR OSL ratio ($Q_{PIR\ K\ std}$) and the quenching factor ($Q_{f\ K\ std}$). For our experiment, we also had a pure quartz sample, as determined by SEM analysis, which were used and set as the quartz standard ($Q_{PIR\ Q\ std}$ and $Q_{f\ Q\ std}$). In this case, the $Q_{PIR\ Q\ std}$ and $Q_{PIR\ K\ std}$ were 0.98 and 4.5 respectively, while the $Q_{f\ Q\ std}$ and $Q_{f\ K\ std}$ were found to be 0.15 and 1.75 respectively. The pure quartz sample was near the (1,1) position, while the pure K-feldspar and plagioclase samples were the most affected by thermal quenching. The 1, 3, 10, and 30% mixtures of quartz and either plagioclase or K-feldspar both plotted on fairly linear trends, which is consistent with the gradual mixture of these two populations. We have not investigated if the differences in slope between these two trends are significant. As mentioned above, this represents the worst case scenario of contamination detection with the composition test, in which very bright quartz is mixed with relatively dim feldspars.

In Fig. 3, the upper right image shows the standard normalization, as outlined above (Lawson et al., 2012). In this plot, it is clearly seen that thermal quenching is more effective at teasing out contamination then the OSL IR depletion ratio. Note that the quartz in this experiment was more affected by thermal quenching then our standard set out in our previous work (Lawson et al., 2012).

3.2. *Single grain measurement*

Samples J0048 and J0452 were measured using the single grain SAR protocol (Duller et al., 2000). The Malibu beach dune sample had an equivalent dose of 16.92 ± 0.24 Gy, as determined through the central age model (Galbraith et al., 1999), from 100 well behaved grains out of a total of 200 grains measured (Fig. 4). The single grain composition test protocol (Table 4) is similar to that presented above. After a 120-s OSL bleach at 125 °C, the disc is given a 100-s beta dose (~11 Gy). It is then preheated to 220 °C (at 5 °C/s), and the entire disc is bleached with IR diodes at 60 °C for expediency. Individual grains are then measured for 3 s of OSL, rather than the 40 s used in the small aliquot protocol. For the single grain composition test, grains were selected with less rigorous criteria than that typically selected for the single grain SAR protocol. The rejection criteria for accepting grains was less than that used for the determination of the equivalent dose, and grains with signals greater than 50 counts initial decay after background subtraction were selected in the hope of showing anomalous grains. In the Malibu beach dune sample (J0048), 125 grains were measured and these plotted very consistently within the nominal quartz range (see Fig. 4A). Despite its high sensitivity, J0048 still had scatter within its response to the thermal quenching of ±20%, which we have not yet investigated.

Table 4
Single grain composition test procedures, properties assessed, and relevant references.

Step				Assesses	
1	OSL bleach	125 °C	120 s		
2	Beta dose (~11 Gy)		100 s		
3	Preheat	220 °C			
4	IR diodes	60 °C	40 s		
5	Single grain OSL	125 °C	3 s each		
	Repeat 2–4				
6	Elevated T single grain OSL	200 °C	3 s each	Thermal quenching (Steps 5, 6, 8 & 11)	(Smith and Rhodes, 1994)
	Repeat 2 and 3				
7	IR diodes	60 °C	40 s		
8	Single grain OSL	125 °C	3 s each	Sensitivity change	
	Repeat 2 and 3				
9	Single grain OSL without IRSL	125 °C	3 s each	OSL IR depletion ratio (Steps 5, 8, 9, 11)	(Duller, 2003)
	Repeat 2 and 3				
10	IR diodes	60 °C	40 s		
11	Single grain OSL	125 °C	3 s each	Sensitivity change	

Sample J0452, however, was less sensitive. Of 200 grains measured, only 46 grains were suitably well behaved to determine an equivalent dose of 5.50 ± 0.26 Gy as determined by the central age model (Galbraith et al., 1999). For the single grain composition test, only 67 grains gave a signal greater than 50 counts per second above background (Fig 4B). Clearly, this sample responded differently, as two grains plot away from the main cluster (Fig. 4B). Frequently we have found a spread of quartz grains' responses to quenching, and it is not atypical to have grains above the (1,1) point. For example, in Fig. 6B a grain plots well above the cluster of grains, having a normalized thermal quenching value of ~1.2. This reflects that the grain has a greater response to quenching than our quartz standard, which was chosen because at the time it had the greatest response to quenching (Lawson et al., 2012). With additional measurements, we have found that some quartz materials quench to a greater degree than our Malibu beach dune sample. We have not yet investigated the cause of this variability within quartz populations.

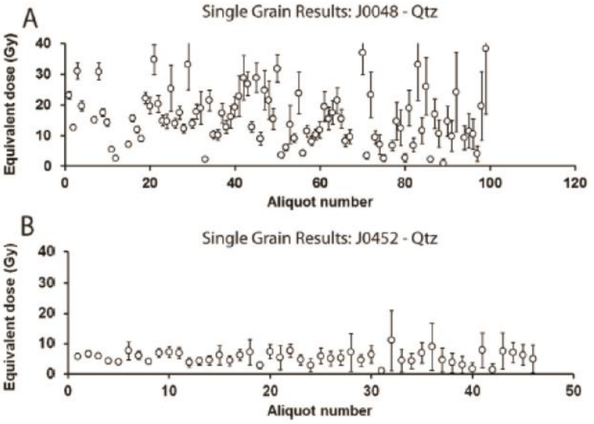

Fig. 4. Single grain results after the measurement of two disks containing ~100 grains each, sorted by sensitivity. (A) Single grain results from sample J0048 quartz, showing the equivalent dose from 100 grains. The samples have an equivalent dose of 16.92 ± 0.24 Gy. (B) Single grain results from sample J0452Q, showing the equivalent dose from 46 grains. The samples have an equivalent dose of 5.50 ± 0.26 Gy.

4. Discussion

The mixture experiment was designed to recreate the worst-case scenario for feldspar contamination. Given the brightness of the quartz sample and the dimness of the feldspar samples, it would be more difficult to determine feldspar contamination within these mixed samples. Typically in Southern California we have the opposite scenario, with dim quartz and bright feldspar, which exacerbates the problem of grain contamination, since just a few grains of feldspar can represent a significant portion of the overall signal. Fig. 3 shows the results of the mixture experiment, which is consistent with what is expected.

Commonly, the presence of an IRSL signal has been used to assess feldspar contamination. Fig. 5 compares the effectiveness of the composition test to IRSL intensity of samples. Remembering that the mixture experiment was designed to be the worst-case scenario for contamination (i.e. bright quartz and dim feldspars), the composition test is as effective as IRSL intensity, if the feldspar grains produce an IRSL signal. If the researcher rejects any aliquots that have any appreciable IRSL signal, then the composition test is less effective. However, feldspars could potentially lack an IRSL signal, and still have an OSL signal (Spooner, personal communication). In this experiment, we used dim feldspar grains, which had a signal an order of magnitude weaker than that of the quartz. In mixed samples containing as much as 30% contamination of feldspar, the signal from such errant feldspar grains would contribute very little to the overall signal and would probably have little effect on subsequent SAR cycles. However, in situations where errant feldspar grains are dramatically more sensitive than the quartz, the composition test would be more effective at detecting contamination which is certainly beneficial, given that such contamination would produce greater errors in subsequent SAR results.

The single grain composition test offers another parameter to evaluate grains for their suitability for the determination of equivalent doses. Given the dramatically decreased signals during single grain measurement, it would be more difficult to determine contamination purely from the shape of decay curves. For our future work, we wish to analyze the underlying cause of the spread of results near the (1,1) position in the composition test when analyzing quartz (Fig. 6). We wish to determine if this is due to inherent variability in the way grains respond to thermal quenching, changes in sensitivity during measurement, or if it is perhaps reflecting some underlying property of quartz, in which grains are responding to other unknown phenomena. We would also like to examine if this result was related to variations in the type of quartz

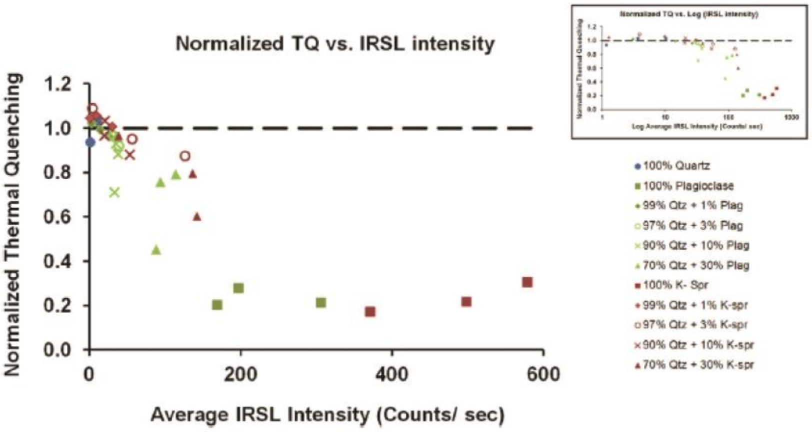

Fig. 5. Comparison of the small aliquot normalized thermal quenching (TQ) to the average IRSL intensity of samples. The upper right plot is a normal-log plot.

examined. Sample J0048 was sand from a beach dune, and has many potential sources. The nearest major stream is the Santa Clara River which enters the Pacific Ocean in Oxnard, and has diverse sedimentary sources within its catchment including pyroclastic volcanic flows, plutonic terraines, metamorphic schist exhumed from Jurassic subduction complexes, and numerous sedimentary sandstone groups (Valles, 1985). Furthermore, longshore drift would have brought additional material from sources further north along the coast, further complicating this issue. As of yet, no systematic examination of effect of source material upon OSL sensitivity has been attempted, beyond Fitzsimmons (2011).

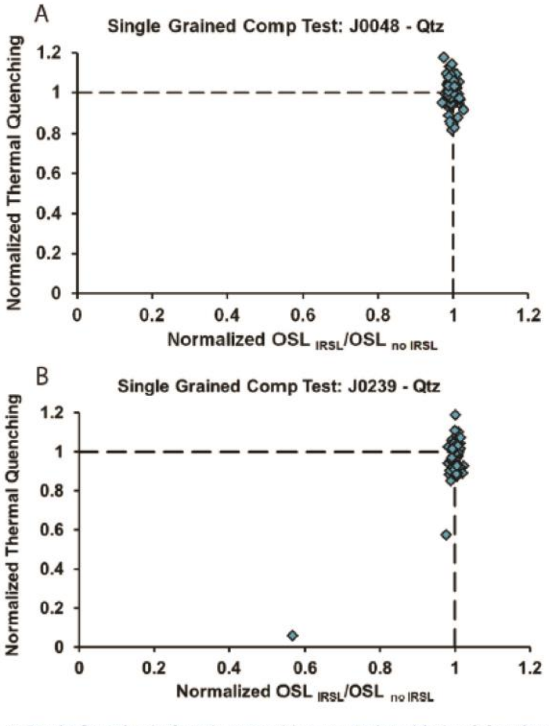

Fig. 6. Results from the single grain composition test. Grains with signals less than 50 counts above background are excluded. (A) Malibu beach dune quartz (J0048) showing good clustering of 125 grains (of 200 measured) at the 1:1 point, reflecting highly quartz-like properties. (B) Results of J0239 quartz, showing 67 grains (of 200 measured). The majority of the grains plot at the 1:1 point, but two grains are potentially contaminated.

Acknowledgements

We would like to thank Utah State University in Logan, Utah for their hospitality during the 9th New World Luminescence Dating Workshop. We thank W.E. Reed for his processing and preparation of our feldspar samples. Finally, we would like to thank the insightful comments of our anonymous reviewers.

References

Bøtter-Jensen, L., Bulur, E., Duller, G.A.T., Murray, A.S., 2000. Advances in luminescence instrument systems. Radiation Measurements 32 (5), 523–528.

Bulur, E., 1996. An alternative technique for optically stimulated luminescence (OSL) experiment. Radiation Measurements 26 (5), 701–709.

Bulur, E., Bøtter-Jensen, L., Murray, A.S., 2000. Optically stimulated luminescence from quartz measured using the linear modulation technique. Radiation Measurements 32 (5), 407–411.

Duller, G.A.T., 1997. Behavioural studies of stimulated luminescence from feldspars. Radiation Measurements 27 (5), 663–694.

Duller, G.A.T., 2003. Distinguishing quartz and feldspar in single grain luminescence measurements. Radiation Measurements 37 (2), 161–165.

Duller, G.A.T., Bøtter-Jensen, L., Murray, A.S., 2000. Optical dating of single sand-sized grains of quartz: sources of variability. Radiation Measurements 32 (5), 453–457.

Fitzsimmons, K.E., 2011. An assessment of the luminescence sensitivity of Australian quartz with respect to sediment history. Geochronometria 38 (3), 199–208.

Fleming, S.J., 1970. Thermoluminescent dating: refinement of the quartz inclusion method. Archaeometry 12 (2), 133–143.

Galbraith, R.F., Roberts, R.G., Laslett, G.M., Yoshida, H., Olley, J.M., 1999. Optical dating of single and multiple grains of quartz from Jinmium rock shelter, northern Australia: part I. Experimental design and statistical models. Archaeometry 41 (2), 339–364.

Graham, D.J., Midgley, N.G., 2000. Graphical representation of particle shape using triangular diagrams: an Excel spreadsheet method. Earth Surface Processes and Landforms 25 (13), 1473–1477.

Huntley, D.J., 2006. An explanation of the power-law decay of luminescence. Journal of Physics: Condensed Matter 18 (4), 1359–1365.

Jaiswal, M.K., Bhat, M.I., Bali, B.S., Ahmad, S., Chen, Y.G., 2009. Luminescence characteristics of quartz and feldspar from tectonically uplifted terraces in Kashmir Basin, Jammu and Kashmir, India. Radiation Measurements 44 (5), 523–528.

Lawson, M.J., Roder, B.J., Stang, D.M., Rhodes, E.J., 2012. OSL and IRSL characteristics of quartz and feldspar from southern California, USA. Radiation Measurements 47 (9), 830–836.

Pietsch, T.J., Olleya, J.M., Nanson, G.C., 2008. Fluvial transport as a natural luminescence sensitiser of quartz. Quaternary Geochronology 3 (4), 365–376.

Porat, N., Duller, G.A.T., Amit, R., Zilberman, E., Enzel, Y., 2009. Recent faulting in the southern Arava, Dead Sea Transform: evidence from single grain luminescence dating. Quaternary International 199 (1), 34–44.

Rhodes, E.J., 2011. Optically stimulated luminescence dating of sediments over the past 200,000 years. Annual Review of Earth and Planetary Sciences 39, 461–488.

Roder, B., Lawson, M., Rhodes, E.J., Dolan, J., McAuliffe, L., McGill, S., 2012. Assessing the potential of luminescence dating for fault slip rate studies on the Garlock fault, Mojave Desert, California, USA. Quaternary Geochronology 10, 285–290.

Sawakuchi, A.O., Blair, M.W., DeWitt, R., Faleiros, F.M., Hyppolito, T., Guedes, C.C.F., 2011. Thermal history versus sedimentary history: OSL sensitivity of quartz grains extracted from rocks and sediments. Quaternary Geochronology 6 (2), 261–272.

Smith, B.W., Rhodes, E.J., 1994. Charge movements in quartz and their relevance to optical dating. Radiation Measurements 23 (2), 329–333.

Spooner, N.A., 1992. Optical dating: preliminary results on the anomalous fading of luminescence from feldspars. Quaternary Science Reviews 11 (1), 139–145.

Spooner, N.A., 1994. The anomalous fading of infrared-stimulated luminescence from feldspars. Radiation Measurements 23 (2), 625–632.

Stokes, S., 1992. Optical dating of young (modern) sediments using quartz: results from a selection of depositional environments. Quaternary Science Reviews 11 (1), 153–159.

Valles, P.K., 1985. Sand composition of the Santa Clara River, California: implications for tectonic setting. M.S. Thesis, University of California, Los Angeles.

Wiggenhorn, H., 1994. IRSL dating of K-feldspar at elevated temperatures and infrared bleaching of TL. Radiation Measurements 23 (2), 387–391.

Wintle, A.G., 1973. Anomalous fading of thermoluminescence in mineral samples. Nature 245, 143–144.

Wintle, A.G., 1997. Luminescence dating: laboratory procedures and protocols. Radiation Measurements 27 (5-6), 769–817.

V. SINUSOIDALLY MODULATED OPTICALLY STIMULATED LUMINESCENCE (SM-OSL).

5.1 Chapter Abstract:

The OSL (Optically Stimulated Luminescence) signal in quartz consists of multiple traps, including components known as the fast, medium, slow1 and slow2 (Bailey et al., 1997, Singarayer and Bailey 2003). These signals are present in continuous illumination, but are also measured through Linearly Modulated Optically Stimulated Luminescence (LM-OSL), in which the illumination intensity (stimulation power) is increased linearly with time (Bulur et al. 2000). Despite providing more detailed information on trap characteristics and providing more robust data for curve fitting, LM-OSL is rarely performed due to long measurement times. The present author presents an alternative to LM-OSL, in which a sinusoidal function is added to the linear function to provide illumination, proposed to be called Sinusoidally Modulated (SM)-OSL. This technique allows for a more gradual increase in intensity change at the beginning of measurement where resolution between fast and medium components is required, with the equivalent slope of LM-OSL measurement that would last several days. The new SM-OSL function builds to close to maximum power more rapidly than LM-OSL, significantly reducing the time required to measure and bleach the slower components. Given the nature of the stimulation curve, change in illumination increases subsequently for improved measurement of the medium and various slow components without oversampling (having redundant data channels). An illumination model, the first order and general kinematic derivation for fitting of an SM-OSL measurement, and theoretical data transposed from LM-OSL measurements are presented below. Data from an approximated SM-OSL are also presented, demonstrating that

only first order kinematic equations fit the data in a realistic manner.

5.2 Introduction

This chapter presents a new method to measure individual traps within quartz luminescence that takes less time than the traditional method, but where the sacrifices to resolution are in the portion of the measurement that are typically oversampled. Typical measurement illumination in Optical or Infrared Stimulated Luminescence is either ramped slowly (as in Linearly Modulated (LM- OSL)), or simply measured at a fixed power - continuous wave (CW-OSL) (Bulur 1996). Quartz has multiple traps, which have different detrapping probabilities at any given power, leading to a complex signal composed of different over-lying components that are difficult to separate from each other (Smith and Rhodes, 1994; Bailey et al., 1997). These different components are often referred to as the fast (and for some samples, ultrafast), medium, and several slow components (slow1, slow2, slow3 etc.) (Smith and Rhodes, 1994). Note that Jain et al. (2003) and others from Jain's research group refer to the slow components using slightly different names. With Continuous Wave (CW), the direct fitting of the OSL decay data utilizing these individual components is problematic, and represents an ill-posed question in mathematical terms. A typical CW-OSL measurement of quartz represents the sum of a series of exponential decays which are hard to differentiate in this form (Fig. 5.1). Typical dating protocol target the fast component, but at times a less stable ultra-fast component can also add uncertainty to age determination.

Although dating depends upon the fast component, the other signals within quartz luminescence are useful. Bailey (2000) and Singarayer et al., (2000) suggest that the slow component has the potential to be used for dating sedimentary materials. The slow component can saturate at hundreds to thousands of Grays (Singarayer et al., 2000). Due to its higher dose saturation, it could be used to extend the limit of luminescence dating in excess of 1 Ma (Singarayer et al., 2000). As well, it has higher thermal stability than other traps. The fast and medium components are associated with the 325º C TL region (Smith et al., 1990). Typically, heating to 400 º C is necessary to remove these two components, while heating under 500 º C does not significantly affect the magnitude of the slow components (Singarayer et al., 2000). “Hot bleaching” typically can remove the vast majority of the slow components after 120 seconds of blue LED stimulation (at 125ºC) (Brown et al., 2015). Singarayer et al. (2000) suggest a “slow” luminescence dating technique may be limited to Aeolian samples, which tend to be well bleached. Further, recent advancements in the statistical analysis of partially bleached samples (Brown et al., 2015) may also be useful in this technique (through finite age model), but is beyond the scope of this work.

With LM-OSL, the sum of the signal from the several components (fast, medium, slow etc.) is easier to differentiate, as each component has a definitive peak in intensity allowing for more precise characterization (Bulur, 1996). Linearly modulated-OSL (LM-OSL) allows the operator to ramp up stimulation power, and thus the signal is skewed such that the faster traps are fully stimulated first, before the later ones have lost much charge. Physically the fast (or ultrafast) components are the least stable to optical stimulation, and thus have a greater probability to being emptied at a particular power. These are followed by other traps: medium, slow1, slow2, slow3 etc. (Bulur, 1996). This method offers good resolution of the different signals, allowing the different components that make up the total signal to be clearly distinguished.

LM-OSL, despite its greater precision in defining the various OSL components, has a significantly longer measurement time (in comparison to CW-OSL), which is not efficient. For the same total light exposure, the LM-OSL measurement time is twice the CW-OSL, but typically even longer exposure times are used, as it is often the details of the different slow components that are being studied (e.g. Rhodes et al., 2006). The slower components have the greater population of traps, and represent the majority of LM-OSL data. This is not useful to those trying to date younger material, where the focus is on the most bleachable components of the signal (Murray and Wintle, 2000). The slow components are rarely used in routine dating, but need to be bleached as thoroughly as possible to reduce error propagation when using approaches such as the SAR (single aliquot regenerative-dose) protocol. In a typical SAR cycle dating measurement, if the slow components are not adequately bleached each cycle, their presence can affect the calculation of background noise and signals.

Finally, measurements made using Risø equipment are typically performed with a preset number of channels per second. Operators generally wish to maximize the resolution at the start of each measurement by increasing the number of channels per second, but this increases the total number of channels. This can lead to oversampling at a later time when resolution is not an issue, and increases the likelihood of communication errors (i.e. a hardware crash) with the equipment, a particular problem with older readers and for single grain measurements. In LM-OSL, most of the interesting data is at the beginning of the measurement. Figure 5.3 show that the fast component represents the first 30 seconds of a 180 second measurement. When configuring the measurement resolution, it is necessary to maximize the channels for the fast component (i.e. the first 30 seconds of measurement), but that resolution carries on through the entire measurement and increases the likelihood of a hardware crash, and may be considered oversampled. Thus the user is left in a situation where a long measurement time is preferable to have good data density for the modeling of the fast components, but the last 75% of the measurement is dominated by slow signals that must be bleached before the next measurement cycle even if not used directly.

5.3 Theoretical Illumination

Equations in the following section will be written so that the maximum intensity can be differentiated from that found in Bulur (1996). In that work, he used I_0 as the maximum illumination, which is confusing since it is conventional to use this for intensity at time = 0s. The present author will use I_{max} to indicate maximum illumination.

With continuous wave (CW) measurements, the sample is illuminated with continuous intensity at a fixed power. This is usually less than 100 percent power, in order to improve stability and diode longevity (or laser in the case of single grain measurement).

$$A_{cw}\,(t) = I_{max} \tag{5.1}$$

With LM-OSL, illumination intensity (A) increases linearly with time by some slope (s):

$$A_{LM-OSL}(t) = \; slope \cdot t + I_{init} = \; s \cdot t + I_{init} \tag{5.2}$$

Where I_{max} is maximum illumination power (typically 90%; I_o in Bulur 1996)

I_{init} is initial illumination power (typically 0%)

t_{max} is total illumination time

t_0 is initial illumination time (typically 0)

Typically I_{init} and t_0 are both zero, and this is the case in the equations from Bulur (1996). For completeness, we will use them as independent variables throughout the derivations until it is necessary to make $T_0 = 0$. The LM-OSL slope from Bulur (1996) would be:

$$s_{LM-OSL} = \left[\frac{I_{max}}{t_{max}}\right] \tag{5.3}$$

But this will be rewritten as:

$$s_{LM-OSL} = \left[\frac{I_{max} - I_{init}}{t_{max} - t_0}\right] \tag{5.4}$$

The amplitude of stimulation per time for LM-OSL can thus be rewritten as:

$$A_{LM-OSL}(t) = s \cdot t + I_{init} \tag{5.5a}$$

$$\boxed{A_{LM-OSL}(t) = \left[\frac{I_{max} - I_{min}}{t_{max} - t_0}\right] t + I_{init}} \tag{5.5b}$$

Sinusoidally Modulated-OSL (SM-OSL) increases due to a sinusoidal function subtracted from a linear function. The linear function has the effect of rotating the sinusoidal function and ensures that the illumination value is always greater than zero. Additional options would have been to use only a sinusoidal function limited to evaluation between -1/2 π and-1/2 π (or 3/2 π to 5/2 π, etc.) shifted above the y-axis such that the illumination would never be equal to or less than 0. As well, a cosine function could have been utilized in a similar method, though it would be limited to evaluation between -π and 0 (or π and 2 π, etc.). The author has not evaluated these other methods.

$$A_{SM-OSL}(t) = \ slope \cdot t + I_{init} - scalar \cdot \sin(scalar \ \cdot t) \qquad (5.6a)$$

or

$$\boxed{A_{SM-OSL}(t) = \left[\frac{I_{max} - I_{init}}{t_{max} - t_o}\right] \cdot t + I_{init} - A \cdot (I_{max} - I_{init}) \cdot sin\left(\frac{2\pi \cdot t}{t_{max} - t_o}\right)}$$

(5.6b)

Where A is SM-OSL amplitude constant (A= 0.159)

I_{max} is maximum illumination (typically 90%; I_o in Bulur 1996)

I_{init} is initial illumination (typically 0%)

t_{max} is total illumination time

t_0 is initial illumination time (typically 0)

To make later calculations more understandable, we will rewrite equation 5.6b utilizing equation 5.5 b as:

$$A_{SM-OSL}(t) = \ A_{LM-OSL}(t) - a_{SM-OSL}(t) \qquad (5.7)$$

Where:

$$a_{SM-OSL}(t) = \ A \cdot (I_{max} - I_{init}) \cdot sin\left(\frac{2\pi \cdot t}{t_{max} - t_o}\right) \qquad (5.8)$$

The SM-OSL amplitude constant (A) is calculated, such that as $t \rightarrow t_{max}$, $A(t) \rightarrow I_{max}$ or such that the slope approaches zero (as $t \rightarrow t_{max}$, $\frac{dA(t)}{dt} \rightarrow 0$). This is done such that there is no knickpoint in illumination as the SM-OSL reaches the maximum illumination (I_{max}). Given the symmetry of the illumination, this is also true at the beginning of measurement. The instantaneous slope after stimulation starts is equivalent to a multiple day LM-OSL. The SM-OSL amplitude constant was estimated by least-squares fitting of measured data (see below).

5.4 First-order kinetics

For first order kinetics, the goal is to calculate the rate of change of the number of electrons for continuous wave illumination. This model assumes that there is no re-trapping of excited electrons, (which is modeled below in the general order equation). As well, this model assumes that the probability of escaping electrons is constant (or $\alpha = constant$). Modified from Bulur (1996) eq:

$$\frac{dn(t)}{dt} = -\alpha \cdot I_{max} \cdot n(t) \qquad \text{(5.9); Bulur 1996}$$

where $n(t)$ is the number of trapped electrons

$\alpha\, I_{max}$ is the probability of escape of the electrons at intensity I_{max}

If you increase stimulation linearly from I_{init} to I_{max}, you can rewrite equation 5.9 as done in Bulur (1996):

$$\frac{dn(t)}{dt} = -\alpha \cdot A_{LM-OSL}(t) \cdot n(t) = -\alpha \cdot \left(\left[\frac{I_{max} - I_{min}}{t_{max} - t_0}\right] \cdot t + I_{init}\right) \cdot n(t)$$ (5.10); Bulur 1996

As $A_{LM-OSL}(t) = \left[\frac{I_{max} - I_{min}}{t_{max} - t_0}\right] \cdot t + I_{init}$ (5.11)

This can be rewritten as:

$$\frac{dn(t)}{dt} = -\alpha \cdot A_{LM-OSL}(t) \cdot n(t) \quad (5.12a)$$

$$\frac{dn(t)}{n(t)} = -\alpha \cdot A_{LM-OSL}(t) \cdot dt \quad (5.12b)$$

This can be integrated as:

$$log(\, n(t)) = -\alpha \cdot \int A_{LM-OSL}(t) \cdot dt + \; const \quad (5.12c)$$

We can then rewrite the equation as:

$$n(t) = K \cdot \exp[-\alpha \cdot \int A_{LM-OSL}(t) \cdot dt + const] \quad (5.12d)$$

Where K is a constant.

To simplify the math, we force $t_0 = 0$ so that:

If $A\,(t) = I_{max} \to \int A(t) \cdot dt = I_{max} \cdot t + const$ (5.13; as in CW)

If $A\,(t) = A_0 \cdot t \to \int A(t) \cdot dt = \frac{1}{2} \cdot A_0 \cdot t^2 + const$ (5.14; as in LM-OSL)

where $A_0 = const$. Thus equation 5.12d:

$$n(t) = K \cdot \exp[-\alpha \cdot \int A_{LM-OSL}(t) \cdot dt + const]$$

Becomes:

$$n(t) = K \cdot \exp\left[-\alpha \cdot \frac{1}{2} \cdot A_0 \cdot t^2 + const\right] \quad (5.15)$$

Or from the presumption that in LM-OSL: $A\ (t) = A_0 \cdot t$ (as in 5.14) we can rewrite this as:

$$n(t) = K \cdot \exp\left[-\alpha \cdot \frac{1}{2} \cdot A(t) \cdot t + const\right] \quad (5.16)$$

Or as stated in Bulur 1996:

$$n_{LM-OSL}(t) = N_0 \cdot \exp\left(-\frac{\alpha}{2} \cdot A_{LM-OSL}(t) \cdot t\right) \qquad (5.17)$$

Or in long form (remembering that $t_0 = 0$):

$$n_{LM-OSL}(t) = N_0 \cdot \exp\left(-\frac{\alpha}{2} \cdot \left[\left[\frac{I_{max} - I_{init}}{t_{max}}\right] \cdot t + I_{init}\right] \cdot t\right) \qquad (5.18)$$

Curve fitting of this equation would use (5.19):

$$I_{LM-OSL}\ (t) = \sum_{i=1}^{p} N_{oi} \cdot \sigma_i \cdot \frac{t}{2} \cdot \left(\frac{(I_{max} - I_{init})}{(t_{max} - t_0)} \cdot t\ +\ I_{init}\right) e^{\left(-\frac{1}{2} \cdot \sigma_i \cdot t^2 \cdot \left(\frac{(I_{max} - I_{init})}{(t_{max} - t_0)} + I_{init}\right)\right)}$$

Or to simplify the math we can assume that I_{init} = t_0 = 0 (eq. 5.20):

$$I_{LM-OSL}\ (t) = \sum_{i=1}^{p} N_{oi} \cdot \sigma_i \cdot \frac{t}{2} \cdot \left(\frac{(I_{max})}{(t_{max})} \cdot t\right) e^{\left(-\frac{1}{2} \cdot \sigma_i \cdot t^2 \cdot \frac{(I_{max})}{(t_{max})}\right)}$$

Equation 5.20 is used to curve fit LM-OSL measurements. Be aware that this equation is different from that in Bulur (1996). For SM-OSL, there are two possible methods of derivation: simple substitution, or direct derivation as outlined above. The first technique works, while the second does not.

Direct derivation:

For SM-OSL recall from equation 5.7 that to go convert from LM-OSL -> SM-OSL

$$A_{SM-OSL}(t) = A_{LM-OSL}(t) - a_{SM-OSL}(t)$$

To calculate the kinematics for SM-OSL, we subtract modifying function $a_{SM-OSL}(t)$ as:

$$\frac{dn(t)}{dt} = -\alpha \cdot (A_{LM-OSL}(t) - a_{SM-OSL}(t)) \cdot n(t) \tag{5.21a}$$

$$\frac{dn(t)}{n(t)} = -\alpha \cdot (A_{LM-OSL}(t) - a_{SM-OSL}(t)) \cdot dt \tag{5.21b}$$

This can be integrated as:

$$log(n(t)) = -\alpha \cdot \int (A_{LM-OSL}(t) - a_{SM-OSL}(t)) \cdot dt + const \tag{5.21c}$$

We can then rewrite the equation as:

$$n(t) = K \cdot \exp[-\alpha \cdot \int (A_{LM-OSL}(t) - a_{SM-OSL}(t)) \cdot dt + const] \tag{5.21d}$$

Or if we break up the integral:

$$n(t) = K \cdot \exp[-\alpha \cdot (\int [A_{LM-OSL}(t) \cdot dt] - \int [a_{SM-OSL}(t) \cdot dt]) + const]$$

(5.21e)

Where K is a constant.

As in 5.13 and 5.14, if we simplify the math and we force $t_0 = 0$ so that:

If $A(t) = A_0 \cdot sin\left(\frac{2\pi \cdot t}{t_{max}}\right) \rightarrow \int A(t) \cdot dt = A_1 \cdot \frac{t_{max}}{2 \cdot \pi} \cdot \cos\frac{2\pi \cdot t}{t_{max}} + const$ (5.22; as in SM-OSL)

Utilizing 5.14 and 5.20, we can simplify 5.19e to become equation 5.23:

$$n(t) = K \cdot \exp\left[-\alpha \cdot \left(\left(\frac{1}{2} \cdot A(t) \cdot t + const\right) - \left(A_1 \cdot \frac{t_{max}}{2 \cdot \pi} \cdot \cos\frac{2\pi \cdot t}{t_{max}} + const\right)\right) + const\right]$$

If we consolidate the constants $(-\alpha \cdot (const - const) + const = const)$

$$n(t) = K \cdot \exp\left[-\alpha \cdot \left(\left(\frac{1}{2} \cdot A(t) \cdot t\right) - \left(A_1 \cdot \frac{t_{max}}{2 \cdot \pi} \cdot \cos\frac{2\pi \cdot t}{t_{max}}\right)\right) + const\right] \tag{5.24}$$

Or in long form (remembering that $t_0 = 0$) we have equation (5.25)

$$n_{SM-OSL}(t) = N_0 \cdot \exp\left[-\alpha \cdot \left(\left[\left(\left[\frac{I_{max} - I_{init}}{t_{max}}\right] \cdot t + I_{init}\right) \cdot \frac{t}{2} + const\right] - \left[A \cdot (I_{max} - I_{init}) \cdot \frac{t_{max}}{2 \cdot \pi} \cdot \cos\frac{2\pi \cdot t}{t_{max}} + const\right]\right) + const\right]$$

Or if we consolidate the constants we have equation (5.26):

$$n_{SM-OSL}(t) = N_0 \cdot \exp\left[\left[\frac{A \cdot \alpha \cdot (I_{max} - I_{init}) \cdot t_{max}}{2 \cdot \pi} \cdot \cos\frac{2\pi \cdot t}{t_{max}}\right] - \left(\left[\frac{I_{max} - I_{init}}{t_{max}}\right] \cdot \frac{t \cdot \alpha}{2}\right) - \frac{I_{init} \cdot \alpha}{2} + const\right]$$

Modeling of this equation shows that this equation does not produce meaningful results as the fundamental shape of the equation does not match observations.

Simple Substitution

Given that equation 5.26 does not work, I went back to the drawing board. The fundamental mechanics of the LM-OSL equation appear to work. We can use linear equation to curve fit in the SM-OSL system by utilizing a modified version of equation 5.19 by replacing equation 5.5b (amplitude of stimulation per time for LM-OSL) with 5.6 b (amplitude of stimulation per time for SM-OSL). Copy of 5.19:

$$I_{LM-OSL}(t) = \sum_{i=1}^{p} N_{oi} \cdot \sigma_i \cdot \frac{t}{2} \cdot \left(\frac{(I_{max} - I_{init})}{(t_{max} - t_0)} \cdot t + I_{init}\right) e^{\left(-\frac{1}{2} \cdot \sigma_i \cdot t \cdot \left(\frac{(I_{max} - I_{init})}{(t_{max} - t_0)} \cdot t + I_{init}\right)\right)}$$

Substitution of the A_{LM-OSL} (equation 5.5b) with the A_{SM-OSL} (equation 5.6b), the equation above this becomes:

$$I_{LM-OSL}(t) = \sum_{i=1}^{p} N_{oi} \cdot \sigma_i \cdot \frac{t}{2} \cdot (A_{LM-OSL})\, e^{\left(-\frac{t}{2} \cdot \sigma_i \cdot (A_{LM-OSL})\right)}$$

$$I_{SM-OSL}(t) = \sum_{i=1}^{p} N_{oi} \cdot \sigma_i \cdot \frac{t}{2} \cdot (A_{SM-OSL})\, e^{\left(-\frac{t}{2} \cdot \sigma_i \cdot (A_{SM-OSL})\right)}$$

OR:

$$I_{SM-OSL}(t) = \sum_{i=1}^{p} N_{oi} \cdot \sigma_i \cdot \frac{t}{2}$$

$$\cdot \left(\left[\frac{I_{max} - I_{init}}{t_{max} - t_0}\right] \cdot t + I_{init} - A \cdot (I_{max} - I_{init})\right.$$

$$\left. \cdot\, sin\left(\frac{2\pi \cdot t}{t_{max} - t_0}\right)\right) e^{\left(-\frac{t}{2} \cdot \sigma_i \cdot \left(\left[\frac{I_{max} - I_{init}}{t_{max} - t_0}\right] \cdot t + I_{init} - A \cdot (I_{max} - I_{init}) \cdot sin\left(\frac{2\pi \cdot t}{t_{max} - t_0}\right)\right)\right)}$$

Which simplifies to:

$$I_{SM-OSL}(t) = \sum_{i=1}^{p} N_{oi} \cdot \left(\frac{\sigma_i \cdot I_{max} \cdot t^2 - \sigma_i \cdot t \cdot t_{max} \cdot A \cdot (I_{max}) \cdot sin\left(\frac{2\pi \cdot t}{t_{max}}\right)}{2 \cdot t_{max}}\right)$$

$$\cdot \exp\left(\frac{\sigma_i \cdot t \cdot t_{max} \cdot A \cdot (I_{max}) \cdot sin\left(\frac{2\pi \cdot t}{t_{max}}\right) - \sigma_i \cdot I_{max} \cdot t^2}{2 \cdot t_{max}}\right)$$

5.5 Modeling SM-OSL

The author utilizes LM-OSL data to create a theoretical SM-OSL measurement. This is first done with the first order kinetics equation for simplicity. First, the author measures quartz from sample J0048, Malibu beach sand that was previously shown to have strong signals (Lawson et al., 2012). The LM-OSL signal is measured, and then curve fit with first order kinematic equation (Bulur 1996). Modeling is done using least squares fitting within Microsoft excel, using “solver” extension to optimize the values the N_{oi} (trap number) and σ_i (trap cross section) for the sum of signals from varied combinations of trap types, restricting this to a small number (e.g. 3 to 6 in total). The sum of the modeled trap signals is compared to the LM-OSL data through the sum of their root mean square (RMS) difference. The ‘Solver’ extension varies the trap constants such that they produced the lowest RMS value. The values for N_{oi} and σ_i for fast, medium, and slow LM-OSL components are then used to create a theoretical SM-OSL by transforming the data using equation 5.23.

5.9 Conclusions

Sinusoidally Modulated OSL (SM-OSL) offers the potential to measure the various trap components of the quartz OSL signal with a resolution similar to LM-OSL, but at significantly greater speed. Given the greater resolution that the traps are probed with in quartz, the technique offers a more systematic method of analyzing trap contributions to luminescence signals.

5.10 Images

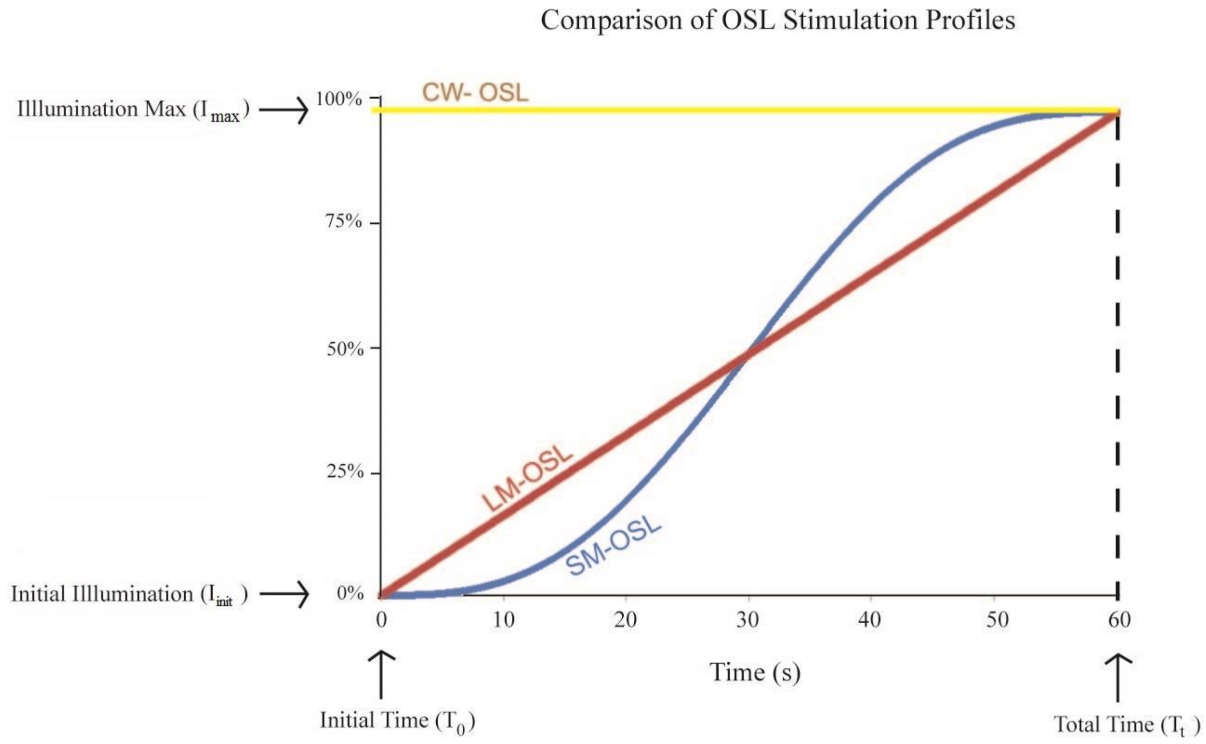

Figure 5.1 Comparison of OSL Stimulation Profiles

The plot describes the differences in illumination per second. This is for Continuous Wave (CW), Linearly Modulated (LM), and Sinusoidally Modulated (SM)- Optically Stimulated Luminescence (OSL). Illumination maximum (I_m) typically ranges around 90-95%.

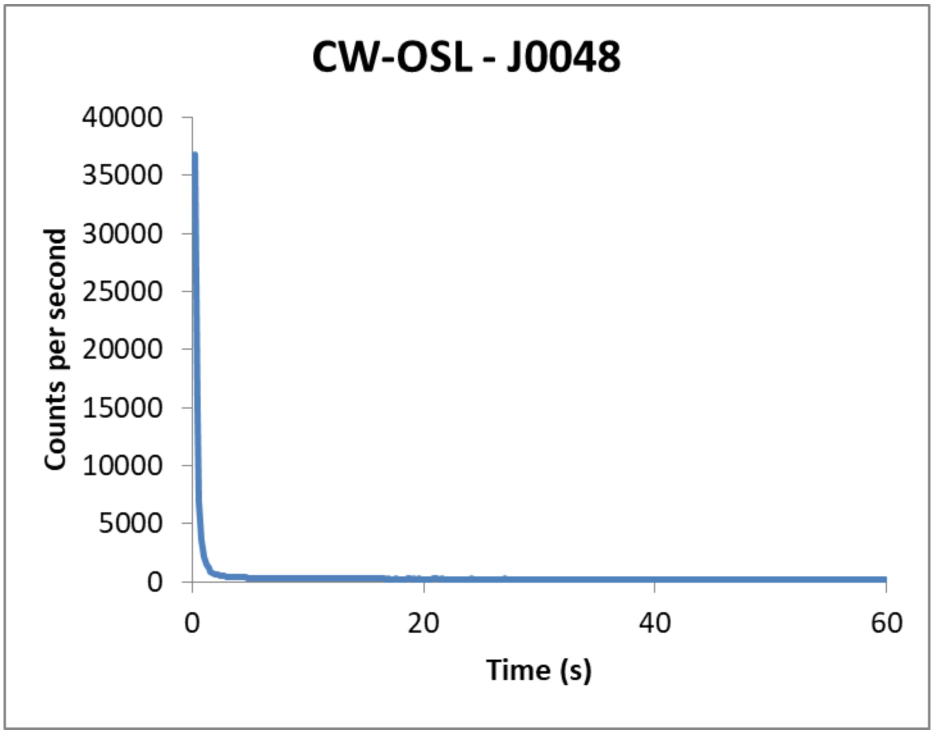

Figure 5.2 Example of the natural signal in Quartz
From Malibu beach dune sand (sample J0048) under Continuous Wave (CW) stimulation.

5.11 Chapter bibliography

Bailey, R.M., Smith, B.W. and Rhodes, E.J., 1997, Partial bleaching and the decay form characteristics of quartz OSL: Radiation Measurements, v. 27 (2), p. 123-136.

Baril, M.R. and Huntley, D.J., 2003, Optical excitation spectra of trapped electrons in irradiated feldspars: Journal of Physics: Condensed Matter, v. 15, p. 8011-8027.

Bulur, E., 1996, An alternative technique for optically stimulated luminescence (OSL) experiment: Radiation Measurements, v. 26, p. 701-709.

Bulur, E., 2000, A simple transformation for converting CW-OSL curves to LM-OSL curves: Radiation Measurements, v. 32 (2), p. 141-145.

Bulur, E., Bøtter-Jensen, L., and Murray, A.S., 2000, Optically stimulated luminescence from quartz measured using the linear modulation technique: Radiation Measurements, v. 32, p. 407–411.

Fattahi, M., and Stokes, S., 2003, Red luminescence from potassium feldspars stimulated by infrared: Radiation Measurements, v. 62, p. 229-264.

Fattahi, M., Singarayer, J.S., and Bailey, R.M., 2006, The linearly modulated IRSL red emission from feldspars: Geochronometria, v. 25, p. 19-28.

Jain, M., and Ankjaergaard, C., 2011, Towards a non-fading signal in feldspar: Insight into charge transport and tunnelling from time-resolved optically stimulated luminescence: Radiation Measurements, v. 46(3), p. 292-309.

Jain, M., Murray, A.S. & Bøtter-Jensen, L., 2003, Characterization of blue-light stimulated luminescence components in different quartz samples: implication for dose measurement: Nuclear Measurements, v. 37, p. 441-449.

Lawson, M.J., Roder, B.J., Stang, D.M., and Rhodes, E.J., 2012, OSL and IRSL characteristics of quartz and feldspar from southern California, USA: Radiation Measurements, v. 47(9), p. 830–836.

Murray, A.S. and Wintle, A.G., 2000, Luminescence dating of quartz using an improved single-aliquot regenerative-dose protocol: Radiation Measurements, v. 32, p. 57-73.

Singarayer, J.S., Bailey, R.M. and Rhodes, E.J., 2000, Potential of the slow component of quartz OSL for age determination of sedimentary samples: Radiation Measurements, v. 32, p. 873-880.

Singarayer, J.S. and Bailey, R.M., 2003, Further investigations of the quartz optically stimulated luminescence components using linear modulation: Radiation Measurements, v. 37, p. 451–458.

Smith, B. W. and Rhodes, E.J., 1994, Charge movements in quartz and their relevance to optical dating: Radiation Measurements, v. 23, p. 329-333.

Smith, B.W., Rhodes, E.J., Stokes, S., and Spooner, N.A., 1990, The optical dating of sediments using quartz: Radiation Protection Dosimetry, v. 34, p. 75-78.

Stokes, S. and Fattahi, M, 2003, Red emission luminescence from quartz and feldspar for dating application: an overview: Radiation Measurements, v. 37, p. 383-395.

Zink, A.J.C., Visocekas, R., and Bos, A.J.J., 1995, Comparison of ‘Blue’ and ‘Infrared’ emission bands in thermoluminescence of alkali feldspars: Radiation Measurements, v. 24(4), p. 513–518.

VI. GEOMORPHOLOGIC SCARP ANALYSIS WITH FAST STATIC GPS AND LUMINESCENCE DATING IN EUREKA VALLEY, DEATH VALLEY NATIONAL PARK

6.1 Chapter Abstract

Although the San Andreas fault is seen as the discrete plate boundary between the North America and Pacific plates, in reality a diffuse plate boundary exists with up to 30 percent of the plate motion occurring inland in the Eastern California Shear Zone (ECSZ). Within this zone, Deep Springs and Eureka Valleys are tectonically controlled basins with very different patterns of deformation despite their proximity. Deep Springs basin is primarily controlled by the normal oblique Deep Springs fault (DSF). Utilizing high accuracy GPS, the rotation of a series of preserved paleoshorelines that have been vertically rotated due to motion on the DSF were investigated. Through IRSL dating, these shorelines are found to be 7.51±0.67 ka and 10.94 ±0.95 ka in age. Eureka Valley has a completely different geometry, where faulting appears as a complex oblique-normal "book case" like structure. Shear causes the rotation of faults that are subsequently reactivated as normal to accommodate extension. This rotation also contracts the shear zone leading to gaps that have been filled by volcanism (in the Saline Range), reverse faulting triggering uplift, and also the formation of the FLVFZ restraining bend north of Eureka Valley.

In Eureka Valley (EV), research was focused on three sites. At Hanging Rock Canyon (HRC) site, complex interactions between a series of oblique normal faults and a second, unmapped right-lateral "master fault" (here propose to be named in memory of Dr. Kurt Frankel) are apparent. At this location, pIRIR dating was combined with scarp diffusion modeling of the unconsolidated fault scarp to determine a new value for the mass diffusivity of $\kappa = 1.79\ m^2ka^{-1}$.

This κ value was then applied to the most active of six scarps in Hanging Rock Canyon (representing 5 faults) and eleven scarp profiles (representing 4 faults) at Dedeckera Canyon site. The vertical slip rate at Hanging Rock Canyon is found in this study to be ~0.7 mm/yr. In Dedeckera Canyon, transects along minor and major alluvial streams suggest that the faulting is still active given that fluvial down cutting has not yet erased scarp offset. Scarp denudation modeling was applied to find the geomorphic ages of scarps where the literature lacks absolute ages, and to derive a slip rate at the Dedeckera Canyon site of ~2 mm/yr vertical displacement. The previously unmapped Frankel fault is obscured in the southern portion of EV, and it is unclear whether it continues under the Eureka Valley Sand Dunes or dies out in a manner similar to the Saline Valley fault. At the final site, surveys at the EV Paleolake suggest that the materials on which it sits are tilting to the Northeast, but it is unclear whether this is due to a normal component on the Frankel fault, differential compaction, or basin subsidence. Ultimately, the faults in Eureka Valley are part of a system with the Saline Valley and Hunter Mountain faults, accommodating shear in a complex oblique normal transfer structure.

6.2 Introduction

This chapter focuses on the interactions between the Fish Lake Valley Fault Zone (FLVFZ) and faults within Deep Springs and Eureka Valleys. The FLVFZ is the northern segment of the Furnace Creek Fault Zone (FCFZ), and may serve as a transfer structure within the Walker Lane Shear Zone (WLSZ). Walker Lane accommodates up to 30% of Pacific-North American plate motion, with the remainder concentrated on the San Andreas fault. In the middle Pleistocene, however, the FLVFZ accommodated all of the strain within this region (11 mm/yr (Reheis and Sawyer, 1997), yet now that strain has decreased dramatically (to between 2.5 and 4.2 mm/yr (Frankel et al., 2007a & b).

The cause of this decrease is poorly understood, and Frankel et al. (2007a & b) suggest that it could be caused by a change in strain regionally or simply a transfer of strain to other unknown structures. This chapter examines whether structures within Eureka or Deep Springs Valleys contribute to this change in strain. A further possibility is that the FLVFZ is becoming locked and strain is transferring to faults north of that fault (Katapody, in prep). It is also possible that current estimates of slip rates do not represent long-term rates. Recurrence intervals could be artificially low due to earthquake clustering, where slip events tend to cluster in time between periods of relative quiescence. This is demonstrated to produce anomalous slip rates on the Garlock fault (Dolan et al., 2016) but its relation to faulting within the Eastern California Shear Zone has not been investigated. Others suggest that discrepancies in the eastern California Shear Zone exist solely on the Garlock and Calico faults, possibly related to post seismic relaxation related to the 1992 M-w 7.3 Landers and 1999 M-w 7.1 Hector Mine earthquakes (Evans et al., 2016). This chapter therefore assesses slip rates in the area, and examines whether they are changing within the Walker Lane region due to strain transfer south, event clustering, or a possible change in strain regimes.

This region is of interest, as it exists at the intersection of three important structural provinces: Basin and Range extensional provinces, the Walker-Lane belt and the Eastern California Shear Zone (ECSZ) (Norton, 2011). The Basin and Range domain is characterized by widespread extension related to the migration of the Mendocino Triple Junction (MTJ) as the North American plate extended to fill in a “hole” caused by the unstable geometry (Ingersoll 1982). The effect of this migration upon Walker Lane, and its southern extension, the ECSZ, is poorly understood. This study investigates the regional context of this migration, and assesses whether the ECSZ is changing as it is recorded by fault motion with Fish Lake Valley Fault

Zone, and oblique normal faulting within Eureka and Deep Springs Valleys.

6.3 Regional structures

Fish Lake Valley Fault Zone

Fish Lake Valley Fault Zone (see Plate 1; Figure 6.1), situated at the northern border of Death Valley National Park, is an important contributor to strike slip motion within the Eastern California Shear Zone. The Pacific-North American relative plate motion is ~50 mm/yr (DeMets and Dixon, 1999) and a majority of this is accommodated by the San Andreas fault. However, up to one-quarter of this motion is distributed within the Walker-Lane and Eastern California shear zones (Wesnousky, 2005). Plate tectonics assumes that plate boundaries are essentially discrete, but clearly in the western United States this not the case and deformation can be more diffuse. The Walker-Lane and the ECSZ are predominately right-lateral strike-slip and transtensional faulting (Stockli et al., 2003) and are interpreted as accommodating 15-25% of the Pacific-North American plate motion (Faulds et al., 2005). The Death Valley Fault System is believed to be the eastern-most extension of that motion (Knott et al., 2005).

Fish Lake Valley Fault Zone (FLVFZ) is a right-oblique zone of faulting, which connects the Death Valley (DV) fault system in the southeast to the northwestern Walker-Lane belt. Reheis and Sawyer (1997) find highly variable slip rates on the FLVFZ, ranging from a long-term rate (since 10 Ma) of 5 mm/yr, and increasing to a maximum of 11 mm/yr in the middle Pleistocene. This rate is remarkable, as this one fault would accommodate nearly the entirety of modern day motion in the 100 km Walker- Lane deformation zone (Oldow et al., 2001). After that maximum, the slip rate on the FLVFZ has since decreased significantly due to unknown causes. Frankel et al. (2007b) utilize offset alluvial fans and ^{10}Be cosmogenic dating along the northern section of the FLVFZ, and found late Pleistocene slip rates of ~2.5 to 3 mm/yr. In another paper that same year, Frankel et al. (2007a) find greater rates within the northern section of the Death Valley Fault Zone, which is interpreted to be contiguous with the FLVFZ. Utilizing ^{10}Be and ^{36}Cl geochronology, offset alluvial fan channels result in a minimum rate of 4.2 +1.9/-1.1 mm/ yr (Frankel et al, 2007a). This variation between the rates on the northern and southern segments of the fault is proposed by previous researchers to be due to strain transience, an increase in the overall strain rate, or due to other unknown structures (Lee et al., 2009). Current research on the Garlock Fault suggests that fault slip events can cluster chronologically, giving apparently variable rates in time (Dolan et al., 2016). If this is the case on the FLVFZ, this could also explain variations in the slip rate in the literature, but no work has yet been done looking at the effect of possible clustering on the network of faults north of the Garlock. This research addresses the following questions: Is the strain in the region changing? Are the apparent changes due to clustering, or has strain transferred south to other structures, such as those within Eureka and Deep Springs Valleys? If the FLVFZ once accommodated nearly the entirety of Walker Lane deformation, why has that motion decreased so precipitously from 11 mm/yr to between 2.5 and 4.2 mm/yr in such a short time geologically? Is the FLVFZ becoming locked, implying greater strain on proximal faults? Finally, why are there inconsistences between slip rates in the northern and southern segment of the FLVFZ? Clearly the FLVFZ merits greater investigation.

Deep Springs

In their study of Deep Springs normal faulting, Lee et al. (2001) find slip rates based upon two volcanic tuffs offset by fault motion. The offset Bishop tuff (753 ± 4 ka) yielded a slip rate of 0.7 mm/yr (horizontal) and 0.9 mm/yr (vertical), while an older unwelded tuff (3.09 ±

0.08 Ma) yielded lower slip rates of 0.2 mm/yr (vertical and horizontal). This disparity between long-term and shorter-term rates indicates an increase in slip rate, possible clustering of fault activity, or the possibility that the missing slip on the FLVFZ is transferring to oblique faults in Deep Springs and possibly Eureka Valley (Wesnousky, 2005). If a more detailed history of slip motion is to be constructed on the FLVFZ, any transfer of slip to proximal structures must be known. In the study, a series of wave-cut platforms in the southeast of Deep Springs are investigated to access block rotation as a check for slip rate (see Plate 2).

Eureka Valley

In the northwest corner of Death Valley National Park lies Eureka Valley, which trends northwest to southeast (see Plate 1). The valley is known primarily for the Eureka Sand Dunes, which have been studied for their geology, biology, and the booming "song of the dunes" (Vriend et al., 2007). Despite this large body of work on the dunes themselves, however, little is known about the Quaternary geology of the valley itself. Dr. Knott (California State University, Fullerton) \ supervises a number of undergraduate research projects in Eureka Valley. Given that they are senior theses, they are part of the grey literature and are difficult to find. Avila, Case, Johnson, Kato, McCarty, Verdadero, Whitmer and Zepeda investigate the tephra chronology, sedimentology, and tectonics within this field area. Further details of their contributions are provided below. Most other studies have focused on the Permian (~298 Ma) Last Chance thrust, which outcrops within the Last Chance range. However, due to Basin and Range extension it is now exposed discontinuously over at least 2500 km^2 (Corbett, 1989; Stevens and Stone, 2005). More recently, on May 17th, 1993 a moment magnitude 6.1 earthquake occurred within Eureka Valley at a depth of 6.8 km (see Plate 1). This measurement was subsequently used by Peltzer and Rosen (1995) in their early study of the remote sensing of earthquakes in remote areas using SAR interferometry.

There are three main sites within Eureka Valley (EV): Hanging Rock Canyon (see Plate 3), EV Paleolake (see Figure 6.2), and Dedeckera Canyon Sites (see Figure 6.3). The primary field area (Hanging Rock Canyon Field Area) is in the eastern margin of Eureka Valley, along Eureka Valley Road where a series of fluvial terraces have been displaced by oblique normal faulting (see Plate 3). Mapping at this site reveals modern right lateral displacement on a fault that had been incorrectly mapped as part of the Last Chance Thrust (Corbett, 1989). Offset stream channels suggest it has been active in the Quaternary. This is the master fault, which I propose be named the "Frankel fault" as detailed below. From this, a series of older segments of this fault are reactivating, typically with some normal component despite being very high angle.

South of Big Pine Road (see Plate 3), there is evidence for extension within Eureka Valley, as the fault outlined above has offset a series of fluvial terraces. High accuracy GPS surveys of the resultant scarps are used to model the apparent offset and then predict the scarp's geomorphic age to determine vertical slip rate changes thru time. Luminescence dating of one of these offset surfaces is used in this study to refine the mass diffusivity constant (κ) for these models.

Given the geometry of observed faults within this study area, it is highly likely that the western-most fault in this area is the northern strand of a fault segment that ruptured on May 17th, 1993 in a 6.1 moment magnitude earthquake. The approximate strike of the faults in this area is ~ 5° north dipping to the west. The earthquake had a hypocenter at a depth of 6.8 km, which combined with the position of the epicenter would place the focus of the earthquake on this fault plane if it had a dip of ~82.5°. This dip value is comparable to what is observed in the field and suggests that the normal faults within the Hanging Rock Field Area are historically active, and thus of interest given their potential hazard.

The second field area is the Dedeckera Canyon Field Area in the southeast corner of Eureka Valley (see Fig 6.3). At this location, a series of normal faults offset fluvial terraces that were used to reconstruct how effective scarp denudation modeling is in this location. Schlom and Knott (2010) are the first to map this area. In this study, the site is used primarily as a test of the validity of scarp denudation modeling, and subsequently applied to scarps along Hanging Rock Canyon site.

Finally, the third field area is located in the main portion of Eureka Valley (see Figure 6.2) where a paleolake located west of the Eureka Valley Sand Dunes was assessed for horizontality. The GPS analysis suggests it is presently dipping to the northeast, most likely due to motion on the Frankel fault (FF). Block rotation rates at this site suggests that there might be normal motion on the FF in addition to the right lateral displacement of modern channels.

6.4 Geomorphic modeling

The chapter uses geomorphic modeling to determine apparent scarp age. If an earthquake has sufficient magnitude to cause ground deformation, with time this deformation will be degraded by erosion due to gravity (simple linear diffusion), wind, rain or biological action. Geomorphic fault modeling simplifies this process mathematically with a term known as the mass diffusivity (κ) constant.

Scarp geomorphological apparent ages are calculated for each scarp based upon Hanks 2000 paper on the dating of scarp-like landforms. A model was created based upon the equation (2) from that paper, which models a hypothetical fault surface u:

$$u\,(x,t) = a\ erf\left(\frac{x}{2\sqrt{\kappa\, t}}\right)$$ (Hanks 2000; eq 6.1)

Where: a represents half the surface offset (m)

κ is the mass diffusivity (m^2ka^{-1})

t is age (ka)

x is the middle point of the scarp (m)

Modeling of this process has been used to approximate the time since a fault has ruptured (Hanks, 2000; Le et al., 2007), but it does not include impacts such as climate or the material being deformed. At the Hanging Rock site, faulting has offset a fluvial terrace that was dated with luminescence dating. The age of this offset unit gives a minimum age for the scarp observed, and is used to calculate the mass diffusivity (κ) constant through comparison of the absolute luminescence age.

6.5 Methods

Methods included traditional mapping techniques (i.e. Brunton field compass, field map, etc.). Scarp studies utilized sub-centimeter GPS measurement with Trimble "Fast Static" units for geomorphic analysis, which are used to construct models of fault scarps. These are subsequently analyzed for offset and apparent geomorphic age.

GSP survey mapping

For geomorphological assessment of fault motion and ages, numerous transects were done with the Trimble kinematic GPS units which can have up to millimeter precision (see Figure 6.4). These systems require two running units for accurate measurements. The base station was placed in a semi-secluded location, stabilized with guidelines attached to rocks to prevent movement and then left to record GPS data for the field day. Rover units were then moved systematically through the field area, perpendicular to the fault scarps and traces, initially found through reconnaissance field mapping. Measurements were made every 0.5 to 20 meters depending on the geomorphic complexity of the area. Measurement spacing was decreased near the axis of the scarp to increase precision of later modeling. The rover station's accuracy was improved through continual measurement for a length of time defined by the operator. Through experimentation, I determined that three minutes was sufficient to get a useful degree of accuracy and yet maintain mobility [see Figure 6.5]. At Hanging Rock Canyon site, the mean vertical accuracy (n=361) was 4.7 cm while the mean horizontal accuracy was 3.1 cm.

Rover measurements were refined against the continuous base station measurements through post processing by 'Trimble Business Center' software. The base station's location was defined very accurately as it recorded, and variations in its apparent location were then used to correct for variations in the corresponding rover station, which increases their accuracy. The difference in accuracy between the Trimble handheld units after post processing, and data from a typical hand held unit is tremendous. The Trimble units, with best-case measurements, could find longitude and latitude positions as accurate as 1 mm [see Figure 6.4; appendix 2], as compared to typical 3-meter resolution with a handheld GPS. For this study, a high degree of elevation accuracy is critical and routinely is accurate to ~4 mm, while typical handheld GPS units are accurate to 10 meters. In Microsoft © Excel, an arbitrary geometric origin was created with a recorded GPS point, and then distances of the other locations are calculated based upon this arbitrary origin. Overall, the accuracy at each of the locations was <1 cm, sufficient for geomorphic modeling, though accuracy overall was lower at Dedeckera Canyon (see Figure 6.4).

For the GPS scarp profiles, the operator moved across surfaces measuring at a specific pace separation (1 pace ~ 1.44 m). For scarps, typically the more distal surfaces were sampled every 2 to 5 paces. Within the more complex scarp surface, separation was between 0.5 paces to 1 pace separation depending upon the complexity of the area. The direction chosen through the scarp surface was such that it was the most representative of the scarp surface, avoiding any minor fluvial cuts into that surface. Some surfaces had large cobbles and GPS position data is limited to the upper-most surface that is not a cobble.

Stream channels were typically sampled every 20 paces. Few bedrock exposures exist in these channels as they are in poorly consolidated alluvial fan deposits. Sampling was done at the highest point where there was evidence of recent fluvial activity, since data collection occurred during a particularly wet period. Paleolake surfaces were sampled in multiple directions to increase the three-dimensional coverage of the surface at a pace separation of 50, or 62 paces.

The distance between two GPS coordinates was calculated following the great circle distance between two points, which is appropriate for close distances. This method does not account for the non-spheroidal shape of the Earth. Given that the surveys in question are fairly small, they are a fair approximation. By finding the distance between two points, I am effectively rotating that distance upon the trend line A-B. Given that this is an arc, and that the main focus of interest is the chord projection (i.e. perpendicular to the trendline), it is also important to correct for the sagitta at each location (see Figure 6.6).

The distance between two points is:

$$d = 2 \cdot R \cdot \left(\sqrt{sin^2\left(\frac{\text{lat}_n - \text{lat}_1}{2}\right) + \cos\,(\text{lat}_n) \cdot \cos\,(\text{lat}_1) \cdot sin^2\left(\frac{\text{long}_n - \text{long}_1}{2}\right)} \right) - \text{S} \quad \text{(eq 6.2)}$$

Where: R is the radius of the Earth (meters); mean Earth radius of 6,371 km for the WGS84 Elipsoid

lat_1 = Latitude reference point n=1

lat_n = Latitude of floating point n

long_1 = Longitude reference point (n=1)

long_n = Longitude of floating point n

S = sagitta correction

Given that this projection onto the trendline is an arc, it is important to correct for the distance between the chord and the arc along the trendline (known as the sagitta). This correction (eq 6.3) is derived in Appendix B, but is:

$$S = 2 \cdot R \cdot \left(\sqrt{sin^2\left(\frac{\text{lat}_r - \text{lat}_n}{2}\right) + \cos\,(\text{lat}_r) \cdot \cos\,(\text{lat}_n) \cdot sin^2\left(\frac{\text{long}_r - \text{long}_n}{2}\right)} \right)$$

$$- \sqrt{4 \cdot R^2 \cdot \left| sin^2\left(\frac{\text{lat}_r - \text{lat}_n}{2}\right) + \cos\,(\text{lat}_r) \cdot \cos\,(\text{lat}_n) \cdot sin^2\left(\frac{\text{long}_r - \text{long}_n}{2}\right) \right| - \frac{(long_n \cdot x - lat_n \cdot y)^2}{|(long_n)^2 + (lat_n)^2|}}$$

Error:

Error for elevation was provided by the Trimble “Fast Static” GPS, after post processing on Trimble© Business software. Error for north-south ($E_{\text{N-S}}$) and east-west ($E_{\text{E-W}}$) is first added to form a total horizontal error ($E_{T)}$ by:

$$E_T = \sqrt{[(E_{N-S})^2 + (E_{E-W})^2} \qquad \text{(eq 6.4)}$$

Where: E_T = total horizontal error

$E_{N\text{-}S}$ = North south Error

$E_{E\text{-}W}$ = East west Error

Error from the reference point is calculated in a similar manner:

$$E \quad = \sqrt{[\left(E_{T\,ref}\right)^2 + \left(E_{T\,float}\right)^2} \qquad \text{(eq 6.5)}$$

Where: E = error

$E_{T\,ref}$ = total horizontal error of reference survey point

$E_{T\,ref}$ = total horizontal error of floating survey point

The error of the measurement tends to be quite low, but gives a false sense of greater precision than the technique allows, so I assume a 15% error for our calculations, which is used by other researchers.

Paleolake block rotation

Measurements at the paleolake were utilized to assess block rotation. This was done by crossing the playa with numerous transects with the high precision GPS, and measuring the upper-most surface. This was plotted in Microsoft © Excel and Mathworks © Matlab to create a three-dimensional view of the surface to assess how the paleolake has rotated away from horizontal. This data was plotted as distance in meters from an arbitrary origin point. By holding the longitude values identical to that in the origin, there is no need for a sagitta correction.

Scarp denudation modeling

Modeling is done in Microsoft© Excel. An arbitrary point was set as the reference point (A). The scarp is defined as having three surfaces: upper surface, scarp surface and lower surface (see Table 1). A linear trend line was created with Excel that approximated each surface, producing an algebraic equation (i.e. $y = ax + b$). These were then used to calculate the parameters defining the scarp geometrically (upper slope, lower slope, scarp slope, scarp height (2H), and scarp offset).

Modeling is also done to create a mathematical expression of the scarp shape. Scarp offsets are modeled based on an idealized scarp geometry (Le et al. 2007; see Figure 6.8). Scarp geomorphologic ages are also calculated for each scarp based on Hanks 2000 equation (eq. 6.1). This equation has two unknowns: mass diffusivity (κ) and time (t). Mass diffusivity (κ) has been shown to be variable in weakly consolidated materials, ranging between 0.1 to 16 m^2ka^{-1} (Hanks, 2000). Within the Basin and Range province, values tend to be within 0.64 to 2 m^2ka^{-1} (Hanks, 2000; Hanks et al., 1984; Hanks and Andrews, 1989; Nash, 1984). Values in California tend to be higher, for instance the San Andreas fault at the Corrizo Plain has a value of 8.5 m^2ka^{-1} (Arrowsmith, 1995). Avouac and Peltzer (1993) found 3.3 ± 1.4 m^2ka^{-1} for fluvial terrace risers in China.

Due to this variability, I utilized luminescence dating to refine the age of a scarp along the western-most expression of the oblique normal fault at the Hanging Rock Canyon site (see

Plate 3). This was used to calculate a κ value for the local geomorphic environment. Since κ is dependent upon material properties and climatic effects, I assumed that determining a local value would produce better results in the calculation of apparent geomorphic ages of scarps later presented.

Luminescence Dating

Within the various field areas, luminescence dating samples are taken to constrain the depositional ages of land surfaces including fluvial terraces and lake shorelines. These are deposited as long flat surfaces, but if they are disturbed by normal faulting they have a ‘s’ like shape. The distance between the two flat surfaces denotes a fault offset, and is measured by Trimble “Fast Static” PPK GPS. Since the fault displaced the terrace, it must be younger than that surface which was deposited continuously, and yet is now broken by fault motion. By dating material offset by fault motion, we can identify 1) the minimum age since that fault was reactived; 2) calculate the geomorphic scarp denudation rate κ (Hanks 2000; eq. 6.1).

Luminescence quantifies the physical process by which ionizing environmental radiation is absorbed within a mineral as trapped electrons, and later released as light upon exposure to a specific wavelength of stimulation (Rhodes, 2011; outlined in Chapter 2). Electrons become trapped between the valence and conduction bands within mineral grains, notably feldspar for fIRSL and quartz for qOSL. Upon exposure to light of the correct wavelength, these electrons are detrapped, move within the crystal structure and upon interaction with luminescence centers emit light whose intensity is relative to their absorbed dose. By comparing the materials’ annual in situ radiation exposure to the total dose the crystal has absorbed, a burial date for a material can be determined. Given that luminescence dating utilizes minerals, such as feldspar and quartz, which are ubiquitous in the sedimentary record, this tool works well in desert environments where carbon 14 dating may suffer a lack of material. Further, OSL and IRSL allow for the dating of the material much older than carbon 14, allowing for sediments to be dated to up to 100,000 years for OSL and 200,000 years for IRSL.

For this research, luminescence dating samples were composed of sand grains collected in the upper 1.5 meters of the ground surface in stratigraphic layers and preserved in steel tubes to prevent their exposure to light until processed in dark room conditions at UCLA. Each sample consisted of two parts: 1) steel tubes approximately 15 cm long and 7.5 cm in diameter, providing approximately 1500 grams of material per sample; 2) small bags of sediment, which were collected for water content measurements and are approximately 4 cm by 4 cm, providing approximately 20 grams of material. In-situ gamma spectrometer measurements were made at each sample location.

6.6 Results

Field mapping of the area was done with traditional geological methods (see Plates 1-3). Scarp surveys are augmented with high accuracy, “fast static” GPS positional data, used to reconstruct apparent geomorphic age. Over 1,300 GPS positions were taken at Dedceckera Canyon (n= 433), Playa (n=206), Deep Springs (n=233), Hanging Rock (n=396) and Willow wash (n= 49).

Determination of κ

The value for κ is a variable in the geomorphic model, and should be tuned given the differences in a) material, b) climate effects or c) any other factors that control sediment transport. A value for κ is determined using geomorphic analysis of the scarp profiles combined with Luminescence dating of units offset by fault motion (see Figure 6.9). Given its location near Death Valley National Park, sampling was limited due to National Park Wilderness requirements. Hanging Rock Canyon Road is a privately owned road but sampling was possible within 500 feet of it. IRSL samples J0687 and J0688 were taken on the scarp as close to the road as possible, despite other locations having better preservation (see Plate 3). Samples were taken in a shallow pit, taken in stratigraphic order and dated using Post IRIR 225. Sample J0687 had a discrete minimum age of 16.3 ±1.7 ka, while the slightly deeper sample J0688 was 16.7±1.6 ka.

The fault modeled was the western-most fault in the Hanging Rock Canyon field area (called “Basin Normal fault”; see figure 6.9). The scarp profile (HB1A) is not ideally shaped. The lower portion of the scarp has been modified through deposition of sediment from a nearby channel and curve fitting only utilized the middle and upper surface in the model. The scarp height is 13.6 ± 2.0 meters, and a vertical offset of 11.0 ± 1.7 meters (assuming 15% error). It is possible that some of the fault offset is obscured due to fluvial deposition or erosion of the lower scarp surface. An additional measurement of a scarp formed by this fault was made approximately one kilometer south of the stream located at Basin Normal fault-south (HB1B). At this location, the scarp height is 13.1 ± 2.0 meters (assuming 15 percent error, and an 11.2 ± 1.7 meter offset). Despite being separated by a kilometer, these scarps have quite similar offsets suggesting that the data is not missing a significant portion of the offset, despite the alteration that has occurred to the northern scarp profile. Analysis of the change in slope shows similarity in the shape of the two scarp profiles (see Figure 6.9).

Utilizing the uppermost IRSL age as a minimum age for scarp HR1A (16.3±1.7 ka), offset was measured as 11.0 ± 1.7 m (scarp height 2H = 13.6 ± 2.0m). Geomorphic modeling of the northern profile of the basin fault results in a mass diffusivity (κ) value of 1.79 ± 0.27 m^2ka^{-1}

(assuming 15% error).

Hanging Rock field area

At the Hanging Rock field area (see Plate 3), a number of fluvial terraces have been elevated due to differential motion on a series high angle normal faults. Most of the faults are oblique, which can be seen geomorphically (see Figure 6.10). Kinematic indicators exist where offset happens to occur in the more consolidated bedrock units (see Plate 3), but indicate normal motion towards the southwest.

The bedrock units consist of Mississippian and Precambrian rocks that have been super-imposed above Mississippian rocks by the Last Chance Thrust (LCT). Precambrian units are Wood Canyon Formation, Carrara Formation, and Bonanza King Formations. The Wood Canyon Formation is primarily fine- to medium-grained, thin-bedded quartzose and quartzofeldspathic sandstones interbedded with siltstones and thin shales (Corbett, 1988). The Carrara Formation is a transgressive sequence. The lower units are thinly bedded sandstones, siltstones, and shales, with Marls replacing shale up-section (Corbett, 1988). The upper units of Carrara are massive limestones (Corbett, 1988). The Bonanza King Formation is buff to grey, thickly bedded dolomite. Mississippian rock units are Rest Spring Shale and the Perdido Formation (Corbett, 1988). The Perdido Formation is commonly siliceous shale, sandstones, and conglomeratic beds (Corbett, 1988). The Rest Spring Shale is black, dark-green phyletic shale that is easily eroded and fractured (Corbet, 1988).

Along the major drainage at the site, there are alluvial fan deposits that have been exposed due to later normal faulting (described below). The western-most deposits are primarily gravels, with imbricated stones that show western motion, which is the same as modern day flow

(Stang, personal communication). Clast counting of Pliocene sediments shows an unroofing sequence of the exposure of the Last Chance Thrust to the east (Knott, personal communication). Within these deposits lie numerous ash beds, including Glass Mountain ash dating to ~3.5 Ma (Knott et al., 2015). South of the road, there are also basalt deposits that continue to the south of the field area. On top of the basalt, a think tephra deposit pinches out to the north and becomes a useful marker bed. The eastern gravels are different in that their color is redder, perhaps due to volcanic components being reworked. On top of these are preserved terrace surfaces with well-developed desert pavements. In most cases the terraces are well sorted, visually flat with a tilt towards the main valley. These can look so flat they appear almost artificial at times. These have been offset due to later normal faulting.

Mississippian and Precambrian rocks are offset by the Last Chance Thrust fault, which outcrops throughout the southwest, stretching (due to Basin and Range Extension) to over 2,500 km^2 (Stevens and Stone, 2005). The LCT is believed to be active in the Early Permian as a decollement, but age control has been difficult (Stevens and Stone, 2005). Locally, Corbett mapped the LCT as part of his thesis map (Corbett, 198l) and later published as a quad (Wrucke and Corbett, 1990). Mitch Casteel (1986) mapped the southern portion of LCT in great detail by (see Figure 6.11).

Portions of the LCT were remapped due to observations in the field. The major change was the observation of a large strike-slip fault that was previously mapped as being a portion of the Last Chance Thrust. However, observations show modern right lateral displacement on this fault (see Figure 6.10) where a series of 4 streams are seen deflecting on contact with this fault. This is partially controlled by sedimentology, as the sandstone of the Wood Canyon Formation is more resistant to weathering than the slate bearing and heavily fractured Carrara Formation. This fault has not been mapped in the south, but is believed to continue at a southern trend under the western edge of the Eureka Valley Sand Dune field. Mapping suggests that this fault does not pass through the Dedeckera Canyon site, given the trend of faulting in that area and the lack of offset between the western deposits of the "J+J" Landslide (Watkins et al., 2015). From this master fault, a series of high angle, right lateral oblique normal faults offset the Pliocene deposits along Big Pine Road.

Exposed normal faults were found to dip 80-87 degrees. Kinematic indicators (where rarely exposed) have a mixed sense of motion. Slicken lines on faults in the middle of the Hanging Rock Canyon area have a pitch of 72- 79 degrees. These faults all split off the master fault, and then allow for "oblique" bookcase faulting that is opening up Eureka Valley. Evidence for strike slip offset on inactive strands of the FF offset portions of the LCT by 200m, 430m, and 550 m (Castell, 1984; see Figure 6.11).

Unnamed strike slip fault

The author proposes that the master fault be named the "Frankel fault", in memory of Dr. Kurt Frankel (see Plate 1) who did much of the early work on the FLVFZ (Frankel, 2007 a & b). Other potential names for this fault have been used elsewhere in the literature. For instance, the "Eureka Valley" fault is already in the literature as occurring in a small valley to the south of EV that is known for its hot springs and a small intermittent nudist colony. Names related to the "Last Chance Mountain" range would likely be confused for the Last Chance Thrust, which has been inactive for millions of years.

In southern Eureka Valley, there are two possibilities for the direction of the Frankel fault: directly under the valley trending nearly south, or simply dying out in the valley due to transfer to the numerous oblique faults to the southwest. Additional reconnaissance is necessary to track the trend of the fault, for instance via gravity surveys in the valley.

Scarp profile derived slip rates

A total of seven scarp profiles were mapped at Hanging Rock Canyon (see Figure 6.12). These have very fresh scarps and may be historically active. As outlined above, I utilized luminescence dating for scarp HR1A. Offset fluvial terraced deposits were dated to 16.3±1.7 ka. The fault has a scarp offset was 11.0 ± 1.7 m, and a vertical slip rate of 0.7 mm/yr.

At Dedeckera field site, the author mapped a similar series of faults to understand how a single fault can vary in three dimensions. This area was previously mapped by Schlom and Knott (2010) who completed four transects. Two transects (DCS2 and DCS3) of the western-most scarp have very similar offsets of 1.6 and 1.8 m respectively, and a geomorphic model age of 0.8 ka using $\kappa = 1.79\ m^2ka^{-1}$. This suggests a vertical slip rate of ~2 mm/yr.

Horizontal rates

There is limited knowledge in the literature of fault geometries in these areas because most of the faults are through gravels that do not preserve kinematic indicators. At the few locations with kinematic indicators, it is limited to within the outcrops of more resistant materials, such as the Mississippian rocks or tephra units. Most of the outcrops of this normal fault sequence are high angle faults (80-87 degrees). One strand of a normal fault that has uplifted Pliocene volcanic deposits which provide two kinematic indicators, with rakes of 73 degrees and 79 degrees respectively, suggesting some degree of left lateral offset that is inconsistent with the right-lateral modern day fluvial offsets on the master fault.

Deep Springs

At Deep Springs, a series of preserved paleoshorelines were dated using pIR-IRSL luminescence dating. They were mapped with high accuracy GPS, and found to be at a slight angle relative to horizontal. The shorelines are in places heavily eroded and preserved between two alluvial fan deposits. Shoreline 1538 (at 1538m elevation) provides the best results (see Figure 6.12). PIRIR dating of this shoreline gives an age of 10.94 +-0.95 ka. Plotting a linear fit, it shows that the shoreline is dipping to the east by a slope of 0.0007 (y = 0.0007x). This shoreline is ~4 km away from the Deep Springs fault, and if we assume that the block under the shoreline is moving only by tectonic motion of the DSF, this slope would correspond to a vertical motion of ~3 meters on the fault. This suggests a rough vertical slip rate of ~0.3 mm/yr since 10.94 +-0.95 ka. This value is identical to the long-term vertical slip rate at the Deep Springs fault (Lee et al., 200?). This technique should probably be considered an over-estimate since it doesn’t account for basin subsidence, or the interactions of other faults.

Eureka Valley paleolake

Eureka Valley paleolake was surveyed with Trimble GPS to determine how much the playa has rotated since its original horizontal deposition. The paleolake is surrounded by alluvial fans to the south, west and north while to the east is the Eureka Valley Dunes. Typically the area is a dry playa, but in the 2016 field season heavy rains in the area made a temporary lake on the eastern portion of the valley, confirming the idea that the eastern side is at a lower elevation. The extent of this temporary lake was not mapped due to concerns about damaging the playa surface.

Observations on the playa show that there were salt blows to the east that probably reflect fluid flow on the near surface. In the western playa, there are surface features that show fluid motion on the surface, but eventually these channels coalesce into larger drainage networks that end in fissures that are up to 2 meters deep. These fissures are not tectonic, as they form a network of cracks at ~90 degree angles to each other in a branching structure. Typically these suddenly stop and have no apparent offset. At some locations, fluid flow is visible on the surface draining into these fissures. The deep fissures on the western paleolake may have allowed fluid to travel in the subsurface, which then percolate in the lower eastern surface as small meter-scale salt blows.

A number of fast static transects were done across the paleolake. The first transects (PL01- 55) were spaced such that the maximum number of observations could be done in a single field day, while accounting for measurement time (3 minutes), transect time across the four kilometer lake, and the time to return to camp. Back of the envelope calculations suggest 55 measurements spaced out 54 paces (1 pace ~ 1.44 m). In practice, additional paces were taken to avoid the occasional fissure, bush, or surface aeolian deposits. Later analysis shows that the separation between points for this first transect were roughly 75-85 meters. The direction of this first transect was chosen such that the entire paleolake could be sampled across the main axis, at a trend along the main axis of the lake. In the field, a Brunton compass was used to find a position on the horizon that matched this trend, and for the day the author walked towards that marker resulting in fairly linear trends.

Observations on the first day of measurements show numerous fissures in the paleolake surface, probably related to fluid flow in the upper surface layers (described above). A number of these fissures are oriented perpendicular to the first day’s transect, and unfortunately parallel to the direction of additionally planned transects. Due to a concern that these fissures might be tectonic in nature, later profiles were done at higher angles to avoid any interference relative to the fissures. These oblique measurements were done at a preferred spacing of 58 paces, which occasionally was stretched to 116 pace separation due to time or weather constraints. Finally, measurements were also taken at the eastern portion of the paleolake in three smaller transects that were approximately parallel to the main axis transect (see Figure 6.13). Field observations suggested that this area was more active geomorphically given that it flooded in the exceptionally wet season of 2015.

Observations show that the EV Paleolake is dipping to the northeast, but additional measurements are necessary to constrain the exact dip direction. From the main axis transect, figure 6.13 shows that there is a consistent dip to the east such that the eastern paleolake is one meter below the elevation of the western portion. The plane of the playa has a broad “hockey stick” shape (see Figure 6.13b). This was fitted to find the trend of the tilt of the paleolake. A transect suggests the playa is dipping to the east at ($y= 0.0003x$), Additional work will be necessary at this site to determine what controls tilting at this location: basin subsidence or tectonics.

6.7 Discussion

The “Frankel fault” is taking slip up some amount of slip from the FLVFZ, which is still active. The slip rate of the fault is unclear, since we do not have age control for strike-slip motion. The FF could also explain why the EV paleolake has a very crisp border while next to a very active Dune field. The oblique motion on this fault would drop down the paleolake side, which would act like a sink for material infiltrating from the dune. The North-South “tear drop” shape of the dune field is possibly related to this faulting as well, with material being offset by motion on the fault though wind is just as likely a candidate.

Shear zones contract perpendicular to the shear direction due to geometric limitations of rotation of blocks within the shear zone. In a perfect world with sub parallel blocks, this could be accommodated by translational motion. However, in the case of Eureka Valley faulting is not oriented in perfect blocks and this contraction is forcing the Hanging Rock Field area to move north relative to the Last Chance Mountains. This migration is the underlying cause of the decrease of slip on the FLVFZ. The compression of this block is forcing a northward movement of the Last Chance Range, creating a bend within the FLVFZ. Observations at the Willow Wash site suggest that the fault is still active, but continued motion on the Frankel fault could eventually lock the fault. As the FLVFZ becomes more locked, additional slip may transfer to Frankel fault. Thus feedback is occurring, potentially draining greater amounts of slip from the FLVFZ through time.

The Frankel fault is part of a larger step over system incorporating the Saline Valley and Hunter Mountain faults that are accommodating shear through oblique normal faulting. This is a small closed system that accommodates extension while any translational motion is transferred onto the rest of the ECSZ system through the HMF and eventually Panamint Valley fault. Volcanism in the south of the valley could be related to the room problem of bookcase faulting.

Reconstructing the slip on the Frankel fault, the LCT lines up more convincingly, being two thrust sheets offset by right lateral motion on the Frankel fault. This is a simpler explanation then the heavily folded and repeated LCT proposed by Corbett (1989). The thrust appears to be a simpler duplex structure that has been repeated by motion on the Frankel fault and its inactive strands. This would need to be tested in greater detail.

6.8 Conclusions

Slip has been shown to be decreasing on the Fish Lake Valley Fault Zone (FLVFZ).

Investigations in Deep Springs suggest that slip is consistent with long term rates. Investigations within Eureka Valley, however, suggest that some portion of the missing slip is transferring to structures within this tectonically controlled valley. P-IRIR dating was combined with scarp denudation analysis suggesting a vertical slip rate of ~0.7 mm/yr. Additional research is necessary to investigate the right lateral component of motion on the "Frankel fault" and access its potential for hazard.

Finally, more research is necessary to look at the Eastern California Shear Zone as a complex network of shearing (see Figure 6.17). Ultimately, it may be that within the ECSZ, while individual faults have low slip values, collectively over the region it adds up to significant displacement. The ECSZ should be investigated with greater rigor, as a significant portion of the North America Pacific slip is within the ECSZ. This study is the first step in that direction.

6.9 Plate descriptions

Plate 1: Index map of Deep Springs and Eureka Valleys.

Overview of the field areas in the study (a.) Deep Springs (b.) Willow Wash (c.) Hanging Rock Canyon (d.) Eureka Paleolake (e.) Dedeckera Canyon field areas. The faults in magenta are inactive Paleozoic thrust faults, including the Last Chance Thrust as remapped in this work, which was been offset in the western margin of the Last Chance mountains by the "Frankel fault". In southern Eureka Valley, there are two possibilities for the direction of the Frankel fault: directly under the valley trending nearly south, or dying out in the valley due to transfer to the numerous oblique faults to the southwest.

Plate 2: Geological Map of Deep Springs paleoshoreline Site, Deep Springs, Inyo County, California.

Plate 3: Geological map of Hanging Rock Canyon Field Area, eastern Eureka Valley, Death Valley National park, California.

6.10 Images

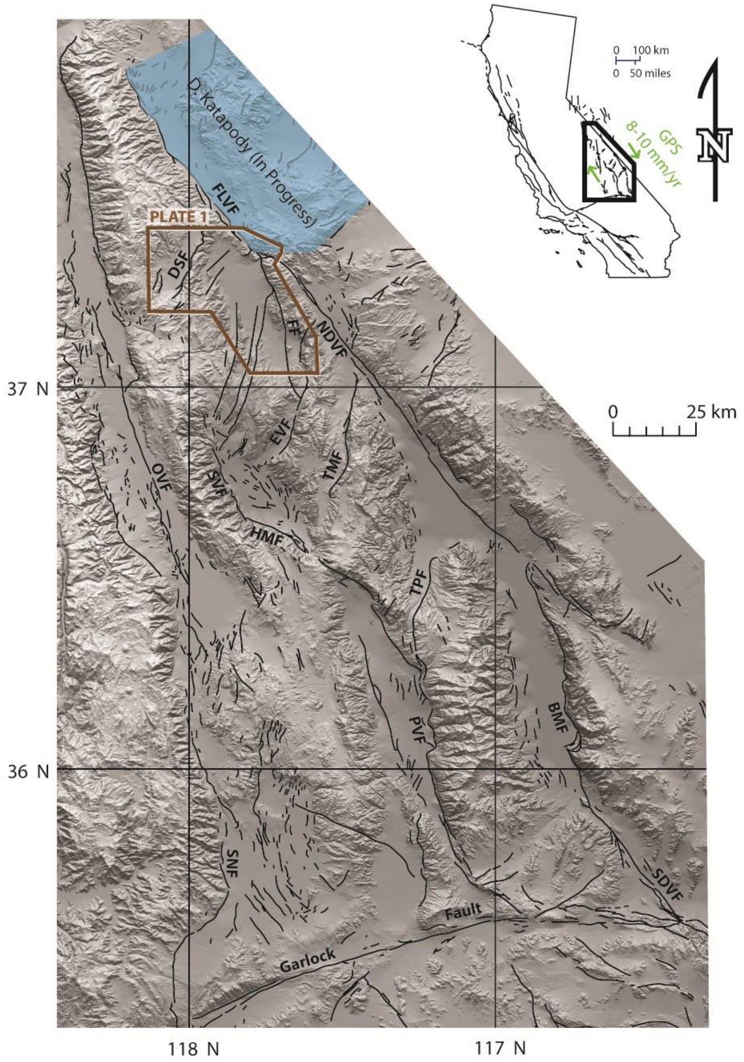

Figure 6.1 Major tectonic structures south of the study area.

The primary field area is located in brown. Deformation consists of complex network of structures accommodating right- lateral shear. The blue area is considered out of date as several major east-west transfer structures have been recently discovered by University of Texas Dallas (Katapody, in prep). The image is modified from Faulks et al., 2007, the base image is rendered from the GeomapApp and major faults are from the SCEC data base. Faults on the image: BMF- Black Mountain fault, DSF - Deep Springs fault, EVF - Eureka Valley fault, FF- Frankel fault, FLVF - Fish Lake Valley fault, HMF- Hunter Mountain fault, NDVF - North Death Valley fault, OVF - Owen’s Valley fault, PVF- Panamint Valley Fault, SDVF- South Death Valley fault SNF- Sierra Nevada fault, SVF- Saline Valley fault, TMF- Tin Mountain fault, TPF - Towne Pass fault.

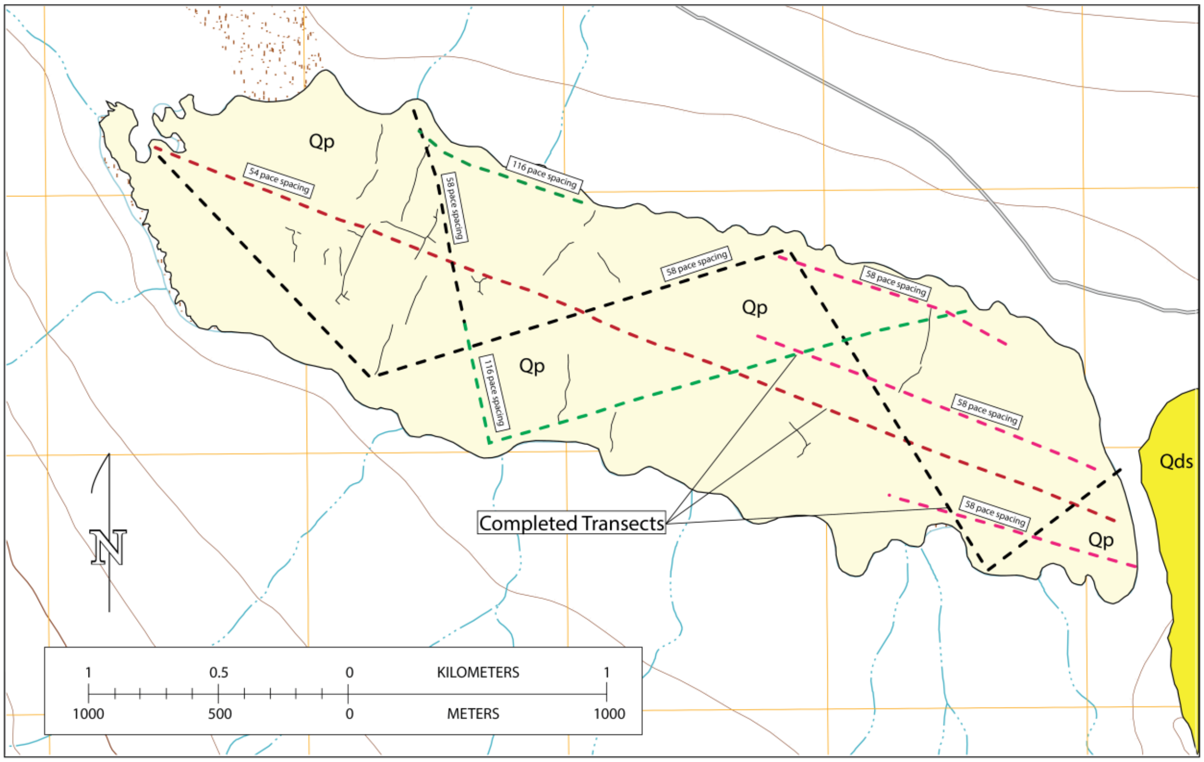

Figure 6.2 EV Paleolake field area.

Dashed lines denote kinematic GPS transects that suggest the Eureka Valley Paleolake is dipping to the northeast. Qp are Quaternary Paleolake deposits. Qds are Quaternary Dune deposits.

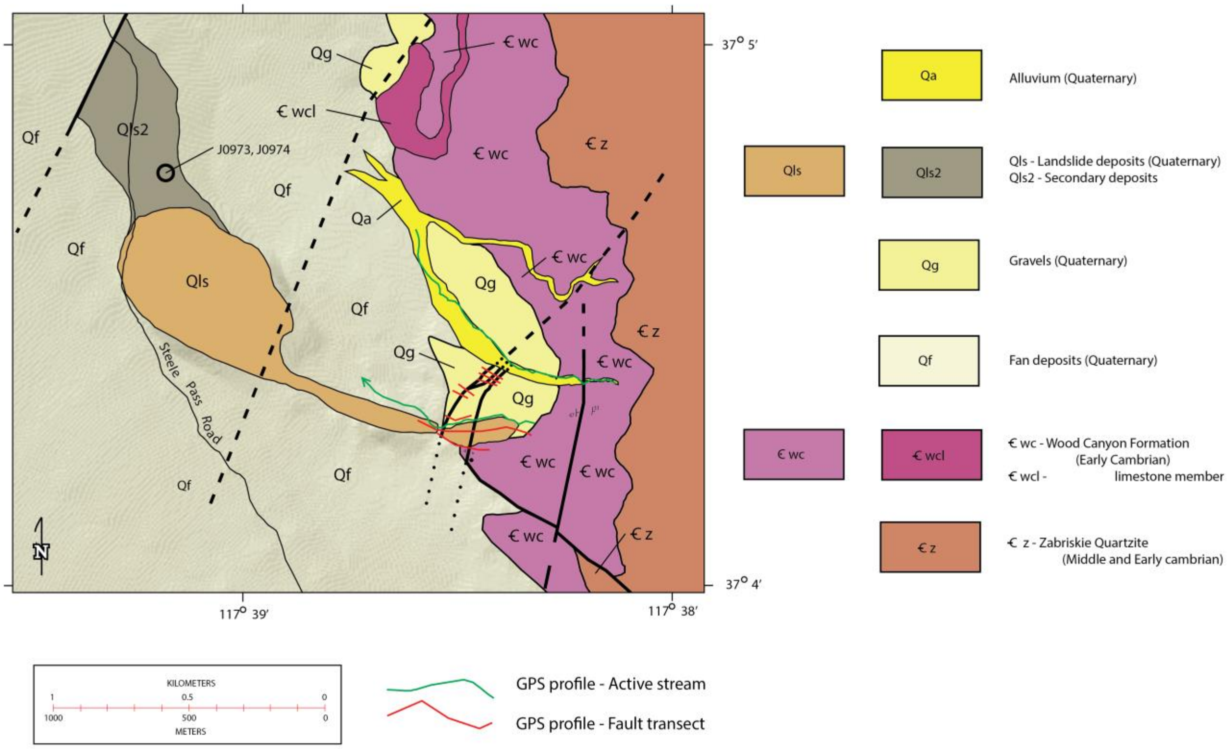

Figure 6.3 Geological map of the Dedeckera field area.

Modified from Schlom and Knott, 2010. GPS Profiles along active streams are in green; profiles across scarps are shown in red. QLs2 are secondary structures post landslide deposition, suggested to be dewatering structure (Watkins et al., in prep).

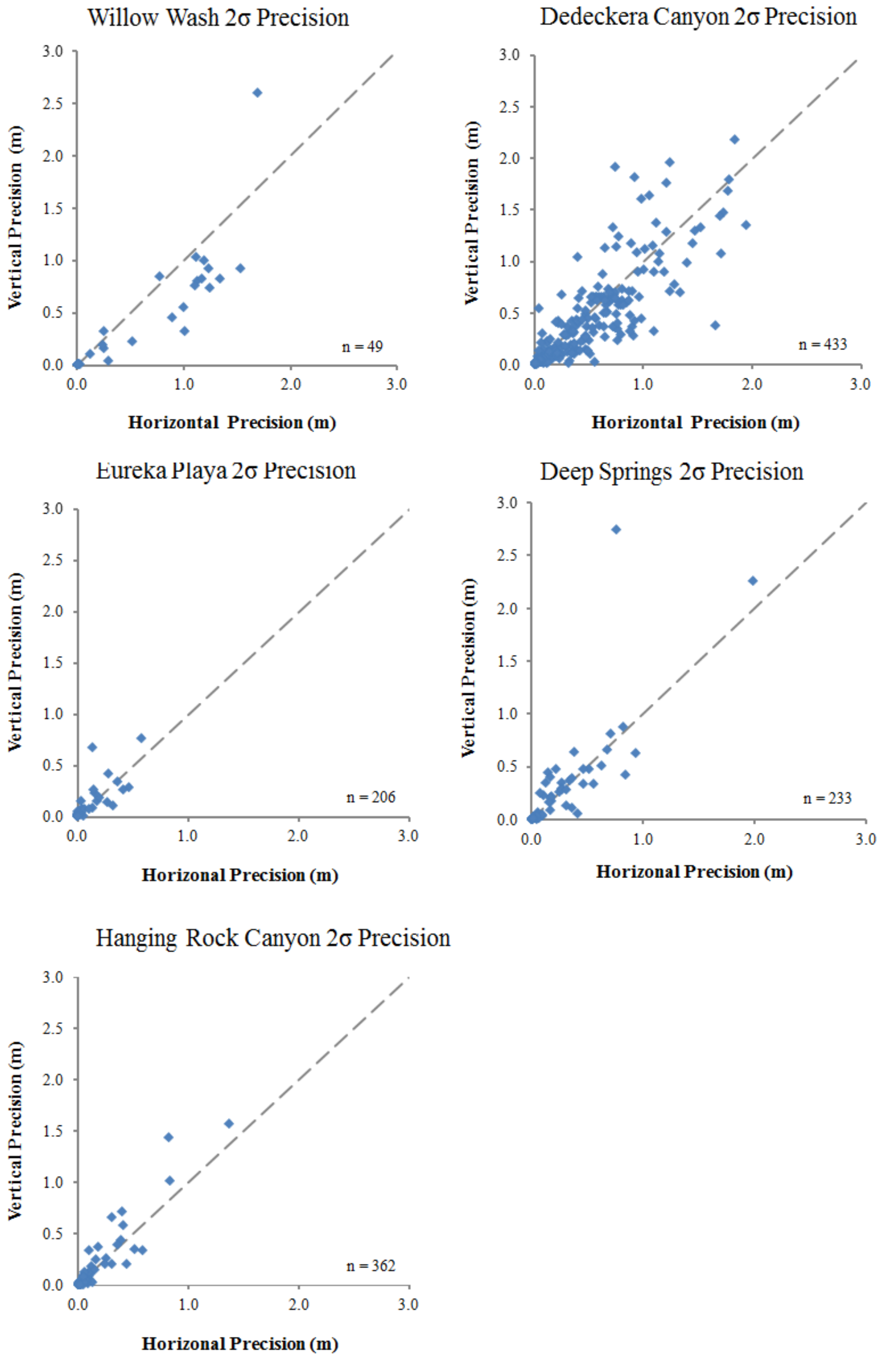

Figure 6.4 Error in Trimble data by site location.

Dedeckera Canyon had greater total error than the other sites, which is interpreted to be due to proximity to cliff face either decreasing the field of view for satellite measurement, or due to reflections off of the cliff surface.

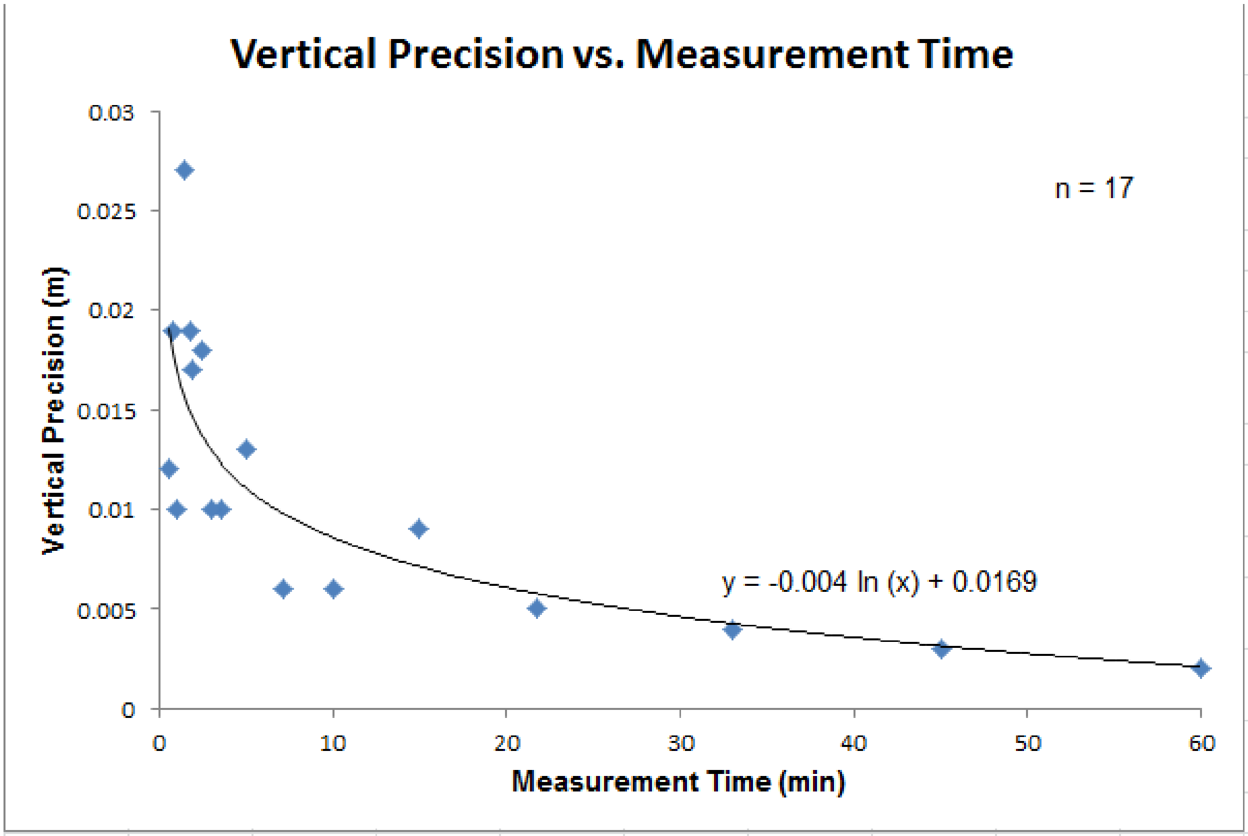

Figure 6.5 Results from a measurement time test at Eureka Valley Paleolake Site. Measurements in the study were completed using 3 minute measurements.

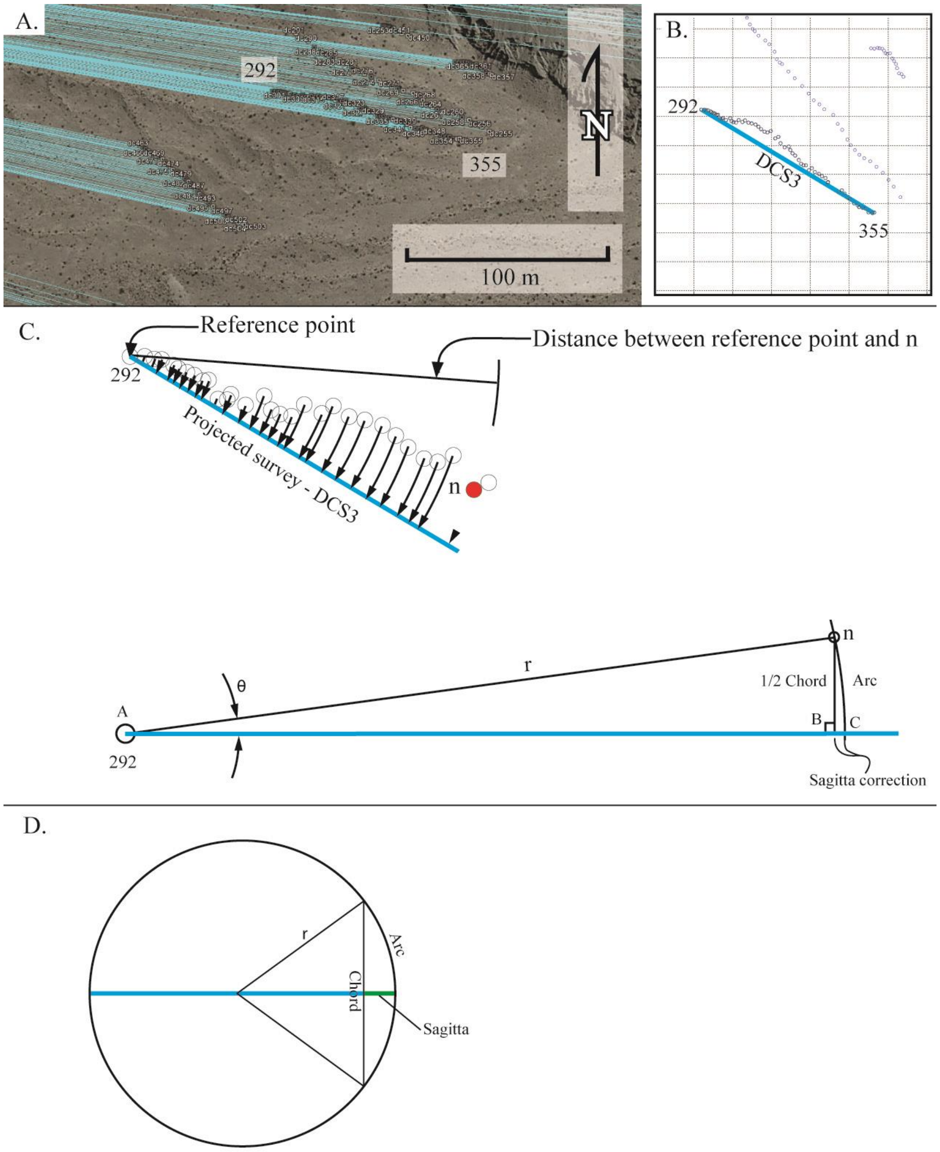

Figure 6.6 Details of how scarp profiles were calculated.

A) Google earth image showing the various surveys. Blue lines denote the location of the base location used in Trimble fast static post processing relative to survey locations. B) Details of the survey DCS3as plotted in Matlab C) Details of the projection, which is calculated using the Great Circle distance between the two GPS positions which in effect rotates the position onto the trendline. A sagitta correction is necessary so that the projection is perpendicular to the GPS position. D) Naming convention.

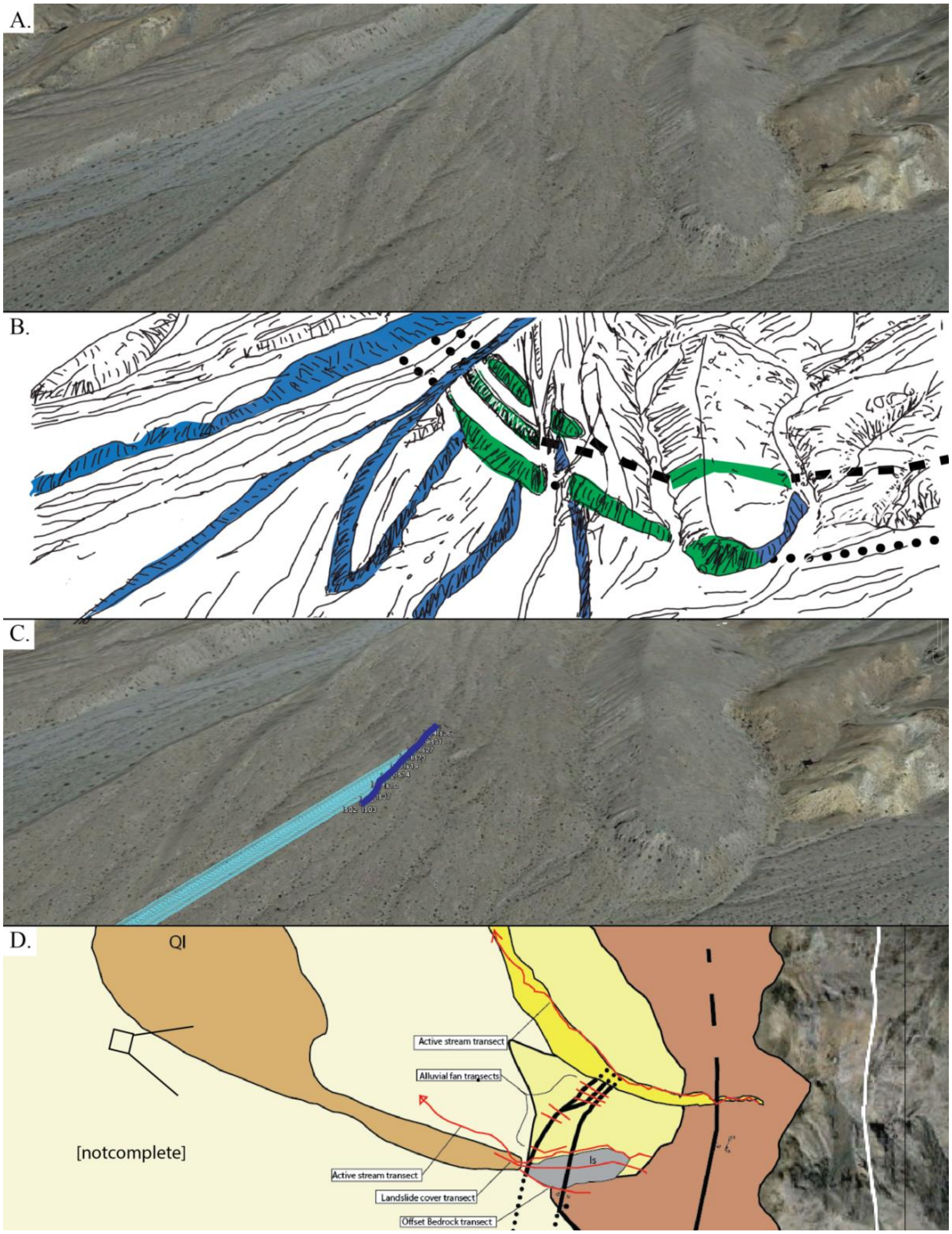

Figure 6.7 Graphic detailing surveys

A) Google Earth image of the Dedeckera Study area. B) Sketch of the area. Blue lines represent erosional scarps, fault scarps are in green. C) Google Earth image showing details of Survey DCS5. The light blue lines are referencing the base station location. D) Geological map of the field area, camera denoting approximate location of the perspective in images A and B (Modified from Schlom and Knott, 2010)

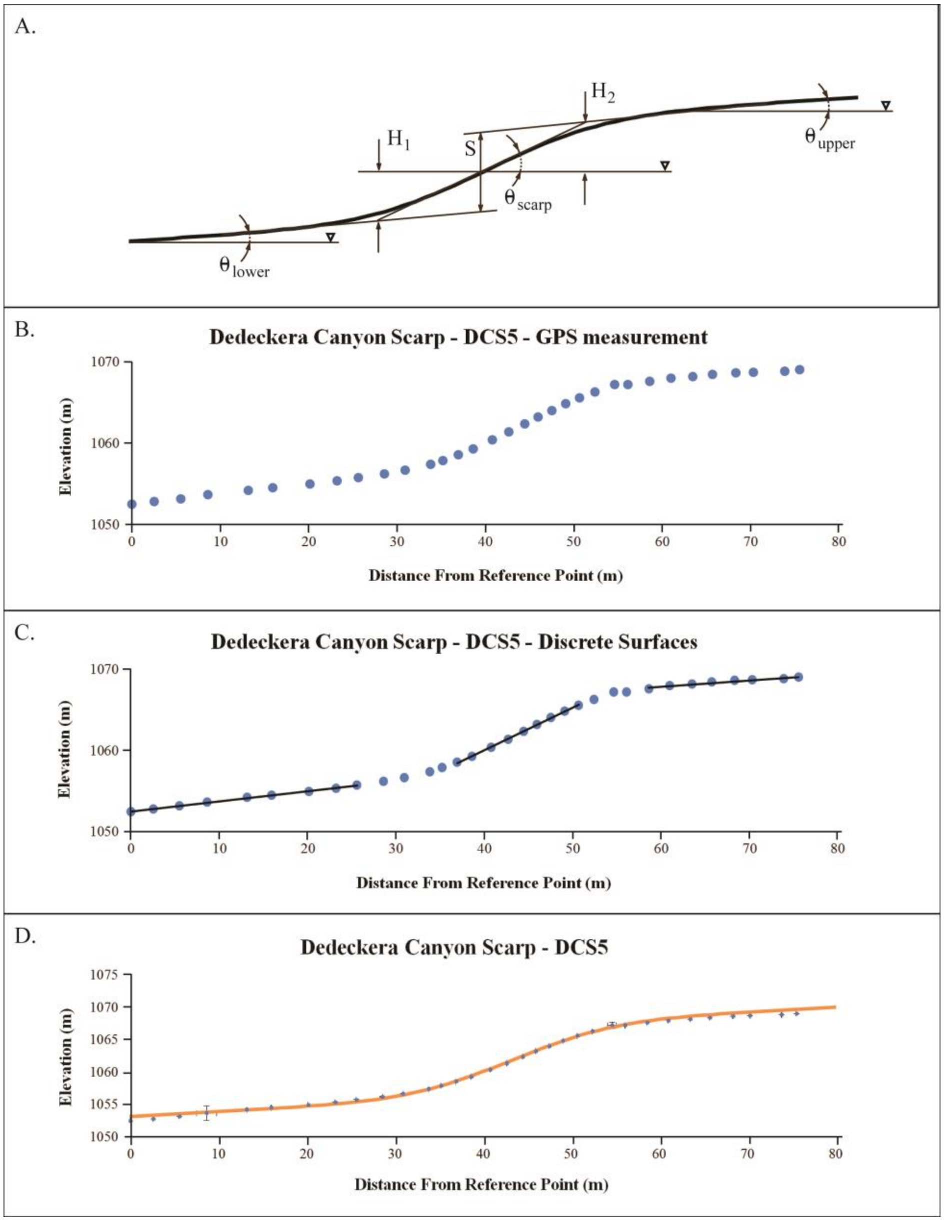

Figure 6.8 Details of how scarp model parameters were determined.

A) Ideal scarp (modified from Le et al., 2007). B) Details of the DCS5 scarp profile data from an arbitrary point as measured by the Trimble GPS. C) Discrete surfaces utilized to determine fault offset. D) Geomorphic model in orange.

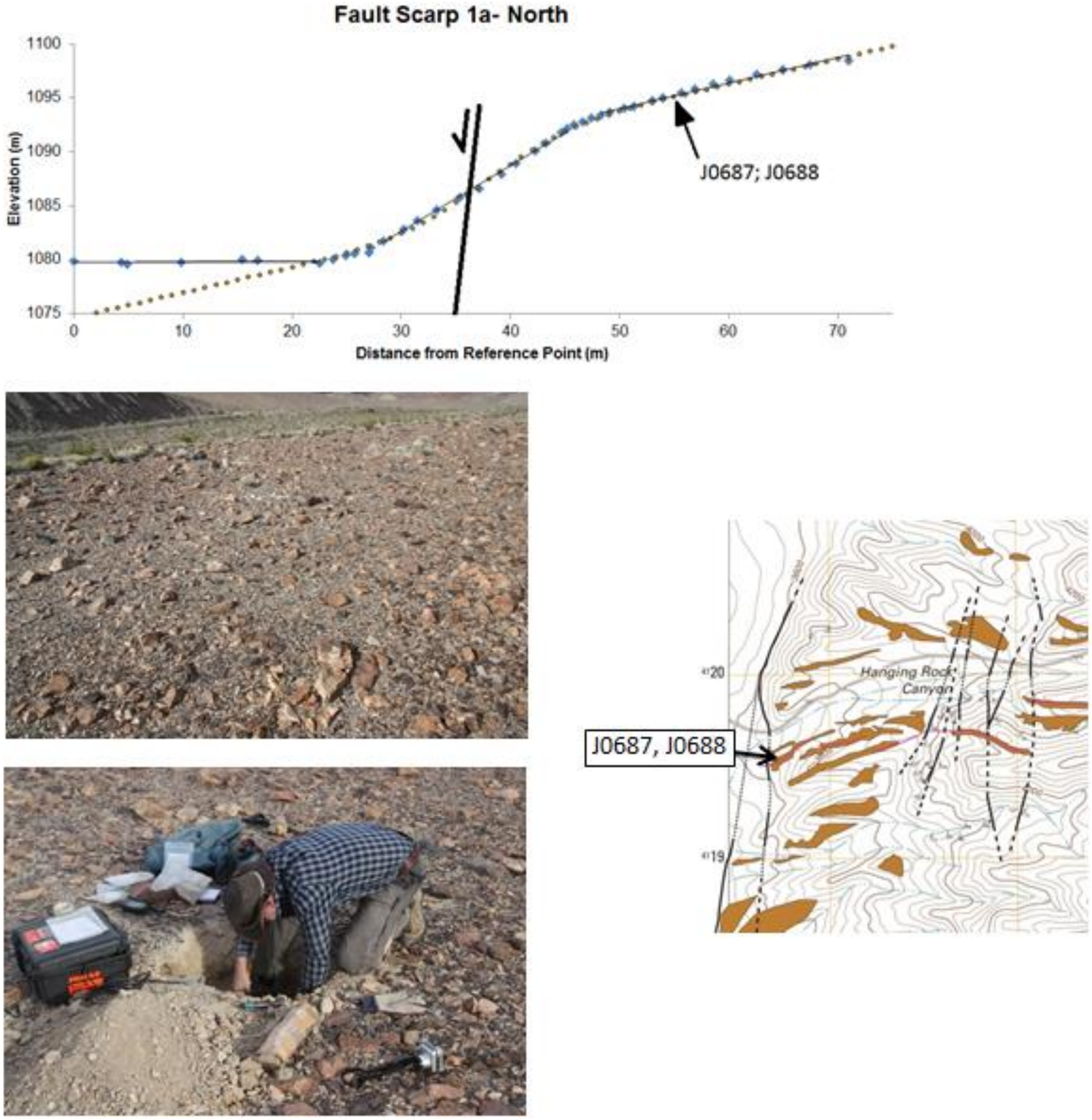

Figure 6.9 Post IRIR samples taken within 500 feet of the Loreta Mine road.

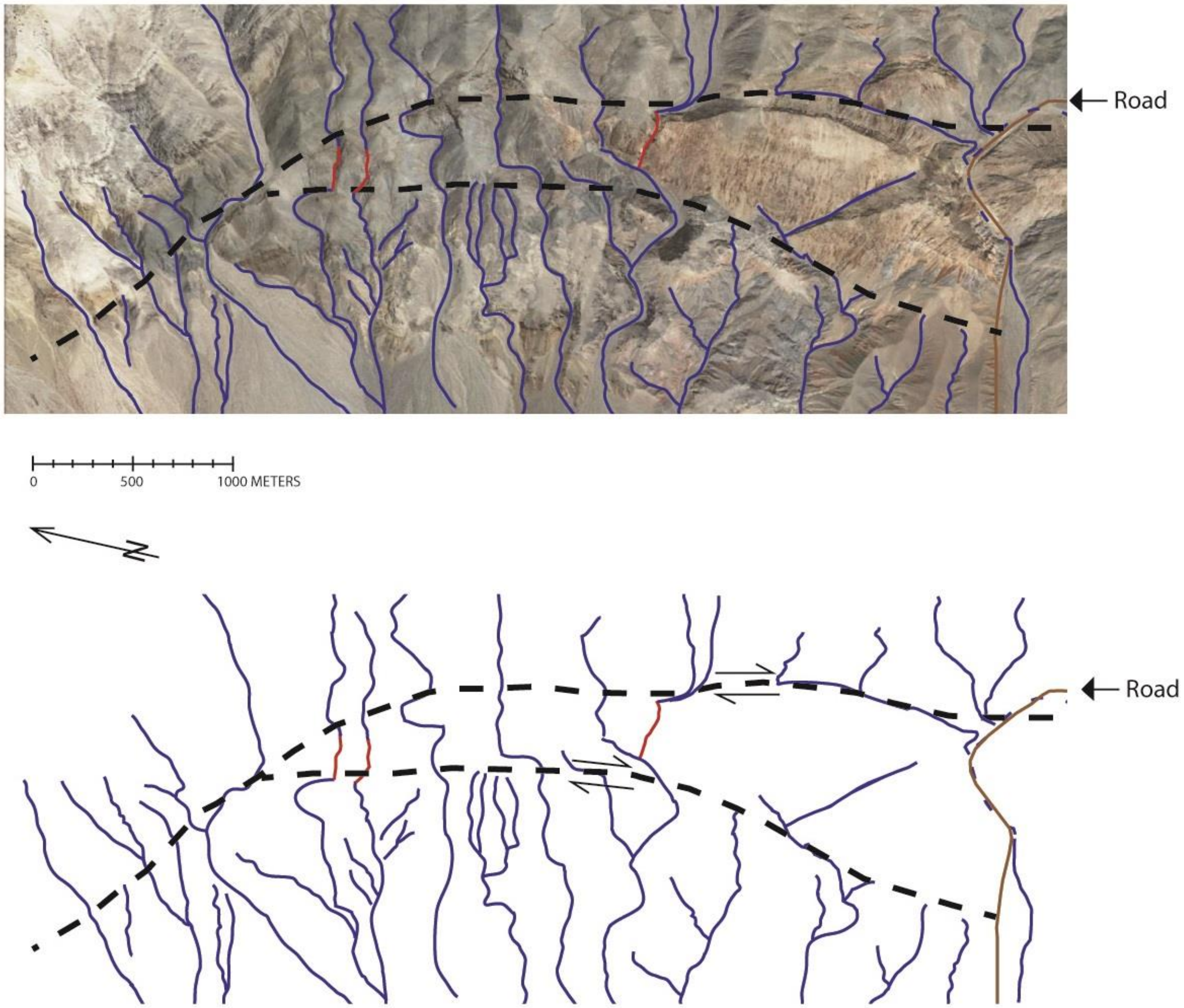

Figure 6.10 Details of streams in the Hanging Rock Canyon Field area, north of the road. Stream channels are in blue. Waterfall-like features are shown in red.

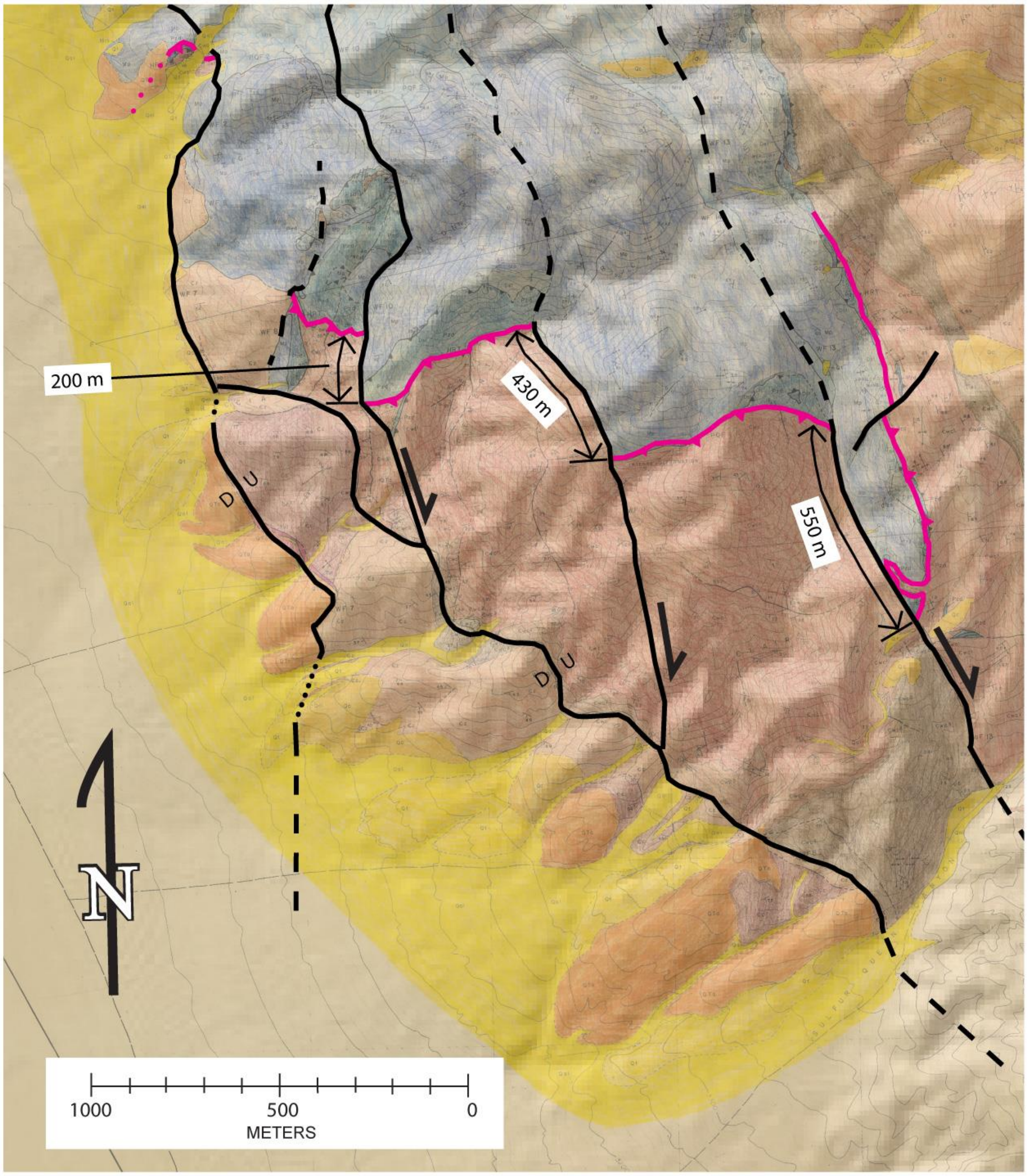

Figure 6.11 Details from the southern portion of Casteel thesis map (1984).
Older traces of the Frankel fault show 550, 430, and 200 m offset. The preferred orientation on the strike slip fault is along the eastern most strand, but shear causes vertical and horizontal rotation of this fault making it deactivate, and eventually reactivates to accommodate local extension thru more normal offset.

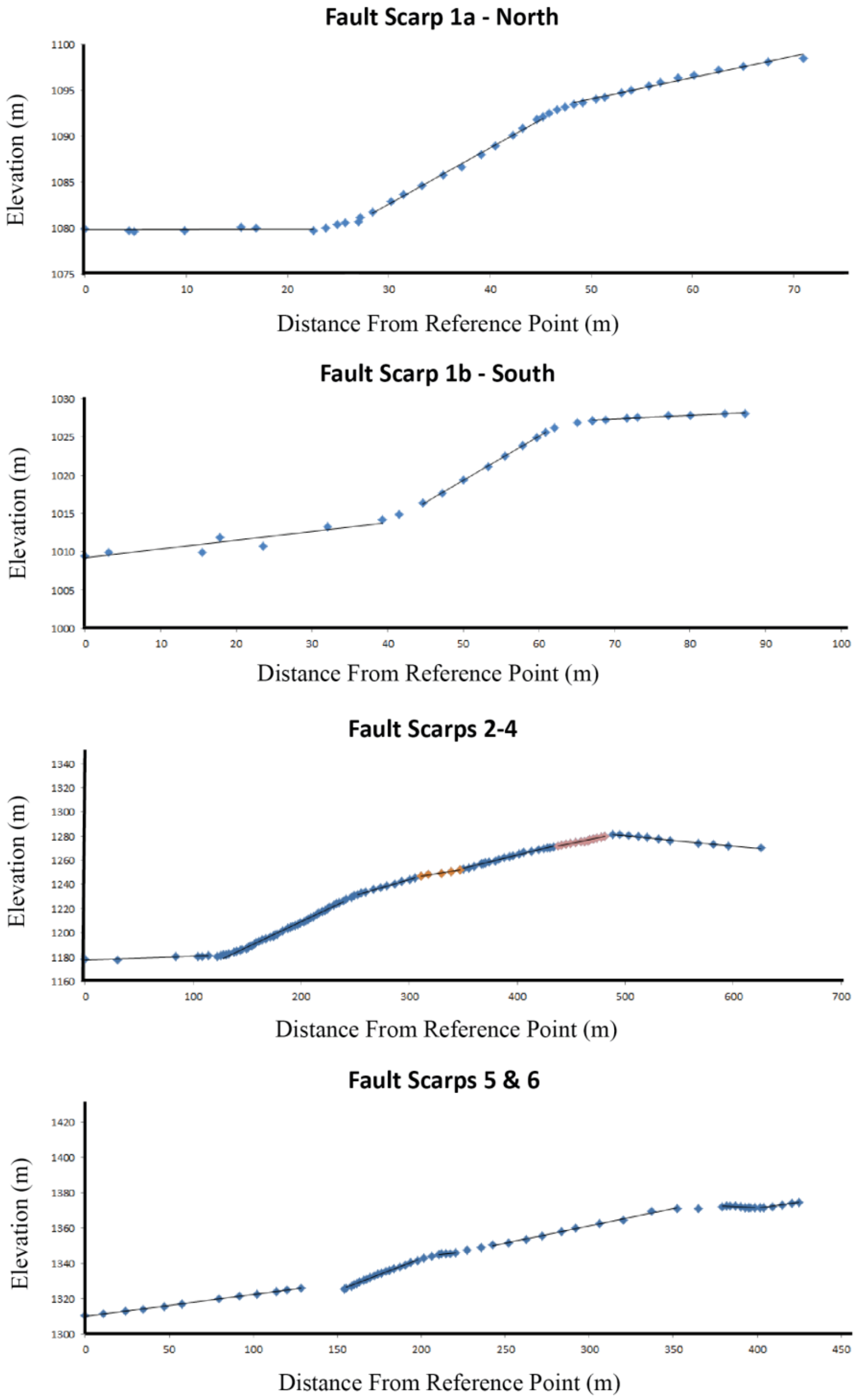

Figure 6.12 Scarp Profiles within Hanging Rock Canyon Field Area.

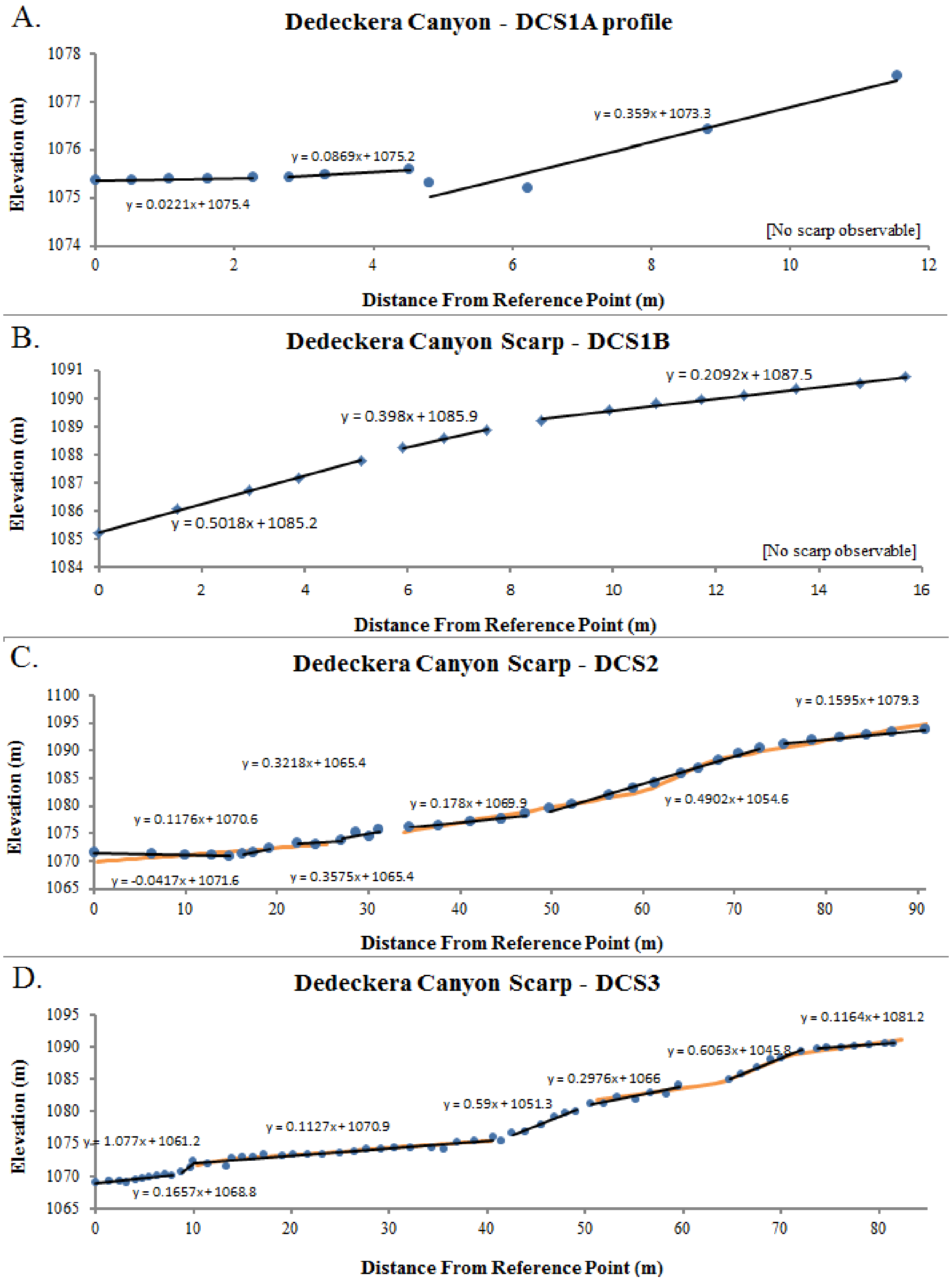
A.
Dedeckera Canyon - DCS1A profile
Elevation (m)
1078
1077
1076
1075
1074
y = 0.0221x + 1075.4
y = 0.0869x + 1075.2
y = 0.359x + 1073.3
[No scarp observable]
0
2
4
6
8
10
12
Distance From Reference Point (m)
B.
Dedeckera Canyon Scarp - DCS1B
Elevation (m)
1091
1090
1089
1088
1087
1086
1085
1084
y = 0.5018x + 1085.2
y = 0.398x + 1085.9
y = 0.2092x + 1087.5
[No scarp observable]
0
2
4
6
8
10
12
14
16
Distance From Reference Point (m)
C.
Dedeckera Canyon Scarp - DCS2
Elevation (m)
1100
1095
1090
1085
1080
1075
1070
1065
y = 0.1176x + 1070.6
y = -0.0417x + 1071.6
y = 0.3218x + 1065.4
y = 0.3575x + 1065.4
y = 0.178x + 1069.9
y = 0.4902x + 1054.6
y = 0.1595x + 1079.3
0
10
20
30
40
50
60
70
80
90
Distance From Reference Point (m)
D.
Dedeckera Canyon Scarp - DCS3
Elevation (m)
1095
1090
1085
1080
1075
1070
1065
y = 1.077x + 1061.2
y = 0.1657x + 1068.8
y = 0.1127x + 1070.9
y = 0.59x + 1051.3
y = 0.2976x + 1066
y = 0.6063x + 1045.8
y = 0.1164x + 1081.2
0
10
20
30
40
50
60
70
80
Distance From Reference Point (m)

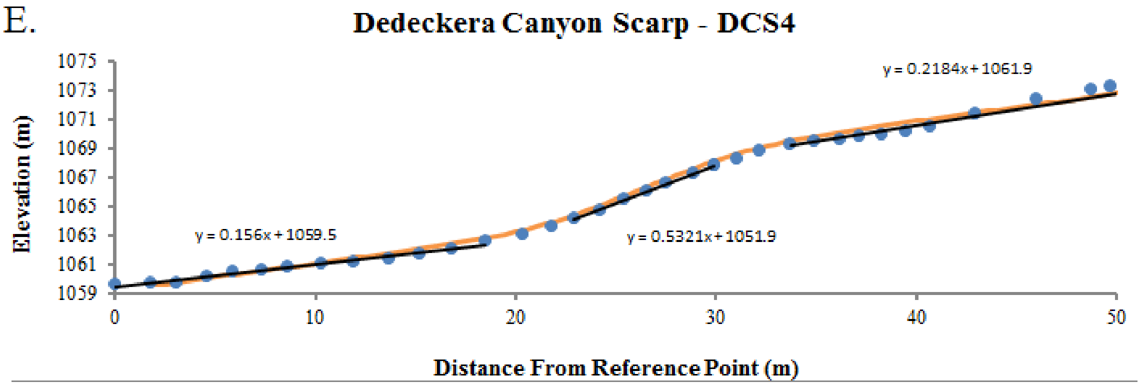
E.
Dedeckera Canyon Scarp - DCS4
y = 0.2184x + 1061.9
y = 0.156x + 1059.5
y = 0.5321x + 1051.9
Elevation (m)
1075
1073
1071
1069
1067
1065
1063
1061
1059
0
10
20
30
40
50
Distance From Reference Point (m)

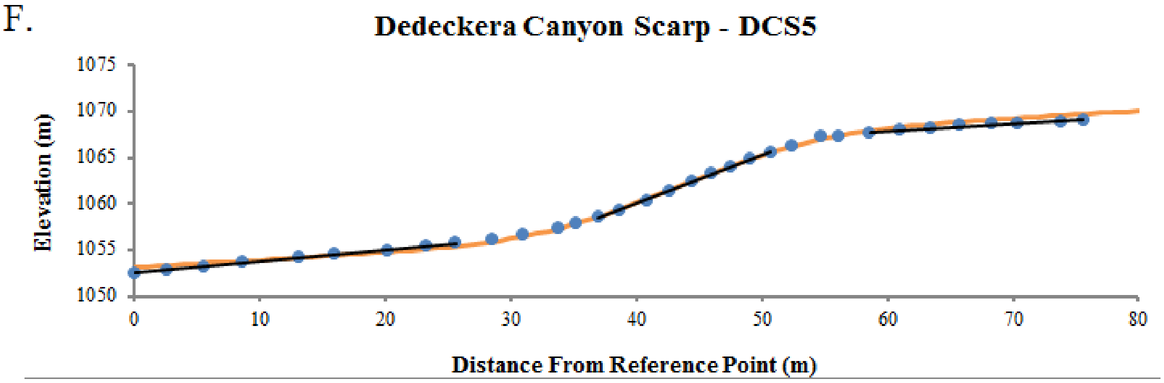
F.
Dedeckera Canyon Scarp - DCS5
Elevation (m)
1075
1070
1065
1060
1055
1050
0
10
20
30
40
50
60
70
80
Distance From Reference Point (m)

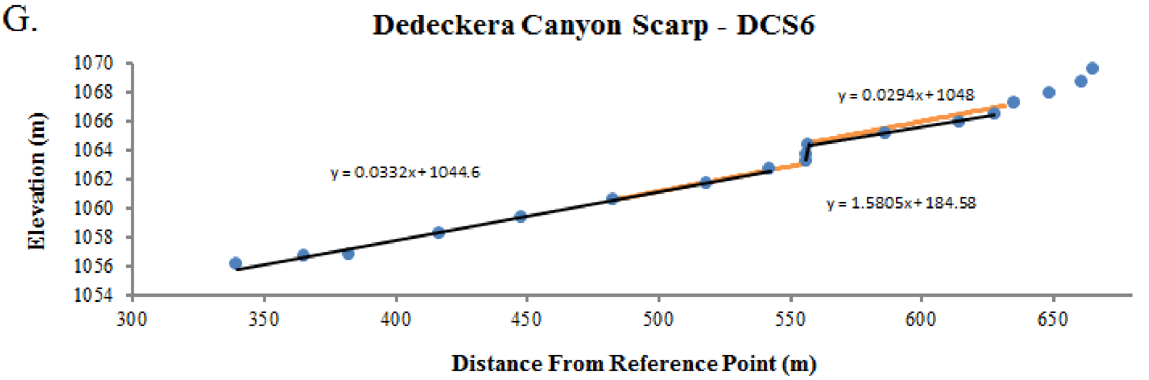
G.
Dedeckera Canyon Scarp - DCS6
y = 0.0294x + 1048
y = 0.0332x + 1044.6
y = 1.5805x + 184.58
Elevation (m)
1070
1068
1066
1064
1062
1060
1058
1056
1054
300
350
400
450
500
550
600
650
Distance From Reference Point (m)

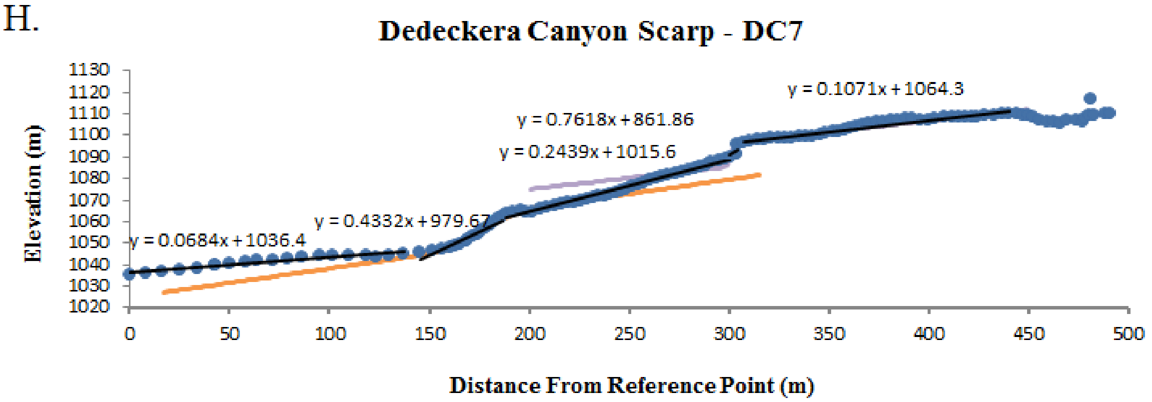
H.
Dedeckera Canyon Scarp - DC7
y = 0.1071x + 1064.3
y = 0.7618x + 861.86
y = 0.2439x + 1015.6
y = 0.4332x + 979.67
y = 0.0684x + 1036.4
Elevation (m)
1130
1120
1110
1100
1090
1080
1070
1060
1050
1040
1030
1020
0
50
100
150
200
250
300
350
400
450
500
Distance From Reference Point (m)

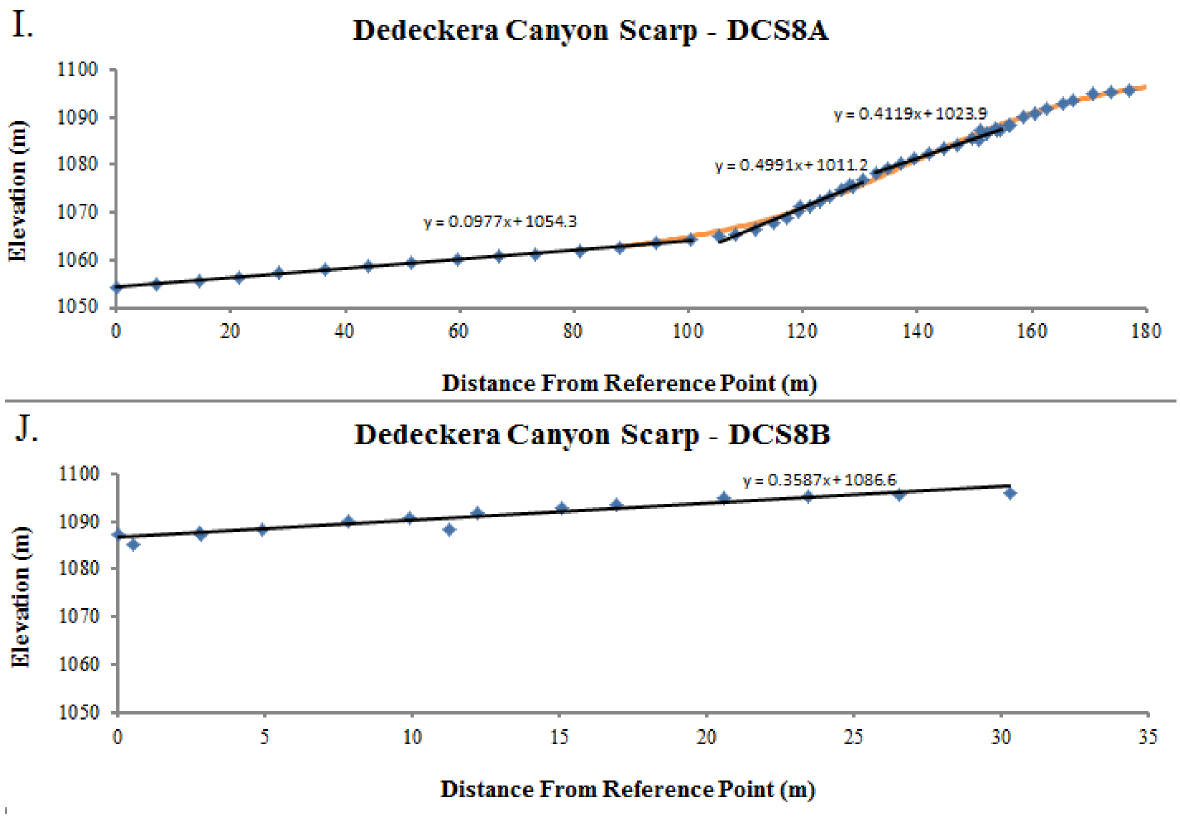

Figure 6.13 A-J Dedeckera scarp profiles.

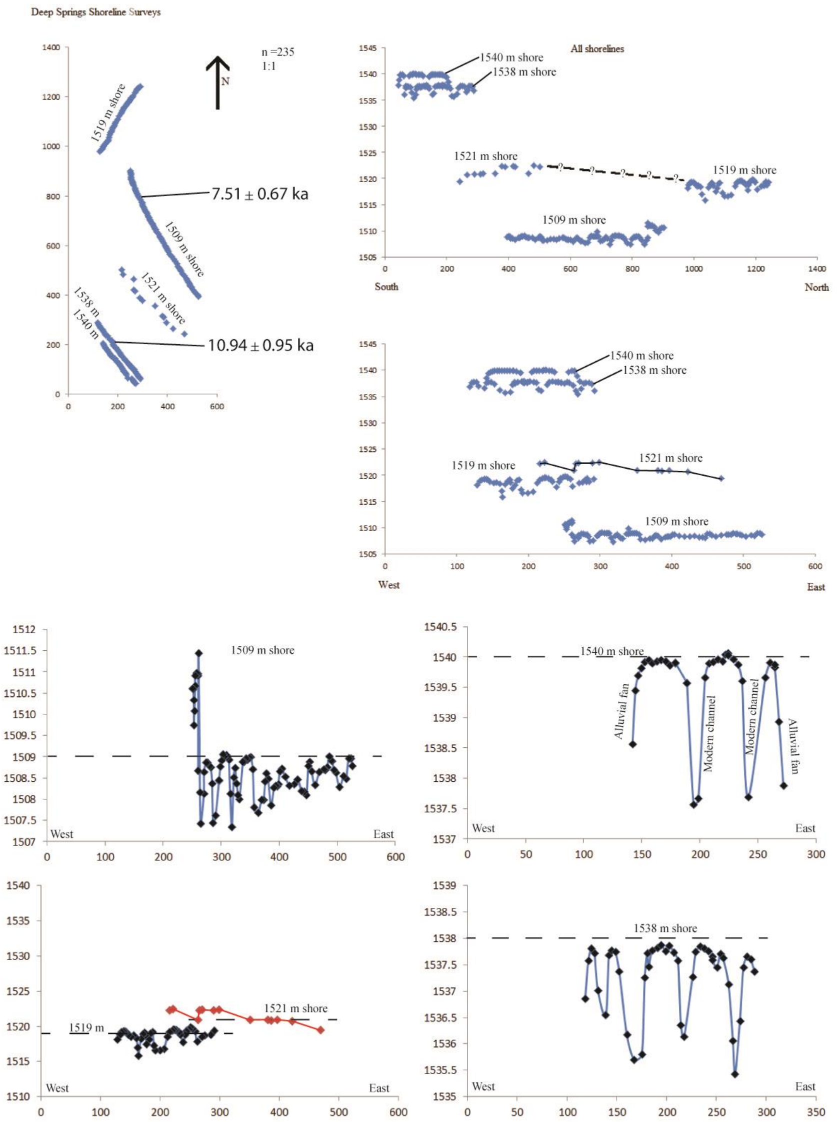

Figure 6.14 Deep springs rotational data.

The shorelines are named by their nearest whole number meter elevation. Shoreline 1509 m is closest to the current lake surface but also the most dissected by current channels. Shorelines 1519 m and 1521 m are possibly the same surface, but greater resolution data is necessary in the 1521 m shoreline. (if they are, that rotation is in the *opposite* direction of DS fault motion) Shorelines 1538 and 1540 m represent the high and low stands for very broad wave cut platform. None of the shores have a very convincing rotation signal for paleorotation in contrast to the Paleolake site in Eureka valley. Post IR-IR dating places the 1509 m shoreline to 7.51 ± 0.67 ka, while shoreline 1538 is 10.94 ± 0.95 ka.

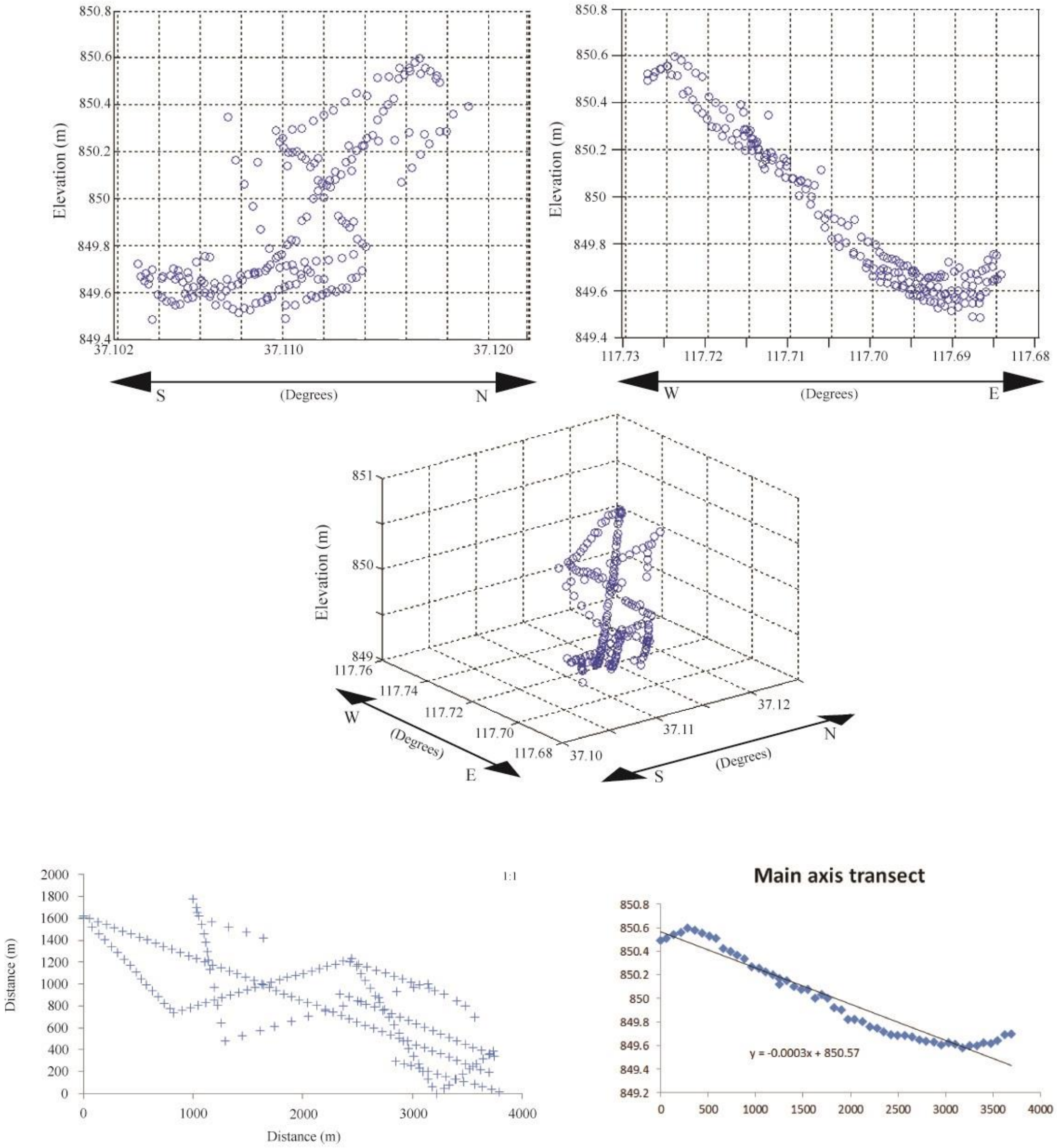

Figure 6.15 Eureka Valley Paleolake Rotation

Details of the GPS transects at the Eureka Valley Paleolake site (see Plate 1).

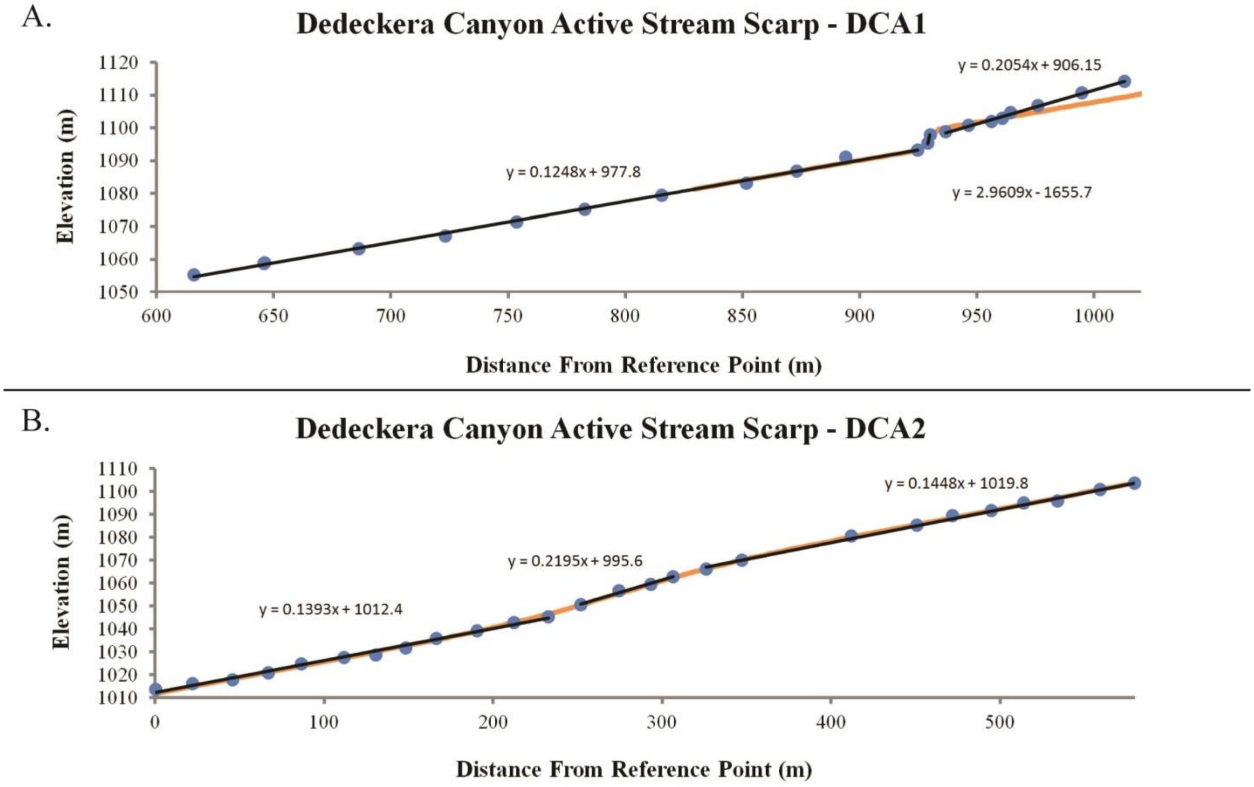

Figure 6.16 A & B Active stream traces, suggesting offset in the active streams.

For active streams, trimble data was collected at the lowest point in the stream, in areas that showed recently active fluvial transport as small streams.A) shows a very clear scarp, need photograph. B) shows a possible slight scarp.

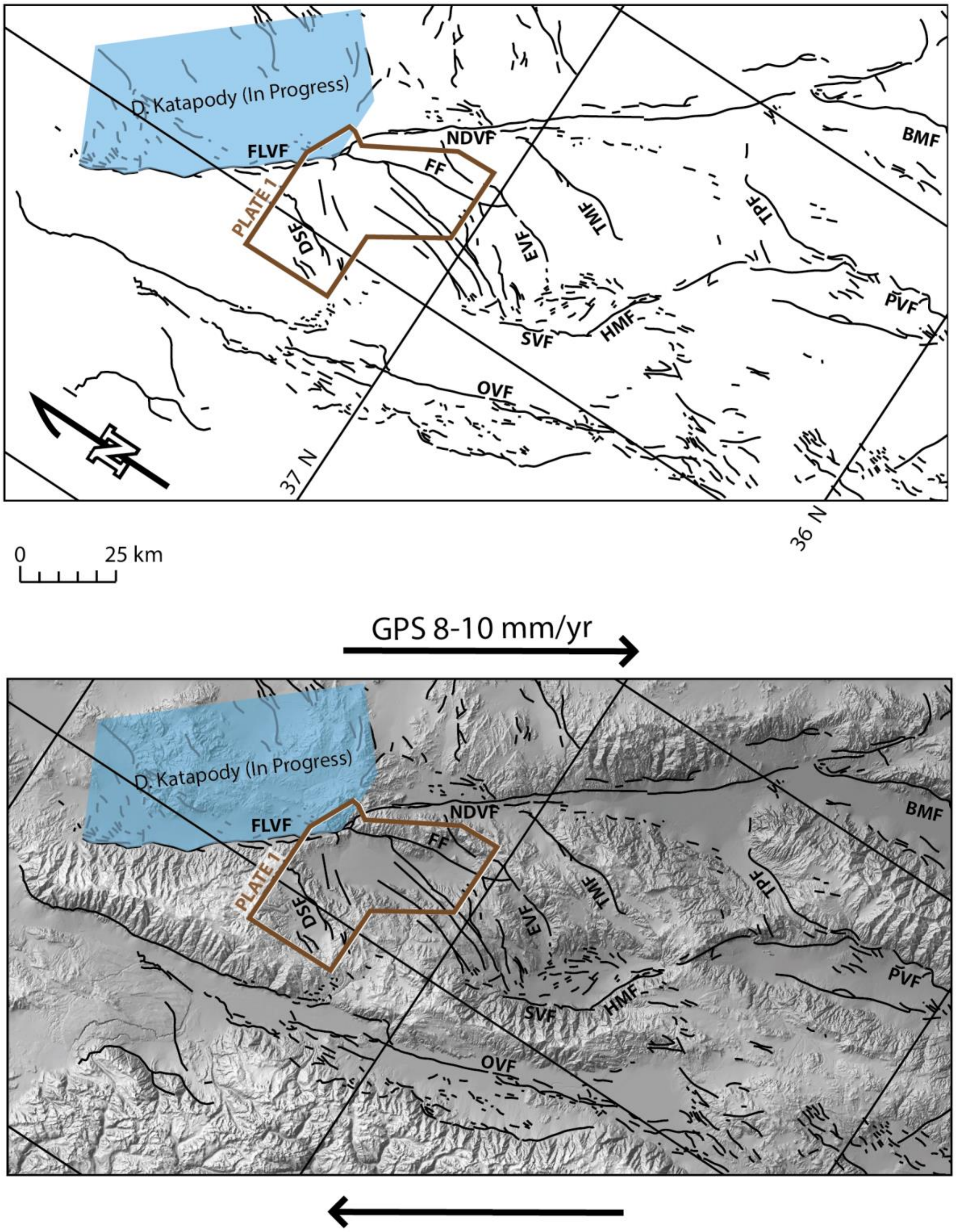

Figure 6.17 Complex of faults accomodating shear.

Table 6.1: Fault offsets at the Dedeckera Canyon site sorted by scarp

								Age			Angles		
	Profile		Offset (m)	Fit quality	Age (ka)	k value	TK value	if (K=1.79)	Fit quality		Lower Surface	Middle Scarp	Upper Surface
Active stream	DCA1		3.27	good	1.94	1.07	2.08	1.16	Poor upper	Fluvial channel	7.1	71.3	11.6
Active stream	DCA2		8.94	good	inf	1.00	n/a		Good	Fluvial channel	7.9	12.4	8.2
Scarp	DCS1A			very poor					Not possible	Alluvial fan	1.3	5.0	19.7
Scarp	DCS1B		0.33	very poor					Not possible	Alluvial fan	26.6	21.7	11.8
Scarp	DCS2	westmost	1.83	poor	1.05	1.33	1.39	0.78	Bad	Alluvial fan	-2.4	19.7	6.7
	DCS2	middle	1.06	poor	2.04	0.49	0.99	0.55	good	Alluvial fan	6.7	17.8	10.1
	DCS2	east	8.27	good	1.60	1.98	3.18	1.78	poor	Alluvial fan	10.1	26.1	9.1
Scarp	DCS3	westmost	1.60	good	1.15	1.27	1.46	0.81	good	Alluvial fan	9.4	47.1	6.4
	DCS3	middle	3.47	good	5.84	1.39	8.14	4.55	good	Alluvial fan	6.4	30.5	16.6
	DCS3	east	2.80	good	1.60	1.98	3.18	1.78	poor	Alluvial fan	16.6	31.2	6.6
Scarp	DCS4		4.05	good	7.88	1.24	9.73	5.44	good	Alluvial fan	8.9	28.0	12.3
Scarp	DCS5		10.74	excellent	38.11	1.10	41.92	23.42	excellent	Alluvial fan	7.1	27.7	4.4
Scarp	DCS6		1.29	poor upper	0.62	0.06	0.04	0.02	good	Alluvial fan	1.9	57.7	1.7
Scarp	DCS7	west	8.31	poor	17.89	4.62	82.62	46.16	poor	landslide cover	3.9	23.4	13.7
	DCS7	east	7.40	poor	2.04	0.57	1.16	0.65	poor	landslide cover	13.7	37.3	6.1
Scarp	DCS8A	west	6.65	excellent	5.48	49.45	270.75	151.26	good	Bed rock	5.6	26.5	22.4

6.10 Chapter Bibliography

Arrowsmith, J.R., 1995, Coupled tectonic deformation and geomorphic degradation along the San Andreas fault Zone. (Doctoral dissertation)

Atwater, T. and Stock, J., 1998, Pacific–North America plate tectonics of the Neogene southwestern United States: an update: International Geology Review, v. 40, p. 375–402.

Avouac, J.P. and Peltzer, G., 1993, Active tectonics in southern Xinjiang, China: Analysis of terrace riser and normal fault scarp degradation along the Hotan-Qira fault system: Journal of Geophysical Research: Solid Earth, v. 98(B12), p. 21773-21807.

Casteel, M., 1986. Geology of a portion of the northwest Last Chance Range, south of Hanging Rock Canyon, Inyo County, California. (Master's thesis)

Corbett, K.P., 1989. Structural geology of the Last Chance Thrust System, East- Central California. (Doctoral dissertation)

DeMets, C. and Dixon,T.H., 1999, New kinematic models for Pacific-North America motion from 3 Ma to present, I: Evidence for steady motion and biases in the NUVEL-1A Model: Geophysical Research Letters, v. 26(13), p. 1921-1924.

Dolan, J., McAuliffe, L.J., Rhodes, E.J., McGill, S.F., and Zinke, R., 2016, Extreme multi-millennial slip rate variations on the Garlock fault, California: Strain super-cycles, potentially time-variable fault strength, and implications for system-level earthquake occurrence: Earth and Planetary Science Letters, v. 446, p 123-136.

Evans, E.L., Thatcher, W.R., Pollitz, F.F. and Murray, J.R., 2016, Persistent slip rate discrepancies in the eastern California (USA) shear zone: Geology, v. 44, p. 691-694.

Faulds, J.E., Henry, C.D., and Hinz, N.H., 2005, Kinematics of the northern Walker Lane: An incipient transform fault along the Pacific- North American plate boundary: Geology, v.

33, p. 505-508.

Frankel, K.L., Brantley, K.S., Dolan, J.F., Finkel, R.C., Klinger, R.E., Knott, J.R., Machette, M.N., Owen, L.A., Phillips, F.M., Slate, J.L., and Wernicke, B.P., 2007a, Cosmogenic 10Be and 36Cl geochronology of offset alluvial fans along the northern Death Valley fault zone: Implications for transient strain in the eastern California shear zone: Journal of Geophysical Research, v. 112, B06407, 18 p., doi: 10.1029/2006JB004350.

Frankel, K.L., Dolan, J.F., Finkel, R.F., Owen, L.A., and Hoeft, J.S., 2007b, Spatial variations in slip rates along the Death Valley–Fish Lake Valley fault system determined from LiDAR topographic data and cosmogenic 10Be geochronology: Geophysical Research Letters, v. 34, L18303, 6 p., doi: 1029/2007GL030549.

Hanks, T.C., 2000, The age of scarplike landforms from diffusion-equation analysis, Quaternary Geochronology: Methods and Applications: p. 313-338.

Hanks, T.C., and Andrews, D.J., 1989, Effect of far-field slope on morphologic dating of scarplike landforms: Journal of Geophysical Research: Solid Earth, v. 94(B1), p. 565-573.

Hanks, T.C., Bucknam, R.C., Lajoie, K.R., and Wallace, R.E., 1984, Modification of wave-cut and fault controlled landforms: Journal of Geophysical Research, v. 89, p. 5771–5790, doi: 10.1029/JB089iB07p05771.

Ingersoll, R.V., 1982, Triple- Junction instability as cause for late Cenozoic extension and fragmentation of the western United States: Geology, v. 10, p. 621-624.

Knott, J. R., et al., 2005, Upper Neogene stratigraphy and tectonics of Death Valley—a review: Earth-Science Reviews v. 73(1), p. 245-270.

Knott, J., Phillips, F., Manoukian, D., Verdadero, C., Wan, E., Lackey, J.S., Nunez, E., Deino, A., Johnson, C., and Whitmer, D., 2014, Late Neogene Geology of the Last Chance Range: Implications for Paleohydrology of the Death Valley Area, Eastern California: Geological Society of America Annual Meeting.

Knott, J.R., Wan, E., Deino, A.L., Casteel, M., Reheis, M.C., Phillips, M.C., Walkup, L., McCarty, K., and Nunez, E., in Prep, Lake Andrei: A Pliocene Pluvial lake in Eureka Valley, Eastern California: GSA Special Volume.

Larson, Ron, Robert P. Hostetler, and Bruce H. Edwards, 2007, Essential Calculus: Early Transcendental Functions, Cengage Learning.

Le, K., Lee, J., Owen, L.A., and Finkel, R., 2007, Late Quaternary slip rates along the Sierra Nevada frontal fault zone, California: Slip partitioning across the western margin of the eastern California shear zone–Basin and Range province: Geological Society of America Bulletin, v. 119, p. 240–256, doi: 10.1130/B25960.1.

Lee, J., Garwood, J., Stockli, D.E., and Gosse, J., 2009, Quaternary faulting in Queen Valley, California-Nevada: Implications for kinematics of fault-slip transfer in the eastern California shear zone–Walker Lane belt: Geological Society of America Bulletin, v. 121, p. 599–614, doi: 10.1130/B26352.1.

Mookerjee, M., Canada, A., and Fortescue, F.Q., 2016, Quantifying thinning and extrusion associated with an oblique subduction zone: An example from the Rosy Finch Shear Zone: Tectonophysics, v. 693(B), p. 290-303.

Nash, D.B., 1984, Morphologic dating of fluvial terrace scarps and fault scarps near West Yellowstone, Montana: Geological Society of America Bulletin, v. 95(12), p. 1413-1424.

Nelson, C.A., 1966, Geological Map of Blanco Mountain quadrangle, Inyo and Mono Counties, California, 1: 62,500

Nelson, C.A., 1966, Geological Map of Waucoba Mountain quadrangle, Inyo County, California, 1: 62,500

Norton, I., 2011, Two- Stage formation of Death Valley: Geological Society of America.

Oldow, J.S., Aiken, C.L.V., Hare, J.L., Ferguson, J.F. and Hardyman, R.F., 2001, Active displacement transfer and differential block motion within the central Walker Lane, western Great Basin: Geology, v. 29(1), p. 19–22.

Peltzer, G., and Rosen, P., 1995, Surface Displacement of the 17 May 1993 Eureka Valley, California, Earthquake Observed by SAR Interferometry: Science, v. 268, p. 1333-1336.

Reheis, M.C., and Sawyer, T.L., 1997, Late Cenozoic history and slip rates of the Fish Lake Valley, Emigrant Peak, and Deep Springs fault zones, Nevada and California: Geological Society of America Bulletin, v. 109(3), p. 280- 299.

Rhodes, E.J., 2011. Optically stimulated luminescence dating of sediments over the past 200,000 years: Annual Review of Earth and Planetary Science, v. 39, p. 461-488.

Stevens, C.H., Stone, P. and Miller, J.S., 2005, A new reconstruction of the Paleozoic continental margin of southwestern North America: Implications for the nature and timing of continental truncation and the possible role of the Mojave-Sonora megashear: Geological Society of America Special Papers, v. 393, p. 597-618.

Stockli, Daniel F., et al., 2003, Cenozoic tectonic evolution of the White Mountains, California and Nevada: Geological Society of America Bulletin, v. 115(7), v. 788-816.

Thatcher, W., Savage, J.C., and Simpson, R.W., 2016, The Eastern California Shear Zone as the northward extension of the southern San Andreas Fault: Journal of Geophysical Research: Solid Earth, v. 121, p. 2904- 2914.

Vriend, N.M., Hunt, M.L., Clayton, R.W., Brennen, C.E., Brantley, K.S., and Ruiz-Angulo, A.,

2007. Solving the mystery of booming sand dunes: Geophysical Research Letters, v. 34, p. 1-6.

Watkins, J., Scully, J.E.C., and Yin, A., in prep, Geomorphologial effects of Mechanical Fluidization as Illustrated by the Eureka Valley Landslide, Eastern California

Whitmer, D., 2012, Clast assemblage in the Last Chance Range of Death Valley, Eastern California (Undergraduate Thesis)

Wrucke,C.T. and Corbett, K.P. 1990, Geologic map of the Last Chance quadrangle, California and Nevada, 1:62,500

Yin, A. and Taylor M.H., 2011, Mechanics of V-shaped conjugate strike-slip faults and the corresponding continuum mode of continental deformation: Geological Society of America Bulletin, v. 123(9-10), p. 1798-1821.

Zepeda, A., 2011 Fault scarp dating and moment magnitude along the Northern Eureka Valley Fault Zone, Eastern California, (Undergraduate Thesis)

APPENDIX A - GPS MEASUREMENTS

Dedeckera Canyon

Survey Point	Latitude	Longitude	Altitude (m)	Horizontal Precision (m)	Vertical Precision (m)	Notes
dc01	N37°04'16.00996"	W117°38'25.42291"	1050.665 m	0.153	0.104	DCS6
dc02	N37°04'15.91895"	W117°38'25.27051"	1051.597 m	1.144	1.080	DCS6
dc03	N37°04'15.88986"	W117°38'25.12258"	1052.019 m	0.132	0.083	DCS6
dc04	N37°04'15.84823"	W117°38'24.95919"	1052.550 m	0.006	0.008	DCS6
dc05	N37°04'15.80656"	W117°38'24.80617"	1052.834 m	0.126	0.123	DCS6
dc06	N37°04'15.76741"	W117°38'24.71280"	1053.099 m	0.006	0.007	DCS6
dc07	N37°04'15.74128"	W117°38'24.62751"	1053.765 m	0.407	0.404	DCS6
dc08	N37°04'15.70771"	W117°38'24.53602"	1054.764 m	0.006	0.007	DCS6
dc09	N37°04'15.68271"	W117°38'24.43457"	1055.666 m	0.007	0.007	DCS6
dc10	N37°04'15.66564"	W117°38'24.34054"	1056.229 m	0.179	0.165	DCS6
dc11	N37°04'15.63672"	W117°38'24.21646"	1056.749 m	0.559	0.443	DCS6
dc12	N37°04'15.61039"	W117°38'24.14117"	1056.929 m	1.737	1.474	DCS6
dc13	N37°04'15.60516"	W117°38'24.04271"	1058.268 m	0.024	0.085	DCS6
dc14	N37°04'15.58913"	W117°38'23.94467"	1059.407 m	0.022	0.027	DCS6
dc15	N37°04'15.56933"	W117°38'23.85151"	1060.615 m	0.009	0.008	DCS6
dc16	N37°04'15.56448"	W117°38'23.76136"	1061.729 m	0.073	0.303	DCS6
dc17	N37°04'15.53809"	W117°38'23.64246"	1062.803 m	0.195	0.173	DCS6
dc18	N37°04'15.58052"	W117°38'23.53986"	1063.271 m	0.009	0.010	DCS6
dc19	N37°04'15.62712"	W117°38'23.42462"	1063.761 m	0.008	0.009	DCS6
dc21	N37°04'15.67591"	W117°38'23.23262"	1064.406 m	0.008	0.009	DCS6
dc20	N37°04'15.76928"	W117°38'23.04873"	1065.237 m	0.008	0.009	DCS6
dc22	N37°04'15.83844"	W117°38'22.86218"	1065.968 m	0.008	0.010	DCS6
dc23	N37°04'15.90311"	W117°38'22.65711"	1066.547 m	0.007	0.010	DCS6
dc24	N37°04'15.96265"	W117°38'22.48637"	1067.249 m	0.016	0.017	DCS6
dc25	N37°04'15.98127"	W117°38'22.28002"	1067.998 m	0.011	0.018	DCS6
dc26	N37°04'16.00419"	W117°38'22.10945"	1068.745 m	0.011	0.017	DCS6
dc27	N37°04'16.07130"	W117°38'21.90488"	1069.655 m	0.006	0.011	DCS6
dc28	N37°04'16.12519"	W117°38'21.68436"	1070.228 m	0.007	0.011	DCS6
dc30	N37°04'15.82220"	W117°38'31.72982"	1035.373 m	0.017	0.032	DCS7
dc31	N37°04'15.70946"	W117°38'31.44398"	1036.095 m	0.006	0.009	DCS7
dc32	N37°04'15.61534"	W117°38'31.12305"	1036.665 m	0.006	0.009	DCS7
dc33	N37°04'15.53686"	W117°38'30.78832"	1037.608 m	0.006	0.009	DCS7
dc34	N37°04'15.46174"	W117°38'30.42328"	1038.472 m	0.007	0.012	DCS7
dc35	N37°04'15.39195"	W117°38'30.08699"	1039.483 m	0.143	0.150	DCS7
dc36	N37°04'15.39288"	W117°38'30.07147"	1039.500 m	0.077	0.097	DCS7

dc37	N37°04'15.34265"	W117°38'29.77890"	1040.554 m	0.005	0.010	DCS7
dc38	N37°04'15.23710"	W117°38'29.50165"	1041.611 m	0.005	0.010	DCS7
dc39	N37°04'15.14318"	W117°38'29.26945"	1041.876 m	0.005	0.010	DCS7
dc40	N37°04'15.04104"	W117°38'28.98557"	1041.977 m	0.008	0.015	DCS7
dc41	N37°04'14.95327"	W117°38'28.70028"	1042.677 m	0.023	0.026	DCS7
dc42	N37°04'14.92304"	W117°38'28.40667"	1043.436 m	0.005	0.009	DCS7
dc43	N37°04'14.84540"	W117°38'28.06195"	1044.038 m	0.005	0.009	DCS7
dc44	N37°04'14.79577"	W117°38'27.81402"	1044.108 m	0.006	0.009	DCS7
dc45	N37°04'14.75193"	W117°38'27.48632"	1044.133 m	1.710	1.075	DCS7
dc46	N37°04'14.65292"	W117°38'27.15081"	1043.931 m	1.783	1.798	DCS7
dc47	N37°04'14.61248"	W117°38'26.96103"	1043.382 m	0.065	0.053	DCS7
dc48	N37°04'14.55616"	W117°38'26.69096"	1044.033 m	0.167	0.130	DCS7
dc49	N37°04'14.48959"	W117°38'26.41296"	1044.835 m	0.006	0.008	DCS7
dc50	N37°04'14.38282"	W117°38'26.12252"	1045.567 m	0.006	0.008	DCS7
dc51	N37°04'14.31595"	W117°38'25.87082"	1046.723 m	0.007	0.008	DCS7
dc52	N37°04'14.27877"	W117°38'25.69514"	1047.079 m	0.008	0.009	DCS7
dc53	N37°04'14.27272"	W117°38'25.52873"	1047.887 m	0.193	0.093	DCS7
dc54	N37°04'14.26297"	W117°38'25.42614"	1048.638 m	0.019	0.019	DCS7
dc55	N37°04'14.23888"	W117°38'25.33219"	1049.708 m	0.020	0.012	DCS7
dc56	N37°04'14.17777"	W117°38'25.21714"	1051.214 m	0.667	0.515	DCS7
dc57	N37°04'14.19795"	W117°38'25.16656"	1051.831 m	0.312	0.291	DCS7
dc58	N37°04'14.17460"	W117°38'25.07418"	1053.006 m	0.007	0.008	DCS7
dc59	N37°04'14.13906"	W117°38'24.99288"	1054.343 m	0.017	0.016	DCS7
dc60	N37°04'14.11677"	W117°38'24.91903"	1055.497 m	0.026	0.030	DCS7
dc61	N37°04'14.09595"	W117°38'24.81781"	1057.291 m	1.453	1.182	DCS7
dc62	N37°04'14.07692"	W117°38'24.73504"	1058.239 m	0.013	0.022	DCS7
dc63	N37°04'14.06533"	W117°38'24.65640"	1059.620 m	0.015	0.015	DCS7
dc64	N37°04'14.05298"	W117°38'24.56167"	1061.143 m	0.007	0.010	DCS7
dc65	N37°04'14.03983"	W117°38'24.49793"	1062.465 m	0.007	0.010	DCS7
ds66	N37°04'14.02362"	W117°38'24.43081"	1063.644 m	0.080	0.013	DCS7
dc67	N37°04'14.02315"	W117°38'24.26335"	1064.412 m	0.124	0.102	DCS7
dc68	N37°04'14.00992"	W117°38'24.11845"	1065.002 m	0.048	0.057	DCS7
dc69	N37°04'14.02145"	W117°38'23.99830"	1064.435 m	0.881	1.180	DCS7
dc70	N37°04'14.05391"	W117°38'23.85695"	1064.664 m	1.476	1.303	DCS7
dc71	N37°04'14.03740"	W117°38'23.70084"	1066.321 m	0.006	0.013	DCS7
dc72	N37°04'14.02612"	W117°38'23.56710"	1066.849 m	0.033	0.056	DCS7
dc73	N37°04'14.02631"	W117°38'23.40818"	1067.455 m	0.084	0.030	DCS7
dc74	N37°04'14.03332"	W117°38'23.26789"	1068.000 m	0.072	0.060	DCS7
dc75	N37°04'14.02867"	W117°38'23.11437"	1068.573 m	0.114	0.104	DCS7
dc76	N37°04'14.04112"	W117°38'22.97781"	1069.201 m	0.012	0.020	DCS7
dc77	N37°04'14.04405"	W117°38'22.84766"	1069.747 m	0.045	0.027	DCS7

dc78	N37°04'14.05865"	W117°38'22.71334"	1070.254 m	0.006	0.017	DCS7
dc79	N37°04'14.07037"	W117°38'22.55915"	1070.927 m	0.011	0.021	DCS7
dc80	N37°04'14.10500"	W117°38'22.44320"	1071.558 m	0.058	0.099	DCS7
dc81	N37°04'14.13284"	W117°38'22.32602"	1072.223 m	0.121	0.226	DCS7
dc82	N37°04'14.14974"	W117°38'22.19925"	1072.954 m	0.114	0.232	DCS7
dc83	N37°04'14.19032"	W117°38'22.08062"	1073.668 m	0.019	0.042	DCS7
dc84	N37°04'14.20586"	W117°38'21.96127"	1074.466 m	0.116	0.077	DCS7
dc85	N37°04'14.21601"	W117°38'21.85015"	1075.184 m	0.248	0.092	DCS7
dc86	N37°04'14.21690"	W117°38'21.71826"	1076.177 m	0.222	0.091	DCS7
dc87	N37°04'14.22566"	W117°38'21.59467"	1077.185 m	0.108	0.019	DCS7
dc88	N37°04'14.24379"	W117°38'21.47354"	1078.150 m	0.325	0.043	DCS7
dc89	N37°04'14.24766"	W117°38'21.35872"	1079.123 m	0.096	0.031	DCS7
dc90	N37°04'14.23894"	W117°38'21.23102"	1080.159 m	0.350	0.175	DCS7
dc91	N37°04'14.23232"	W117°38'21.11002"	1081.000 m	0.035	0.033	DCS7
dc92	N37°04'14.23800"	W117°38'20.97460"	1081.830 m	0.058	0.055	DCS7
dc93	N37°04'14.22803"	W117°38'20.83681"	1082.594 m	0.007	0.009	DCS7
dc94	N37°04'14.23704"	W117°38'20.70261"	1083.085 m	0.008	0.009	DCS7
dc95	N37°04'14.23336"	W117°38'20.56449"	1083.587 m	0.007	0.008	DCS7
dc96	N37°04'14.22609"	W117°38'20.42730"	1084.357 m	0.009	0.011	DCS7
dc97	N37°04'14.24195"	W117°38'20.30758"	1085.251 m	0.007	0.008	DCS7
dc98	N37°04'14.22780"	W117°38'20.19482"	1086.258 m	0.006	0.008	DCS7
dc99	N37°04'14.19914"	W117°38'20.08516"	1087.272 m	0.006	0.007	DCS7
dc100	N37°04'14.19110"	W117°38'19.93159"	1088.571 m	0.006	0.007	DCS7
dc101	N37°04'14.16157"	W117°38'19.81710"	1089.484 m	0.006	0.007	DCS7
dc102	N37°04'14.14483"	W117°38'19.72863"	1090.107 m	0.007	0.008	DCS7
dc103	N37°04'14.14367"	W117°38'19.56876"	1091.006 m	0.007	0.008	DCS7
dc104	N37°04'14.10758"	W117°38'19.60290"	1096.153 m	0.006	0.014	DCS7
dc105	N37°04'14.12598"	W117°38'19.44410"	1096.689 m	0.011	0.016	DCS7
dc106	N37°04'14.13633"	W117°38'19.32048"	1097.238 m	0.007	0.016	DCS7
dc107	N37°04'14.12709"	W117°38'19.16424"	1097.918 m	0.070	0.035	DCS7
dc108	N37°04'14.11495"	W117°38'19.03217"	1098.409 m	0.368	0.159	DCS7
dc109	N37°04'14.12479"	W117°38'18.87886"	1098.732 m	0.136	0.067	DCS7
dc110	N37°04'14.14106"	W117°38'18.72073"	1098.915 m	1.190	0.904	DCS7
dc111	N37°04'14.15782"	W117°38'18.58290"	1099.099 m	0.337	0.113	DCS7
dc112	N37°04'14.19338"	W117°38'18.42877"	1099.194 m	0.228	0.066	DCS7
dc113	N37°04'14.20990"	W117°38'18.26180"	1099.403 m	0.313	0.015	DCS7
dc115	N37°04'14.24168"	W117°38'18.12613"	1099.622 m	0.551	0.030	DCS7
dc114	N37°04'14.28791"	W117°38'17.99166"	1099.823 m	0.478	0.369	DCS7
dc116	N37°04'14.30770"	W117°38'17.83538"	1100.355 m	0.008	0.011	DCS7
dc117	N37°04'14.32680"	W117°38'17.72814"	1100.759 m	0.008	0.010	DCS7
dc118	N37°04'14.32115"	W117°38'17.57644"	1101.493 m	0.037	0.025	DCS7

dc119	N37°04'14.34046"	W117°38'17.46208"	1102.045 m	0.791	0.296	DCS7
dc120	N37°04'14.33707"	W117°38'17.33639"	1102.717 m	0.635	0.503	DCS7
dc121	N37°04'14.36588"	W117°38'17.20965"	1103.427 m	0.871	0.484	DCS7
dc122	N37°04'14.38224"	W117°38'17.08373"	1103.945 m	0.390	0.135	DCS7
dc123	N37°04'14.39104"	W117°38'16.96090"	1104.610 m	0.018	0.017	DCS7
dc124	N37°04'14.39372"	W117°38'16.81804"	1105.310 m	0.893	0.366	DCS7
dc125	N37°04'14.41928"	W117°38'16.66108"	1106.053 m	0.464	0.488	DCS7
dc126	N37°04'14.42429"	W117°38'16.52131"	1106.350 m	0.328	0.338	DCS7
dc127	N37°04'14.43446"	W117°38'16.36741"	1107.062 m	0.340	0.422	DCS7
dc128	N37°04'14.41543"	W117°38'16.21526"	1107.422 m	0.222	0.155	DCS7
dc129	N37°04'14.38899"	W117°38'16.06106"	1107.772 m	0.497	0.242	DCS7
dc130	N37°04'14.39437"	W117°38'15.92811"	1107.634 m	0.900	0.709	DCS7
dc131	N37°04'14.38652"	W117°38'15.78915"	1106.898 m	1.340	0.699	DCS7
dc132	N37°04'14.39482"	W117°38'15.61761"	1106.980 m	1.663	0.384	DCS7
dc133	N37°04'14.38857"	W117°38'15.46753"	1108.107 m	1.943	1.359	DCS7
dc134	N37°04'14.37164"	W117°38'15.27701"	1108.445 m	0.034	0.044	DCS7
dc135	N37°04'14.38367"	W117°38'15.12373"	1108.446 m	0.221	0.429	DCS7
dc136	N37°04'14.39997"	W117°38'14.97205"	1108.389 m	0.355	0.118	DCS7
dc137	N37°04'14.41888"	W117°38'14.85487"	1108.652 m	0.763	0.240	DCS7
dc138	N37°04'14.44668"	W117°38'14.71069"	1108.793 m	0.049	0.050	DCS7
dc139	N37°04'14.47447"	W117°38'14.59833"	1108.801 m	0.117	0.122	DCS7
dc140	N37°04'14.47637"	W117°38'14.44032"	1109.226 m	0.025	0.023	DCS7
dc141	N37°04'14.48125"	W117°38'14.26446"	1109.456 m	0.442	0.240	DCS7
dc142	N37°04'14.45063"	W117°38'14.09267"	1110.076 m	0.271	0.290	DCS7
dc143	N37°04'14.44213"	W117°38'13.95086"	1110.405 m	0.161	0.066	DCS7
dc144	N37°04'14.38878"	W117°38'13.80648"	1109.880 m	0.739	0.363	DCS7
dc145	N37°04'14.37215"	W117°38'13.66008"	1109.549 m	0.594	0.385	DCS7
dc146	N37°04'14.33199"	W117°38'13.57763"	1109.648 m	0.746	1.145	DCS7
dc147	N37°04'14.28964"	W117°38'13.46932"	1108.300 m	0.248	0.679	DCS7
dc148	N37°04'14.26217"	W117°38'13.35053"	1107.362 m	0.040	0.024	DCS7
dc149	N37°04'14.21589"	W117°38'13.20491"	1106.659 m	0.642	0.269	DCS7
dc150	N37°04'14.16742"	W117°38'13.08542"	1106.109 m	0.631	0.365	DCS7
dc151	N37°04'14.13749"	W117°38'12.95064"	1105.899 m	1.142	1.000	DCS7
dc152	N37°04'14.06721"	W117°38'12.80925"	1106.711 m	0.769	1.248	DCS7
dc154	N37°04'14.05610"	W117°38'12.64255"	1106.736 m	0.737	1.913	DCS7
dc155	N37°04'13.98731"	W117°38'12.49396"	1106.009 m	1.683	4.453	DCS7
dc156	N37°04'13.95517"	W117°38'12.48289"	1107.571 m	0.350	0.302	DCS7
dc157	N37°04'13.88198"	W117°38'12.39894"	1109.577 m	0.582	0.753	DCS7
dc158	N37°04'13.85101"	W117°38'12.37747"	1116.911 m	5.184	17.133	DCS7
dc159	N37°04'13.83373"	W117°38'12.30421"	1108.996 m	0.440	0.717	DCS7
dc160	N37°04'13.84491"	W117°38'12.08083"	1110.298 m	0.468	0.525	DCS7

dc161	N37°04'13.81263"	W117°38'11.98779"	1110.399 m	1.014	1.120	DCS7
dc162	N37°04'15.04366"	W117°38'11.15918"	1103.589 m	0.536	0.314	
dc163	N37°04'15.27204"	W117°38'11.94027"	1100.699 m	0.761	0.345	
dc164	N37°04'15.30323"	W117°38'12.97514"	1095.650 m	0.998	0.928	
dc165	N37°04'15.15380"	W117°38'13.83328"	1094.813 m	0.684	0.725	
dc166	N37°04'15.53740"	W117°38'14.53270"	1091.534 m	0.388	0.431	
dc167	N37°04'15.73173"	W117°38'15.44420"	1089.417 m	0.807	0.624	
dc168	N37°04'16.22345"	W117°38'16.20788"	1085.218 m	0.845	0.604	
dc169	N37°04'15.99598"	W117°38'17.02811"	1107.825 m	7.241	32.398	
dc170	N37°04'16.11433"	W117°38'17.82932"	1080.458 m	0.746	0.640	
dc173	N37°04'15.73354"	W117°38'20.59677"	1070.087 m	0.770	0.582	
dc174	N37°04'15.64007"	W117°38'21.50230"	1065.988 m	0.793	0.580	
dc176	N37°04'15.62473"	W117°38'22.34038"	1062.877 m	0.816	0.585	
dc177	N37°04'15.28842"	W117°38'23.02652"	1059.430 m	1.213	1.293	
dc178	N37°04'15.09803"	W117°38'23.90568"	1056.625 m	0.864	0.623	
dc179	N37°04'15.28845"	W117°38'24.79829"	1050.571 m	1.208	1.759	
DC200	N37°04'13.14990"	W117°38'26.00247"	1054.224 m	0.362	0.204	DCS8A
DC201	N37°04'13.07258"	W117°38'25.73493"	1054.922 m	0.009	0.012	DCS8A
dc202	N37°04'12.92867"	W117°38'25.47823"	1055.620 m	0.092	0.050	DCS8A
DC203	N37°04'12.87530"	W117°38'25.20013"	1056.333 m	0.402	0.651	DCS8A
dc204	N37°04'12.79993"	W117°38'24.93569"	1057.205 m	0.027	0.026	DCS8A
dc205	N37°04'12.73120"	W117°38'24.61955"	1058.061 m	0.005	0.007	DCS8A
dc206	N37°04'12.60894"	W117°38'24.34285"	1058.758 m	0.006	0.007	DCS8A
dc207	N37°04'12.50477"	W117°38'24.07757"	1059.337 m	0.005	0.007	DCS8A
dc208	N37°04'12.44801"	W117°38'23.74776"	1060.136 m	0.006	0.007	DCS8A
dc209	N37°04'12.35430"	W117°38'23.48374"	1060.759 m	0.363	0.107	DCS8A
dc210	N37°04'12.26968"	W117°38'23.24851"	1061.141 m	0.073	0.082	DCS8A
dc211	N37°04'12.17657"	W117°38'22.94857"	1062.023 m	1.087	1.150	DCS8A
dc212	N37°04'12.18162"	W117°38'22.64679"	1062.422 m	0.644	1.133	DCS8A
dc213	N37°04'12.20986"	W117°38'22.36450"	1063.726 m	0.906	0.280	DCS8A
dc214	N37°04'12.25661"	W117°38'22.08311"	1064.436 m	0.007	0.009	DCS8A
dc215	N37°04'12.20947"	W117°38'21.89169"	1065.108 m	0.007	0.009	DCS8A
dc216	N37°04'12.15919"	W117°38'21.78578"	1065.443 m	0.007	0.011	DCS8A
dc217	N37°04'12.18578"	W117°38'21.63052"	1066.364 m	0.007	0.010	DCS8A
dc218	N37°04'12.15710"	W117°38'21.51401"	1067.730 m	0.007	0.011	DCS8A
dc219	N37°04'12.11934"	W117°38'21.43182"	1068.952 m	0.288	0.287	DCS8A
dc220	N37°04'12.12606"	W117°38'21.33286"	1070.154 m	0.006	0.010	DCS8A
dc221	N37°04'12.12733"	W117°38'21.24972"	1071.181 m	0.007	0.012	DCS8A
dc222	N37°04'12.19232"	W117°38'21.30140"	1071.365 m	0.006	0.010	DCS8A
dc223	N37°04'12.14656"	W117°38'21.17170"	1072.293 m	0.006	0.010	DCS8A
dc224	N37°04'12.13103"	W117°38'21.10387"	1073.397 m	0.006	0.012	DCS8A

dc225	N37°04'12.12563"	W117°38'21.02455"	1074.624 m	0.006	0.011	DCS8A
dc226	N37°04'12.10400"	W117°38'20.96330"	1075.640 m	0.017	0.019	DCS8A
dc227	N37°04'12.27688"	W117°38'20.89301"	1075.582 m	0.007	0.013	DCS8A
dc228	N37°04'12.08870"	W117°38'20.87851"	1076.922 m	0.007	0.013	DCS8A
dc229	N37°04'12.07359"	W117°38'20.78977"	1078.174 m	0.007	0.007	DCS8A
dc230	N37°04'12.01323"	W117°38'20.71886"	1079.328 m	0.031	0.028	DCS8A
dc231	N37°04'11.94734"	W117°38'20.64136"	1080.511 m	0.007	0.009	DCS8A
dc232	N37°04'11.90124"	W117°38'20.56487"	1081.553 m	0.010	0.013	DCS8A
dc233	N37°04'11.83847"	W117°38'20.47592"	1082.546 m	0.015	0.013	DCS8A
dc234	N37°04'11.80062"	W117°38'20.38611"	1083.545 m	0.177	0.080	DCS8A
dc235	N37°04'11.75672"	W117°38'20.30488"	1084.318 m	0.007	0.009	DCS8A
dc236	N37°04'11.73129"	W117°38'20.20062"	1085.397 m	0.366	0.320	DCS8A
dc237	N37°04'11.74468"	W117°38'20.08015"	1086.633 m	0.086	0.048	DCS8A
dc238	N37°04'11.73681"	W117°38'19.98583"	1087.299 m	0.093	0.041	DCS8A
dc239	N37°04'12.03039"	W117°38'20.03731"	1087.389 m	1.244	1.957	DCS8A
dc240	N37°04'12.04600"	W117°38'20.04310"	1085.081 m	0.943	1.094	DCS8A
dc241	N37°04'12.02248"	W117°38'19.92518"	1087.538 m	0.951	0.906	DCS8A
dc242	N37°04'12.02303"	W117°38'19.92203"	1087.366 m	0.027	0.047	DCS8A
dc243	N37°04'12.02300"	W117°38'19.83788"	1088.470 m	0.880	0.322	DCS8A
dc244	N37°04'12.02986"	W117°38'19.72019"	1090.070 m	0.750	0.495	DCS8A
dc245	N37°04'12.05113"	W117°38'19.63720"	1090.788 m	0.092	0.084	DCS8A
dc246	N37°04'12.06052"	W117°38'19.54437"	1091.812 m	0.009	0.018	DCS8A
dc247	N37°04'12.07155"	W117°38'19.42844"	1092.880 m	0.220	0.403	DCS8A
dc248	N37°04'12.31097"	W117°38'19.74559"	1088.228 m	0.674	0.734	DCS8A
dc249	N37°04'12.06868"	W117°38'19.35349"	1093.542 m	0.023	0.036	DCS8A
dc250	N37°04'12.07596"	W117°38'19.20543"	1094.876 m	0.113	0.215	DCS8A
dc251	N37°04'12.05258"	W117°38'19.08617"	1095.476 m	0.200	0.419	DCS8A
dc252	N37°04'12.02287"	W117°38'18.96200"	1095.825 m	0.140	0.253	DCS8A
dc253	N37°04'12.02729"	W117°38'18.80958"	1096.029 m	0.199	0.139	DCS8A
dc254	N37°04'10.30849"	W117°38'17.94801"	1102.681 m	0.301	0.132	
dc255	N37°04'19.95953"	W117°38'16.57217"	1093.754 m	0.008	0.030	DCS2
dc256	N37°04'20.02430"	W117°38'16.69257"	1093.284 m	0.009	0.010	DCS2
dc257	N37°04'20.06707"	W117°38'16.79544"	1092.825 m	0.032	0.021	DCS2
dc258	N37°04'20.11067"	W117°38'16.89798"	1092.406 m	0.008	0.008	DCS2
dc259	N37°04'20.14692"	W117°38'17.01386"	1091.977 m	0.008	0.008	DCS2
dc260	N37°04'20.18082"	W117°38'17.12963"	1091.241 m	0.008	0.008	DCS2
dc261	N37°04'20.20009"	W117°38'17.24083"	1090.538 m	0.008	0.008	DCS2
dc262	N37°04'20.22172"	W117°38'17.32953"	1089.576 m	0.008	0.008	DCS2
dc263	N37°04'20.25095"	W117°38'17.41377"	1088.272 m	0.008	0.009	DCS2
dc264	N37°04'20.28053"	W117°38'17.49163"	1086.969 m	0.010	0.009	DCS2
dc265	N37°04'20.31473"	W117°38'17.55734"	1085.770 m	0.008	0.009	DCS2

dc266	N37°04'20.37518"	W117°38'17.65270"	1084.297 m	0.008	0.009	DCS2
dc267	N37°04'20.41315"	W117°38'17.73142"	1083.193 m	0.008	0.010	DCS2
dc268	N37°04'20.46858"	W117°38'17.81548"	1081.914 m	0.008	0.010	DCS2
dc269	N37°04'20.50363"	W117°38'17.98194"	1080.417 m	0.010	0.014	DCS2
dc270	N37°04'20.53318"	W117°38'18.07331"	1079.654 m	0.009	0.013	DCS2
dc271	N37°04'20.55902"	W117°38'18.17833"	1078.560 m	0.011	0.019	DCS2
dc272	N37°04'20.60001"	W117°38'18.27219"	1077.683 m	0.012	0.020	DCS2
dc273	N37°04'20.60006"	W117°38'18.27211"	1077.689 m	0.011	0.021	DCS2
dc274	N37°04'20.64566"	W117°38'18.39458"	1077.117 m	0.012	0.022	DCS2
dc275	N37°04'20.69501"	W117°38'18.52830"	1076.511 m	0.011	0.023	DCS2
dc276	N37°04'20.73648"	W117°38'18.64579"	1076.174 m	0.012	0.026	DCS2
dc277	N37°04'20.78200"	W117°38'18.76760"	1075.638 m	0.010	0.025	DCS2
dc278	N37°04'20.81266"	W117°38'18.86565"	1075.283 m	0.009	0.023	DCS2
dc280	N37°04'20.79063"	W117°38'18.80932"	1074.603 m	0.624	0.882	DCS2
dc281	N37°04'20.85738"	W117°38'18.90610"	1073.885 m	1.520	1.330	DCS2
dc282	N37°04'20.90412"	W117°38'19.00430"	1073.159 m	0.722	1.328	DCS2
dc283	N37°04'20.92845"	W117°38'19.07921"	1073.372 m	0.009	0.008	DCS2
dc284	N37°04'20.95721"	W117°38'19.20263"	1072.310 m	0.009	0.008	DCS2
dc285	N37°04'20.98609"	W117°38'19.27059"	1071.600 m	0.009	0.009	DCS2
dc286	N37°04'20.99904"	W117°38'19.31024"	1071.276 m	0.009	0.009	DCS2
dc287	N37°04'21.02602"	W117°38'19.36147"	1070.963 m	0.009	0.008	DCS2
dc288	N37°04'21.06935"	W117°38'19.41622"	1071.111 m	0.009	0.009	DCS2
dc289	N37°04'21.10704"	W117°38'19.52737"	1071.076 m	0.009	0.010	DCS2
dc290	N37°04'21.19407"	W117°38'19.63190"	1071.367 m	0.008	0.010	DCS2
dc291	N37°04'21.30696"	W117°38'19.84690"	1071.586 m	0.008	0.010	DCS2
dc292	N37°04'20.50044"	W117°38'20.26528"	1068.985 m	0.009	0.012	DCS3
dc293	N37°04'20.50089"	W117°38'20.20926"	1069.154 m	0.012	0.019	DCS3
dc294	N37°04'20.49619"	W117°38'20.16691"	1069.261 m	0.007	0.011	DCS3
dc295	N37°04'20.49573"	W117°38'20.13847"	1068.929 m	0.392	1.044	DCS3
dc296	N37°04'20.48861"	W117°38'20.09775"	1069.461 m	0.011	0.020	DCS3
dc297	N37°04'20.48519"	W117°38'20.07299"	1069.534 m	0.653	0.498	DCS3
dc298	N37°04'20.47965"	W117°38'20.04243"	1069.758 m	0.006	0.012	DCS3
dc299	N37°04'20.47455"	W117°38'20.01176"	1070.012 m	0.280	0.288	DCS3
dc300	N37°04'20.46890"	W117°38'19.97953"	1070.229 m	0.506	0.108	DCS3
dc301	N37°04'20.46799"	W117°38'19.94868"	1070.029 m	1.057	1.646	DCS3
dc302	N37°04'20.44342"	W117°38'19.91689"	1070.696 m	0.920	1.817	DCS3
dc303	N37°04'20.44259"	W117°38'19.87769"	1071.270 m	0.077	0.033	DCS3
dc304	N37°04'20.45025"	W117°38'19.86300"	1072.245 m	0.390	0.547	DCS3
dc305	N37°04'20.43613"	W117°38'19.80408"	1071.865 m	0.298	0.371	DCS3
dc306	N37°04'20.44656"	W117°38'19.72594"	1071.484 m	1.777	1.688	DCS3
dc307	N37°04'20.42929"	W117°38'19.70456"	1072.661 m	0.469	0.153	DCS3

dc308	N37°04'20.42258"	W117°38'19.66481"	1072.877 m	0.420	0.133	DCS3
dc309	N37°04'20.41883"	W117°38'19.61767"	1072.941 m	0.469	0.277	DCS3
dc310	N37°04'20.43559"	W117°38'19.56942"	1073.449 m	1.237	0.710	DCS3
dc311	N37°04'20.42372"	W117°38'19.49801"	1073.255 m	0.018	0.013	DCS3
dc312	N37°04'20.43331"	W117°38'19.45057"	1073.445 m	0.336	0.197	DCS3
dc313	N37°04'20.42000"	W117°38'19.39289"	1073.448 m	0.151	0.083	DCS3
dc314	N37°04'20.41556"	W117°38'19.32915"	1073.447 m	0.008	0.010	DCS3
dc315	N37°04'20.40753"	W117°38'19.26095"	1073.573 m	0.012	0.013	DCS3
dc316	N37°04'20.39502"	W117°38'19.20046"	1073.771 m	0.467	0.276	DCS3
dc317	N37°04'20.38033"	W117°38'19.15119"	1074.131 m	0.394	0.421	DCS3
dc318	N37°04'20.36409"	W117°38'19.09110"	1074.264 m	0.058	0.027	DCS3
dc319	N37°04'20.35953"	W117°38'19.03986"	1074.443 m	0.245	0.168	DCS3
dc320	N37°04'20.36947"	W117°38'18.97098"	1074.379 m	0.955	0.653	DCS3
dc321	N37°04'20.32195"	W117°38'18.88969"	1074.424 m	0.490	0.137	DCS3
dc322	N37°04'20.33151"	W117°38'18.83554"	1074.193 m	0.547	0.457	DCS3
dc323	N37°04'20.29339"	W117°38'18.79074"	1075.255 m	0.979	0.451	DCS3
dc324	N37°04'20.26714"	W117°38'18.71884"	1075.365 m	0.714	0.374	DCS3
dc325	N37°04'20.27235"	W117°38'18.64351"	1076.066 m	0.489	0.450	DCS3
dc326	N37°04'20.25095"	W117°38'18.61416"	1075.405 m	0.760	0.400	DCS3
dc327	N37°04'20.23008"	W117°38'18.57011"	1076.721 m	0.366	0.364	DCS3
dc328	N37°04'20.21542"	W117°38'18.52152"	1076.850 m	0.436	0.431	DCS3
dc329	N37°04'20.18982"	W117°38'18.45681"	1077.894 m	0.519	0.607	DCS3
dc330	N37°04'20.16527"	W117°38'18.41036"	1079.245 m	0.633	0.660	DCS3
dc331	N37°04'20.15622"	W117°38'18.36447"	1079.893 m	0.612	0.658	DCS3
dc332	N37°04'20.15736"	W117°38'18.32020"	1080.061 m	0.592	0.657	DCS3
dc333	N37°04'20.12671"	W117°38'18.26655"	1081.195 m	0.574	0.657	DCS3
dc334	N37°04'20.13889"	W117°38'18.20977"	1081.325 m	0.559	0.657	DCS3
dc335	N37°04'20.11527"	W117°38'18.15567"	1082.246 m	0.544	0.659	DCS3
dc336	N37°04'20.10281"	W117°38'18.08341"	1081.946 m	0.530	0.661	DCS3
dc337	N37°04'20.09053"	W117°38'18.02472"	1082.897 m	0.518	0.663	DCS3
dc338	N37°04'20.07707"	W117°38'17.96036"	1082.775 m	0.689	0.620	DCS3
dc339	N37°04'20.05351"	W117°38'17.91161"	1083.862 m	0.659	0.576	DCS3
dc340	N37°04'20.05111"	W117°38'17.91600"	1084.210 m	0.691	0.616	DCS3
dc343	N37°04'19.98966"	W117°38'17.71571"	1085.055 m	1.842	2.185	DCS3
dc344	N37°04'20.00151"	W117°38'17.66026"	1085.735 m	0.700	0.629	DCS3
dc345	N37°04'19.98198"	W117°38'17.60075"	1086.763 m	0.704	0.635	DCS3
dc346	N37°04'19.95564"	W117°38'17.54941"	1088.079 m	0.713	0.648	DCS3
dc347	N37°04'19.94544"	W117°38'17.50884"	1088.330 m	0.714	0.654	DCS3
dc348	N37°04'19.92143"	W117°38'17.42956"	1089.350 m	0.721	0.666	DCS3
dc349	N37°04'19.90983"	W117°38'17.36589"	1089.813 m	0.729	0.680	DCS3
dc350	N37°04'19.89873"	W117°38'17.33199"	1089.856 m	0.741	0.699	DCS3

dc351	N37°04'19.89417"	W117°38'17.26869"	1090.013 m	0.741	0.651	DCS3
dc352	N37°04'19.88833"	W117°38'17.21663"	1090.226 m	0.798	0.733	DCS3
dc353	N37°04'19.86618"	W117°38'17.15803"	1090.424 m	0.642	0.622	DCS3
dc354	N37°04'19.86117"	W117°38'17.08933"	1090.599 m	0.869	0.709	DCS3
dc355	N37°04'19.86565"	W117°38'17.05401"	1090.664 m	0.353	0.328	DCS3
dc357	N37°04'20.70267"	W117°38'16.51860"	1090.750 m	0.060	0.029	DCS1B
dc358	N37°04'20.71965"	W117°38'16.54967"	1090.517 m	0.914	0.423	DCS1B
dc359	N37°04'20.72457"	W117°38'16.60048"	1090.366 m	0.429	0.230	DCS1B
dc360	N37°04'20.75725"	W117°38'16.63024"	1090.087 m	0.023	0.022	DCS1B
dc361	N37°04'20.78160"	W117°38'16.65627"	1089.946 m	0.067	0.030	DCS1B
dc362	N37°04'20.80027"	W117°38'16.68684"	1089.815 m	0.031	0.021	DCS1B
dc363	N37°04'20.81780"	W117°38'16.72016"	1089.567 m	0.054	0.067	DCS1B
dc364	N37°04'20.84843"	W117°38'16.76802"	1089.211 m	0.010	0.011	DCS1B
dc365	N37°04'20.84436"	W117°38'16.81255"	1088.893 m	0.010	0.009	DCS1B
dc366	N37°04'20.84867"	W117°38'16.84592"	1088.581 m	0.008	0.010	DCS1B
dc367	N37°04'20.86441"	W117°38'16.87614"	1088.245 m	0.007	0.010	DCS1B
dc368	N37°04'20.87750"	W117°38'16.90862"	1087.786 m	0.008	0.011	DCS1B
dc369	N37°04'20.87992"	W117°38'16.95809"	1087.175 m	0.008	0.011	DCS1B
dc370	N37°04'20.88031"	W117°38'16.99612"	1086.743 m	0.012	0.020	DCS1B
dc371	N37°04'20.87695"	W117°38'17.05373"	1086.050 m	0.012	0.021	DCS1B
dc372	N37°04'20.87963"	W117°38'17.11545"	1085.207 m	0.013	0.023	DCS1B
dc380	N37°04'41.89665"	W117°38'30.25903"	982.147 m	0.093	0.030	active stream
dc381	N37°04'41.13983"	W117°38'28.72804"	986.229 m	0.007	0.009	active stream
dc382	N37°04'39.87174"	W117°38'27.96982"	990.363 m	0.532	0.358	active stream
dc383	N37°04'38.42612"	W117°38'28.93978"	995.188 m	0.007	0.009	active stream
dc385	N37°04'37.05472"	W117°38'28.92735"	999.401 m	0.006	0.008	active stream
dc384	N37°04'35.69871"	W117°38'28.89417"	1003.727 m	0.006	0.008	active stream
dc386	N37°04'34.43951"	W117°38'28.36409"	1007.991 m	0.251	0.392	active stream
dc387	N37°04'33.25619"	W117°38'27.31871"	1013.046 m	0.034	0.068	active stream
dc388	N37°04'32.30621"	W117°38'26.08321"	1017.953 m	0.122	0.029	active stream
dc389	N37°04'30.93876"	W117°38'25.59531"	1022.567 m	1.703	1.446	active stream
dc391	N37°04'30.12172"	W117°38'24.34701"	1027.589 m	0.114	0.108	active stream
dc392	N37°04'29.56391"	W117°38'22.77230"	1032.528 m	0.007	0.008	active stream
dc393	N37°04'28.45403"	W117°38'21.95434"	1037.620 m	0.006	0.008	active stream
dc396	N37°04'27.45088"	W117°38'21.11026"	1042.691 m	0.008	0.010	active stream
dc397	N37°04'26.31821"	W117°38'20.52262"	1046.227 m	0.006	0.009	active stream
dc398	N37°04'25.18326"	W117°38'19.33294"	1050.742 m	0.007	0.010	active stream
dc399	N37°04'24.40651"	W117°38'18.24933"	1055.264 m	0.006	0.009	active stream
dc400	N37°04'23.95920"	W117°38'16.79713"	1058.700 m	0.014	0.024	active stream
dc401	N37°04'23.95989"	W117°38'16.79671"	1058.692 m	0.006	0.011	active stream
dc410	N37°04'23.95867"	W117°38'16.77143"	1058.790 m	0.028	0.029	active stream

dc411	N37°04'23.01137"	W117°38'15.58098"	1063.063 m	0.007	0.009	active stream
dc412	N37°04'22.11856"	W117°38'14.55450"	1067.093 m	0.006	0.010	active stream
dc413	N37°04'21.70135"	W117°38'13.10016"	1071.331 m	0.007	0.011	active stream
dc414	N37°04'21.46732"	W117°38'11.46628"	1075.172 m	0.006	0.010	active stream
dc415	N37°04'21.04921"	W117°38'09.95299"	1079.414 m	0.006	0.011	active stream
dc416	N37°04'20.67078"	W117°38'08.20584"	1083.145 m	0.006	0.011	active stream
dc417	N37°04'20.55305"	W117°38'07.03222"	1086.838 m	0.006	0.012	active stream
dc418	N37°04'20.72925"	W117°38'05.51382"	1090.993 m	0.010	0.023	active stream
dc419	N37°04'19.90859"	W117°38'04.79679"	1093.219 m	0.006	0.011	active stream
dc420	N37°04'20.19101"	W117°38'04.10826"	1097.834 m	0.036	0.548	active stream
dc421	N37°04'20.05431"	W117°38'04.33939"	1095.239 m	1.114	1.380	active stream
dc422	N37°04'20.31130"	W117°38'03.56979"	1098.753 m	0.055	0.216	active stream
dc423	N37°04'20.24528"	W117°38'03.08253"	1100.786 m	1.282	0.782	active stream
dc424	N37°04'20.18754"	W117°38'02.60938"	1101.998 m	1.100	0.325	active stream
dc425	N37°04'20.25632"	W117°38'02.25243"	1102.925 m	0.692	0.702	active stream
dc426	N37°04'20.23057"	W117°38'02.09164"	1104.547 m	0.017	0.009	active stream
dc427	N37°04'20.22982"	W117°38'01.43700"	1106.687 m	0.981	1.610	active stream
dc428	N37°04'20.27350"	W117°38'00.35335"	1110.655 m	0.337	0.113	active stream
dc429	N37°04'19.83972"	W117°37'59.83968"	1114.151 m	0.277	0.182	active stream
dc450	N37°04'21.25135"	W117°38'17.90385"	1077.543 m	0.006	0.010	DCS1A
dc451	N37°04'21.28640"	W117°38'18.00529"	1076.416 m	0.212	0.220	DCS1A
dc452	N37°04'21.31683"	W117°38'18.10332"	1075.198 m	1.096	0.901	DCS1A
dc253	N37°04'21.35450"	W117°38'18.14748"	1075.315 m	1.402	0.994	DCS1A
dc454	N37°04'21.35841"	W117°38'18.15821"	1075.579 m	0.361	0.205	DCS1A
dc455	N37°04'21.36885"	W117°38'18.20590"	1075.479 m	0.008	0.018	DCS1A
dc456	N37°04'21.37784"	W117°38'18.22505"	1075.426 m	0.017	0.021	DCS1A
dc457	N37°04'21.38331"	W117°38'18.24521"	1075.416 m	0.017	0.022	DCS1A
dc458	N37°04'21.38560"	W117°38'18.27184"	1075.402 m	0.049	0.032	DCS1A
dc460	N37°04'21.39367"	W117°38'18.29289"	1075.395 m	0.006	0.017	DCS1A
dc461	N37°04'21.39045"	W117°38'18.31560"	1075.368 m	0.006	0.017	DCS1A
dc462	N37°04'21.39498"	W117°38'18.33608"	1075.371 m	0.076	0.151	DCS1A
dc463	N37°04'19.72807"	W117°38'22.68760"	1059.661 m	0.037	0.140	DCS4
dc465	N37°04'19.69555"	W117°38'22.62824"	1059.799 m	0.038	0.046	DCS4
dc464	N37°04'19.68164"	W117°38'22.57856"	1059.758 m	0.135	0.089	DCS4
dc466	N37°04'19.65426"	W117°38'22.52520"	1060.206 m	0.199	0.088	DCS4
dc467	N37°04'19.63222"	W117°38'22.48103"	1060.547 m	0.196	0.107	DCS4
dc468	N37°04'19.60475"	W117°38'22.43395"	1060.718 m	0.060	0.038	DCS4
dc469	N37°04'19.58784"	W117°38'22.38386"	1060.917 m	0.059	0.038	DCS4
dc470	N37°04'19.56870"	W117°38'22.31801"	1061.084 m	0.084	0.066	DCS4
dc471	N37°04'19.54019"	W117°38'22.26348"	1061.244 m	0.121	0.102	DCS4
dc472	N37°04'19.50252"	W117°38'22.20899"	1061.473 m	0.135	0.122	DCS4

dc473	N37°04'19.46836"	W117°38'22.16169"	1061.818 m	0.018	0.018	DCS4
dc474	N37°04'19.43719"	W117°38'22.10897"	1062.136 m	0.007	0.010	DCS4
dc475	N37°04'19.39588"	W117°38'22.06343"	1062.630 m	0.007	0.009	DCS4
dc476	N37°04'19.37285"	W117°38'21.98972"	1063.086 m	0.570	0.619	DCS4
dc477	N37°04'19.34881"	W117°38'21.94125"	1063.627 m	0.008	0.009	DCS4
dc478	N37°04'19.32776"	W117°38'21.90374"	1064.162 m	0.060	0.053	DCS4
dc479	N37°04'19.30011"	W117°38'21.86580"	1064.796 m	0.008	0.008	DCS4
dc480	N37°04'19.27694"	W117°38'21.82565"	1065.493 m	0.007	0.008	DCS4
dc481	N37°04'19.25329"	W117°38'21.78762"	1066.066 m	0.008	0.008	DCS4
dc482	N37°04'19.23600"	W117°38'21.75756"	1066.593 m	0.007	0.008	DCS4
dc483	N37°04'19.20610"	W117°38'21.71460"	1067.323 m	0.008	0.008	DCS4
dc484	N37°04'19.18519"	W117°38'21.68286"	1067.863 m	0.045	0.052	DCS4
dc485	N37°04'19.18509"	W117°38'21.68306"	1067.870 m	0.007	0.008	DCS4
dc486	N37°04'19.16537"	W117°38'21.64277"	1068.334 m	0.008	0.009	DCS4
dc487	N37°04'19.14181"	W117°38'21.60927"	1068.869 m	0.008	0.009	DCS4
dc488	N37°04'19.09740"	W117°38'21.56935"	1069.254 m	0.008	0.010	DCS4
dc489	N37°04'19.06991"	W117°38'21.53461"	1069.472 m	0.008	0.010	DCS4
dc490	N37°04'19.05064"	W117°38'21.48984"	1069.683 m	0.008	0.010	DCS4
dc491	N37°04'19.02420"	W117°38'21.46456"	1069.836 m	0.008	0.011	DCS4
dc492	N37°04'19.00324"	W117°38'21.42761"	1069.990 m	0.008	0.012	DCS4
dc493	N37°04'18.97468"	W117°38'21.39134"	1070.240 m	0.011	0.018	DCS4
dc494	N37°04'18.94727"	W117°38'21.35536"	1070.545 m	0.012	0.021	DCS4
dc495	N37°04'18.90988"	W117°38'21.27954"	1071.382 m	0.011	0.021	DCS4
dc496	N37°04'18.85167"	W117°38'21.17671"	1072.458 m	0.019	0.030	DCS4
dc497	N37°04'18.80872"	W117°38'21.07820"	1073.077 m	0.011	0.022	DCS4
dc498	N37°04'18.79367"	W117°38'21.04594"	1073.260 m	0.010	0.023	DCS4
dc499	N37°04'18.76433"	W117°38'21.00104"	1073.464 m	0.010	0.024	DCS4
dc500	N37°04'18.73571"	W117°38'20.94919"	1073.656 m	0.009	0.023	DCS4
dc501	N37°04'18.71058"	W117°38'20.89103"	1073.858 m	0.008	0.023	DCS4
dc502	N37°04'18.69319"	W117°38'20.82672"	1074.054 m	0.203	0.112	DCS4
dc503	N37°04'18.66760"	W117°38'20.72074"	1074.277 m	0.007	0.020	DCS4
dc504	N37°04'18.63809"	W117°38'20.61376"	1074.549 m	0.007	0.018	DCS4
LS01	N37°04'19.21213"	W117°38'24.07904"	1052.268 m	1.092	2.017	
LS02	N37°04'19.19092"	W117°38'23.98517"	1052.473 m	0.174	0.083	
LS03	N37°04'19.19000"	W117°38'23.98475"	1052.470 m	0.003	0.007	
LS04	N37°04'19.17511"	W117°38'23.88216"	1052.783 m	0.004	0.007	
LS05	N37°04'19.12939"	W117°38'23.77349"	1053.158 m	0.003	0.006	
LS06	N37°04'19.10613"	W117°38'23.65073"	1053.659 m	0.951	1.136	
LS07	N37°04'19.06751"	W117°38'23.47254"	1054.207 m	0.003	0.007	
LS08	N37°04'19.04687"	W117°38'23.36251"	1054.514 m	0.006	0.010	
LS09	N37°04'18.99857"	W117°38'23.20326"	1054.944 m	0.003	0.006	

LS10	N37°04'18.96126"	W117°38'23.08715"	1055.355 m	0.003	0.005	
LS11	N37°04'18.93720"	W117°38'22.99468"	1055.744 m	0.004	0.007	
LS12	N37°04'18.89671"	W117°38'22.88415"	1056.196 m	0.003	0.005	
LS13	N37°04'18.87336"	W117°38'22.79351"	1056.666 m	0.004	0.005	
LS14	N37°04'18.83604"	W117°38'22.68544"	1057.373 m	0.003	0.004	
LS16	N37°04'18.82104"	W117°38'22.63195"	1057.875 m	0.003	0.004	
LS17	N37°04'18.79850"	W117°38'22.56835"	1058.536 m	0.003	0.004	
LS18	N37°04'18.77320"	W117°38'22.50642"	1059.272 m	0.003	0.004	
LS19	N37°04'18.73442"	W117°38'22.43024"	1060.373 m	0.004	0.004	
LS20	N37°04'18.70641"	W117°38'22.36155"	1061.359 m	0.004	0.004	
LS21	N37°04'18.68002"	W117°38'22.29622"	1062.378 m	0.004	0.004	
LS22	N37°04'18.65959"	W117°38'22.24170"	1063.225 m	0.004	0.004	
LS23	N37°04'18.63693"	W117°38'22.18565"	1064.023 m	0.004	0.004	
LS24	N37°04'18.61608"	W117°38'22.12690"	1064.831 m	0.004	0.004	
LS25	N37°04'18.59548"	W117°38'22.06735"	1065.580 m	0.004	0.004	
LS26	N37°04'18.56928"	W117°38'22.00563"	1066.278 m	0.004	0.004	
LS27	N37°04'18.54225"	W117°38'21.92102"	1067.202 m	0.790	0.483	
LS28	N37°04'18.52026"	W117°38'21.86738"	1067.206 m	0.004	0.005	
LS29	N37°04'18.49049"	W117°38'21.77367"	1067.613 m	0.004	0.006	
LS30	N37°04'18.46229"	W117°38'21.68396"	1067.974 m	0.004	0.006	
LS31	N37°04'18.44614"	W117°38'21.58269"	1068.153 m	0.004	0.006	
LS32	N37°04'18.43536"	W117°38'21.49091"	1068.421 m	0.004	0.006	
LS34	N37°04'18.42317"	W117°38'21.38259"	1068.620 m	0.004	0.006	
LS35	N37°04'18.40317"	W117°38'21.30748"	1068.686 m	0.004	0.006	
LS36	N37°04'18.35761"	W117°38'21.17425"	1068.835 m	0.004	0.007	
LS38	N37°04'18.34196"	W117°38'21.10803"	1069.015 m	0.004	0.007	

Deep Springs

Survey Point	Latitude	Longitude	Altitude (m)	Horizontal Precision (m)	Vertical Precision (m)	notes
ds35	N37°16'27.76543"	W118°04'45.37377"	1508.749 m	0.006	0.009	
ds36	N37°16'27.62549"	W118°04'45.23688"	1509.000 m	0.006	0.010	1509 m shoreline
ds37	N37°16'27.45542"	W118°04'45.08300"	1508.912 m	0.005	0.009	1509 m shoreline
ds38	N37°16'27.27610"	W118°04'45.03384"	1508.901 m	0.005	0.010	1509 m shoreline
ds39	N37°16'27.11715"	W118°04'44.88254"	1508.684 m	0.008	0.015	1509 m shoreline
ds40	N37°16'26.97098"	W118°04'44.75436"	1508.620 m	0.005	0.010	1509 m shoreline
ds41	N37°16'26.64704"	W118°04'44.51065"	1508.280 m	0.005	0.010	1509 m shoreline
ds42	N37°16'26.37201"	W118°04'44.22630"	1508.539 m	0.005	0.009	1509 m shoreline
ds43	N37°16'26.18718"	W118°04'44.04580"	1508.479 m	0.005	0.009	1509 m shoreline

ds44	N37°16'26.06787"	W118°04'43.87234"	1508.966 m	0.005	0.009	1509 m shoreline
ds45	N37°16'25.95370"	W118°04'43.72897"	1508.958 m	0.005	0.009	1509 m shoreline
ds46	N37°16'25.79426"	W118°04'43.59903"	1508.785 m	0.005	0.009	1509 m shoreline
ds47	N37°16'35.37284"	W118°04'51.27516"	1508.881 m	0.006	0.009	1509 m shoreline
ds48	N37°16'35.63074"	W118°04'51.51817"	1507.997 m	0.006	0.008	1509 m shoreline
ds49	N37°16'35.83652"	W118°04'51.61995"	1508.099 m	0.009	0.012	1509 m shoreline
ds50	N37°16'35.83663"	W118°04'51.62005"	1508.091 m	0.006	0.008	1509 m shoreline
ds51	N37°16'36.04541"	W118°04'51.72055"	1508.369 m	0.007	0.008	1509 m shoreline
ds52	N37°16'36.16738"	W118°04'51.82943"	1508.729 m	0.006	0.007	1509 m shoreline
ds53	N37°16'36.29065"	W118°04'51.92266"	1508.516 m	0.006	0.007	1509 m shoreline
ds54	N37°16'36.55554"	W118°04'52.04505"	1507.351 m	0.006	0.007	1509 m shoreline
ds55	N37°16'36.72919"	W118°04'52.17107"	1508.131 m	0.007	0.007	1509 m shoreline
ds56	N37°16'36.86144"	W118°04'52.26363"	1508.922 m	0.006	0.007	1509 m shoreline
ds57	N37°16'37.05915"	W118°04'52.36736"	1508.991 m	0.006	0.007	1509 m shoreline
ds58	N37°16'37.23156"	W118°04'52.44120"	1509.034 m	0.007	0.007	1509 m shoreline
ds59	N37°16'37.41302"	W118°04'52.55704"	1509.007 m	0.007	0.007	1509 m shoreline
ds60	N37°16'37.57982"	W118°04'52.69242"	1509.049 m	0.007	0.007	1509 m shoreline
ds61	N37°16'37.76272"	W118°04'52.79116"	1508.918 m	0.007	0.007	1509 m shoreline
ds62	N37°16'37.94594"	W118°04'52.85763"	1508.763 m	0.008	0.009	1509 m shoreline
ds63	N37°16'38.08114"	W118°04'52.94968"	1508.443 m	0.007	0.008	1509 m shoreline
ds65	N37°16'38.08115"	W118°04'52.94964"	1508.432 m	0.006	0.008	1509 m shoreline
ds66	N37°16'38.38989"	W118°04'53.19217"	1507.610 m	0.006	0.008	1509 m shoreline
ds67	N37°16'38.71288"	W118°04'53.36888"	1507.446 m	0.006	0.008	1509 m shoreline
ds68	N37°16'38.88485"	W118°04'53.43807"	1508.366 m	0.006	0.009	1509 m shoreline
ds69	N37°16'39.06148"	W118°04'53.53840"	1508.745 m	0.006	0.009	1509 m shoreline
ds70	N37°16'39.21633"	W118°04'53.63498"	1508.786 m	0.006	0.009	1509 m shoreline
ds71	N37°16'39.39888"	W118°04'53.74684"	1508.868 m	0.006	0.009	1509 m shoreline
ds72	N37°16'39.58886"	W118°04'53.85968"	1508.866 m	0.006	0.009	1509 m shoreline
ds73	N37°16'39.74819"	W118°04'54.00498"	1508.645 m	0.006	0.010	1509 m shoreline
ds74	N37°16'39.91371"	W118°04'54.01978"	1508.127 m	0.006	0.010	1509 m shoreline
ds75	N37°16'40.22628"	W118°04'54.23633"	1507.425 m	0.006	0.010	1509 m shoreline
ds76	N37°16'40.41208"	W118°04'54.28939"	1508.164 m	0.006	0.010	1509 m shoreline
ds77	N37°16'40.57639"	W118°04'54.40775"	1508.675 m	0.017	0.031	1509 m shoreline
ds80	N37°16'40.57652"	W118°04'54.39533"	1511.437 m	1.987	2.261	1509 m shoreline
ds81	N37°16'40.56205"	W118°04'54.40930"	1510.903 m	0.006	0.008	1509 m shoreline
ds82	N37°16'40.75535"	W118°04'54.41117"	1510.952 m	0.043	0.048	1509 m shoreline
ds83	N37°16'40.91992"	W118°04'54.54306"	1510.965 m	0.035	0.014	1509 m shoreline
ds84	N37°16'41.06697"	W118°04'54.62782"	1510.911 m	0.006	0.008	1509 m shoreline
ds85	N37°16'41.23238"	W118°04'54.63308"	1510.672 m	0.006	0.008	1509 m shoreline
ds86	N37°16'41.40520"	W118°04'54.67974"	1510.079 m	0.059	0.020	1509 m shoreline
ds87	N37°16'41.65681"	W118°04'54.71199"	1509.734 m	0.365	0.114	1509 m shoreline

ds88	N37°16'41.83200"	W118°04'54.72212"	1510.335 m	0.026	0.011	1509 m shoreline
ds89	N37°16'41.99904"	W118°04'54.77839"	1510.594 m	0.007	0.009	1509 m shoreline
ds90	N37°16'42.21924"	W118°04'54.79132"	1510.607 m	0.053	0.068	1509 m shoreline
ds91	N37°16'52.93651"	W118°04'53.55410"	1518.814 m	2.237	5.479	1509 m shoreline
ds92	N37°16'52.91172"	W118°04'53.54859"	1519.152 m	2.182	4.400	1509 m shoreline
ds93	N37°16'52.92326"	W118°04'53.54240"	1519.384 m	0.181	0.217	1509 m shoreline
ds94	N37°16'52.85099"	W118°04'53.63283"	1519.113 m	0.249	0.265	1509 m shoreline
ds95	N37°16'53.19574"	W118°04'53.16336"	1519.351 m	0.346	0.372	1509 m shoreline
ds96	N37°16'53.05946"	W118°04'53.39887"	1518.768 m	0.554	0.338	1509 m shoreline
ds97	N37°16'52.69223"	W118°04'53.79442"	1518.712 m	0.005	0.011	1509 m shoreline
ds98	N37°16'52.42875"	W118°04'53.97275"	1518.499 m	0.005	0.012	1509 m shoreline
ds99	N37°16'51.98351"	W118°04'54.34089"	1517.861 m	0.179	0.179	1509 m shoreline
ds100	N37°16'51.79322"	W118°04'54.46472"	1519.328 m	0.011	0.013	1509 m shoreline
ds101	N37°16'51.65916"	W118°04'54.63870"	1519.530 m	0.930	0.627	1509 m shoreline
ds102	N37°16'51.65723"	W118°04'54.64546"	1519.633 m	0.005	0.013	1509 m shoreline
ds104	N37°16'51.52041"	W118°04'54.76969"	1519.832 m	0.820	0.876	1509 m shoreline
ds105	N37°16'51.37900"	W118°04'54.89277"	1519.610 m	0.005	0.012	1509 m shoreline
ds107	N37°16'51.24107"	W118°04'55.03910"	1519.319 m	0.515	0.483	1509 m shoreline
ds106	N37°16'51.23897"	W118°04'55.03892"	1519.401 m	0.019	0.027	1509 m shoreline
ds103	N37°16'51.11846"	W118°04'55.13007"	1518.823 m	0.005	0.012	1509 m shoreline
ds108	N37°16'51.01007"	W118°04'55.27562"	1517.774 m	0.005	0.012	1509 m shoreline
ds109	N37°16'50.79795"	W118°04'55.48409"	1518.826 m	0.008	0.017	1509 m shoreline
ds110	N37°16'50.66178"	W118°04'55.55953"	1519.208 m	0.005	0.012	1509 m shoreline
ds111	N37°16'50.50601"	W118°04'55.72999"	1519.461 m	0.005	0.012	1509 m shoreline
ds112	N37°16'50.34192"	W118°04'55.85164"	1519.528 m	0.005	0.012	1509 m shoreline
ds113	N37°16'50.17140"	W118°04'55.94367"	1519.529 m	0.006	0.012	1509 m shoreline
ds114	N37°16'50.01849"	W118°04'56.04770"	1519.364 m	0.094	0.034	1509 m shoreline
ds115	N37°16'49.87816"	W118°04'56.19640"	1519.184 m	0.030	0.014	1509 m shoreline
ds116	N37°16'49.67630"	W118°04'56.36446"	1518.498 m	0.006	0.010	1509 m shoreline
ds117	N37°16'49.32138"	W118°04'56.59783"	1516.832 m	0.006	0.010	1509 m shoreline
ds118	N37°16'48.91611"	W118°04'56.88435"	1516.598 m	0.006	0.010	1509 m shoreline
ds119	N37°16'48.57720"	W118°04'57.20492"	1516.626 m	0.006	0.009	1509 m shoreline
ds120	N37°16'48.37534"	W118°04'57.27261"	1517.283 m	0.005	0.008	1509 m shoreline
ds121	N37°16'48.10476"	W118°04'57.38710"	1519.163 m	0.005	0.007	1509 m shoreline
ds122	N37°16'47.97775"	W118°04'57.48980"	1519.017 m	0.005	0.007	1509 m shoreline
ds123	N37°16'47.83302"	W118°04'57.60735"	1518.162 m	0.044	0.008	1509 m shoreline
ds124	N37°16'47.69341"	W118°04'57.76710"	1517.505 m	0.009	0.012	1509 m shoreline
ds125	N37°16'47.43837"	W118°04'57.85807"	1518.685 m	0.007	0.009	1509 m shoreline
ds126	N37°16'47.27352"	W118°04'57.92435"	1519.112 m	0.007	0.009	
ds127	N37°16'47.27391"	W118°04'57.92366"	1519.111 m	0.005	0.007	
ds128	N37°16'47.12315"	W118°04'58.03274"	1518.920 m	0.005	0.007	

ds129	N37°16'46.91974"	W118°04'58.17615"	1518.228 m	0.005	0.007	
ds130	N37°16'46.57468"	W118°04'58.32797"	1515.833 m	0.007	0.009	1519 m shoreline
ds131	N37°16'46.22533"	W118°04'58.37440"	1516.934 m	0.007	0.009	1519 m shoreline
ds132	N37°16'46.04964"	W118°04'58.49343"	1518.350 m	0.006	0.008	1519 m shoreline
ds133	N37°16'45.89747"	W118°04'58.68102"	1518.680 m	0.006	0.008	1519 m shoreline
ds134	N37°16'45.72626"	W118°04'58.83384"	1518.494 m	0.005	0.008	1519 m shoreline
ds135	N37°16'45.61232"	W118°04'59.02872"	1518.775 m	0.005	0.008	1519 m shoreline
ds136	N37°16'45.44476"	W118°04'59.16821"	1519.157 m	0.005	0.008	1519 m shoreline
ds137	N37°16'45.27630"	W118°04'59.24653"	1519.259 m	0.008	0.012	1519 m shoreline
ds138	N37°16'45.09604"	W118°04'59.33720"	1519.327 m	0.050	0.049	1519 m shoreline
ds139	N37°16'45.09556"	W118°04'59.33805"	1519.320 m	0.005	0.009	1519 m shoreline
ds140	N37°16'44.96872"	W118°04'59.49429"	1519.214 m	0.006	0.010	1519 m shoreline
ds141	N37°16'44.85352"	W118°04'59.60943"	1518.843 m	0.007	0.014	1519 m shoreline
ds142	N37°16'44.73429"	W118°04'59.76182"	1518.087 m	0.007	0.013	1519 m shoreline
ds150	N37°16'26.66186"	W118°04'54.18051"	1522.243 m	0.168	0.214	1519 m shoreline
ds151	N37°16'26.47455"	W118°04'54.01726"	1522.368 m	0.006	0.008	1519 m shoreline
ds152	N37°16'25.57404"	W118°04'53.22384"	1522.294 m	0.006	0.009	1519 m shoreline
ds153	N37°16'25.24125"	W118°04'52.85722"	1522.406 m	0.040	0.011	1519 m shoreline
ds154	N37°16'24.54311"	W118°04'50.70243"	1520.959 m	0.006	0.009	1519 m shoreline
ds155	N37°16'23.26748"	W118°04'49.50267"	1520.922 m	0.006	0.009	1519 m shoreline
ds156	N37°16'23.04816"	W118°04'49.29548"	1520.854 m	0.006	0.010	1519 m shoreline
ds157	N37°16'22.40458"	W118°04'48.88566"	1520.892 m	0.006	0.010	1519 m shoreline
ds158	N37°16'21.59781"	W118°04'47.82453"	1520.739 m	0.006	0.010	1519 m shoreline
ds159	N37°16'20.86093"	W118°04'45.91709"	1519.447 m	0.014	0.016	1519 m shoreline
ds160	N37°16'28.04763"	W118°04'54.27602"	1520.969 m	0.005	0.012	1519 m shoreline
ds161	N37°16'28.61502"	W118°04'55.96169"	1522.444 m	0.170	0.088	1519 m shoreline
ds162	N37°16'29.22346"	W118°04'56.19744"	1522.226 m	0.005	0.015	1519 m shoreline
ds163	N37°16'19.02885"	W118°04'57.16579"	1537.563 m	1.682	3.107	1519 m shoreline
ds164	N37°16'19.03942"	W118°04'57.17208"	1537.910 m	0.006	0.010	1519 m shoreline
ds165	N37°16'17.75999"	W118°04'57.55057"	1539.782 m	0.006	0.010	1519 m shoreline
ds166	N37°16'17.90131"	W118°04'57.71409"	1539.891 m	0.021	0.020	1519 m shoreline
ds167	N37°16'17.90186"	W118°04'57.71404"	1539.899 m	0.006	0.009	1519 m shoreline
ds168	N37°16'18.03808"	W118°04'57.90736"	1539.860 m	0.005	0.008	1519 m shoreline
ds169	N37°16'18.21586"	W118°04'58.04822"	1539.927 m	0.005	0.008	1519 m shoreline
ds170	N37°16'18.36337"	W118°04'58.22392"	1539.944 m	0.005	0.007	1519 m shoreline
ds171	N37°16'18.51546"	W118°04'58.37204"	1539.923 m	0.006	0.008	1519 m shoreline
ds172	N37°16'18.67741"	W118°04'58.52485"	1539.891 m	0.006	0.008	1519 m shoreline
174	N37°16'18.83505"	W118°04'58.63985"	1539.945 m	0.005	0.007	1519 m shoreline
ds173	N37°16'18.98658"	W118°04'58.78417"	1539.916 m	0.005	0.007	1519 m shoreline
ds175	N37°16'19.14094"	W118°04'58.90426"	1539.810 m	0.005	0.007	1519 m shoreline
ds177	N37°16'19.31737"	W118°04'59.01965"	1539.697 m	0.005	0.007	1519 m shoreline

ds176	N37°16'19.49058"	W118°04'59.12048"	1539.446 m	0.006	0.008	1519 m shoreline
ds178	N37°16'19.65299"	W118°04'59.22093"	1538.558 m	0.006	0.008	1519 m shoreline
ds180	N37°16'17.64451"	W118°04'57.31129"	1539.569 m	0.006	0.007	1519 m shoreline
ds181	N37°16'17.64456"	W118°04'57.31132"	1539.573 m	0.006	0.007	1519 m shoreline
ds182	N37°16'17.39744"	W118°04'57.08099"	1537.568 m	0.461	0.343	1519 m shoreline
ds185	N37°16'17.25082"	W118°04'56.91608"	1537.663 m	0.007	0.007	1519 m shoreline
ds183	N37°16'17.01543"	W118°04'56.67750"	1539.655 m	0.025	0.019	1519 m shoreline
ds184	N37°16'16.83973"	W118°04'56.54651"	1539.892 m	0.007	0.007	1519 m shoreline
ds186	N37°16'16.66275"	W118°04'56.38948"	1539.915 m	0.007	0.007	1521 m shoreline
ds187	N37°16'16.50417"	W118°04'56.23442"	1539.957 m	0.007	0.007	1521 m shoreline
ds188	N37°16'16.34816"	W118°04'56.07237"	1539.931 m	0.007	0.007	1521 m shoreline
ds189	N37°16'16.15780"	W118°04'55.97963"	1540.035 m	0.007	0.007	1521 m shoreline
ds190	N37°16'15.98579"	W118°04'55.87564"	1540.063 m	0.008	0.008	1521 m shoreline
ds191	N37°16'15.98760"	W118°04'55.87544"	1540.023 m	0.008	0.008	1521 m shoreline
ds192	N37°16'15.89168"	W118°04'55.67981"	1539.960 m	0.008	0.008	1521 m shoreline
ds193	N37°16'15.69760"	W118°04'55.52762"	1539.873 m	0.008	0.009	1521 m shoreline
ds194	N37°16'15.54548"	W118°04'55.38360"	1539.599 m	0.014	0.016	1521 m shoreline
ds196	N37°16'15.16087"	W118°04'55.17591"	1537.689 m	0.221	0.484	1521 m shoreline
ds195	N37°16'14.99161"	W118°04'54.56726"	1539.654 m	0.008	0.010	1521 m shoreline
ds197	N37°16'14.83137"	W118°04'54.39447"	1539.909 m	0.008	0.011	1521 m shoreline
ds198	N37°16'14.64879"	W118°04'54.24159"	1539.871 m	0.714	0.815	1521 m shoreline
ds199	N37°16'14.65030"	W118°04'54.24168"	1539.830 m	0.007	0.011	
ds200	N37°16'14.52149"	W118°04'54.08624"	1538.927 m	0.007	0.011	
ds201	N37°16'14.41790"	W118°04'53.93742"	1537.884 m	0.039	0.013	1540 m shoreline
ds202	N37°16'15.05468"	W118°04'53.11417"	1536.035 m	0.065	0.016	1540 m shoreline
ds203	N37°16'15.17188"	W118°04'53.27342"	1537.368 m	0.006	0.012	1540 m shoreline
ds204	N37°16'15.32972"	W118°04'53.42353"	1537.600 m	0.035	0.012	1540 m shoreline
ds205	N37°16'15.49483"	W118°04'53.58794"	1537.646 m	0.419	0.056	1540 m shoreline
ds206	N37°16'15.67685"	W118°04'53.72798"	1537.445 m	0.007	0.013	1540 m shoreline
ds207	N37°16'15.84681"	W118°04'53.87058"	1536.430 m	0.007	0.011	1540 m shoreline
ds208	N37°16'16.02806"	W118°04'54.06664"	1535.434 m	0.006	0.010	1540 m shoreline
ds209	N37°16'16.22140"	W118°04'54.15780"	1536.062 m	0.060	0.051	1540 m shoreline
ds210	N37°16'16.34489"	W118°04'54.33546"	1537.128 m	0.006	0.010	1540 m shoreline
ds211	N37°16'16.40629"	W118°04'54.56180"	1537.618 m	0.006	0.009	1540 m shoreline
ds212	N37°16'16.58758"	W118°04'54.67111"	1537.699 m	0.006	0.009	1540 m shoreline
ds213	N37°16'16.75908"	W118°04'54.81001"	1537.441 m	0.007	0.010	1540 m shoreline
ds214	N37°16'16.90191"	W118°04'54.98283"	1537.580 m	0.628	0.517	1540 m shoreline
ds215	N37°16'16.90066"	W118°04'54.98601"	1537.644 m	0.006	0.011	1540 m shoreline
ds216	N37°16'17.06415"	W118°04'55.15040"	1537.754 m	0.007	0.010	1540 m shoreline
ds217	N37°16'17.23627"	W118°04'55.31996"	1537.802 m	0.070	0.030	1540 m shoreline
ds218	N37°16'17.36698"	W118°04'55.49867"	1537.837 m	0.158	0.170	1540 m shoreline

ds219	N37°16'17.50233"	W118°04'55.67006"	1537.736 m	0.269	0.345	1540 m shoreline
ds220	N37°16'17.66662"	W118°04'55.80698"	1537.263 m	0.108	0.235	1540 m shoreline
ds221	N37°16'17.95608"	W118°04'56.15085"	1536.131 m	0.845	0.427	1540 m shoreline
ds222	N37°16'18.10247"	W118°04'56.27817"	1536.358 m	0.682	0.664	1540 m shoreline
ds223	N37°16'18.28884"	W118°04'56.40174"	1537.576 m	0.317	0.139	1540 m shoreline
ds224	N37°16'18.47227"	W118°04'56.56664"	1537.729 m	0.096	0.045	1540 m shoreline
ds225	N37°16'18.62243"	W118°04'56.76237"	1537.861 m	0.272	0.295	1540 m shoreline
ds226	N37°16'18.77746"	W118°04'56.88953"	1537.756 m	0.276	0.288	1540 m shoreline
ds227	N37°16'18.95930"	W118°04'57.09101"	1537.872 m	0.078	0.253	1540 m shoreline
ds228	N37°16'19.16123"	W118°04'57.21841"	1537.819 m	0.017	0.018	1540 m shoreline
ds229	N37°16'19.31658"	W118°04'57.46465"	1537.760 m	0.368	0.397	1540 m shoreline
ds230	N37°16'19.49682"	W118°04'57.59686"	1537.463 m	0.133	0.355	1540 m shoreline
ds231	N37°16'19.70193"	W118°04'57.65601"	1537.714 m	0.149	0.446	1540 m shoreline
ds232	N37°16'19.88191"	W118°04'57.75602"	1537.246 m	0.168	0.407	1540 m shoreline
ds233	N37°16'20.03874"	W118°04'57.87435"	1535.802 m	0.463	0.484	1540 m shoreline
ds234	N37°16'20.22212"	W118°04'58.18893"	1535.699 m	0.308	0.281	1540 m shoreline
ds235	N37°16'20.57982"	W118°04'58.48721"	1536.168 m	0.387	0.640	1540 m shoreline
ds236	N37°16'20.74621"	W118°04'58.79721"	1537.363 m	0.006	0.011	1540 m shoreline
ds237	N37°16'20.92214"	W118°04'58.95714"	1537.734 m	0.005	0.011	1538 m shoreline
ds238	N37°16'21.12714"	W118°04'59.11240"	1537.771 m	0.005	0.011	1538 m shoreline
ds239	N37°16'21.31551"	W118°04'59.22373"	1537.673 m	0.006	0.012	1538 m shoreline
ds240	N37°16'21.52524"	W118°04'59.35015"	1536.545 m	0.044	0.039	1538 m shoreline
ds241	N37°16'21.68893"	W118°04'59.67210"	1537.014 m	0.006	0.012	1538 m shoreline
ds242	N37°16'21.82913"	W118°04'59.81492"	1537.720 m	0.012	0.022	1538 m shoreline
ds243	N37°16'22.01925"	W118°04'59.93915"	1537.798 m	0.006	0.011	1538 m shoreline
ds244	N37°16'22.17957"	W118°05'00.06452"	1537.568 m	0.006	0.011	1538 m shoreline
ds245	N37°16'22.34316"	W118°05'00.19030"	1536.852 m	0.021	0.011	1538 m shoreline

Hanging Rock Canyon

Survey Point	Latitude	Longitude	Altitude (m)	Horizontal Precision (m)	Vertical Precision (m)
LO 02	N37°13'16.28644"	W117°44'51.40179"	1091.662 m	0.004	0.004
LO 03	N37°13'11.63519"	W117°44'52.53023"	1079.731 m	0.004	0.005
LO 04	N37°13'11.62706"	W117°44'52.35441"	1079.868 m	0.004	0.005
LO 05	N37°13'11.61304"	W117°44'52.15784"	1079.598 m	0.004	0.004
LO 06	N37°13'11.62081"	W117°44'51.95459"	1079.735 m	0.003	0.004
LO 07	N37°13'11.62851"	W117°44'51.72808"	1080.042 m	0.004	0.005
LO 08	N37°13'11.62537"	W117°44'51.66799"	1079.945 m	0.004	0.005
LO 09	N37°13'11.63213"	W117°44'51.43829"	1079.698 m	0.004	0.005

LO 10	N37°13'11.63539"	W117°44'51.38915"	1080.021 m	0.003	0.005
LO 11	N37°13'11.63599"	W117°44'51.34146"	1080.390 m	0.003	0.005
LO 12	N37°13'11.63201"	W117°44'51.30784"	1080.595 m	0.003	0.006
OL 01	N37°13'11.64791"	W117°44'51.25514"	1080.654 m	0.818	1.439
OL 02	N37°13'11.64581"	W117°44'51.24924"	1081.125 m	0.003	0.007
LO 13	N37°13'11.64100"	W117°44'51.20107"	1081.746 m	0.003	0.006
LO 14	N37°13'11.67047"	W117°44'51.07558"	1083.604 m	0.003	0.008
OL 03	N37°13'11.65788"	W117°44'51.12593"	1082.845 m	0.003	0.008
OL 04	N37°13'11.70367"	W117°44'50.91993"	1085.736 m	0.005	0.008
LO 15	N37°13'11.68406"	W117°44'51.00346"	1084.639 m	0.015	0.034
LO 16	N37°13'11.69543"	W117°44'50.84500"	1086.597 m	0.003	0.006
OL 08	N37°13'11.72993"	W117°44'50.76702"	1087.941 m	0.003	0.006
LO 17	N37°13'11.74892"	W117°44'50.71530"	1088.881 m	0.003	0.006
OL 09	N37°13'11.76402"	W117°44'50.64484"	1090.087 m	0.005	0.010
LO 18	N37°13'11.78464"	W117°44'50.60614"	1090.849 m	0.003	0.005
LO 19	N37°13'11.79683"	W117°44'50.52795"	1092.148 m	0.002	0.005
OL 10	N37°13'11.78706"	W117°44'50.55038"	1091.796 m	0.003	0.005
LO 20	N37°13'11.80364"	W117°44'50.50247"	1092.489 m	0.003	0.005
OL 11	N37°13'11.80647"	W117°44'50.43879"	1093.133 m	0.003	0.005
LO 21	N37°13'11.80580"	W117°44'50.47337"	1092.823 m	0.003	0.005
OL 12	N37°13'11.80943"	W117°44'50.40374"	1093.426 m	0.003	0.005
LO 22	N37°13'11.81186"	W117°44'50.37063"	1093.638 m	0.003	0.005
OL 13	N37°13'11.80689"	W117°44'50.31589"	1094.009 m	0.003	0.005
LO 23	N37°13'11.81362"	W117°44'50.27939"	1094.251 m	0.003	0.005
OL 14	N37°13'11.82320"	W117°44'50.21276"	1094.744 m	0.003	0.005
LO 24	N37°13'11.83525"	W117°44'50.17448"	1095.020 m	0.003	0.005
OL 15	N37°13'11.83714"	W117°44'50.10598"	1095.508 m	0.003	0.005
LO 25	N37°13'11.84325"	W117°44'50.05795"	1095.855 m	0.071	0.098
OL 16	N37°13'11.83467"	W117°44'49.98549"	1096.332 m	0.003	0.005
LO 26	N37°13'11.84456"	W117°44'49.92447"	1096.608 m	0.003	0.005
OL 17	N37°13'11.85138"	W117°44'49.82622"	1097.158 m	0.003	0.005
LO 27	N37°13'11.85060"	W117°44'49.72597"	1097.626 m	0.003	0.005
OL 18	N37°13'11.86882"	W117°44'49.62802"	1098.085 m	0.003	0.004
LO 28	N37°13'11.85689"	W117°44'49.48300"	1098.472 m	0.003	0.004
OL 19	N37°13'12.49004"	W117°44'48.24541"	1101.369 m	0.003	0.004
LO 29	N37°13'12.11799"	W117°44'48.90291"	1099.843 m	0.003	0.004
OL 20	N37°13'12.99165"	W117°44'47.28875"	1103.686 m	0.003	0.004
LO 30	N37°13'13.36755"	W117°44'46.45701"	1105.519 m	0.003	0.004
OL 21	N37°13'13.71033"	W117°44'45.69281"	1107.159 m	0.004	0.004
LO 31	N37°13'14.02121"	W117°44'45.09385"	1108.531 m	0.006	0.005
OL 22	N37°13'14.37947"	W117°44'44.49749"	1109.353 m	0.005	0.005

LO 32	N37°13'14.77939"	W117°44'43.82063"	1110.590 m	0.004	0.004
OL 23	N37°13'15.48835"	W117°44'42.50660"	1112.836 m	0.004	0.004
LO 33	N37°13'16.11393"	W117°44'41.35820"	1115.201 m	0.004	0.004
LO 34	N37°13'15.31666"	W117°44'40.03484"	1120.682 m	0.004	0.004
OL 24	N37°13'15.57394"	W117°44'40.78791"	1116.296 m	0.004	0.004
LO 35	N37°13'15.45610"	W117°44'39.22951"	1123.863 m	0.004	0.004
OL 25	N37°13'15.57821"	W117°44'37.94597"	1128.480 m	0.004	0.004
LO 36	N37°13'15.77261"	W117°44'36.58644"	1131.862 m	0.004	0.004
OL 26	N37°13'16.06471"	W117°44'35.43905"	1134.622 m	0.004	0.004
LO 37	N37°13'16.23680"	W117°44'34.14081"	1136.986 m	0.004	0.004
LO 38	N37°13'16.74964"	W117°44'32.23914"	1141.209 m	0.582	0.344
OL 28	N37°13'17.09002"	W117°44'31.21633"	1143.909 m	0.435	0.210
OL 29	N37°13'17.38493"	W117°44'29.85096"	1145.958 m	0.026	0.015
LO 39	N37°13'14.03993"	W117°44'28.96791"	1160.227 m	0.006	0.012
OL 30	N37°13'14.27876"	W117°44'28.10420"	1161.813 m	0.014	0.030
LO 40	N37°13'14.48687"	W117°44'26.60021"	1163.943 m	0.125	0.180
LO 41	N37°13'14.81598"	W117°44'25.40535"	1166.819 m	0.119	0.042
OL 31	N37°13'15.26669"	W117°44'24.25315"	1169.924 m	0.057	0.038
LO 42	N37°13'15.43436"	W117°44'23.07951"	1172.453 m	0.086	0.022
OL 32	N37°13'15.73376"	W117°44'22.11650"	1174.512 m	0.126	0.028
LO 43	N37°13'15.93330"	W117°44'20.95047"	1176.927 m	0.024	0.011
OL 33	N37°13'16.24873"	W117°44'20.35033"	1177.802 m	0.032	0.012
LO 44	N37°13'16.63954"	W117°44'19.24331"	1177.274 m	0.012	0.009
OL 34	N37°13'17.50667"	W117°44'17.33436"	1180.137 m	0.020	0.011
LO 45	N37°13'18.13854"	W117°44'16.81967"	1180.345 m	0.045	0.097
OL 35	N37°13'18.18947"	W117°44'16.40757"	1180.736 m	0.012	0.026
LO 46	N37°13'18.16368"	W117°44'16.66814"	1180.420 m	0.165	0.246
OL 36	N37°13'18.20679"	W117°44'16.01503"	1180.509 m	0.101	0.097
LO 47	N37°13'18.19274"	W117°44'15.87645"	1181.098 m	0.022	0.016
OL 37	N37°13'18.17935"	W117°44'15.75383"	1181.567 m	0.004	0.008
LO 48	N37°13'18.17400"	W117°44'15.61269"	1182.013 m	0.044	0.050
OL 38	N37°13'18.16406"	W117°44'15.52181"	1182.652 m	0.004	0.009
LO 49	N37°13'18.16119"	W117°44'15.30549"	1183.882 m	0.006	0.009
OL 39	N37°13'18.13605"	W117°44'15.14601"	1184.473 m	0.388	0.440
LO 50	N37°13'18.13110"	W117°44'15.02536"	1185.406 m	0.309	0.208
OL 40	N37°13'18.10234"	W117°44'14.91103"	1186.037 m	0.020	0.013
LO 51	N37°13'18.11604"	W117°44'14.75188"	1187.020 m	0.011	0.010
OL 41	N37°13'18.10672"	W117°44'14.67294"	1187.822 m	0.007	0.008
LO 52	N37°13'18.08767"	W117°44'14.59438"	1188.694 m	0.013	0.035
OL 42	N37°13'18.07051"	W117°44'14.52724"	1188.739 m	0.099	0.339
LO 53	N37°13'18.10431"	W117°44'14.42110"	1190.701 m	0.069	0.101

OL 43	N37°13'18.08921"	W117°44'14.33555"	1191.800 m	0.252	0.267
Lo 54 A	N37°13'18.10280"	W117°44'13.97903"	1194.800 m	0.091	0.086
LO 54B	N37°13'18.10339"	W117°44'14.22956"	1192.748 m	0.004	0.005
OL 44	N37°13'18.09708"	W117°44'14.09894"	1193.845 m	0.004	0.005
OL 45	N37°13'18.12087"	W117°44'13.78732"	1196.438 m	0.016	0.007
OL 55	N37°13'18.15147"	W117°44'13.70570"	1197.153 m	0.112	0.102
TB 1	N37°13'17.93737"	W117°44'13.58064"	1197.097 m	0.090	0.109
LO 56	N37°13'18.16571"	W117°44'13.60198"	1198.230 m	0.004	0.005
OL 47	N37°13'18.14465"	W117°44'13.11818"	1203.406 m	0.004	0.005
LO 57	N37°13'18.17576"	W117°44'13.52669"	1198.924 m	0.051	0.035
OL 46	N37°13'18.17432"	W117°44'13.32091"	1201.570 m	0.512	0.346
LO 58	N37°13'18.07124"	W117°44'13.23590"	1206.470 m	0.830	1.014
OL 47	N37°13'18.14465"	W117°44'13.11818"	1203.406 m	0.004	0.005
LO 59	N37°13'18.18015"	W117°44'13.02012"	1204.262 m	0.004	0.004
OL 48	N37°13'18.15762"	W117°44'12.92266"	1205.148 m	0.004	0.005
LO 60	N37°13'18.17395"	W117°44'12.81966"	1206.019 m	0.004	0.005
OL 49	N37°13'18.16392"	W117°44'12.71774"	1206.952 m	0.004	0.005
LO 61	N37°13'18.15965"	W117°44'12.60342"	1207.923 m	0.016	0.016
LO 62	N37°13'18.16856"	W117°44'12.48697"	1209.045 m	0.004	0.005
LO 63	N37°13'18.12567"	W117°44'12.29449"	1211.051 m	0.052	0.035
IOL 59	N37°13'18.15972"	W117°44'12.38704"	1210.073 m	0.004	0.005
OL 50	N37°13'18.11587"	W117°44'12.18825"	1212.234 m	0.004	0.005
LO65	N37°13'18.09004"	W117°44'12.06899"	1213.515 m	0.004	0.005
LO66	N37°13'18.06779"	W117°44'11.93508"	1215.024 m	0.004	0.005
OL 51	N37°13'18.05476"	W117°44'11.83844"	1216.049 m	0.004	0.005
LO 67	N37°13'18.06943"	W117°44'11.72998"	1217.440 m	0.004	0.005
OL 52	N37°13'18.05072"	W117°44'11.62710"	1218.657 m	0.004	0.005
LO 68	N37°13'18.06061"	W117°44'11.50825"	1220.026 m	0.004	0.005
OL 53	N37°13'18.05744"	W117°44'11.43052"	1220.993 m	0.004	0.005
LO 69	N37°13'18.04850"	W117°44'11.28113"	1222.661 m	0.004	0.005
LO 70	N37°13'18.03112"	W117°44'11.04500"	1225.175 m	0.004	0.006
OL 54	N37°13'18.01328"	W117°44'11.16937"	1224.039 m	0.005	0.007
LO 71	N37°13'18.03921"	W117°44'10.89317"	1226.669 m	0.004	0.006
OL 55	N37°13'18.01878"	W117°44'10.77104"	1227.957 m	0.029	0.020
LO 73	N37°13'18.05075"	W117°44'10.59436"	1229.477 m	0.004	0.005
OL 56	N37°13'18.05755"	W117°44'10.47386"	1230.543 m	0.005	0.008
LO74	N37°13'18.00579"	W117°44'10.33465"	1231.704 m	0.005	0.007
OL 57	N37°13'18.04053"	W117°44'10.19792"	1232.695 m	0.004	0.005
LO 75	N37°13'18.04120"	W117°44'10.03108"	1233.701 m	0.037	0.016
OL 58	N37°13'18.07816"	W117°44'09.73197"	1235.620 m	0.041	0.018
LLO 75	N37°13'18.08141"	W117°44'09.48326"	1237.125 m	0.005	0.007

OL 59	N37°13'18.09912"	W117°44'09.22216"	1238.838 m	0.018	0.008
LO 76	N37°13'18.12965"	W117°44'08.94658"	1240.524 m	0.076	0.039
OL 60	N37°13'18.16071"	W117°44'08.66433"	1242.234 m	0.004	0.005
LO77	N37°13'18.17004"	W117°44'08.38969"	1243.983 m	0.104	0.126
?	N37°13'18.22525"	W117°44'08.19336"	1245.141 m	0.004	0.005
LO78	N37°13'18.27003"	W117°44'07.96544"	1246.679 m	0.043	0.064
LO 79	N37°13'18.18693"	W117°44'07.66367"	1248.144 m	0.305	0.659
LO 80	N37°13'18.04595"	W117°44'07.11796"	1249.138 m	0.004	0.004
LO 81	N37°13'17.94386"	W117°44'06.73075"	1250.553 m	0.004	0.005
LO 82	N37°13'17.87386"	W117°44'06.37793"	1251.671 m	0.004	0.006
LO 83	N37°13'17.84531"	W117°44'06.25004"	1252.394 m	0.004	0.004
LO 84	N37°13'17.80325"	W117°44'06.05058"	1253.646 m	0.004	0.004
LO 85	N37°13'17.77212"	W117°44'05.82143"	1255.180 m	0.028	0.043
LO 86	N37°13'17.74178"	W117°44'05.55689"	1257.043 m	0.004	0.005
LO 87	N37°13'17.73171"	W117°44'05.41239"	1258.060 m	0.004	0.005
OL 100	N37°12'40.94368"	W117°45'04.84470"	1009.419 m	0.003	0.005
OL 101	N37°12'40.96059"	W117°45'04.71956"	1009.907 m	0.003	0.005
OL 102	N37°12'41.00277"	W117°45'04.22120"	1009.936 m	0.003	0.005
OL 103	N37°12'41.06091"	W117°45'03.89917"	1010.697 m	0.007	0.011
OL 104	N37°12'41.69082"	W117°45'03.93641"	1013.236 m	0.003	0.004
OL 105	N37°12'41.51431"	W117°45'04.75057"	1011.905 m	0.003	0.004
OL 106	N37°12'41.72545"	W117°45'03.58484"	1014.130 m	0.003	0.004
OL 107	N37°12'41.73571"	W117°45'03.47846"	1014.902 m	0.003	0.004
OL 108	N37°12'41.77731"	W117°45'03.35862"	1016.373 m	0.004	0.004
OL 110	N37°12'41.80290"	W117°45'03.25404"	1017.668 m	0.004	0.004
OL 111	N37°12'41.83703"	W117°45'03.14719"	1019.344 m	0.004	0.004
OL 112	N37°12'41.87484"	W117°45'03.01859"	1021.088 m	0.004	0.004
OL 113	N37°12'41.89325"	W117°45'02.92715"	1022.463 m	0.004	0.004
OL 14	N37°12'41.90924"	W117°45'02.82655"	1023.912 m	0.004	0.004
OL 115	N37°12'41.92715"	W117°45'02.75222"	1024.957 m	0.004	0.004
OL 116	N37°12'41.93482"	W117°45'02.70566"	1025.582 m	0.004	0.004
LP 01	N37°12'41.94027"	W117°45'02.65230"	1026.138 m	0.004	0.004
OL 117	N37°12'41.95797"	W117°45'02.43423"	1027.064 m	0.004	0.004
LP 02	N37°12'41.95088"	W117°45'02.51992"	1026.826 m	0.004	0.004
OL 118	N37°12'41.95797"	W117°45'02.43423"	1027.064 M	0.004	0.004
LP 03	N37°12'41.95898"	W117°45'02.35348"	1027.191 m	0.004	0.004
OL 119	N37°12'41.99198"	W117°45'02.24861"	1027.417 m	0.004	0.004
LP 04	N37°12'42.01467"	W117°45'02.19490"	1027.555 m	0.004	0.004
OL 120	N37°12'42.04385"	W117°45'02.02958"	1027.738 m	0.004	0.004
LP 05	N37°12'42.05724"	W117°45'01.90619"	1027.793 m	0.004	0.005
?	N37°12'42.06896"	W117°45'01.70750"	1028.018 m	0.004	0.006

LP 06	N37°12'42.05874"	W117°45'01.58220"	1027.975 m	0.004	0.005
LQ01	N37°13'17.67646"	W117°44'05.49299"	1256.838 m	0.003	0.006
LQ02	N37°13'17.66487"	W117°44'05.38145"	1257.474 m	0.004	0.010
LQ03	N37°13'17.63852"	W117°44'05.23399"	1258.240 m	0.004	0.009
LQ04	N37°13'17.60086"	W117°44'05.01868"	1259.560 m	0.004	0.009
LQ05	N37°13'17.56001"	W117°44'04.85746"	1260.628 m	0.004	0.009
LQ06	N37°13'17.51927"	W117°44'04.64980"	1261.894 m	0.004	0.010
LQ07	N37°13'17.49221"	W117°44'04.45592"	1262.958 m	0.004	0.010
LQ08	N37°13'17.43034"	W117°44'04.30165"	1263.956 m	0.003	0.010
LQ09	N37°13'17.39465"	W117°44'04.08072"	1265.215 m	0.003	0.010
LQ10	N37°13'17.35113"	W117°44'03.91223"	1266.221 m	0.003	0.010
LQ11	N37°13'17.24713"	W117°44'03.60321"	1267.610 m	0.003	0.009
LQ12	N37°13'17.14301"	W117°44'03.31506"	1268.825 m	0.003	0.008
LQ13	N37°13'17.08816"	W117°44'03.11288"	1269.553 m	0.003	0.008
LQ14	N37°13'17.01480"	W117°44'02.99032"	1269.895 m	0.061	0.133
LQ15	N37°13'16.93323"	W117°44'02.86814"	1270.335 m	0.004	0.008
LQ16	N37°13'16.84055"	W117°44'02.72544"	1270.806 m	0.004	0.008
LQ17	N37°13'16.72870"	W117°44'02.57487"	1271.536 m	0.004	0.008
LQ18	N37°13'16.62655"	W117°44'02.40892"	1272.407 m	0.004	0.008
LQ19	N37°13'16.52686"	W117°44'02.24813"	1272.935 m	0.004	0.007
LQ20	N37°13'16.45450"	W117°44'02.08181"	1273.631 m	0.004	0.007
LQ21	N37°13'16.38081"	W117°44'01.87952"	1274.300 m	0.004	0.007
LQ22	N37°13'16.30187"	W117°44'01.67970"	1275.049 m	0.004	0.007
LQ23	N37°13'16.25371"	W117°44'01.54520"	1275.668 m	0.004	0.006
LQ24	N37°13'16.20315"	W117°44'01.41041"	1276.433 m	0.004	0.005
LQ25	N37°13'16.17805"	W117°44'01.34494"	1276.796 m	0.004	0.005
LQ26	N37°13'16.13837"	W117°44'01.21780"	1277.496 m	0.004	0.005
LQ27	N37°13'16.07978"	W117°44'01.08189"	1278.246 m	0.004	0.005
LQ28	N37°13'15.99767"	W117°44'00.93242"	1279.123 m	0.004	0.005
LQ29	N37°13'15.92312"	W117°44'00.79176"	1279.817 m	0.004	0.005
LQ30	N37°13'15.76199"	W117°44'00.48845"	1281.259 m	0.004	0.005
LQ31	N37°13'15.58184"	W117°44'00.22613"	1280.951 m	0.004	0.005
LQ32	N37°13'15.40687"	W117°43'59.93070"	1280.813 m	0.004	0.005
LA33	N37°13'15.26948"	W117°43'59.55755"	1280.003 m	0.004	0.005
LQ34	N37°13'15.15848"	W117°43'59.23664"	1278.708 m	0.004	0.005
LQ35	N37°13'15.03227"	W117°43'58.81487"	1277.406 m	0.005	0.010
LQ36	N37°13'14.91941"	W117°43'58.40024"	1276.420 m	0.004	0.005
LQ37	N37°13'14.66224"	W117°43'57.35655"	1273.863 m	0.004	0.005
LQ38	N37°13'14.52823"	W117°43'56.79860"	1272.872 m	0.004	0.006
LQ39	N37°13'14.39729"	W117°43'56.24563"	1271.868 m	0.006	0.009
LQ40	N37°13'14.02245"	W117°43'55.07425"	1270.019 m	0.004	0.005

OL201a	N37°13'23.55398"	W117°43'54.41044"	1257.404 m	0.004	0.006
OL201b	N37°13'23.55414"	W117°43'54.41048"	1257.409 m	0.004	0.005
OL202	N37°13'23.44128"	W117°43'53.65558"	1259.834 m	0.004	0.004
OL203	N37°13'23.42470"	W117°43'53.16415"	1261.004 m	0.004	0.004
OL204	N37°13'23.30354"	W117°43'52.73063"	1262.896 m	0.004	0.005
OL205	N37°13'23.18535"	W117°43'52.29851"	1263.988 m	0.004	0.004
OL206	N37°13'23.07204"	W117°43'51.80479"	1264.856 m	0.004	0.005
OL207	N37°13'23.02419"	W117°43'51.36105"	1265.624 m	0.004	0.006
OL208A	N37°13'22.95399"	W117°43'50.44627"	1266.458 m	0.071	0.055
OL208B	N37°13'22.95422"	W117°43'50.44439"	1266.445 m	0.002	0.005
OL210	N37°13'22.89497"	W117°43'49.95993"	1266.899 m	0.002	0.005
OL211	N37°13'22.87249"	W117°43'49.50708"	1267.916 m	0.002	0.005
OL212	N37°13'22.84389"	W117°43'49.08546"	1268.761 m	0.002	0.005
OL213	N37°13'22.78683"	W117°43'48.50737"	1269.344 m	0.002	0.005
ol214	N37°13'22.72482"	W117°43'47.74430"	1270.429 m	0.002	0.005
ol215	N37°13'22.73077"	W117°43'46.92831"	1272.393 m	0.003	0.005
ol216	N37°13'22.77618"	W117°43'46.09135"	1274.400 m	0.003	0.005
ol217	N37°13'22.72475"	W117°43'45.13009"	1276.561 m	0.003	0.006
ol218	N37°13'22.67703"	W117°43'44.23632"	1278.816 m	0.003	0.006
ol219	N37°13'22.63757"	W117°43'43.40717"	1280.964 m	0.003	0.006
ol220	N37°13'22.64494"	W117°43'42.39102"	1282.440 m	0.003	0.005
ol221	N37°13'22.69748"	W117°43'41.54396"	1283.250 m	0.003	0.005
ol222	N37°13'22.77699"	W117°43'40.57911"	1284.404 m	0.003	0.006
ol223	N37°13'22.93485"	W117°43'39.34866"	1285.806 m	0.004	0.006
ol224	N37°13'18.95929"	W117°43'38.23655"	1275.458 m	0.021	0.035
ol225	N37°13'19.08057"	W117°43'37.61485"	1277.141 m	0.003	0.004
ol226	N37°13'19.47120"	W117°43'36.57608"	1279.773 m	0.004	0.005
ol228	N37°13'19.97482"	W117°43'35.26083"	1283.587 m	0.037	0.019
ol229	N37°13'20.21540"	W117°43'34.39378"	1285.892 m	0.004	0.004
ol230	N37°13'20.63960"	W117°43'33.53669"	1288.228 m	0.004	0.004
ol331	N37°13'21.03042"	W117°43'32.42068"	1291.123 m	0.004	0.004
ol232	N37°13'20.86348"	W117°43'31.49263"	1293.250 m	0.004	0.004
ol233	N37°13'20.84702"	W117°43'30.57363"	1295.609 m	0.004	0.004
ol234	N37°13'20.81186"	W117°43'29.53293"	1298.216 m	0.004	0.005
ol235	N37°13'20.74474"	W117°43'28.52710"	1300.730 m	0.007	0.006
ol236	N37°13'23.96715"	W117°43'27.56369"	1303.613 m	0.004	0.004
ol237	N37°13'23.86984"	W117°43'26.76382"	1306.073 m	0.004	0.004
o238	N37°13'23.50983"	W117°43'25.92673"	1308.528 m	0.004	0.004
ol239	N37°13'23.43094"	W117°43'25.38733"	1310.186 m	0.004	0.004
ol240	N37°13'23.12645"	W117°43'24.50071"	1312.767 m	0.004	0.005
ol241	N37°13'22.91320"	W117°43'23.58744"	1315.573 m	0.004	0.006

?	N37°13'22.64164"	W117°43'22.78016"	1320.229 m	1.367	1.567
ol238	N37°13'22.37535"	W117°43'21.44937"	1322.515 m	0.034	0.013
ol243	N37°13'22.00872"	W117°43'20.84168"	1324.684 m	0.004	0.007
ol244	N37°13'20.14448"	W117°43'20.60496"	1326.059 m	0.004	0.006
ol245	N37°13'20.07843"	W117°43'20.42556"	1327.698 m	0.004	0.005
ol246	N37°13'20.05416"	W117°43'20.27251"	1329.139 m	0.004	0.005
ol247	N37°13'20.04391"	W117°43'20.08587"	1330.928 m	0.004	0.005
ol248	N37°13'19.98842"	W117°43'19.89535"	1332.897 m	0.004	0.006
ol249	N37°13'19.91517"	W117°43'19.75028"	1334.242 m	0.008	0.021
?	N37°13'19.84916"	W117°43'19.57217"	1336.133 m	0.043	0.012
lr03	N37°13'23.41428"	W117°43'53.33444"	1260.583 m	0.004	0.006
lr04	N37°13'23.36116"	W117°43'52.95717"	1262.082 m	0.004	0.005
lr05	N37°13'23.24512"	W117°43'52.52173"	1263.232 m	0.004	0.004
lr06	N37°13'23.14164"	W117°43'52.04123"	1264.506 m	0.004	0.005
lr07	N37°13'23.02761"	W117°43'51.59683"	1265.261 m	0.004	0.005
lr08	N37°13'23.01412"	W117°43'51.14740"	1265.773 m	0.004	0.006
lr09	N37°13'22.98026"	W117°43'50.66993"	1266.129 m	0.002	0.005
lr10	N37°13'22.92787"	W117°43'50.17859"	1266.568 m	0.002	0.005
lr11	N37°13'22.88647"	W117°43'49.74700"	1267.256 m	0.002	0.005
lr12	N37°13'22.86035"	W117°43'49.29098"	1268.280 m	0.002	0.005
lr13	N37°13'22.82585"	W117°43'48.87563"	1268.846 m	0.002	0.005
lr15	N37°13'22.74171"	W117°43'48.08796"	1270.073 m	0.002	0.005
lr16	N37°13'22.74587"	W117°43'47.32075"	1271.361 m	0.002	0.005
lr17	N37°13'22.76388"	W117°43'46.52995"	1273.307 m	0.003	0.005
lr18	N37°13'22.72066"	W117°43'45.64965"	1275.388 m	0.002	0.005
lr19	N37°13'22.64518"	W117°43'44.70801"	1277.679 m	0.003	0.006
lr20	N37°13'22.63507"	W117°43'43.83734"	1280.035 m	0.003	0.006
lr21	N37°13'22.60864"	W117°43'42.88826"	1281.961 m	0.003	0.006
lr22	N37°13'22.63691"	W117°43'41.95799"	1282.872 m	0.003	0.005
lr23	N37°13'22.70455"	W117°43'41.07347"	1283.775 m	0.004	0.007
lr24	N37°13'22.78534"	W117°43'40.07457"	1285.379 m	0.004	0.006
lr26	N37°13'22.88200"	W117°43'39.63809"	1286.020 m	0.004	0.006
lr27	N37°13'18.87301"	W117°43'38.75382"	1273.871 m	0.406	0.584
lr28	N37°13'19.17733"	W117°43'37.10729"	1278.361 m	0.005	0.006
lr29	N37°13'19.57708"	W117°43'36.08481"	1280.980 m	0.004	0.004
lr30	N37°13'19.77075"	W117°43'35.64595"	1282.227 m	0.005	0.006
lr31	N37°13'20.10829"	W117°43'34.82676"	1284.824 m	0.004	0.004
lr32	N37°13'20.40792"	W117°43'33.98495"	1287.001 m	0.004	0.004
lr33	N37°13'20.80083"	W117°43'33.03438"	1289.459 m	0.004	0.004
lr34	N37°13'20.91609"	W117°43'32.01053"	1292.072 m	0.004	0.004
lr35	N37°13'20.82546"	W117°43'30.96259"	1294.582 m	0.004	0.005

lr36	N37°13'20.81436"	W117°43'30.06117"	1296.983 m	0.004	0.005
lr37	N37°13'20.80241"	W117°43'29.03876"	1299.399 m	0.005	0.005
lr38	N37°13'20.63001"	W117°43'27.99868"	1302.018 m	0.004	0.004
lr39	N37°13'23.90211"	W117°43'27.29029"	1304.522 m	0.004	0.004
lr40	N37°13'23.66771"	W117°43'26.29107"	1307.447 m	0.004	0.004
lr41	N37°13'23.30828"	W117°43'24.96807"	1311.346 m	0.004	0.005
lr42	N37°13'23.02470"	W117°43'24.08791"	1314.043 m	0.011	0.013
lr44	N37°13'22.75877"	W117°43'23.19528"	1316.838 m	0.004	0.007
lr45	N37°13'22.58215"	W117°43'22.32698"	1319.658 m	0.009	0.008
lr46	N37°13'22.44771"	W117°43'21.86554"	1321.139 m	0.004	0.007
lr47	N37°13'22.19736"	W117°43'21.03089"	1323.961 m	0.004	0.014
lr48	N37°13'21.93241"	W117°43'20.52332"	1325.807 m	0.004	0.007
lr49	N37°13'20.13218"	W117°43'20.68211"	1325.355 m	0.004	0.005
lr50	N37°13'20.09602"	W117°43'20.50296"	1326.982 m	0.004	0.005
lr51	N37°13'20.07045"	W117°43'20.34096"	1328.429 m	0.004	0.005
lr53	N37°13'20.04618"	W117°43'20.16569"	1330.195 m	0.004	0.005
lr55	N37°13'20.01043"	W117°43'19.98565"	1331.952 m	0.004	0.005
lr56	N37°13'19.95327"	W117°43'19.81950"	1333.974 m	0.354	0.395
lr57	N37°13'19.86173"	W117°43'19.65275"	1335.274 m	0.004	0.007
lr58	N37°13'19.78109"	W117°43'19.48888"	1336.901 m	0.004	0.005
lr59	N37°13'19.70418"	W117°43'19.37793"	1338.023 m	0.004	0.005
lr60	N37°13'19.65135"	W117°43'19.26205"	1339.139 m	0.004	0.006
lr61	N37°13'19.62512"	W117°43'19.12760"	1340.241 m	0.011	0.008
lr62	N37°13'19.57596"	W117°43'18.95917"	1341.440 m	0.004	0.005
lr64	N37°13'19.54921"	W117°43'18.79851"	1342.710 m	0.004	0.005
lr65	N37°13'19.50042"	W117°43'18.61034"	1343.881 m	0.004	0.005
lr67	N37°13'19.51139"	W117°43'18.38256"	1344.888 m	0.004	0.006
lr66	N37°13'19.51438"	W117°43'18.30169"	1345.153 m	0.004	0.005
lr68	N37°13'19.51395"	W117°43'18.18635"	1345.441 m	0.004	0.005
lr69	N37°13'19.53120"	W117°43'18.03571"	1345.622 m	0.004	0.006
lr70	N37°13'19.51076"	W117°43'17.90090"	1345.831 m	0.004	0.006
lr71	N37°13'19.29229"	W117°43'17.73463"	1347.377 m	0.004	0.006
lr72	N37°13'19.04977"	W117°43'17.53359"	1348.765 m	0.004	0.005
lr74	N37°13'18.84660"	W117°43'17.39229"	1350.158 m	0.004	0.005
lr75	N37°13'18.61660"	W117°43'17.12084"	1351.649 m	0.004	0.005
lr76	N37°13'18.35626"	W117°43'16.83592"	1353.382 m	0.004	0.005
lr77	N37°13'18.10623"	W117°43'16.57981"	1355.488 m	0.062	0.026
lr78	N37°13'17.78281"	W117°43'16.31007"	1358.066 m	0.004	0.006
lr79	N37°13'17.59168"	W117°43'16.04680"	1359.768 m	0.005	0.007
lr80	N37°13'17.29012"	W117°43'15.61778"	1362.363 m	0.004	0.005
lr81	N37°13'16.96363"	W117°43'15.20887"	1364.614 m	0.004	0.005

lr82	N37°13'16.61125"	W117°43'14.68486"	1369.229 m	0.004	0.005
lr83	N37°13'16.26748"	W117°43'14.23757"	1371.107 m	0.004	0.005
lr84	N37°13'15.98574"	W117°43'13.86797"	1371.107 m	0.004	0.005
lr85	N37°13'15.60994"	W117°43'13.49024"	1372.135 m	0.004	0.006
lr86	N37°13'15.57100"	W117°43'13.39143"	1372.311 m	0.005	0.011
lr87	N37°13'15.54019"	W117°43'13.31228"	1372.287 m	0.004	0.005
lr88	N37°13'15.48508"	W117°43'13.20884"	1372.171 m	0.004	0.005
lr89	N37°13'15.45213"	W117°43'13.07875"	1371.981 m	0.154	0.153
lr90	N37°13'15.41574"	W117°43'12.97113"	1371.625 m	0.004	0.005
lr91	N37°13'15.41271"	W117°43'12.88422"	1371.478 m	0.004	0.005
lr92	N37°13'15.39940"	W117°43'12.82507"	1371.382 m	0.004	0.005
lr93	N37°13'15.37594"	W117°43'12.73238"	1371.345 m	0.003	0.005
lr94	N37°13'15.34491"	W117°43'12.60338"	1371.359 m	0.004	0.006
lr95	N37°13'15.32246"	W117°43'12.49322"	1371.472 m	0.003	0.005
lr96	N37°13'15.28928"	W117°43'12.26132"	1371.958 m	0.003	0.006
lr97	N37°13'15.24220"	W117°43'12.00625"	1372.854 m	0.003	0.005
lr98	N37°13'15.18468"	W117°43'11.76274"	1373.730 m	0.003	0.006
lr99	N37°13'15.16831"	W117°43'11.56545"	1374.258 m	0.239	0.206
lr100	N37°13'30.99114"	W117°43'22.52576"	1281.751 m	0.003	0.007
lr101	N37°13'30.71158"	W117°43'24.04638"	1278.642 m	0.003	0.006
lr102	N37°13'30.95631"	W117°43'25.48081"	1275.887 m	0.013	0.008
lr103	N37°13'30.80604"	W117°43'30.20767"	1266.442 m	0.178	0.376
lr104A	N37°13'29.77565"	W117°43'36.28963"	1253.621 m	0.394	0.715
LR104B	N37°13'28.60576"	W117°43'42.70853"	1239.932 m	0.047	0.079
base	N37°13'14.41353"	W117°44'51.43758"	1086.810 m	0.001	0.001

Paleolake

Survey Point	Latitude	Longitude	Altitude (m)	Horizontal Precision (m)	Vertical Precision (m)
pl01	N37°06'17.22462"	W117°41'07.76937"	849.699 m	0.005	0.014
PL02	N37°06'18.07625"	W117°41'10.74020"	849.692 m	0.005	0.012
PL04	N37°06'19.83458"	W117°41'16.51253"	849.620 m	0.006	0.012
PL05	N37°06'20.80127"	W117°41'19.52624"	849.623 m	0.006	0.011
PL06	N37°06'21.81505"	W117°41'22.50787"	849.600 m	0.006	0.010
PL07	N37°06'22.72028"	W117°41'25.55859"	849.598 m	0.006	0.009
PL08	N37°06'23.60006"	W117°41'28.60374"	849.581 m	0.006	0.008
PL09	N37°06'24.46538"	W117°41'31.65760"	849.613 m	0.006	0.008
PL10	N37°06'25.44416"	W117°41'34.76526"	849.624 m	0.005	0.007
PL11	N37°06'26.45956"	W117°41'37.85134"	849.605 m	0.005	0.007

PL12	N37°06'27.38447"	W117°41'40.97410"	849.628 m	0.005	0.007
PL13	N37°06'28.34225"	W117°41'44.13242"	849.635 m	0.005	0.007
PL14	N37°06'29.27701"	W117°41'47.21215"	849.650 m	0.005	0.007
PL15	N37°06'30.24367"	W117°41'50.27467"	849.676 m	0.005	0.007
PL16	N37°06'31.17899"	W117°41'53.42086"	849.685 m	0.006	0.007
PL17	N37°06'32.15768"	W117°41'56.51979"	849.686 m	0.006	0.007
PL18	N37°06'33.16261"	W117°41'59.36994"	849.691 m	0.006	0.007
PL19	N37°06'34.13205"	W117°42'02.27384"	849.718 m	0.006	0.007
PL20	N37°06'35.06867"	W117°42'05.25682"	849.746 m	0.006	0.008
PL21	N37°06'36.00334"	W117°42'08.33000"	849.764 m	0.006	0.007
PL22	N37°06'37.03964"	W117°42'11.44717"	849.805 m	0.006	0.008
PL23	N37°06'37.78563"	W117°42'14.70948"	849.824 m	0.006	0.008
PL24	N37°06'38.61743"	W117°42'17.81200"	849.821 m	0.006	0.008
PL25	N37°06'39.55176"	W117°42'20.61390"	849.905 m	0.006	0.009
PL26	N37°06'40.43856"	W117°42'23.52573"	849.921 m	0.006	0.009
PL27	N37°06'41.49731"	W117°42'26.36382"	850.000 m	0.006	0.010
PL28	N37°06'42.44129"	W117°42'29.00298"	850.032 m	0.006	0.010
PL29	N37°06'43.43241"	W117°42'31.79631"	850.002 m	0.006	0.010
PL30	N37°06'44.38623"	W117°42'34.69841"	850.076 m	0.006	0.010
PL31	N37°06'45.39435"	W117°42'37.69904"	850.080 m	0.006	0.011
PL33	N37°06'46.36161"	W117°42'40.69250"	850.103 m	0.006	0.010
PL34	N37°06'47.19481"	W117°42'43.76564"	850.154 m	0.006	0.010
PL03	N37°06'18.95455"	W117°41'13.75500"	849.644 m	0.008	0.019
PL35	N37°06'48.17353"	W117°42'46.85593"	850.118 m	0.138	0.673
PL36	N37°06'48.17389"	W117°42'46.85592"	850.168 m	0.006	0.008
PL37	N37°06'49.03265"	W117°42'49.84020"	850.204 m	0.007	0.008
PL38	N37°06'49.97885"	W117°42'52.90404"	850.226 m	0.007	0.008
PL39	N37°06'50.93286"	W117°42'55.79806"	850.257 m	0.007	0.008
PL40	N37°06'51.85798"	W117°42'58.85027"	850.271 m	0.007	0.008
PL41	N37°06'52.77076"	W117°43'01.87076"	850.336 m	0.007	0.009
PL42	N37°06'53.71808"	W117°43'04.92733"	850.371 m	0.007	0.010
PL43	N37°06'54.54459"	W117°43'07.99139"	850.402 m	0.007	0.010
PL44	N37°06'55.46609"	W117°43'11.04712"	850.424 m	0.006	0.011
PL45	N37°06'56.42221"	W117°43'13.99673"	850.513 m	0.008	0.012
PL46	N37°06'57.32799"	W117°43'17.05778"	850.527 m	0.006	0.012
PL47	N37°06'58.22546"	W117°43'20.15538"	850.557 m	0.179	0.147
PL48	N37°06'59.13452"	W117°43'23.17220"	850.581 m	0.006	0.012
PL49	N37°07'00.05939"	W117°43'26.24373"	850.599 m	0.027	0.060
PL50	N37°07'00.96899"	W117°43'29.19897"	850.558 m	0.007	0.013
PL51	N37°07'01.89959"	W117°43'32.26153"	850.544 m	0.007	0.014
PL53	N37°07'02.82686"	W117°43'35.26005"	850.510 m	0.007	0.015

PL55	N37°07'03.53577"	W117°43'37.70994"	850.494 m	0.009	0.019
PL60	N37°07'02.26668"	W117°43'58.57790"	860.157 m	0.040	0.034
PL61	N37°07'03.37891"	W117°43'55.80581"	857.414 m	0.208	0.187
PL62	N37°07'04.30651"	W117°43'49.65180"	852.062 m	0.023	0.024
PL63	N37°07'11.53285"	W117°43'46.26440"	852.038 m	0.008	0.009
PL64	N37°07'11.53293"	W117°43'46.26442"	852.038 m	0.008	0.009
pla01	N37°07'03.03438"	W117°43'37.70670"	850.925 m	0.050	0.071
pla02	N37°07'00.24911"	W117°43'34.44209"	850.933 m	0.008	0.027
pla03	N37°06'58.40580"	W117°43'32.02435"	850.943 m	0.015	0.016
pla04	N37°06'56.49152"	W117°43'29.65756"	850.955 m	0.007	0.009
pla05	N37°06'54.60278"	W117°43'27.35548"	850.919 m	0.006	0.009
pla06	N37°06'52.71777"	W117°43'25.00583"	850.917 m	0.006	0.009
pla07	N37°06'50.81256"	W117°43'22.62546"	850.837 m	0.006	0.010
pla08	N37°06'48.92870"	W117°43'20.32794"	850.852 m	0.007	0.010
pla09	N37°06'46.92272"	W117°43'18.26418"	850.812 m	0.007	0.011
pla10	N37°06'45.02946"	W117°43'16.40065"	850.778 m	0.006	0.011
pla11	N37°06'43.24589"	W117°43'14.36129"	850.755 m	0.006	0.011
pla12	N37°06'41.41108"	W117°43'12.16601"	850.730 m	0.006	0.011
pla13	N37°06'39.56223"	W117°43'09.93655"	850.698 m	0.006	0.011
pla14	N37°06'37.73434"	W117°43'07.89887"	850.693 m	0.006	0.011
pla15	N37°06'36.11440"	W117°43'05.62925"	850.658 m	0.006	0.010
pla16	N37°06'34.92568"	W117°43'04.30142"	850.690 m	0.006	0.010
pla17	N37°06'35.58474"	W117°43'01.16286"	850.643 m	0.007	0.008
pla18	N37°06'36.29106"	W117°42'58.13670"	850.617 m	0.007	0.008
pla19	N37°06'37.13656"	W117°42'55.29731"	850.598 m	0.007	0.008
pla20	N37°06'37.90650"	W117°42'52.36229"	850.598 m	0.007	0.008
pla21	N37°06'38.71146"	W117°42'49.41592"	850.602 m	0.008	0.009
pla22	N37°06'39.53143"	W117°42'46.37488"	850.580 m	0.007	0.008
pla23	N37°06'40.26245"	W117°42'43.32736"	850.569 m	0.007	0.008
pla24	N37°06'40.97705"	W117°42'40.26020"	850.535 m	0.007	0.008
pla25	N37°06'41.68798"	W117°42'37.20326"	850.550 m	0.007	0.009
pla26	N37°06'42.43021"	W117°42'34.28989"	850.478 m	0.007	0.009
pla28	N37°06'43.12823"	W117°42'31.17522"	850.466 m	0.006	0.009
pla27	N37°06'43.90084"	W117°42'28.21755"	850.457 m	0.006	0.010
pla29	N37°06'44.61057"	W117°42'25.11060"	850.449 m	0.006	0.010
pla30	N37°06'45.37657"	W117°42'22.21276"	850.516 m	0.467	0.279
pla31	N37°06'45.94476"	W117°42'19.27405"	850.326 m	0.006	0.011
pla32	N37°06'46.54249"	W117°42'16.21830"	850.305 m	0.006	0.011
pla33	N37°06'47.25892"	W117°42'13.28025"	850.292 m	0.006	0.011
pla34	N37°06'47.93589"	W117°42'10.43875"	850.276 m	0.006	0.012
pla35	N37°06'48.62807"	W117°42'07.49224"	850.301 m	0.006	0.012

pla36	N37°06'49.29557"	W117°42'04.51432"	850.227 m	0.010	0.018
pla37	N37°06'50.13054"	W117°42'01.52865"	850.209 m	0.006	0.015
pla38	N37°06'50.90037"	W117°41'58.52724"	850.193 m	0.010	0.014
pla39	N37°06'48.71767"	W117°41'56.70813"	850.162 m	0.006	0.012
pla40	N37°06'46.55656"	W117°41'54.97423"	850.144 m	0.009	0.012
pla41	N37°06'44.35483"	W117°41'53.33920"	850.138 m	0.006	0.011
pla42	N37°06'42.12958"	W117°41'51.53803"	850.133 m	0.006	0.010
pla43	N37°06'40.03978"	W117°41'49.77111"	850.130 m	0.023	0.020
pla44	N37°06'37.87264"	W117°41'48.01940"	850.117 m	0.015	0.015
pla445	N37°06'35.78183"	W117°41'46.25135"	850.107 m	0.074	0.068
pla46	N37°06'33.60960"	W117°41'44.56634"	850.103 m	0.007	0.008
pla47	N37°06'31.40214"	W117°41'42.79484"	850.084 m	0.007	0.008
pla48	N37°06'31.40243"	W117°41'42.79476"	850.075 m	0.007	0.007
pla49	N37°06'28.89028"	W117°41'40.90020"	850.074 m	0.007	0.007
pla50	N37°06'26.66570"	W117°41'39.24409"	850.055 m	0.008	0.007
pla51	N37°06'24.43019"	W117°41'37.50094"	850.041 m	0.008	0.007
pla52	N37°06'22.05447"	W117°41'35.62917"	850.051 m	0.007	0.007
pla53	N37°06'19.85609"	W117°41'33.80539"	850.061 m	0.007	0.007
pla54	N37°06'17.58086"	W117°41'32.02410"	850.056 m	0.008	0.008
pla55	N37°06'15.35983"	W117°41'30.31898"	850.067 m	0.007	0.008
pla56	N37°06'13.10329"	W117°41'28.65802"	850.060 m	0.007	0.009
pla57	N37°06'11.03692"	W117°41'26.98064"	850.123 m	0.007	0.010
pla58	N37°06'12.41930"	W117°41'24.32750"	850.081 m	0.008	0.011
pla59	N37°06'13.53026"	W117°41'22.40803"	850.097 m	0.008	0.011
pla60	N37°06'15.17014"	W117°41'19.86990"	850.059 m	0.008	0.012
pla61	N37°06'16.71717"	W117°41'17.28429"	850.072 m	0.008	0.013
pla62	N37°06'18.29327"	W117°41'14.77783"	850.070 m	0.008	0.014
pla63	N37°06'19.83434"	W117°41'12.28654"	850.084 m	0.008	0.015
pla64	N37°06'21.35203"	W117°41'09.93226"	850.131 m	0.008	0.016
pla65	N37°06'22.82893"	W117°41'07.36029"	850.155 m	0.007	0.016
pla66	N37°06'23.55123"	W117°41'06.05944"	850.152 m	0.008	0.020
pla70	N37°06'56.91712"	W117°42'31.02052"	848.469 m	0.006	0.009
pla71	N37°06'58.84057"	W117°42'37.36805"	848.531 m	0.006	0.009
pla72	N37°07'00.34535"	W117°42'43.91484"	848.590 m	0.006	0.010
pla73	N37°07'01.79225"	W117°42'50.13973"	848.634 m	0.006	0.011
pla74	N37°07'04.69779"	W117°42'55.45696"	848.688 m	0.007	0.012
pla75	N37°07'08.54692"	W117°42'57.13391"	848.792 m	0.006	0.011
pla76	N37°07'06.00326"	W117°42'55.84981"	848.759 m	0.006	0.011
pla77	N37°07'03.54963"	W117°42'54.83586"	848.688 m	0.006	0.010
pla78	N37°07'00.93940"	W117°42'53.98528"	848.675 m	0.006	0.010
pla79	N37°06'58.29469"	W117°42'53.21768"	848.681 m	0.006	0.010

pla80	N37°06'55.69024"	W117°42'52.51471"	848.649 m	0.006	0.010
pla81	N37°06'52.97766"	W117°42'51.86232"	848.645 m	0.006	0.009
pla82	N37°06'50.37845"	W117°42'51.41419"	848.623 m	0.007	0.009
pla83	N37°06'47.71136"	W117°42'50.73815"	848.625 m	0.006	0.008
pla84	N37°06'42.38366"	W117°42'49.35117"	848.572 m	0.007	0.009
pla85	N37°06'37.08633"	W117°42'48.03471"	848.537 m	0.007	0.008
pla86	N37°06'31.79084"	W117°42'46.69456"	848.555 m	0.007	0.008
pla87	N37°06'26.60797"	W117°42'45.33836"	848.749 m	0.007	0.008
pla88	N37°06'28.03168"	W117°42'38.92363"	848.563 m	0.009	0.009
pla89	N37°06'29.50487"	W117°42'32.51341"	848.462 m	0.008	0.008
pla90	N37°06'30.96753"	W117°42'27.02558"	848.365 m	0.007	0.008
pla91	N37°06'32.37376"	W117°42'20.82530"	848.268 m	0.007	0.008
pla93	N37°06'33.89984"	W117°42'14.54024"	848.187 m	0.007	0.008
pla92	N37°06'35.40111"	W117°42'08.18616"	848.156 m	0.007	0.008
pla94	N37°06'36.85285"	W117°42'01.56974"	848.115 m	0.062	0.011
pla95	N37°06'38.21798"	W117°41'55.02918"	848.094 m	0.006	0.009
pla96	N37°06'39.51466"	W117°41'48.51781"	848.078 m	0.006	0.009
pla97	N37°06'41.08490"	W117°41'41.88594"	848.086 m	0.420	0.265
pla99	N37°06'42.49185"	W117°41'35.45311"	848.057 m	0.006	0.010
pla100	N37°06'43.49394"	W117°41'30.19998"	848.054 m	0.006	0.010
pla110	N37°06'33.59655"	W117°41'12.93639"	849.577 m	0.006	0.010
pla111	N37°06'33.59670"	W117°41'12.93636"	849.577 m	0.006	0.010
pla112	N37°06'33.58155"	W117°41'12.92803"	849.571 m	0.006	0.010
pla113	N37°06'36.85435"	W117°41'16.43379"	849.544 m	0.006	0.010
pla113	N37°06'36.85435"	W117°41'16.43378"	849.544 m	0.006	0.010
pla114	N37°06'36.85375"	W117°41'16.43450"	849.488 m	0.006	0.010
pla115	N37°06'36.85487"	W117°41'16.43437"	849.546 m	0.006	0.010
pla116	N37°06'38.51707"	W117°41'19.52779"	849.545 m	0.006	0.010
pla117	N37°06'40.43993"	W117°41'24.34219"	849.568 m	0.006	0.010
pla118	N37°06'41.30676"	W117°41'27.76688"	849.585 m	0.006	0.010
pla119	N37°06'42.12293"	W117°41'29.86955"	849.578 m	0.006	0.010
pla120	N37°06'43.13253"	W117°41'33.26449"	849.592 m	0.006	0.008
pla121	N37°06'43.97231"	W117°41'36.48255"	849.599 m	0.006	0.008
pla122	N37°06'44.84682"	W117°41'39.78478"	849.609 m	0.006	0.007
pla123	N37°06'45.72637"	W117°41'42.94183"	849.602 m	0.006	0.007
pla124	N37°06'46.63304"	W117°41'46.10149"	849.617 m	0.006	0.007
pla125	N37°06'47.55123"	W117°41'49.37115"	849.617 m	0.007	0.007
pla126	N37°06'48.36304"	W117°41'52.79066"	849.661 m	0.007	0.007
pla127	N37°06'49.21312"	W117°41'55.97800"	849.662 m	0.007	0.007
pla128	N37°06'50.08716"	W117°41'59.26866"	849.694 m	0.008	0.009
ola129	N37°06'40.53747"	W117°42'02.77999"	849.697 m	0.007	0.008

pla130	N37°06'39.57515"	W117°41'59.52945"	849.659 m	0.007	0.008
pla131	N37°06'38.52973"	W117°41'56.33417"	849.634 m	0.007	0.008
pla132	N37°06'37.50838"	W117°41'53.27898"	849.631 m	0.007	0.008
pla133	N37°06'36.54433"	W117°41'50.08293"	849.625 m	0.007	0.008
pla134	N37°06'35.52912"	W117°41'46.78040"	849.612 m	0.007	0.009
pla135	N37°06'34.52196"	W117°41'43.72106"	849.582 m	0.006	0.008
pla136	N37°06'33.55772"	W117°41'40.63627"	849.578 m	0.165	0.226
pla137	N37°06'32.53638"	W117°41'37.56632"	849.559 m	0.275	0.143
pla138	N37°06'31.58123"	W117°41'34.58744"	849.554 m	0.142	0.089
pla139	N37°06'30.56600"	W117°41'31.56878"	849.526 m	0.010	0.010
pla140	N37°06'29.61873"	W117°41'28.51721"	849.533 m	0.006	0.010
pla141	N37°06'28.56357"	W117°41'25.47160"	849.514 m	0.006	0.010
pla142	N37°06'27.64872"	W117°41'22.49605"	849.530 m	0.006	0.011
pla143	N37°06'26.64948"	W117°41'19.50922"	849.546 m	0.148	0.263
pla144	N37°06'25.63345"	W117°41'16.52230"	849.584 m	0.288	0.414
pla145	N37°06'24.66548"	W117°41'13.52431"	849.547 m	0.013	0.022
pla146	N37°06'23.72948"	W117°41'10.52672"	849.596 m	0.006	0.012
pla147	N37°06'22.59007"	W117°41'07.74819"	849.639 m	0.041	0.152
pla148	N37°06'22.12614"	W117°41'05.72917"	849.647 m	0.013	0.044
pla149	N37°06'11.51815"	W117°41'03.84845"	849.667 m	0.018	0.016
pla150	N37°06'12.19819"	W117°41'06.88015"	849.647 m	0.006	0.010
pla151	N37°06'12.90816"	W117°41'10.03799"	849.635 m	0.006	0.010
pla152	N37°06'13.62251"	W117°41'13.14375"	849.484 m	0.365	0.341
pla153	N37°06'14.53241"	W117°41'17.12819"	849.592 m	0.323	0.109
pla154	N37°06'15.30465"	W117°41'20.37909"	849.578 m	0.007	0.008
pla155	N37°06'16.09483"	W117°41'23.63666"	849.560 m	0.007	0.008
pla156	N37°06'16.84996"	W117°41'26.95018"	849.560 m	0.007	0.007
pla157	N37°06'17.62253"	W117°41'30.19163"	849.545 m	0.007	0.007
pla158	N37°06'18.40349"	W117°41'33.36723"	849.550 m	0.007	0.007
pla159	N37°06'19.17445"	W117°41'36.55714"	849.594 m	0.008	0.007
pla160	N37°06'19.80283"	W117°41'39.18767"	849.575 m	0.007	0.007
pla161	N37°06'20.51615"	W117°41'42.29856"	849.578 m	0.110	0.076

Willow Wash

Survey Point	Latitude	Longitude	Altitude (m)	Horizontal Precision (m)	Vertical Precision (m)
WW01	N37°19'46.76991"	W117°42'26.68474"	1803.070 m	0.006	0.007
WW02	N37°19'46.35824"	W117°42'26.69835"	1804.491 m	0.006	0.007
WW03	N37°19'45.77251"	W117°42'26.86249"	1806.270 m	0.006	0.007
WW04	N37°19'45.14282"	W117°42'27.38808"	1809.210 m	0.008	0.011

WW05	N37°19'44.91965"	W117°42'27.71173"	1810.419 m	1.113	1.041
WW06	N37°19'43.96071"	W117°42'28.01309"	1814.803 m	0.248	0.167
WW07	N37°19'43.15774"	W117°42'28.06231"	1818.280 m	0.008	0.013
WW08	N37°19'42.26055"	W117°42'27.96877"	1823.372 m	0.033	0.016
WW09	N37°19'41.65184"	W117°42'27.56123"	1829.548 m	1.240	0.738
WW10	N37°19'41.25687"	W117°42'27.00687"	1833.686 m	0.006	0.011
WW11	N37°19'41.46042"	W117°42'25.62265"	1836.653 m	0.006	0.010
WW12	N37°19'42.14051"	W117°42'25.45684"	1831.916 m	0.006	0.010
WW13	N37°19'43.94720"	W117°42'25.18304"	1822.325 m	0.006	0.009
WW14	N37°19'45.53518"	W117°42'24.44860"	1813.604 m	0.894	0.460
WW15	N37°19'46.60248"	W117°42'23.95872"	1806.481 m	0.006	0.008
WW16	N37°19'48.35083"	W117°42'23.04662"	1794.946 m	1.012	0.326
WW17	N37°19'50.23812"	W117°42'23.14544"	1784.299 m	1.131	0.805
WW18	N37°19'51.28403"	W117°42'23.00836"	1779.341 m	1.233	0.931
WW19	N37°19'52.90552"	W117°42'22.52324"	1767.865 m	0.779	0.848
WW20	N37°19'55.51051"	W117°42'22.31718"	1747.939 m	1.000	0.559
WW21	N37°19'56.32547"	W117°42'21.90114"	1741.839 m	0.245	0.198
WW23	N37°19'57.39236"	W117°42'22.08889"	1735.883 m	0.521	0.227
WW24	N37°19'58.06844"	W117°42'22.09716"	1732.293 m	0.006	0.009
WW25	N37°19'58.60374"	W117°42'22.00427"	1729.660 m	0.006	0.010
ww16 01	N37°19'38.64334"	W117°42'31.15641"	1835.541 m	0.007	0.009
ww16 02	N37°19'37.79156"	W117°42'31.62386"	1839.819 m	0.249	0.329
ww16 03	N37°19'37.07390"	W117°42'32.26089"	1843.222 m	0.007	0.009
ww16 04	N37°19'36.22566"	W117°42'32.73627"	1847.700 m	1.694	2.602
ww16 05	N37°19'36.20529"	W117°42'32.72615"	1847.383 m	0.007	0.010
ww16 06	N37°19'35.33612"	W117°42'33.34994"	1851.341 m	0.019	0.013
ww16 07	N37°19'34.29414"	W117°42'33.85412"	1855.970 m	0.293	0.047
ww16 08	N37°19'33.42200"	W117°42'34.34826"	1860.144 m	1.169	0.826
ww16 09	N37°19'32.66898"	W117°42'34.92044"	1863.555 m	0.006	0.010
ww16 10	N37°19'39.58198"	W117°42'30.72545"	1832.116 m	0.128	0.106
ww16 11	N37°19'40.48146"	W117°42'30.07034"	1828.339 m	1.528	0.922
ww16 12	N37°19'41.42923"	W117°42'29.63282"	1823.532 m	1.336	0.824
ww16 13	N37°19'42.35983"	W117°42'29.52624"	1819.567 m	1.185	0.999
ww16 14	N37°19'43.27234"	W117°42'29.78670"	1815.951 m	0.007	0.010
ww16 15	N37°19'44.39854"	W117°42'29.68519"	1811.217 m	1.106	0.762
ww16 16	N37°19'45.41794"	W117°42'29.74439"	1807.650 m	0.010	0.010
ww16 17	N37°19'46.44184"	W117°42'29.38618"	1803.842 m	0.006	0.010
ww16 18	N37°19'47.31245"	W117°42'28.88073"	1800.139 m	0.006	0.009
ww16 19	N37°19'48.25782"	W117°42'28.30678"	1796.228 m	0.006	0.009
ww16 20	N37°19'48.59457"	W117°42'28.06138"	1794.830 m	0.007	0.010
ww16 21	N37°19'49.55279"	W117°42'28.15678"	1790.767 m	0.006	0.009

ww16 22	N37°19'50.24481"	W117°42'29.03786"	1786.313 m	0.007	0.009
ww16 23	N37°19'50.67780"	W117°42'28.28107"	1786.321 m	0.007	0.009
ww16 25	N37°19'49.88347"	W117°42'27.68377"	1790.095 m	0.007	0.010
ww16 24	N37°19'49.04972"	W117°42'27.51273"	1793.018 m	0.007	0.011

APPENDIX B - DETAILS OF THE SAGITTA CORRECTION

Unfortunately a slight correction must be done to the distance between two positions. First latitude/ longitude measurements were converted to an x-y coordinate scheme with a preferred scale of meters. This is done by keeping the longitude constant, while finding the distance between the first reference point and the subsequent points to find the latitude direction distance in meters. These values use the distance equation (equation 6.1). For example, to convert the second survey point (n =2), use (lat_1, $long_1$) and (lat_2, $long_1$). The third survey point would thus be (lat_1, $long_1$) and (lat_3, $long_1$) until point n which would use (lat_1, $long_1$) and (lat_n, $long_1$). For the y coordinates, the same procedure would be done to find the y- values for the survey point, but reversed between the latitude and the longitude. For point n, use (lat_1, $long_1$) and (lat_1, $long_n$).

For the sagitta correction, two reference points are needed. The author used the first and last point measured in a survey line (see figure). The sagitta has been derived as (Larson and Hostetler, 2007):

$$s = r - \sqrt{r^2 - l^2} \qquad \text{(equation B.1)}$$

Where s is sagitta distance

r is the radius

l is half length of the cord

The half-length of the cord is the distance between the survey point and the trend line;

for the radius, we use the distance equation between a point and a line. The line in this case is the perpendicular line to the trendline (see figure XX). For that equation we use the distance between a point and a line, where the line is the trendline and the point is the GPS measurement. This equation is (Larson and Hostetler, 2007) :

$$d = \frac{| a \cdot x_o + b \cdot y_o + c |}{\sqrt{a^2 + b^2}} \qquad \text{(eq B.2)}$$

where d - distance between a line and a point

$a \cdot x_o + b \cdot y_o + c$ is the equation for the line $a \cdot x_o + b \cdot y_o + c = 0$

$(x_n,\ y_n)$ is the point

Trendline is the linear line between the first and last points in a scarp survey. First point is n=1 at (lat_1, $long_1$) typically (0,0), final point is n= n, or (lat_n, $long_n$)

If we define n =1 as the origin, or (0,0):

$$y = slope \cdot x + 0 \qquad \text{(eq B.3)}$$

The slope between these points (n=1, (lat_1, $long_1$) = (0,0) or n = n, (lat_n, $long_n$)) would be:

$$y = \frac{(long_n - long_1)}{(lat_n - lat_1)} \cdot x + 0 \qquad \text{(eq B.4)}$$

Or

$$y = \frac{long_n}{lat_n} \cdot x + 0 \qquad \text{(eq B.5)}$$

Equation 6.6 can be rewritten in the form of $a \cdot x_o + b \cdot y_o + c = 0$:

$$long_n \cdot x - lat_n \cdot y + 0 \cdot c = 0 \qquad \text{(eq B.6)}$$

Or simplified as:

$$long_n \cdot x - lat_n \cdot y = 0 \qquad \text{(eq B.7)}$$

If we use the above equation with equation 6.3 for the distance between a point and a line we have:

$$d = \frac{| a \cdot x_0 + b \cdot y_0 + c |}{\sqrt{a^2 + b^2}} \qquad \text{(copy of eq B.2)}$$

$$l = \frac{1}{2} length\,of\,cord = \frac{| long_n \cdot x - lat_n \cdot y |}{\sqrt{(long_n)^2 + (lat_n)^2}} \qquad \text{(eq B.8)}$$

Equation for the sagitta correction will be:

$$s = r - \sqrt{r^2 - l^2} \qquad \text{(copy eq B.1)}$$

Where *l* is equation B.6 (1/2 length of cord)

And r is equation B.1 (distance between two points):

If we use substitute these formula we get a more complicated sagitta correction (eq B.7)

s =

$$2 \cdot R \cdot \left(\sqrt{sin^2\left(\frac{\mathrm{lat}_r - \mathrm{lat}_n}{2}\right) + \cos\left(\mathrm{lat}_r\right) \cdot \cos\left(\mathrm{lat}_n\right) \cdot sin^2\left(\frac{\mathrm{long}_r - \mathrm{long}_n}{2}\right)} \right) - \sqrt{4 \cdot R^2 \cdot \left| sin^2\left(\frac{\mathrm{lat}_r - \mathrm{lat}_n}{2}\right) + \cos\left(\mathrm{lat}_r\right) \cdot \cos\left(\mathrm{lat}_n\right) \cdot sin^2\left(\frac{\mathrm{long}_r - \mathrm{long}_n}{2}\right) \right| - \frac{(long_n \cdot x - lat_n \cdot y)^2}{\left|(long_n)^2 + (lat_n)^2\right|}}$$

(Eq B.9)

The final distances used for the projection onto a trendline $long_n \cdot x - lat_n \cdot y = 0$ with reference end points of n =1 (lat_1, long_1) and n = n (lat_n, long_n). Equation (B.10):

$$d = 2 \cdot R \cdot \left(\sqrt{sin^2\left(\frac{\mathrm{lat}_r - \mathrm{lat}_n}{2}\right) + \cos\left(\mathrm{lat}_r\right) \cdot \cos\left(\mathrm{lat}_n\right) \cdot sin^2\left(\frac{\mathrm{long}_r - \mathrm{long}_n}{2}\right)} \right) - \text{sagitta correction (s)}$$

Or (eq B.11):

$$\begin{aligned} d &= 2 \cdot R \cdot \left(\sqrt{sin^2\left(\frac{\mathrm{lat}_r - \mathrm{lat}_n}{2}\right) + \cos\left(\mathrm{lat}_r\right) \cdot \cos\left(\mathrm{lat}_n\right) \cdot sin^2\left(\frac{\mathrm{long}_r - \mathrm{long}_n}{2}\right)} \right) - 2 \cdot R \\ &\cdot \left(\sqrt{sin^2\left(\frac{\mathrm{lat}_r - \mathrm{lat}_n}{2}\right) + \cos\left(\mathrm{lat}_r\right) \cdot \cos\left(\mathrm{lat}_n\right) \cdot sin^2\left(\frac{\mathrm{long}_r - \mathrm{long}_n}{2}\right)} \right) \\ &- \sqrt{4 \cdot R^2 \cdot \left| sin^2\left(\frac{\mathrm{lat}_r - \mathrm{lat}_n}{2}\right) + \cos\left(\mathrm{lat}_r\right) \cdot \cos\left(\mathrm{lat}_n\right) \cdot sin^2\left(\frac{\mathrm{long}_r - \mathrm{long}_n}{2}\right) \right| - \frac{(long_n \cdot x - lat_n \cdot y)^2}{\left|(long_n)^2 + (lat_n)^2\right|}} \end{aligned}$$

APPENDIX C - GEOLOGIC OBSERVATIONS

Survey point	Latitude	Longitude	Strike	Dip	Foliation		Cleavage
SD001	37° 13.591' N	117° 44.667' w	355° N	5° W			
SD002	37° 13.609' N	117° 44.604' W	340° N	13° W			
SD003	37° 13.389' N	117° 44.688' W	270° N	11° W			
SD004	37° 13.525' N	117° 43.690' W	140° N	19° E			
SD005	37° 13.648' N	117° 43.073' W	350° N	60° W			
SD006	37° 13.600' N	117° 43.684' W	70° N	23° E			
SD007	37° 13.697' N	117° 43.802 ' W	185° N	19° E			
SD008	37° 13.992' N	117° 44.079' W	155° N	35° E			
SD009	37° 14.066' N	117° 43.912' W	140° N	64° S			
SD010	37° 14.055' N	117° 43.828' W	86° N	43° S			
SD011	37° 14.060' N	117° 43.706' W	320° N	38° E			
SD012	37° 13.959' N	117° 43.418' W	128° N	38° S			
SD013	37° 13.864' N	117° 43.497' W	280° N	23° S			
SD014	37° 13.684' N	117° 43.252' W			142° N	83° NE	
SD015	37° 13.684' N	117° 43.252' W	2° N	76° W			
SD016	37° 13.684' N	117° 43.252' W			285° N	73° W	
SD017	37° 13.728' N	117° 43.185' W	340° N	86° E			
SD018	37° 13.739' N	117° 43.290' W	300° N	66° W			
SD019	37° 14.204' N	117° 43.931' W			327° N	20° E	
SD020	37° 14.208' N	117° 43.923' W			218° N	15° E	
SD021	37° 14.208' N	117° 43.923' W			183° N	50° W	
SD022	37° 14.213' N	117° 43.936' W	112° N	20° SW			
SD023	37° 14.384' N	117° 43.836' W	188° N	40° W			
SD024	37° 14.384' N	117° 43.836' W			171° N	56° W	
SD025	37° 14.358' N	117° 43.841' W	233° N	14° E			
SD026	37° 14.358' N	117° 43.841' W	104° N	34° S			
SD027	37° 14.342' N	117° 43.701' W			138° N	18° SW	
SD028	37° 14.310' N	117° 43.446' W			4° N	85° W	
SD029	37° 14.296' N	117° 43.374' W	156° N	24° W			
SD030	37° 14.274' N	117° 43.428' W	292° N	35° W			
SD031	37° 14.230' N	117° 43.432' W	180° N	37° E			
SD032	37° 14.159' N	117° 43.562' W			182° N	71° W	
SD033	37° 14.111' N	117° 43.581' W			344° N	40° W	
SD034	37° 13.417' N	117° 44.169' W	155° N	6° W			
SD035	37° 13.358' N	117° 44.160' W	355° N	45° E			
SD036	37° 13.358' N	117° 44.160' W	204° N	40° W			
SD037	37° 13.368' N	117° 44.174' W	10° N	53° E			

SD038	37° 13.403' N	117° 44.095' W	335° N	43° E				
SD039	37° 13.402' N	117° 43.995' W	126° N	7° S				
SD040	37° 13.411' N	117° 44.016' W	150° N	26° W				
SD041	37° 13.349' N	117° 43.977' W	68° N	15° S				
SD042	37° 13.302' N	117° 43.886' W	233° N	24° S				
SD043	37° 13.317' N	117° 43.704' W	226° N	46°S				
SD044	37° 13.349' N	117° 43.620' W	211° N	26° SE				
SD045	37° 13.152' N	117° 43.610' W	11° N	15° S				
SD046	37° 13.076' N	117° 43.874' W	25° N	10° SE				
SD047	37° 13.079' N	117° 43.907' W	55° N	15° N				
SD048	37° 13.029' N	117° 44.088' W	9° N	16° E				
SD049	37° 12.994' N	117° 44.112' W	22° N	46° E				
SD050	37° 13.000' N	117° 44.155' W	194° N	50° E				
SD051	37° 12.989' N	117° 44.214' W	202° N	37° E				
SD052	37° 13.310' N	117° 44.223' W	15° N	40° E				
SD053	37° 13.267' N	117° 44.239' W	225° N	21° E				
SD054	37° 13.210' N	117° 44.217' W	165° N	46° N				
SD055	37° 13.209' N	117° 44.271' W	38° N	26° N				
SD056	37° 13.183' N	117° 44.256' W	35° N	25° E				
SD057	37° 13.113' N	117° 44.204' W	70° N	20° E				
SD058	37°15'56.15"N	118° 5'14.34"W	5° N	90°				
SD059	37°16'4.53"N	118° 5'13.62"W	32° N	85° E				
SD060	37°16'3.47"N	118° 5'17.32"W			175° N	80° W		
SD061	37°16'3.47"N	118° 5'17.32"W	355° N	80° E				
SD062	37°16'4.05"N	118° 5'24.81"W	5° N	46° E				
SD063	37°16'6.41"N	118° 5'24.85"W	153° N	33° N				
SD064	37°16'10.92"N	118° 5'28.68"W	163° N	31° E				
SD065	37°16'15.60"N	118° 5'36.59"W					21° N	70° W
SD066	37°16'15.60"N	118° 5'36.59"W			70° N	76° SE		
SD067	37°16'17.82"N	118° 5'42.11"W			165° N	23° NE		
SD068	37°16'18.89"N	118° 5'51.19"W			243° N	22° N		
SD069	37°18'42.22"N	118° 8'2.67"W	265° N	21° S				
SD070	37°17'13.26"N	118° 5'28.12"W	23° N	35° E				
SD071	37°17'27.92"N	118° 6'7.33"W	23° N	35° E				
SD072	37°17'29.06"N	118° 6'10.33"W	48° N	83° W				
SD073	37°17'31.09"N	118° 6'20.63"W	205° N	36° E				
SD074	37°17'32.88"N	118° 6'23.82"W	8° N	29° E				
SD075	37°17'33.51"N	118° 6'29.17"W	49° N	42° E ?				
SD076	37°17'39.81"N	118° 6'32.96"W	303° N	26° N				
SD077	37°17'34.14"N	118° 6'33.65"W	216° N	26° E				
SD078	37°17'30.66"N	118° 6'32.46"W	218° N	33° E				

SD079	37°15'53.18"N	118° 8'11.05"W	208° N 31° W		
SD080	37°16'4.45"N	118° 8'0.67"W	50° N 24° W		
SD081	37°16'10.13"N	118° 7'59.21"W	215° N 27° W		
SD082	37°16'10.13"N	118° 7'59.21"W		2° N 54° W	
SD083	37°16'15.34"N	118° 7'56.84"W	35° N 55° W		
SD084	37°16'21.34"N	118° 7'57.87"W	37° N 44° W		
SD085	37°16'27.55"N	118° 7'54.59"W	30° N 50° W		
SD086	37°16'33.03"N	118° 7'53.19"W	31° N 54° N		
SD087	37°16'40.74"N	118° 7'56.76"W	228° N 64° N		
SD088	37°16'50.97"N	118° 7'55.17"W	219° N 47° E		
SD089	37°16'51.97"N	118° 7'48.84"W	62° N 23° E		
SD090	37°17'4.07"N	118° 7'39.98"W	295° N 18° N		
SD091	37°17'6.50"N	118° 7'30.56"W	45° N 18° W		
SD092	37°17'11.09"N	118° 7'5.83"W	45° N 41° E		
SD093	37°17'10.57"N	118° 6'51.03"W	212° N 49° E		
SD094	37°17'15.46"N	118° 6'44.69"W	65° N 44° E		
SD095	37°17'17.43"N	118° 6'19.49"W	64° N 60° W		
SD096	37°17'17.43"N	118° 6'19.49"W			238° N 65° W
SD097	37°17'13.18"N	118° 5'28.78"W	283° N 28° E		
SD098	37°16'45.49"N	118° 4'55.69"W	30° N 29° NW		
SD099	37°16'21.54"N	118° 5'10.86"W			355° N 40° W
SD100	37°16'21.93"N	118° 5'11.18"W	325° N 80° E		
SD101	37°16'28.70"N	118° 5'10.24"W	200° N 76° W		
SD102	37°16'29.85"N	118° 5'11.47"W			10° N 70° W
SD103	37°16'31.91"N	118° 5'8.54"W			15° N 53° W
SD104	37°13'51.63"N	117°38'30.56"W	357° N 11° E		
SD105	37°13'45.04"N	117°38'30.13"W	43° N 45° N		
SD106	37°13'39.81"N	117°38'28.33"W	30° N 58° N		
SD107	37°13'32.81"N	117°38'27.98"W	208° N 55° NW		
SD108	37°13'23.74"N	117°38'26.60"W	239° N 24° S		
SD109	37°13'16.62"N	117°38'25.13"W	303° N 90°		
SD110	37°12'55.62"N	117°38'34.64"W	282° N 4° E		
SD111	37°12'44.94"N	117°38'41.49"W	238° N 3° E		
SD112	37°12'13.37"N	117°39'34.91"W	191° N 50° E		
SD113	37°11'35.13"N	117°40'19.42"W	310° N 43° E		
SD114	37°11'33.34"N	117°41'16.31"W	44° N 58° E		
SD115	37°11'52.84"N	117°41'23.97"W	5° N 65° E		
SD116	37°12'5.62"N	117°41'27.68"W	208° N 60° E		
SD117	37°13'15.12"N	117°41'1.60"W	143° N 73° N		
SD118	37°14'29.73"N	117°41'7.39"W	154° N 40° N		
SD119	37°11'47.17"N	117°42'40.00"W	0° N 71° E		

SD120	37°12'52.40"N	117°42'40.93"W	167° N	45° W			
SD121	37°12'42.14"N	117°41'49.90"W				310° N	60° E
SD122	37°12'59.21"N	117°41'59.25"W	18° N	78°			
SD123	37°13'13.53"N	117°42'11.09"W				78° N	30° S
SD124	37°13'45.68"N	117°42'46.16"W	0° N	71° W			
SD125	37°13'47.60"N	117°42'52.14"W	204° N	16° W			
SD126	37°13'44.76"N	117°42'57.07"W	345° N	33° W			
SD127	37°13'43.70"N	117°42'58.88"W	163° N	55° W			
SD128	37°13'41.00"N	117°43'1.02"W	173° N	45° W			
SD129	37°13'36.82"N	117°43'3.38"W				154° N	69° W
SD130	37°13'37.33"N	117°43'4.51"W				170° N	65° W
SD131	37°13'36.54"N	117°43'6.87"W	178° N	61° W			
SD132	37°13'32.88"N	117°43'13.86"W				90° N	39° S
SD133	37°13'32.35"N	117°43'15.34"W	230° N	7° S			
SD134	37°13'31.36"N	117°43'17.79"W	26° N	26° W			
SD135	37°13'28.51"N	117°43'28.02"W	76° N	12° W			
SD136	37°13'28.51"N	117°43'28.02"W	219° N	24° S			
SD137	37°13'27.84"N	117°43'32.62"W	232° N	31° S			
SD138	37°13'26.74"N	117°43'38.01"W	8° N	34° E			
SD139	37°13'26.67"N	117°43'38.78"W	228° N	20° E			
SD140	37°13'26.03"N	117°43'46.04"W	213° N	14° SE			
SD141	37°13'26.22"N	117°43'48.14"W	220° N	21° E			
SD142	37°13'25.34"N	117°43'52.42"W	248° N	34° E			
SD143	37°13'25.58"N	117°43'53.47"W	67° N	20° S			
SD144	37°13'25.78"N	117°43'57.97"W	275° N	4° W			
SD145	37°13'25.94"N	117°44'0.56"W	322° N	20° S			
SD146	37°13'25.94"N	117°44'0.56"W	202° N	20° W			
SD147	37°13'20.89"N	117°44'23.08"W	120° N	12° W			
SD148	37°13'20.69"N	117°44'27.31"W	82° N	12° E			
SD149	37° 4'16.43"N	117°38'6.57"W	8° N	29° E			
SD150	37° 4'16.44"N	117°38'4.96"W	181° N	47° E			
SD151	37° 4'16.33"N	117°38'3.86"W	8° N	33° E			
SD152	37° 4'16.10"N	117°38'4.02"W				20° N	16° E
SD154	37° 4'16.01"N	117°38'8.19"W	162° N	25° E			
SD155	37° 4'14.17"N	117°38'10.65"W	173° N	44° E			
SD156	37° 4'11.82"N	117°38'13.29"W	8° N	38° E			
SD157	37° 4'10.97"N	117°38'16.80"W	9° N	29° E			
SD158	37° 4'12.16"N	117°38'18.24"W	12° N	15° W			
SD159	37° 4'12.70"N	117°38'19.53"W	4° N	4° W			
SD160	37° 4'11.15"N	117°38'20.54"W	169° N	28° W			
SD161	37° 4'11.49"N	117°38'21.23"W	72° N	20° N			

SD162	37° 4'12.04"N	117°38'22.71"W	223° N 33° NW		
SD163			243° N 12° SW		
SD164	37° 4'12.13"N	117°38'21.23"W	189° N 10° S		
SD165	37° 4'12.30"N	117°38'20.76"W	105° N ~2° S		
SD166	37° 4'11.95"N	117°38'20.99"W	213° N 12° SW		
SD167	37° 4'43.18"N	117°38'30.13"W	25° N 18° W		
SD168	37° 4'21.09"N	117°38'9.97"W	20° N 18° E		
SD169	"	"			28° N 60° E
SD170	37° 4'20.61"N	117°38'8.02"W	176° N 37° E		
SD171	37° 4'20.46"N	117°38'5.92"W	199° N 26° E		
SD172	37° 4'20.46"N	117°38'5.92"W			22° N 63° E
SD173	37° 4'19.81"N	117°38'4.78"W	9° N 41° E		
SD174	37° 4'20.25"N	117°38'3.63"W	15° N 35° E		
SD175	37° 4'19.94"N	117°38'2.64"W	188° N 41° E		
SD176	37° 4'20.37"N	117°38'0.47"W	10° N 52° E		
SD177	37° 4'19.76"N	117°38'10.56"W	193° N 34° E		